

# **Tungsten isotope constraints on Archean geodynamics**

Inaugural-Dissertation

zur

Erlangung des Doktorgrades

der Mathematisch-Naturwissenschaftlichen Fakultät

der Universität zu Köln

vorgelegt von

**Jonas Tusch**

aus Meerbusch

Köln, 2020



Berichterstatter: Prof. Dr. Carsten Munker  
PD Dr. Daniel Herwartz  
Dr. Kristoffer Szilas

Tag der mündlichen Prüfung: 10.09.2020

*This thesis is dedicated to my wife Lena*

## Table of contents

<b>I. Abstract.....</b>	<b>1</b>
<b>II. Kurzzusammenfassung .....</b>	<b>3</b>
<b>III. Introduction .....</b>	<b>6</b>
<b>Origin and evolution of the Earth .....</b>	<b>6</b>
<b>Early Earth Processes (Moon-forming impact, accretion history, late veneer) .....</b>	<b>7</b>
<b>Tectonic Regimes, Archean rocks and their spatial distribution .....</b>	<b>10</b>
<b>Application of short-lived isotope systems .....</b>	<b>14</b>
<b>Mobility and secondary overprint of W and the implication for <sup>182</sup>W anomalies.....</b>	<b>16</b>
<b><sup>182</sup>W isotope systematics of the terrestrial mantle .....</b>	<b>16</b>
<b>Significance of constraints on the dynamics of Early Earth processes .....</b>	<b>19</b>
<b>IV. Sythesis .....</b>	<b>21</b>
<b>1 Uniform <sup>182</sup>W isotope compositions in Eoarchean rocks from the Isua region, SW Greenland: the role of early silicate differentiation and missing late veneer.....</b>	<b>25</b>
<b>1.1 Abstract .....</b>	<b>25</b>
<b>1.2 Introduction.....</b>	<b>26</b>
<b>1.3 Methods.....</b>	<b>28</b>
1.3.1 Whole rock major, trace element and isotope dilution measurements (HFSE, Th & U).....	29
1.3.2 Ion exchange protocol for high precision W isotope measurements .....	30
1.3.3 Mass spectrometry for high precision <sup>182</sup> W isotope measurements.....	34
<b>1.4 Geological background and samples .....</b>	<b>37</b>
<b>1.5 Results.....</b>	<b>43</b>
<b>1.6 Discussion .....</b>	<b>48</b>
1.6.1 Methodology .....	48
1.6.2 Elemental behavior of W in rocks from the Isua region.....	53
1.6.3 Significance of uniform <sup>182</sup> W isotope compositions .....	57
1.6.4 Significance of the <sup>182</sup> W and W/Th signatures in mantle-like peridotites .....	59
1.6.5 Origin of <sup>182</sup> W isotope anomalies in SW Greenland.....	60
<b>1.7 Conclusion .....</b>	<b>64</b>

<b>2</b>	<b>Convective isolation of Hadean mantle reservoirs through Archean time.</b>	<b>66</b>
2.1	Abstract .....	66
2.2	Introduction .....	67
2.3	Geological background and samples .....	68
2.4	Results .....	71
2.5	Discussion .....	75
2.6	Conclusion .....	77
2.7	Method Section .....	78
2.7.1	<i>Analytical protocol</i> .....	78
2.7.2	<i>Geological background</i> .....	81
2.7.3	<i>Sample selection</i> .....	83
2.7.4	<i>Secular evolution of <sup>182</sup>W isotope anomalies</i> .....	86
<b>3</b>	<b>Long-term preservation of Hadean protocrust in Earth's mantle .....</b>	<b>88</b>
3.1	Abstract .....	88
3.2	Introduction .....	89
3.3	Geological and methodological overview .....	90
3.4	Results .....	90
3.5	Discussion .....	91
3.6	Conclusions .....	101
3.7	Method section .....	101
3.7.1	<i>Geological background of our sample selection</i> .....	101
3.7.2	<i>Lower protocrust delamination model</i> .....	106
3.7.3	<i>Analytical protocol</i> .....	110
	<b>References .....</b>	<b>113</b>
	<b>Appendix .....</b>	<b>137</b>
	Appendix A.....	137
	Appendix B.....	145
	Appendix C.....	159
	<b>Acknowledgements .....</b>	<b>165</b>
	<b>Erklärung .....</b>	<b>167</b>

## I. Abstract

Geodynamics on Earth are active since more than 4 billion years and have continuously lead to differentiation and homogenization of mantle and crust. However, evidence from short-lived nuclide decay systems (e.g.  $^{129}\text{I} - ^{129}\text{Xe}$  and  $^{146}\text{Sm} - ^{142}\text{Nd}$ ) suggest that primordial heterogeneities, which formed in the early Hadean Eon (i.e. during the first ca. 100 million years after formation of the Earth), survived for a long period of time – in some cases for Eons and until present day. Studying rocks that display variations in the decay products of short-lived nuclide decay systems offer two intriguing perspectives: (1) The cause for their formation refers to processes that must have had operated at a time when no other witnesses preserved in the geological rock record. (2) Understanding the mechanisms that allowed for their long-term preservation provides important insights into the temporal evolution of the bulk silicate Earth (BSE) and into the processes that lead to the present-day state of the mantle, including the onset of plate tectonic processes on Earth.

One of the short-lived decay series that has increasingly been applied in geochemistry is the  $^{182}\text{Hf}-^{182}\text{W}$  decay system with a half-life of 8.9 million years (Vockenhuber et al., 2004)). Over the past decade, several studies investigated W isotope systematics in terrestrial rocks and found differences in the relative abundance of  $^{182}\text{W}$ . While Archean rocks were found to exhibit predominantly elevated  $^{182}\text{W}$  isotope compositions compared to the modern depleted mantle, modern oceanic island basalts (OIBs) and one Archean komatiites system (the ca. 3.55 Ga Schapenburg komatiite suite from the Kaapvaal Craton, southern Africa) were shown to display negative anomalies. These findings were interpreted as evidence for the preservation of early-formed heterogeneities in the sources of Archean rocks and taken as evidence for the presence of primordial mantle components that participate to the provenance of modern igneous reservoirs. However, the processes that lead to the formation of these reservoirs remained ambiguous. These processes include (1) incomplete equilibration of the mantle source with late accretionary material (late accretion hypothesis), (2) early fractionation of Hf from W by silicate crystal-liquid fractionation, e.g., in an early magma ocean, or (3) core-mantle interaction. Matters are further complicated because secondary processes (fluid-mediated alteration) often obscured primary W budgets of metamorphosed Archean rock assemblages and the analytical standards to obtain

high-precision  $^{182}\text{W}$  isotope measurements turned out to be challenging. In this study, an analytical protocol is presented to obtain high-precision  $^{182}\text{W}$  isotope measurements on samples with low bulk-rock W concentrations (several ng/g). In three chapters we report high-precision  $^{182}\text{W}$  isotope data for Archean rocks from the ca. 3.9-3.6 Ga Itsaq Gneiss Complex of southern West Greenland (**chapter 1**), the ca. 3.6-3.2 Ga Pilbara Craton, NW Australia (**chapter 2**), and the ca. 3.6-3.2 Ga Kaapvaal Craton, southern Africa (**chapter 3**). In all studies, we combine  $^{182}\text{W}$  isotope analysis with high-precision isotope dilution measurements for high field strength element (HFSE), U, and Th abundances, to assess the elemental W systematics in our samples. This allows us to obtain a precise understanding of the primary and secondary processes that modified the W abundances and isotope compositions. As we demonstrate, the elemental W budgets of many mantle-derived rocks are dominated by metasomatic agents that mix reservoirs of variable  $^{182}\text{W}$  isotope compositions and obscure primary signatures (**chapters 1 and 2**). If not taken into consideration, this can lead to ambiguous interpretations of  $^{182}\text{W}$  isotope compositions observed in Archean lithostratigraphic successions. Our studies on rocks from different Archean cratons reveal that several processes are responsible for the origin of  $^{182}\text{W}$  isotope anomalies. Excesses of  $^{182}\text{W}$  in rocks from the Pilbara Craton (**chapter 2**) are best explained by missing late accreted additions in their mantle sources. Anomalies in rocks from the Itsaq Gneiss Complex (**chapter 1**) and the Kaapvaal Craton (**chapter 3**) instead were inherited from mantle sources that underwent early silicate differentiation during the lifetime of  $^{182}\text{Hf}$  (i.e. in the first ca. 60 million years after Solar System formation). Our results demonstrate that these Hadean signatures remained isolated in the mantle for several hundred million years. Understanding the evolution of  $^{182}\text{W}$  isotope systematics in the BSE through time requires comprehensive studies of lithostratigraphic successions that cover relatively long time frames of Archean geodynamic evolution, as shown by our study on the geological rock record of the Pilbara Craton (**chapter 2**). We further demonstrate that information about the temporal evolution of  $^{182}\text{W}$  isotope systematics of individual cratons is archived in Archean shales, which provide an average of the  $^{182}\text{W}$  isotope composition of the upper crust (**chapter 2**). These findings allow for observational constraints, which have important implications for understanding timescales of geodynamic processes on the early Earth (e.g. mantle stirring rates). As reported in **chapter 3**, rocks from the Kaapvaal Craton display correlations between  $^{182}\text{W}$  isotope compositions and initial



$\epsilon\text{Nd}_{(t)}$  and  $\epsilon\text{Hf}_{(t)}$  values. To our knowledge, this is the very first co-variation observed between  $^{182}\text{W}$  isotope systematics and long-lived radiogenic nuclides ( $^{147}\text{Sm}$ - $^{143}\text{Nd}$  and  $^{176}\text{Lu}$ - $^{176}\text{Hf}$  systematics). The only plausible model to explain these patterns is the presence of recycled mafic restites from Hadean protocrust in the ancient mantle beneath the Kaapvaal Craton. As further demonstrated by our model, the striking isotopic similarity between recycled restites from Hadean protocrust and the low  $^{182}\text{W}$  endmember of modern OIBs might also be the missing link bridging  $^{182}\text{W}$  isotope systematics in Archean and young mantle-derived rocks. This finding offers important constraints on the geodynamic evolution of Earth's mantle through time, indicating inefficient homogenization of Hadean silicate reservoirs.

## II. Kurzzusammenfassung

Seit über vier Milliarden Jahren haben geodynamische Prozesse kontinuierlich zur Homogenisierung und Differenzierung des Erdmantels und der kontinentalen Kruste geführt. Allerdings gibt es Hinweise von kurzlebigen Zerfallssystemen (z.B.  $^{129}\text{I} - ^{129}\text{Xe}$  und  $^{146}\text{Sm} - ^{142}\text{Nd}$ ), die primordiale Heterogenitäten, welche sich im Hadaikum gebildet haben (d.h. während der ersten ca. 100 Millionen Jahre nach Entstehung der Erde), über sehr lange Zeiträume erhalten geblieben sind – in einigen Fällen über Äonen und bis zum heutigen Tag. Die Untersuchung von Isotopenvariationen von Nukliden kurzlebiger Zerfallssysteme an terrestrischen Gesteinen sind in zweierlei Hinsicht von Bedeutung: (1) Die Ursache für die Entstehung der Variationen verweist auf Prozesse die zu einem Zeitpunkt stattgefunden haben müssen von dem keine weiteren geologischen Zeugen erhalten geblieben sind. (2) Das Verständnis der Mechanismen, welche für die Erhaltung dieser primordialen Signaturen verantwortlich sind, erlaubt Rückschlüsse über die zeitliche Entwicklung der Silikaterde und über Prozesse welche den Zustand des heutigen Erdmantels herbeigeführt haben (z.B. Einsetzen moderner Plattentektonik).

Ein kurzlebiges Zerfallssystem welches in der Geochemie intensiv verwendet wird ist  $^{182}\text{Hf}$ - $^{182}\text{W}$  (Halbwertszeit 8.9 Millionen Jahre (Vockenhuber et al., 2004)). Innerhalb des letzten Jahrzehnts fanden mehrere Studien in terrestrischen Gesteinen Unterschiede in den relativen Häufigkeiten von  $^{182}\text{W}$ .

Während Gesteine aus dem Archaikum im Verhältnis zum heutigen verarmten Mantel vorwiegend erhöhte  $^{182}\text{W}$  Zusammensetzungen aufweisen, finden sich für moderne Ozean Inselbasalte (OIB) und eine Suite archaischer Komatiite (die 3.55 Milliarden Jahre alten Schapenburg Komatiite aus dem Kaapvaal Kraton im südlichen Afrika) negative Anomalien. Dies wurde als Nachweis für die Erhaltung von primordialen Domänen im Erdmantel und deren Partizipation bei der Bildung moderner Mantelschmelzen interpretiert. Allerdings besteht Uneinigkeit darüber welche Prozesse für die Bildung dieser Manteldomänen verantwortlich sind. Diskutiert wird (1) die unvollständige Äquilibration mit Material aus der Spätphase der Akkretion (*late accretion hypothesis*), (2) frühe Fraktionierung von Hf und W während Kristall – Silikatschmelz Fraktionierung, z.B. zu Zeiten eines frühen Magma-Ozeans, oder (3) Interaktion zwischen Erdkern und Erdmantel. Weiterhin kommt erschwerend hinzu, dass die W Gehalte metamorph überprägter archaischer Gesteine durch sekundäre Prozesse verändert wurden (fluidkontrollierte Alteration) und die analytischen Standards für Hochpräzisionsmessungen von  $^{182}\text{W}$  höchst anspruchsvoll sind.

In dieser Studie präsentieren wir ein analytisches Protokoll, welches die Durchführung von Hochpräzisionsmessungen von  $^{182}\text{W}$  an Gesteinen ermöglicht die eine geringe W Konzentration aufweisen (wenige ng/g). In drei Kapiteln stellen wir die Ergebnisse unserer  $^{182}\text{W}$  Isotopenstudien vor die wir an Archaischen Gesteinen durchgeführt haben. Dies umfasst den 3.9-3.6 Milliarden Jahren alten Itsaq Gneiss Complex von SW Grönland (**Kapitel 1**), den ca. 3.6-3.2 Milliarden Jahre alten Pilbara Kraton, NW Australien (**Kapitel 2**), sowie den ca. 3.6-3.2 Milliarden Jahre alten Kaapvaal Kraton im südlichen Afrika (**Kapitel 3**). In allen drei Studien kombinieren wir unsere  $^{182}\text{W}$  Daten mit hoch präzisen Konzentrationsbestimmungen (Isotopenverdünnungsanalysen) für Elemente hoher Feldstärke (*high field strength elements*, HFSE), U und Th um das elementare Verhalten von W in unseren Proben zu evaluieren. Dies dient dem Verständnis von primären und sekundären Prozessen welche eine Veränderung der W Gehalte und W Isotopenzusammensetzungen herbeiführen können. Wie wir zeigen werden sind die W Konzentrationen in vielen Mantelgesteinen von metasomatischen Prozessen dominiert. Dadurch können primäre Signaturen überprägt werden, da Reservoir unterschiedlicher W Isotopenzusammensetzung miteinander gemischt werden (**Kapitel 1** und **Kapitel 2**). Wenn dies nicht berücksichtigt wird kommt es zu falschen Interpretationen von  $^{182}\text{W}$  Isotopendaten an archaischen Gesteinen. Unsere Studien an Gesteinen aus

verschiedenen archaischen Kratonen bezeugen, dass unterschiedliche Prozesse als Ursache für  $^{182}\text{W}$  Isotopenanomalien verantwortlich sind. Erhöhte  $^{182}\text{W}$  Isotopenhäufigkeiten in Gesteinen aus dem Pilbara Kraton (**Kapitel 2**) lassen sich durch die unvollständige Äquilibration mit Material der späten Akkretionsphase der Erde erklären. Anomalien in Gesteinen aus dem Itsaq Gneiss Complex (**Kapitel 1**) und dem Kaapvaal Kraton (**Kapitel 3**) hingegen sind auf Mantelquellen zurückzuführen welche zu Lebzeiten von  $^{182}\text{Hf}$  (d.h. innerhalb der ersten 60 Millionen Jahre nach Entstehung des Sonnensystems) eine Silikatdifferenzierung erfahren haben. Unsere Ergebnisse zeigen auf, dass Reservoirs, welche diese primordialen Signale archivieren, für mehrere hundert Millionen Jahre isoliert wurden. Wie unsere Analysen der geologischen Formationen aus dem Pilbara Kraton zeigt (**Kapitel 2**), sind umfangreiche Studien an Gesteinsformationen erforderlich, welche lange Zeiträume archaischer geodynamischer Prozesse archivieren, um die zeitliche Entwicklung der  $^{182}\text{W}$  Isotopenzusammensetzung der Silikaterde verstehen zu können. Unsere Forschung kann weiterhin darlegen, dass archaisches Schiefergestein Informationen über die zeitliche Entwicklung der  $^{182}\text{W}$  Isotopenzusammensetzung für einzelne Kratone liefert, da Schiefergestein repräsentativ für die obere kontinentale Kruste ist. Diese Erkenntnisse ermöglichen die Erhebung wissenschaftlicher Daten welche für das Verständnis von Zeiträumen geodynamischer Prozesse (z.B. Zeiträume der Mantelkonvektion), wie sie in der frühen Erde abgelaufen sind, von großer Bedeutung sind. Wie in **Kapitel 3** aufgezeigt, weisen archaische Gesteine aus dem Kaapvaal Kraton Korrelationen zwischen ihren  $^{182}\text{W}$  Isotopenzusammensetzungen und initialen  $\epsilon\text{Nd}(t)$ - sowie  $\epsilon\text{Hf}(t)$ -Werten auf. Nach unserem Kenntnisstand ist eine solche Korrelation zwischen  $^{182}\text{W}$  und langlebigen Radionukliden (in diesem Fall die Isotopensysteme  $^{147}\text{Sm}$ - $^{143}\text{Nd}$  und  $^{176}\text{Lu}$ - $^{176}\text{Hf}$ ) bislang einmalig. Die Partizipation recycelter mafischer Restite hadaischer Protokruste während der Petrogenese ist das einzige Modell welches diese Korrelation erklären kann. Weiterhin zeigen unsere Modellierungen, dass es eine auffallende Ähnlichkeit in der isotopischen Zusammensetzung zwischen den recycelten Restiten hadaischer Protokruste und einem Endglied moderner OIBs gibt welche besonders negative  $^{182}\text{W}$  Isotopenanomalien aufweist. Dies kann den *missing link* für die  $^{182}\text{W}$  Isotopensystematik zwischen archaischen und rezenten Gesteinen darstellen. Unsere Forschungsergebnisse bezeugen die ineffiziente Homogenisierung

hadaischer Reservoirs und liefern bedeutende Erkenntnisse für die geodynamische Entwicklung des Erdmantels.

### III. Introduction

#### Origin and evolution of the Earth

Studying the oldest terrestrial rocks allows us to address important questions not only to the primordial stages of our planet, but also to the early evolution of our Solar System and planetesimals in general. Knowledge about the initial stages of terrestrial planets is an important prerequisite to understand how planets became habitable, and how life evolved and became sustainable.

Models for Solar System and terrestrial planet formation were summarized in previous review papers (Chambers, 2004; Williams and Cieza, 2011; Norman, 2019) and mainly rely on astronomical observations from other solar systems, the geochemical properties of the Earth and meteorites, and the structure of our Solar System. Based on these constraints terrestrial planetary formation is the result of multistage processes that began with the collapse of a solar nebula within a cold and dense molecular cloud into a rotating protoplanetary disk. After the dust became concentrated in the midplane of the disk, it accreted to bodies that were dubbed *planetesimals* (~10 – 100km diameter). This happened during the very first few million years of the Solar System. Witnesses of these early stages are meteorite fragments of large parent bodies that accumulated from earliest formed detritus. Thus, components from meteorites offer important insights into nebular and asteroidal processes such as absolute age constraints for earliest formed solids (calcium-aluminium-rich inclusions) of our Solar System that date back to 4.568 billion years (Bouvier and Wadhwa, 2010). Subsequently, the accretion of material in the protoplanetary disk evolved to *planetary embryos* (~100 – 5000km diameter) mainly as a result of gravitational interactions (*runaway growth*) that culminated in *oligarchic growth*, where the largest planetary embryos grew at the expense of smaller planetary embryos. The final stage of accretion from embryos to planets was highly chaotic and slower than the initial material coagulation processes because the mechanics of growth were mainly caused by gravitational perturbations between a few dozen embryos, where the outcome of individual events dictated the evolutionary pathway for a solar system. This last stage of terrestrial planet formation was characterized by multiple highly energetic collisions

(O'Brien et al., 2006) that caused a series of magma ocean events with fundamental consequences for core formation (Rubie et al., 2007; Rubie et al., 2011). Most likely, one of these highly energetic collisions was responsible for the formation of the Earth-Moon system (Canup, 2012).

### **Early Earth Processes** (*Moon-forming impact, accretion history, late veneer*)

Many dynamical scenarios have been considered to explain the formation of the Earth-Moon system, for instance loss of material from a fast-spinning proto-Earth (Ćuk and Stewart, 2012) or being the product of multiple impacts (Rufu et al., 2017). However, most models are in favor of a giant-impact hypothesis which assumes that the Moon grew gravitationally from debris in a circumterrestrial disk that remained after a large collision between the proto-Earth and a Mars-sized planetesimal named *Theia* (Hartmann and Davis, 1975; Cameron and Ward, 1976; Cameron, 1997; Canup and Asphaug, 2001). The giant Moon-forming impact seems to be the most plausible scenario as it can reconcile for many observations such as the nearly identical isotopic composition between the Earth and Moon, the angular momentum of the Earth-Moon system, the level of lunar volatile depletion and the depletion in Fe-Ni as implied by the Moon's low bulk density (Melosh, 2014). The timing of the Moon-forming impact is still highly debated but was probably close the end of primary accretion, maybe as early as 50 Ma after the formation of the Solar System (Thiemens et al., 2019).

It is in general challenging to estimate the exact timing for the formation of the terrestrial planets of our Solar System because it is difficult to disentangle the processes of core formation and accretion. As already mentioned, planetesimal accretion and core formation most likely represent protracted periods that occurred contemporaneously (Kramers, 1998). One chronometer that was often applied to date core formation on asteroids and Earth is the extinct  $^{182}\text{Hf} - ^{182}\text{W}$  system (half-life 8.9 million years (Vockenhuber et al., 2004)). The short half-life provides an excellent time resolution to determine the timescale for Earth's core formation. Furthermore, its parent and daughter isotopes show markedly different geochemical affinities during metal-silicate differentiation. Hafnium behaves strongly lithophile and mainly remained in the bulk silicate Earth (BSE), while W is a moderately siderophile element that was strongly sequestered into the metallic core (e.g. Rammensee and Wänke, 1977; Palme and

Rammensee, 1981). Thus, the early BSE (< 60 Ma after solar system formation) had elevated Hf/W, which caused a stronger radiogenic ingrowth of  $^{182}\text{W}$  when compared to the Earth's core or Chondrites, a meteorite group that remained undifferentiated and is taken as a canonical reference for the bulk Earth composition (Harper and Jacobsen, 1996; Kleine et al., 2002; Schoenberg et al., 2002b; Yin et al., 2002). Therefore, accretion and metal-silicate fractionation chronologies on planetary bodies are calculated relative to the chondritic  $^{182}\text{Hf} - ^{182}\text{W}$  isotope evolution. Assuming that core formation was a single stage process that took place in a short, "catastrophic" event, a maximum age of 38 Ma after Solar System formation is obtained (König et al., 2011). This maximum age for core formation probably also constrains the final stages of accretion as the latter process was shown to sustain core formation (Kramers, 1998).

Elements that behave chalcophile or siderophile should be highly depleted in the BSE as they were nearly completely removed by segregating into Fe-alloys during core-formation (McDonough, 2013). However, the absolute abundances for highly siderophile elements (HSE, e.g. platinum-group elements (PGE), Re, Au) are substantially higher than expected from their metal-silicate partitioning behavior during core-formation (Walker, 2009; Mann et al., 2012; Siebert and Shahar, 2015). Even more surprising, HSE display near-chondritic relative abundances, although their experimentally derived metal-silicate partitioning behavior would suggest strong fractionation during core-formation (Walker, 2009; Mann et al., 2012; Siebert and Shahar, 2015) (see Fig. III.1). Based on these observations it has been proposed that the Earth accreted material with chondritic bulk HSE compositions after equilibrium partitioning and chemical interexchange between mantle and core had ceased (Kimura et al., 1974; Chou, 1978; Wänke et al., 1984). This late accretion of a small fraction (~0.5% of the mass of the mantle (Walker, 2009)) of material with bulk chondritic composition has been termed *late veneer* (Chou, 1978). The replenishment of HSE during the final stages of Earth's accretion was also related to the *late heavy bombardment* (Chou, 1978), which was a period of intense cratering and basin formation. This bombardment continued for several hundred million years after formation of the Solar System as inferred from age constraints in lunar impact rocks and "photogeological" observations on other bodies such as Mars, Mercury, Mimas and Callisto (Tera et al., 1974; Kring and Cohen, 2002). However, but this is only my personal view, both terms are grounded on different observational constraints and it

should be allowed to discuss if the late veneer falls (at least in part) in the period of the late heavy bombardment, but for semantics the terms should always be kept separately. Moreover, it has been pointed out that both terms (*late veneer* and *late heavy bombardment*) are not synonymous (Carlson et al., 2015) because constraints from recent studies (Norman et al., 2010; Miljković et al., 2013) suggest that the contribution from the late heavy bombardment, was too small to have any consequences for the bulk composition of Earth.

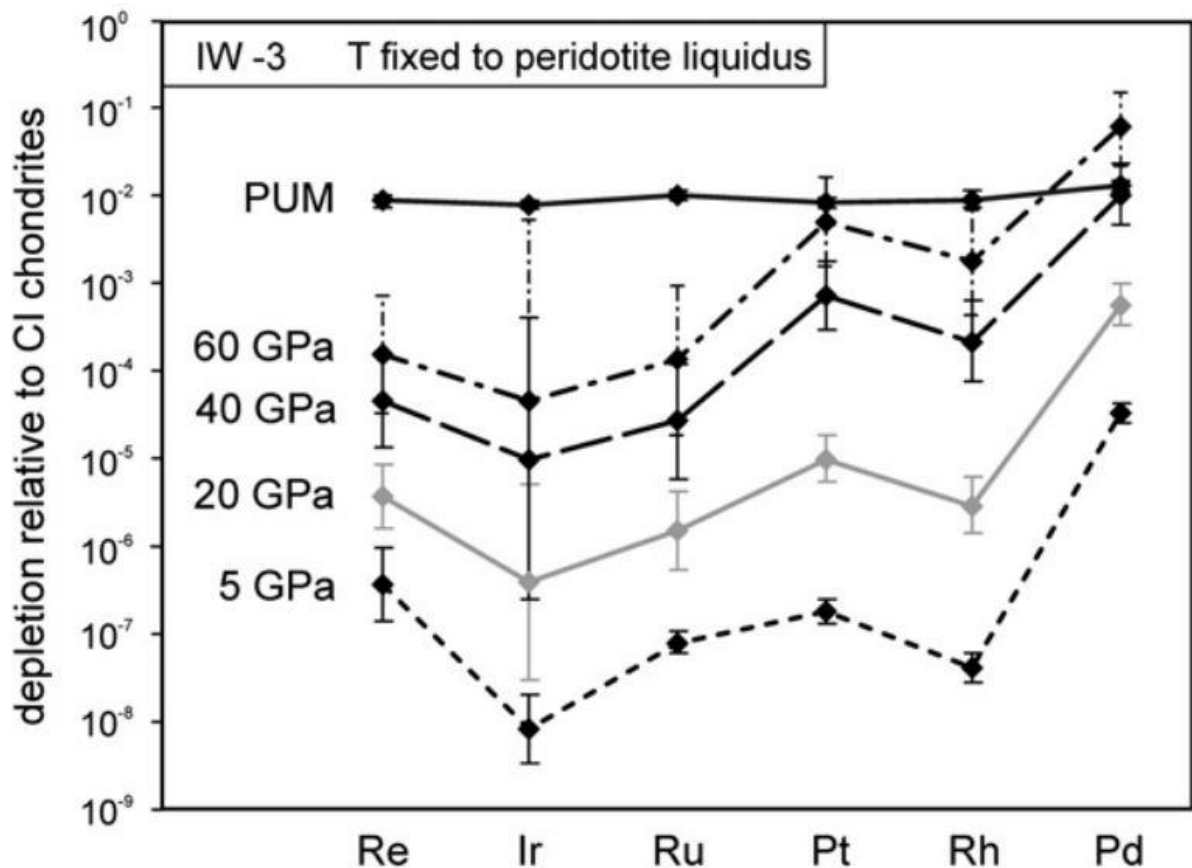


**Figure III.1: Highly siderophile element concentrations, normalized to CI chondrite, predicted for the primitive upper mantle (PUM) as a result of metal-silicate partitioning at various P-T conditions in a magma ocean.** Taken from Mann et al. (2012).

Besides elemental systematics from HSE abundances in terrestrial rocks there are also isotopic constraints on the contribution and nature of a putative late veneer. Since analytical improvements have improved the precision for  $^{182}\text{W}$  isotope measurements into a range of <5ppm (Willbold et al., 2011; Touboul et al., 2012) it has been documented that Archean rocks are predominantly enriched in the isotope  $^{182}\text{W}$  relative to the modern mantle. The modern-mantle value is inferred from certified

standard solutions, either NIST SRM 3163 or AMES W-metal, which both have similar  $^{182}\text{W}$  isotope abundancies (Peters et al., 2014). Primitive meteorites of bulk chondritic composition display  $^{182}\text{W}$  isotope deficits of around 200 ppm (Kleine et al., 2004). Thus, missing late accretionary additions of chondritic compositions provide an explanation for elevated  $^{182}\text{W}$  isotope abundancies observed in Archean rocks (Willbold et al., 2011). Considering the effect of missing late accreted material on the HSE budget of the Earth, the parental sources of these mantle reservoirs should also display markedly lower HSE abundances than the modern-mantle. Indeed, these conceptual assumptions are in agreement with observational constraints for Archean rocks from the Abitibi Greenstone Belt, Canada (Puchtel et al., 2018) or the Pilbara Craton, Australia (Maier et al., 2009; Archer et al., 2019, **chapter 2** this study). For other locations, however, combined HSE –  $^{182}\text{W}$  isotope systematics are incompatible with the late veneer hypothesis (Touboul et al., 2012; Rizo et al., 2016b) requiring different processes to explain  $^{182}\text{W}$  isotope anomalies (e.g. early silicate differentiation, see below). The investigation of mass-independent ruthenium isotopic variations within Archean rocks might provide an unambiguous test of whether mantle domains did not receive the full complement of late veneer material (Fischer-Gödde et al., 2020). In a very recent study, ruthenium isotopic variations within Archean rocks reveal that primordial mantle heterogeneities arise from missing late accretionary additions to the sources of Archean rocks (Fischer-Gödde et al., 2020).

## **Tectonic Regimes, Archean rocks and their spatial distribution**

The vast majority of the Earth's early rock record and therewith an important archive that can provide geological evidence for Early Earth processes was lost due to active plate tectonics. The oldest rocks on Earth that remained isolated from the convective mantle are preserved in cratons (*kratos* is Greek for strength), which represent nuclei of early Archean rocks that are often found within the cores of continents (see Fig. III.2).



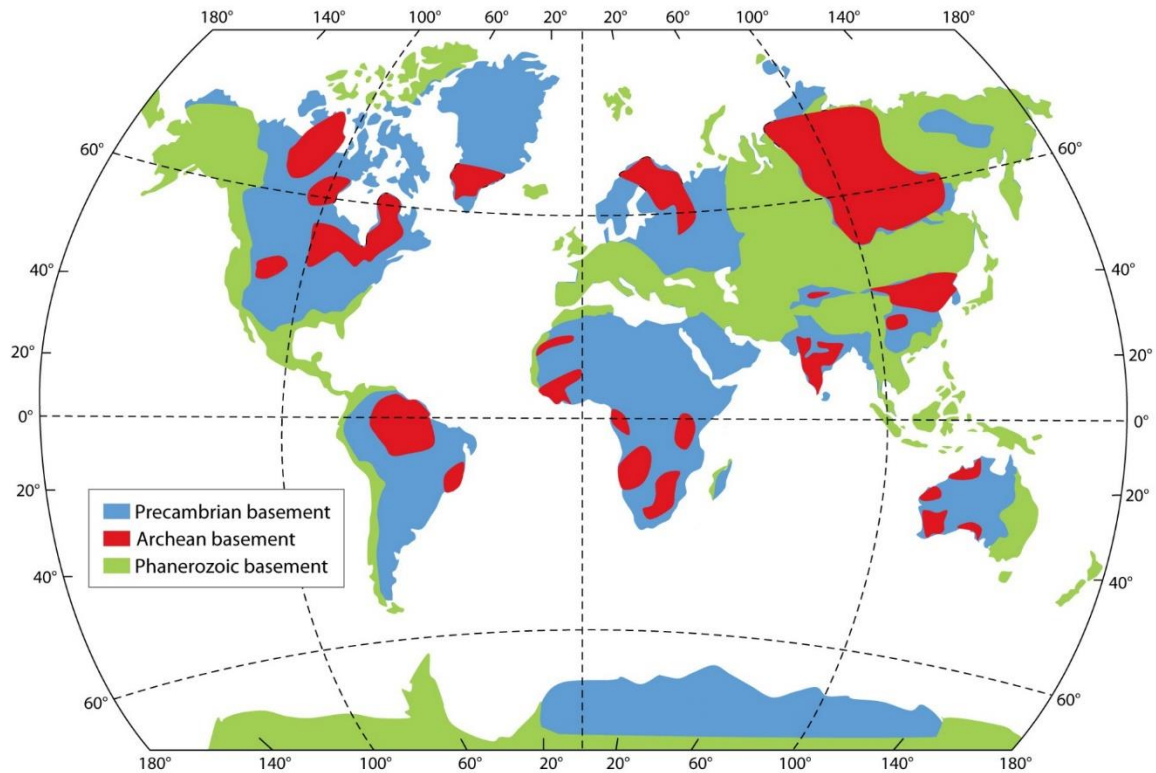


**Figure III.2: Spatial distribution of Archean cratons (shown in red), Precambrian (>540 Ma), and Phanerozoic (<540 Ma) basement.** Taken from Lee et al. (2011).

This Archean (2.5-4.0 Ga) embryonic crust is exposed in about 35 cratons (Bleeker, 2003) and accounts for around 7-15% of the present continental surface area (Bowring and Williams, 1999; Hawkesworth et al., 2010). Small areas within these crustal fragments have preserved Paleoarchean lithologies, for example ~4 Ga old tonalitic gneiss units in the Acasta Gneiss Complex within the Slave Craton of the Northwest Territories of Canada (Bowring and Williams, 1999; J. R. Reimink et al., 2016), the 3.85-3.60 Ga Itsaq Gneiss Complex, Greenland (Nutman et al., 1996; Nutman and Friend, 2009), or the Napier Complex, Antarctica (3.98-3.8 Ga (Black et al., 1986; Harley et al., 2019). The Hadean Eon (4.0-4.5 Ga) is almost devoid of available rock samples except from reputed 4.4-4.3 Ga mafic rocks from the Nuvvuagittuq greenstone belt in northern Quebec, Canada (O'Neil et al., 2008; O'Neil et al., 2012). Other available samples older than ~4 Ga have been destroyed, probably as a result of recycling into the mantle, leaving no direct samples of Earth's primordial crust. Thus, little is known of the first ca. 500 million years after accretion. The only undisputed material from the Hadean Eon and physical evidence from the earliest phase of Earth's evolution are rare xenocrystic zircon grains that have been identified in orthogneisses from West Greenland (Mojzsis et al., 2001) and Northern Canada (Iizuka et al., 2006).

Detrital zircon grains found in the Jack Hills conglomerate within the Narryer Complex from the Yilgarn Craton in Western Australia date back to ~ 4.4 Ga (Wilde et al., 2001; Valley et al., 2014). Trace element systematics, isotopic compositions and mineral inclusions within these zircons provide insights into Early Earth processes and into the conditions extant on our planet at that time. For example, oxygen isotope ratios on zircons indicate the early evolution of an Hadean hydrosphere and the presence of liquid surface water (Mojzsis et al., 2001; Wilde et al., 2001) as well as the emergence of habitability (Valley, 2008). Trace element compositions refer to the type of host rock that a zircon crystallized in (Iizuka et al., 2006) and mineral inclusion studies provide information about the ancient tectonic environment (Hopkins et al., 2008; Hopkins et al., 2010).

The recognition that Komatiites and rock samples from the so-called tonalite-trondhjemite-granodiorite series (TTGs (Jahn et al., 1981; Moyen and Martin, 2012)) are almost exclusively restricted to the Archean has caused considerable interest in the geological community.

Komatiites are most abundant in the Archean (Sossi et al., 2016) but Proterozoic (Waterton et al., 2017) and Phanerozoic occurrences (Echevarria, 1980; Alvarado et al., 1997) are also reported. The type locality of komatiites is the Komati Formation in the Barberton Greenstone Belt in the Kaapvaal Craton, Southern Africa (Viljoen and Viljoen, 1969). Komatiites are ultramafic volcanic rocks with high MgO content (>18 wt% (Arndt and Nisbet, 1982)). They typically display diagnostic spinifex textures (see Fig. III.3) that are elongated crystals of olivine and pyroxene with a dendritic morphology, commonly considered to have been rapidly crystallized by quenching at a high thermal gradient (Faure et al., 2006). It has been proposed that the melting conditions to produce komatiitic lavas require high degrees of partial melting (Herzberg, 1992) at high temperatures and pressures (Green, 1981; Nisbet et al., 1993; Puchtel et al., 2013). The most accepted petrological model for the generation of komatiitic lavas suggest adiabatic decompression melting of relatively anhydrous, anomalously hot mantle plumes (Green, 1975; Ohtani, 1984; Nisbet et al., 1993; Herzberg and O'hara, 2002; Arndt, 2003; Robin-Popieul et al., 2012; Sossi et al., 2016). As summarized by Barnes and Arndt (2019), the frequent occurrence of komatiites in the Archean rock record and a temporal change in the sub-types of komatiites through the Archean can be attributed to higher potential mantle temperatures that slightly declined with time. The association of komatiitic rocks with

basalts that display geochemical characteristics of basalts from modern oceanic plateau settings and the lack of coexisting rocks that display petrological and geochemical features of modern arc lavas indicate that horizontal plate tectonics with active subduction were only (if at all) of subordinate importance in the Archean Eon.



**Figure III.3: Komatiite from the Ruth Well Formation (Pilbara Craton, NW Australia) with diagnostic spinifex textures.** The term spinifex refers to the *spinifex* grass, which has a similar appearance and is endemic to Western Australia (visible in the right-hand corner). Photo taken by Jonas Tusch

The other group of rocks that is typical for the Archean are granitoids from the TTG suite which are the most dominant members of grey gneisses that make up to 90% of the Archean crust (Hoffmann et al., 2019). As TTGs are highly evolved felsic rocks, most studies focused on questions about craton formation, the emergence of Earth's earliest continental crust and temporal changes of these processes. Previous studies showed that geochronology (e.g. Kröner et al., 1989), geochemistry (Hoffmann et al., 2011a; Hoffmann et al., 2014; Hoffmann et al., 2016; Champion and Smithies, 2019),

phase and geochemical modeling (Nagel et al., 2012; Johnson et al., 2017; Wiemer et al., 2018) are excellent tools to investigate the early geological archive of felsic rocks in order to infer the tectonic setting of felsic crust formation and the geodynamic environments on early Earth. Although many questions (e.g. their petrogenesis and the tectonic environment) still remain unsolved after more than 40 years (Moyen and Martin, 2012), it is widely accepted that the source rocks for Archean TTG magmas were hydrous mafic rocks. The dehydration melting of such basaltic protoliths can be explained by a variety of conditions and geodynamic environments. While several studies presented evidence for the formation of TTGs in settings that involve subduction-like processes (Bindeman et al., 2005; Nair and Chacko, 2008; Polat, 2012; Wyman, 2013) other models assume a non-uniformitarian origin for Archean TTGs that do not require active subduction (Bédard, 2006; Bédard, 2013; Zhang et al., 2013; Johnson et al., 2017; Smit et al., 2020). Thus, the study of Komatiites and TTGs offers important insights into the genesis of the Archean mantle and the formation mechanisms of early continental crust.

There is still no consensus in the scientific community on how continental crust formed in the Archean and what tectonic regime was operating. Both types of models (subduction vs. non-subduction) have their shortcomings in reconciling all observations. For example, higher Archean mantle temperatures probably inhibited the subduction of oceanic lithosphere (Sizova et al., 2010). Moreover, important products of horizontal plate tectonics (e.g. paired metamorphic belts (Brown, 2010)) are not preserved in the Archean rock record, although the associated rock types have a high preservation potential. However, some geological features that are preserved in early Archean successions (e.g. terrane juxtaposition in Greenland (Friend et al., 1988)) seem to require modern-style horizontal tectonics. Such findings led to observation-based models which are able to demonstrate that different tectonic modes can coexist (Capitanio et al., 2019) and that the Archean Earth was largely stagnant, perhaps with short-lived intermittent periods of horizontal tectonic activity (O'Neill and Debaille, 2014).

### **Application of short-lived isotope systems**

Considering the aforementioned conditions, many dynamics of the Hadean and early Archean Earth remain enigmatic, mainly because the terrestrial rock record is highly

fragmented for the Archean and almost completely lost for the Hadean Eon. Moreover, most ancient geological events were strongly overprinted by the continuing geological activity of the planet. Consequently, our knowledge about the Hadean Eon does not come from classical geological approaches but rather indirect conclusions drawn from geochemical observations. From the geochemists toolbox, short-lived nuclide series such as  $^{129}\text{I} - ^{129}\text{Xe}$ ,  $^{146}\text{Sm} - ^{142}\text{Nd}$ , and  $^{182}\text{Hf} - ^{182}\text{W}$  have proven particularly useful to improve our knowledge about processes that happened during the earliest stages of planetary evolution. The big advantage of such isotope systems is that parent/daughter isotope fractionation within their relatively short half-life periods, cause comparatively large variations in the relative abundances of their radiogenic nuclides. In contrast to long-lived decay-series that remained analytically inactive within the first ca. 100 Ma, relative large variations in the decay products of short-lived nuclide decay series can be measured with extraordinary precision which translates into a high resolution power for constraints that address primordial processes (e.g. decreasing errors for absolute age determinations (Allègre, 2008)). As such, short-lived nuclide series like  $^{129}\text{I} - ^{129}\text{Xe}$  (15.7 Ma (Audi et al., 2017)),  $^{146}\text{Sm} - ^{142}\text{Nd}$  (half-life 103 Ma (Marks et al., 2014)), and  $^{182}\text{Hf} - ^{182}\text{W}$  (half-life 8.9 Ma (Vockenhuber et al., 2004)) can help to constraint the timing of early outgassing, planetary silicate differentiation, or core formation. Taking into consideration the current precision of isotope ratio measurements and the magnitude of parent/daughter isotope fractionation, by 6 half-life periods a radionuclide can be considered functionally extinct, so after ~ 100 Ma for  $^{129}\text{I}$ , ~ 600 Ma for  $^{146}\text{Sm}$ , and ~ 60 Ma for  $^{182}\text{Hf}$ .

The detection of variabilities in the relative abundances of the decay products  $^{129}\text{Xe}$ ,  $^{142}\text{Nd}$ , and  $^{182}\text{W}$  in terrestrial rocks provided firm evidence that primordial reservoirs were not fully homogenized by mantle-dynamics, but played a significant role during the formation of the first continental crust (Allègre et al., 1987; Caro et al., 2003; Willbold et al., 2011). The very recent discovery of  $^{182}\text{W}$ ,  $^{142}\text{Nd}$ , and  $^{129}\text{I}$  anomalies in modern mantle-derived rocks (Mukhopadhyay, 2012; Mundl et al., 2017; Peters et al., 2018) demonstrate that primordial reservoirs are still accessible and that their investigation provides new perspectives on the origin of short-lived nuclide isotope heterogeneities throughout Earth's history. While anomalous  $^{129}\text{I}$  and  $^{142}\text{Nd}$  isotope compositions in mantle-derived rocks can primarily be assigned to early planetary outgassing and early silicate crystal-liquid fractionation, respectively, the presence of  $^{182}\text{W}$  isotope anomalies in terrestrial rocks can mirror multiple processes (see below).

## **Mobility and secondary overprint of W and the implication for $^{182}\text{W}$ anomalies**

It has been demonstrated that W concentrations in silicate rocks can be strongly modified by alteration and metamorphism (König et al., 2008; König et al., 2011). During silicate crystal-liquid fractionation, W behaves highly incompatible, similar to Th and U (e.g. Palme and Rammensee, 1981; Adam and Green, 2006; König et al., 2011). Hence, ratios of W/Th in both, fresh OIB (oceanic island basalt) and MORB (mid-ocean-ridge basalt) samples, are confined to a canonical range between 0.04 and 0.23 (OIB) and between 0.09 and 0.24 (MORB) (König et al., 2011; Jenner and O'Neill, 2012). In contrast to MORBs and OIBs, samples from arc environments display mainly elevated W/Th ratios (König et al., 2008; König et al., 2011). This has been ascribed to the higher fluid-mobility of W in subduction zone fluids (König et al., 2008; Bali et al., 2012). Based on these observations, elemental W systematics in Archean rocks revealed that the elemental W budgets of many samples were affected by fluid-mediated second stage enrichment (Touboul et al., 2014; Liu et al., 2016; Rizo et al., 2016b; Tusch et al., 2019, **chapter 1**). In particular, ultramafic rocks were shown to be extremely susceptible for second stage enrichment of W (Tusch et al., 2019, **chapter 1**). Such an elemental re-distribution of W on the whole rock scale might also affect accompanying  $^{182}\text{W}$  isotope systematics. Therefore, high-precision concentration measurements for W, U, and Th are required to identify samples with primary W abundances to restrict further consideration primarily to samples with  $^{182}\text{W}$  isotope composition unmodified by secondary processes.

## **$^{182}\text{W}$ isotope systematics of the terrestrial mantle**

The discovery of anomalous  $^{182}\text{W}$  isotope compositions in Archean rocks was not a chance find. Pioneering studies that investigated the  $^{182}\text{W}$  isotope systematics of Archean rocks (Schoenberg et al., 2002b; Willbold et al., 2011) rather expected to find anomalous  $^{182}\text{W}$  isotope compositions as HSE systematics on Archean mantle-derived rocks documented the preservation of pre-late veneer mantle domains and suggested a progressive in-mixing of late accretionary additions during the Archean Eon (Maier et al., 2009). Recent analytical improvements in multicollector inductively coupled

plasma - and thermal ionization mass spectrometry (MC-ICP-MS and TIMS, respectively) allowed high-precision  $^{182}\text{W}$  isotope measurements with analytical uncertainties below 5 ppm (Willbold et al., 2011; Touboul and Walker, 2012). The findings of positive  $^{182}\text{W}$  isotope anomalies in Archean mantle-derived rocks (Willbold et al., 2011; Touboul et al., 2012) spurred many studies to investigate  $^{182}\text{W}$  isotope systematics in rocks from other ancient terranes. Over the past ca. 10 years, 14 studies reported  $^{182}\text{W}$  isotope compositions for Archean rocks. The rocks that were analyzed, predominantly display positive  $^{182}\text{W}$  anomalies. As already mentioned above some studies interpret this prevalence as evidence for disproportional accretion of late veneer (Willbold et al., 2011; Archer et al., 2019). Others however have pointed out that this view may be a simplification as constraints from HSE abundances (Touboul et al., 2012) and  $^{142}\text{Nd}$  isotope systematics (Puchtel et al., 2016a; Rizo et al., 2016b) suggest other processes to be involved. These studies suggest that anomalous  $^{182}\text{W}$  isotope compositions within the terrestrial mantle could have been also produced in-situ during the lifetime of  $^{182}\text{Hf}$  (i.e., during the first ca. 60 Ma after solar system formation). Following their arguments, Hf could have been substantially fractionated from W during silicate crystal-liquid fractionation, thus explaining  $^{182}\text{W}$  isotope heterogeneities within the Archean mantle. Further evidence for such ancient signatures comes from anomalies in the relative abundances of  $^{142}\text{Nd}$  which is the decay product of the short-lived  $^{146}\text{Sm}$  (half-life 103 Ma (Marks et al., 2014)). As for  $^{182}\text{Hf}$ - $^{182}\text{W}$ , the incompatibility is higher for the radiogenic nuclide – so positive correlations between  $^{182}\text{W}$  and  $^{142}\text{Nd}$  are expected if silicate differentiation is involved. However, even in cases where missing late veneer contributions can be excluded on the basis of HSE systematics, correlations between  $^{182}\text{W}$  and  $^{142}\text{Nd}$  are not always observed (Touboul et al., 2014). Therefore, in many cases the origin of  $^{182}\text{W}$  isotope anomalies in Archean rocks remains ambiguous.

Irrespective of what caused  $^{182}\text{W}$  isotope anomalies in Archean rocks, the temporal evolution from predominantly positive  $^{182}\text{W}$  isotope anomalies in the Archean to modern depleted upper mantle (no  $^{182}\text{W}$  isotope anomaly) is only poorly constrained. Most studies have only provided snapshots within the  $^{182}\text{W}$  isotope evolution of individual Archean cratons (Touboul et al., 2012; Touboul et al., 2014; Liu et al., 2016; Puchtel et al., 2016a; Puchtel et al., 2018). Moreover, only 15 out of 118 Archean samples (ca. 13%), which were analyzed for their W isotope composition, have preserved their pristine W budget (canonical W/Th). As demonstrated by our study on

rocks from the Pilbara Craton (**chapter 2**), the W isotope composition of mantle-derived rocks with supracanonical W/Th ratios are dominated by metasomatic agents that re-mix reservoirs of variable W isotope compositions. This might indicate that the scatter seen for Archean rocks in Fig. III.4 does not necessarily represent analytical noise. Secondary overprint might cause ambiguous models on the time-scales of

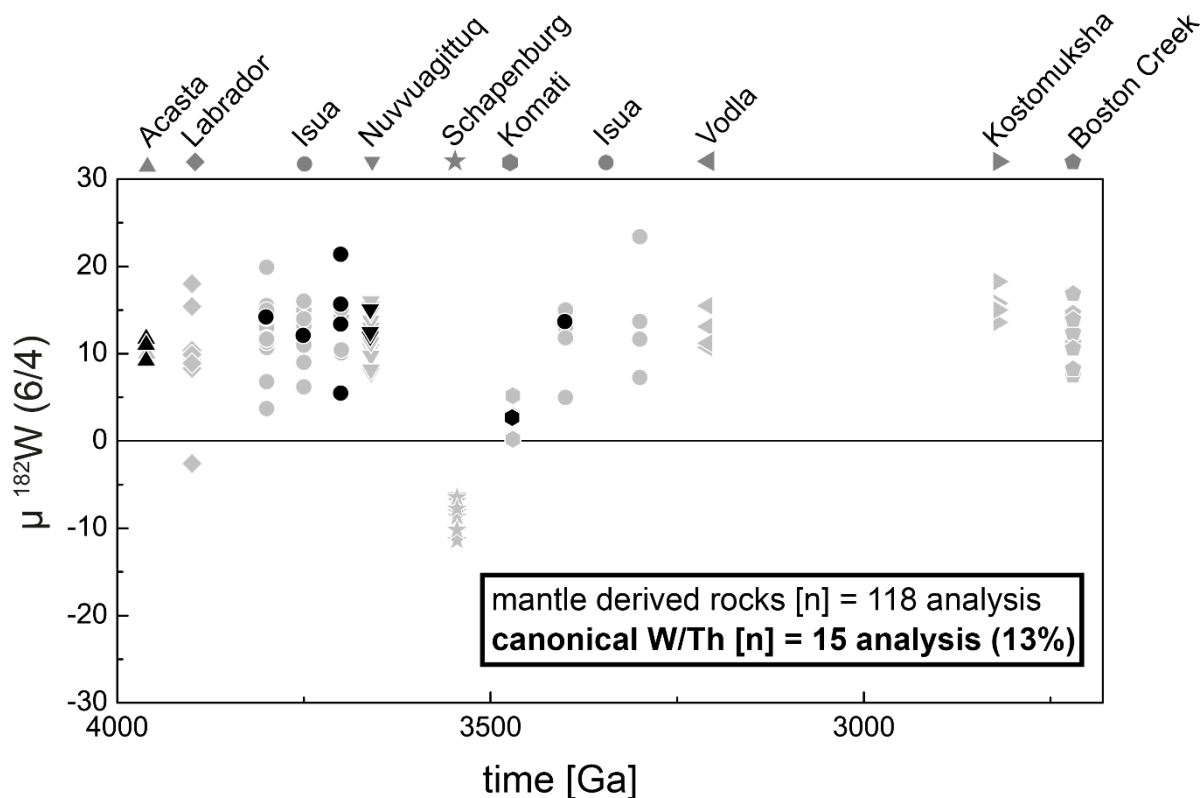


**Figure III.4: Compilation illustrating the secular  $^{182}\text{W}$  isotope evolution of the Archean terrestrial mantle.** This dataset includes all available  $^{182}\text{W}$  isotope literature data for mantle-derived rocks (for references see Table B2, appendix B). For Nuvvuagittuq we assume a minimum emplacement age of 3.75 Ga (Cates and Mojzsis, 2007), being well aware that it might be older (O’Neil et al., 2008). The literature data are subdivided into samples with overprinted elemental W budgets (grey) and samples with canonical W/Th (black).

mantle convection that progressively homogenize early formed mantle heterogeneities. Furthermore, the evolution of  $^{182}\text{W}$  isotope anomalies through time is further complicated by the scarcity of data for the Proterozoic Eon. There is little known about the W isotope composition of the terrestrial mantle at that time. The only available data comes from 2.4 Ga old komatiitic basalts from the Vetreny Belt (Fennoscandian Shield) that were strongly affected by crustal contamination (Puchtel et al., 2016b).



Surprisingly, recent studies revealed that some modern OIBs display extremely variable  $^{182}\text{W}$  isotope anomalies (Rizo et al., 2016a; Mundl et al., 2017) ranging from excesses of up to +48 ppm (Rizo et al., 2016a) to deficits of up to ca. -20 ppm (Mundl et al., 2017). While the extreme positive anomalies are controversial and could not be confirmed by a later study (Kruijer and Kleine, 2018), combined  $^3\text{He}/^4\text{He} - ^{182}\text{W}$  systematics indicate that different mantle reservoirs contribute to the geochemical heterogeneity of modern OIBs. These reservoirs include an un-degassed component (Mundl et al., 2017) that may have undergone metal-liquid silicate equilibration at the core mantle boundary (Mundl-Petermeier et al., 2020). A partially molten silicate layer, either representing a remnant of an ancient basal magma ocean or recycled oceanic lithosphere, might have inherited the negative  $^{182}\text{W}$  isotope composition of the outer core via chemical and isotopic equilibration (Mundl-Petermeier et al., 2019; Mundl-Petermeier et al., 2020). The presence of such mantle reservoirs and the role of mantle plumes in the Archean is poorly constrained yet but is investigated in **chapter 3** using the W isotope composition of Archean rocks from the Kaapvaal Craton, southern Africa.

## **Significance of constraints on the dynamics of Early Earth processes**

The presence of seismically detectable large low-shear-wave velocity provinces (LLSVPs (Torsvik et al., 2016)) combined with trace element and radiogenic isotope data on basalts from ocean island basalts and oceanic plateaus (Hofmann, 1997) provide clear evidence that the present-day Earth mantle exhibits domains with strong geophysical and geochemical differences. However, direct geophysical observations to constrain the Earth's interior dynamics back in geological time are missing. Thus, we only know very little about the evolutionary histories of the Earth's present-day heterogeneous mantle (see Fig. III.5). The only data available come from the geological rock record that comprise mantle-derived rocks. These "messengers from below" provide important observational constraints, which constitute boundary conditions for and define the evolutionary pathway of computational numerical models. Therefore, cross-disciplinary efforts that integrate geochemical observations, computational models, and geophysical data are required to resolve the relationship between modern observed and the past heterogeneity, respectively.

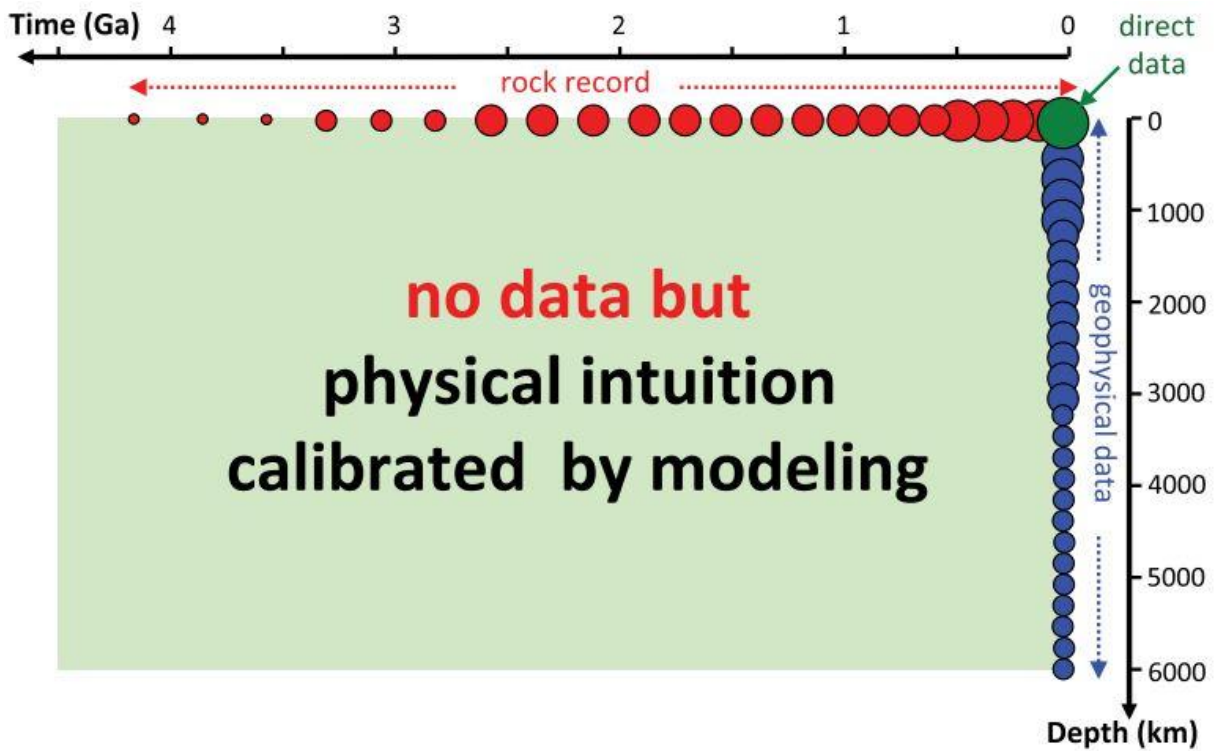


**Figure III.5: Time-depth diagram for the availability of data for constraining geodynamic relationships for the Earth.** Size of data points reflect abundance of available data. Taken from Gerya (2019).

## IV. Synthesis

For our first project (**chapter 1**) we developed a new ion exchange separation scheme that permits W isotope measurements on samples with W abundances in the lower ng/g range, where gram-sized amounts of samples need to be processed. This is of particular importance for high precision  $^{182}\text{W}$  isotope measurements on rocks such as peridotites or depleted basalts, that often exhibit W concentrations in the range of only several ng/g. As demonstrated in our first project our analytical approach allows for high precision  $^{182}\text{W}$  isotope measurements with uncertainties typically better than  $\pm 5$  ppm (95% confidence interval (CI),  $n > 5$ ). Over the course of our projects (see **chapter 2 and 3**) we continuously developed our separation and measurement protocols, which resulted in markedly improved analytical precision and accuracy. This is demonstrated by repeated measurements of three in-house reference materials that were always passed through our separation protocol (*LP1* - historical 1480 OIB from La Palma (Kurzweil et al., 2019), *AGC 351* - a 3455 Ma grey gneiss from the Kaapvaal Craton, Southern Africa (Kröner et al., 2014), and sample *160245* – a 3.27 Ga Komatiite from the Pilbara Craton, NW Australia (**chapter 3**)). The analytical uncertainty of our measurements significantly improved over the course of my PhD project.

To ultimately test our analytical approach we analyzed lithostratigraphic units from the Eoarchean Itsaq Gneiss Complex (IGC), SW Greenland, that has previously been subject to detailed  $^{182}\text{W}$  studies (Willbold et al., 2011; Rizo et al., 2016b; Dale et al., 2017). In order to cross-reference with these previous studies, we included lithostratigraphic units with known  $^{182}\text{W}$  isotope compositions. In part, we even analyzed the same powder aliquots that were previously investigated by others (Rizo et al., 2016b). In addition, we provided the W isotopic composition for recently recognized mantle-like peridotites from several Eoarchean key units, that were shown to display the full inventory of HSE found in modern mantle peridotites (van de Löcht et al., 2018a). Throughout our projects (**chapter 1-3**) we always combined our W isotope composition analyses with isotope dilution measurements for U, Th, W, and other high-field strength elements (Zr, Nb, Ta) to get high precision concentration data that allow for the inspection of the whole-rock elemental W budget. In case for rocks from the IGC it turned out that redistribution of W, as shown by non-canonical W/Th and W/Ta ratios in most samples, is the most plausible explanation for a homogeneous  $^{182}\text{W}$  isotope excess of  $+12.8 \pm 1.0$  ppm (95% CI). The magnitude of this excess is in

line with previous studies (Willbold et al., 2011; Rizo et al., 2016b; Dale et al., 2017). Although HSE and  $^{182}\text{W}$  isotope systematics are clearly decoupled in the mantle-like peridotites we argue that missing late veneer additions are unlikely to be the only cause of the  $^{182}\text{W}$  excesses in rocks from SW Greenland. Rather, the formation of an early silicate reservoir by  $>4.50$  Ga is a more plausible explanation, as previously suggested by  $^{142}\text{Nd}$  studies in the Isua region (e.g. H. Rizo et al., 2016b; Saji et al., 2018).

For our second project (**chapter 2**) we examined Paleo- to Neoarchean rocks from the Pilbara Craton, Western Australia. As already outlined in the introduction, surprisingly few studies have assessed the  $^{182}\text{W}$  record of lithostratigraphic successions that span a relatively long time frame of Archean geodynamic evolution. Rather, most studies have only provided snapshots within the  $^{182}\text{W}$  isotope evolution of individual Archean cratons. In order to assess the  $^{182}\text{W}$  isotope evolution of a particular region over a long time period, we analyzed rocks from the Pilbara Craton, that preserve a unique geological archive covering 800 Ma of Archean history (3.58-2.76 Ga). To allow for a more comprehensive understanding of Archean geodynamic evolution, we employed two strategies in selecting our samples. Firstly, we analyzed mafic-ultramafic rocks that tapped the ambient asthenospheric mantle. Secondly, to understand the evolution of the lithospheric mantle and to obtain average crustal compositions we analyzed mafic dikes, sediments and granitoids of different ages.

We found that pristine  $^{182}\text{W}$  signatures are only preserved in unaltered samples with near canonical W/Th ratios. The oldest samples, early Paleoarchean, juvenile, igneous rocks from the East Pilbara Terrane, display a uniform  $^{182}\text{W}$  excess of  $12.6 \pm 1.4$  ppm (95% CI), a magnitude similar to rocks from other Archean cratons (Willbold et al., 2011; Touboul et al., 2014; Willbold et al., 2015; Liu et al., 2016). These pristine  $^{182}\text{W}$  isotope signatures progressively vanish from ca. 3.3 Ga onwards and are only preserved in younger igneous rocks of the craton that tap stabilized ancient lithosphere and that integrate the W isotope composition of the average Pilbara Craton. The origin of  $^{182}\text{W}$  isotope anomalies and their decline to modern-mantle like values is in line with previous findings that found evidence for an incomplete late veneer contribution to the mantle sources of rocks from the Pilbara Craton (Maier et al., 2009; Archer et al., 2019). Collectively, our data indicate that Hadean, pre-late veneer mantle was preserved for more than 1 billion years, much longer than evident from other cratons (Touboul et al., 2014; Rizo et al., 2016b). These are important observational constraints on the Archean mantle, which are indispensable for numerical simulations

as such input parameters define the evolutionary pathway of computational convection models (Weller and Lenardic, 2012). Moreover, our detailed investigation of the elemental W systematics demonstrate that metasomatic agents progressively redistributed W from different reservoirs and thereby re-mixed variable W isotope compositions. We argue that prevalent  $^{182}\text{W}$  isotope excesses reported in the literature and the scatter observed is not a pervasive signature with its associated analytical noise but rather an integrated dataset of  $^{182}\text{W}$  isotope compositions of a transient Archean mantle. Consequently, the long-standing apparent mismatch between virtually constant  $^{182}\text{W}$  isotope excesses and progressively vanishing  $^{142}\text{Nd}$  anomalies through Archean time (Rizo et al., 2016b) is therefore well explained by the larger mobility of W compared to Nd and its re-distribution during secondary processes.

In our third project, we investigated Paleoarchean samples from the eastern Kaapvaal Craton, southern Africa, to further evaluate the processes that account for  $^{182}\text{W}$  anomalies in Archean rocks. Lithologies from this craton are well suited to search for vestiges of early silicate differentiation, because they were shown to display both heterogeneous  $^{142}\text{Nd}$  and  $^{182}\text{W}$  anomalies (Touboul et al., 2012; Puchtel et al., 2016a; Schneider et al., 2018). We performed high-precision  $^{182}\text{W}$  isotope analyses on a comprehensive suite of 17 samples.

Interestingly, our dataset reveals a co-variation of  $^{182}\text{W}$  isotope composition with initial  $\epsilon^{143}\text{Nd}_{(t)}$  and  $\epsilon^{176}\text{Hf}_{(t)}$ . To our knowledge, this is the very first discovery of a co-variation between  $^{182}\text{W}$  anomalies and long-lived radiogenic nuclides. The observed co-variation for our samples is further strengthened by literature data for komatiites from the Schapenburg Greenstone Remnant (SGR, Puchtel et al., 2016) and the Komati Formation from the Barberton Greenstone Belt (BGB, Touboul et al., 2012; Puchtel et al., 2013). As the observed co-variations of  $^{182}\text{W}$  with  $\epsilon^{143}\text{Nd}_{(t)}$  and  $\epsilon^{176}\text{Hf}_{(t)}$  are largely defined by ultramafic-mafic samples, the observed trend reflects the mixing of different mantle-source reservoirs. One mantle endmember exhibits no resolvable  $^{182}\text{W}$  isotope anomaly at near chondritic initial  $\epsilon^{143}\text{Nd}_{(t)}$  and  $\epsilon^{176}\text{Hf}_{(t)}$  values, most likely representing the near primitive mantle. The other endmember is best characterized by komatiites from the SGR that exhibit the largest  $^{182}\text{W}$  isotope deficits of up to -11.4 ppm and strongly elevated initial  $\epsilon^{143}\text{Nd}_{(t)}$  and  $\epsilon^{176}\text{Hf}_{(t)}$  values of up to +2.6 and +6.2  $\epsilon$  units, respectively (Puchtel et al., 2016a).

As we demonstrate in **chapter 3**, the only plausible model to explain these patterns is the presence of recycled mafic restites from a Hadean protocrust in the ancient mantle

beneath the Kaapvaal Craton. Moreover, our proposed geodynamic model for the Kaapvaal Craton also provides an intriguing explanation for  $^{182}\text{W}$  isotope variations in modern OIBs. As we show in **chapter 3**, modern OIBs and our samples from the Kaapvaal Craton show striking similarities in their combined  $^{182}\text{W} - ^{143}\text{Nd} - ^{176}\text{Hf}$  isotope patterns. We therefore speculate, that lower crustal restites from a Hadean protocrust were delaminated and ultimately recycled into the lower mantle, where they might be part of large low shear-wave velocity provinces (LLSVPs) in the present day mantle that were interpreted to contribute to rising mantle plumes (Burke et al., 2008). In this regard, our model provides an alternative explanation for the origin of negative  $^{182}\text{W}$  isotope anomalies in modern OIBs and bridges  $^{182}\text{W}$  isotope systematics in Archean mantle derived rocks with observations from modern-day mantle plumes.

# Chapter 1

## 1 Uniform $^{182}\text{W}$ isotope compositions in Eoarchean rocks from the Isua region, SW Greenland: the role of early silicate differentiation and missing late veneer

### 1.1 Abstract

Eoarchean rocks from the Isua region in southern West Greenland are known to exhibit isotope anomalies of  $^{182}\text{W}$  and  $^{142}\text{Nd}$ . The excess  $^{182}\text{W}$  in many rocks from the Isua region have been explained by two endmember models: (1) missing late veneer or (2) silicate differentiation shortly after Earth's formation. Furthermore, it has been proposed that pristine W isotope systematics in rocks from the Isua region (herein the Isua supracrustal belt and adjacent area) have been obscured by metamorphic disturbance. To address these issues, we present a comprehensive dataset, combining high precision  $^{182}\text{W}$  isotope data with trace element data, including high precision elemental W-Th-U abundance data. We present an improved analytical protocol that allows processing gram-sized samples with W abundances in the lower ng/g range. This protocol also results in markedly improved ion exchange column yields and cleaner W fractions, thereby minimizing nuclear volume effects on  $^{183}\text{W}$ . To compare with previous studies, our dataset includes some samples from previously investigated units in the Isua region (Isua Supracrustal Belt (ISB) mafic-ultramafic assemblages and Ameralik dikes). In addition, several Eoarchean key units in the Isukasia terrane (Isua region) and the Færingehavn terrane (Nuuk region) have been examined for their W isotope composition in this study for the first time. These newly investigated units include recently recognized mantle-like peridotites from both terranes that display PGE abundances and patterns similar to modern depleted mantle peridotites, felsic lithologies from the ISB, as well as key amphibolite and TTG localities from low-strain domains south of the ISB. Virtually all rocks from the Isua region show significant W enrichment with W/Th of up to 160 in mafic to ultramafic samples. None of the samples from SW Greenland that were object of  $^{182}\text{W}$  isotope analysis in this study and virtually all previous studies appear to have preserved near canonical W/Th

ratios (i.e., between 0.09 and 0.24). Independent of W enrichment, however, it can now be shown that there is a uniform  $^{182}\text{W}$  isotope excess in the different rock types from the Itsaq Gneiss Complex (IGC) (average  $12.8 \text{ ppm} \pm 1 \text{ ppm}$ , 95% confidence interval). Importantly, none of the rock suites investigated exhibit modern mantle-like  $^{182}\text{W}$  isotope signatures of  $\mu^{182}\text{W} = 0$ . By combining  $^{182}\text{W}$  signatures in the different lithologies with elemental W systematics, we therefore can infer that the  $^{182}\text{W}$  excess in Eoarchean rocks from the Isua region is widespread, and independent of W enrichment. Hence, we regard the  $^{182}\text{W}$  excess as an intrinsic feature of the Eoarchean assemblages in the Isua region. Notably, mantle-like peridotites from both the Isukasia and F eringehavn terranes display the same  $^{182}\text{W}$  excess, as all other units, although they have been shown to display the full inventory of Highly Siderophile Elements (HSE) found in Phanerozoic mantle peridotites. Evidently, the W isotope budget in these rocks is clearly decoupled from HSE systematics, which hampers a straightforward explanation for  $^{182}\text{W}$  isotope excesses in terms of the missing late veneer model. As Platinum Group Element (PGE) patterns in mantle-like Eoarchean peridotites from the Isua region are similar to those in Phanerozoic rocks, we rather propose that to a large extent the  $^{182}\text{W}$  excesses are a vestige of early silicate differentiation processes, in line with positive  $^{142}\text{Nd}$  anomalies found in rocks from the Isua region, suggesting initial silicate differentiation prior to 4.50 Ga.

## 1.2 Introduction

The short-lived  $^{182}\text{Hf} - ^{182}\text{W}$  isotope system (half-life = 8.9 Ma, Vockenhuber et al., 2004) has become a key tool in understanding differentiation processes in the Early Earth. Since analytical improvements have allowed resolution of  $^{182}\text{W}$  compositions at the lower ppm (0.01  $\epsilon$ -unit) level, the  $^{182}\text{Hf} - ^{182}\text{W}$  decay system has not only provided insights to processes such as early planetary core formation, but also into early silicate differentiation processes, or late veneer addition. The discovery of small-scale anomalies in Archean (e.g. Willbold et al., 2011; Touboul et al., 2012) and modern rocks (Rizo et al., 2016a; Mundl et al., 2017) have spurred a discussion about the origin of terrestrial  $^{182}\text{W}$  anomalies. These  $^{182}\text{W}$  isotope excesses have been explained as either vestige of a missing late veneer component (Willbold et al., 2011; Willbold et al., 2015) or as the result of early silicate differentiation (e.g. Touboul et al., 2012; Touboul et al., 2014; Rizo et al., 2016b) during the lifetime of  $^{182}\text{Hf}$ . This issue is still under



debate, largely because the results from other geochemical tracers like  $^{142}\text{Nd}$  or HSE systematics are apparently contradictory (e.g. Puchtel et al., 2016) and the geochemical behavior of W in Archean rocks is still poorly understood.

Interpreting the origin of  $^{182}\text{W}$  anomalies with respect to a missing late veneer hinges on tightly constraining the Archean mantle abundances of highly siderophile elements (HSE). However, most HSE estimates for Archean mantle composition are based on their mafic derivatives, an approach with large uncertainties (Maier et al., 2009; Dale et al., 2017). Many  $^{182}\text{W}$  isotope studies do not include HSE measurements (e.g. Willbold et al., 2011; Willbold et al., 2015). Coupled HSE and  $^{182}\text{W}$  compositions have only been measured on mafic-ultramafic assemblages (e.g. Touboul et al., 2014; Rizo et al., 2016b; Dale et al., 2017), in which the ultramafic rocks were not mantle peridotites or of ambiguous origin. Other geochemical studies proposed that the fluid-mobility of W (e.g. König et al., 2008) can lead to selective W enrichment and obscure the elemental W budget, in particular in Archean rocks (Rizo et al., 2016b). Such an overprint may severely hamper the understanding of the origin of anomalous W isotope compositions. While pioneering  $^{182}\text{W}$  studies focused on Eoarchean rocks from the Isua region (Schoenberg et al., 2002a; Iizuka et al., 2010; Willbold et al., 2011), anomalous  $^{182}\text{W}$  patterns have now been found in several other Eoarchean cratons (e.g. Superior Province, Touboul et al., 2014; Slave Craton, Willbold et al., 2015; Kapvaal craton, ; Puchtel et al., 2016), now also including rock suites that show deficits in  $^{182}\text{W}$  (Schapenburg komatiites of the Kaapvaal craton, Puchtel et al., 2016). Yet, the origin of the  $^{182}\text{W}$  anomalies has remained contentious.

In particular the Isua region within the Eoarchean Itsaq Gneiss Complex (IGC) has been subject to detailed  $^{182}\text{W}$  studies that were combined with  $^{142}\text{Nd}$  studies and HSE-systematics (Willbold et al., 2011; Rizo et al., 2016b; Dale et al., 2017). The pioneering study by Willbold et al. (2011) reported the first positive  $^{182}\text{W}$  isotope excesses in Archean rocks from the Isua Supracrustal Belt (ISB) and proposed that the magnitude of  $^{182}\text{W}$  excesses (ca.10-20 ppm) is consistent with a pre-late veneer mantle that is largely devoid of chondritic material added after core formation. For the Isua region this hypothesis was supported by  $^{182}\text{W}$  studies that included HSE systematics (Rizo et al., 2016b; Dale et al., 2017). Both studies however have come to markedly different conclusions on the origin of  $^{182}\text{W}$  anomalies. Most importantly, the studies by Rizo et al. (2016b) and Dale et al. (2017) reported heterogeneous  $^{182}\text{W}$  excesses in Eoarchean

rocks from the Isua region. Recently, van de Löcht et al. (2018a) confirmed previous studies (Bennett et al., 2002; Friend et al., 2002; Nutman et al., 2007) that >3.800 Ma ultramafic inclusions in the IGC from South of the ISB and from the Narssaq peninsula in the Nuuk region are residual mantle peridotites. The authors have shown that the HSE concentrations in these mantle-like peridotites overlap with the modern mantle, which clearly demonstrates that the ambient mantle beneath the North Atlantic Craton has received a nearly complete late veneer contribution (60 – 100%). These peridotites are good candidates to investigate the origin of  $^{182}\text{W}$  isotope anomalies.

Here, we report a comprehensive  $^{182}\text{W}$  dataset covering several Eoarchean lithostratigraphic units from the IGC. To enable high precision  $^{182}\text{W}$  measurements in samples with W abundances at the lower ppb level we developed a new separation technique that allows processing of large sample quantities. We analyzed 26 samples from a variety of Eoarchean lithologies, including mafic-ultramafic assemblages, TTGs, and Paleoarchean samples from the Ameralik dike swarm (3.5 -3.26 Ga, Nutman et al., 2004). In order to cross-reference with other studies, we included lithostratigraphic units with known  $^{182}\text{W}$  isotope compositions. Beyond these samples, several Eoarchean key units in the Isukasia terrane (Isua region) and the Færingehavn terrane (Nuuk region) have been examined for the first time, and our dataset also includes  $^{182}\text{W}$  data for the mantle-like peridotites from Narssaq peninsula (Nuuk region) and the region south of the ISB (SOISB) reported by van de Löcht et al. (2018a). The high precision  $^{182}\text{W}$  isotope data are combined with trace element data that for the first time includes high precision elemental W-Th-U-Ta data, obtained by isotope dilution. The combined high precision  $^{182}\text{W}$  and trace element dataset now allows for better evaluation of the effects of secondary W redistribution and the role of missing late veneer contributions.

### 1.3 Methods

All samples were cleaned of visibly weathered surfaces and veins using a rock saw. Subsequently, the samples were crushed to rock chips with a steel hand mortar or steel jaw crusher. A representative powder aliquot of these chips was prepared in an agate mill for bulk rock analyses.

### 1.3.1 Whole rock major, trace element and isotope dilution measurements (HFSE, Th & U)

For most samples, major elements were analyzed by XRF on melt tablets after Li-tetraborate-fusion using a Philips PW 2400 spectrometer at Cologne. Trace element concentrations were determined after high-pressure acid digestion by quadrupole ICPMS using an Agilent 7500cs mass spectrometer at University of Kiel, following the analytical protocol of Garbe-Schönberg (1993) and Hoffmann et al., (2011a). Replicates and reference material *BHVO-2* were measured during the analytical sessions. Results for major and trace elements are shown in Table A1 (appendix A). For the majority of the major and trace elements, the reproducibility for the reference material and replicates were better than  $\pm 10\%$ . Whole rock major and trace element abundances for samples from a magma *mingling association* from the ISB were measured by ACME labs/Bureau Veritas in Vancouver, Canada by XRF and ICP-MS, with precisions of  $\pm 5\%$  and  $\pm 15\%$ , respectively.

The abundances of W, Th, and U in all samples, as well as Zr, Hf, Nb, Ta, and Lu in the majority of samples, were determined by isotope dilution using a Thermo Fisher® Neptune Plus Multicollector ICP-MS at University of Cologne. Analytical details followed the protocols given in Münker et al. (2001), Weyer et al. (2002), Kleine et al. (2004), and Luo et al. (1997). Prior to sample digestion in Savillex PFA vials, all vials were cleaned with HNO<sub>3</sub>, reverse aqua regia, concentrated HF, and 1mM DTPA, respectively (Peters et al., 2015). To ensure the complete digestion of the samples, our protocol includes a Parr® bomb digestion step, in which the Savillex vials are placed for 24 hours at 180°C in closed steel containers to ensure complete dissolution of residual phases during high pressure acid digestion (e.g. Hoffmann et al., 2010). According to Kleine et al. (2004) Savillex vials may contain significant amounts of W that can be released during high pressure bombing. Therefore, we assessed the individual beaker - blank contribution of older Savillex vials that were bombed in advance (24 hours at 180 °C). Inadequate vials with high W blanks (> 80 pg) were rejected to ensure low blank contributions ( $\leq 0.5\%$ ) from bombing.

For the isotope dilution measurements, sample splits of ~100 mg were spiked with mixed <sup>233-236</sup>U – <sup>229</sup>Th and <sup>183</sup>W – <sup>180</sup>Ta – <sup>180</sup>Hf – <sup>176</sup>Lu – <sup>94</sup>Zr tracers (Weyer et al., 2002; Münker, 2010). Complete digestion of the samples was achieved by several steps. First, samples were dissolved in a 1:1 concentrated HF – concentrated HNO<sub>3</sub>

mixture (6 ml) in closed pre-bombarded Savillex vials on a hotplate for at least 12 hours (120° C) and subsequently dried down, before they were placed for 24 hours at 180° C in Parr® bombs using a 3:1 HF – HNO<sub>3</sub> mixture (6 ml). Subsequently, 1 ml of HClO<sub>4</sub> was added to each sample prior to a progressive dry down (Yokoyama et al., 1999). The residues were then evaporated to dryness in 2 ml concentrated HNO<sub>3</sub> and trace HF (0.024 M) before they were dissolved in 6 ml 6 M HCl – 0.06 M HF for 5-6 hours at 120° C to achieve full sample-spike equilibrium. In case of complete HFSE separation, a 20% aliquot was taken from the 6 ml of 6 M HCl – 0.06 M HF solution for W separation. For the elements Lu, Hf, Ta, Zr, and Nb we applied a three step ion exchange chromatography procedure (Münker et al., 2001), in which a U-Th aliquot was taken during loading on the second stage ion exchange column. Tungsten separation followed a shortened procedure described by Kleine et al. (2004), while separation of Th and U was achieved on TRU-Spec following Luo et al. (1997). In cases where only W, Th and U were separated, the fully digested samples were divided into two splits before W and U-Th separations were each performed separately, following the protocols described above. All isotope dilution measurements were conducted on the Thermo Fisher Neptune MC-ICP-MS at Cologne, analytical uncertainties and further references are given in Münker (2010). For <sup>229</sup>Th/<sup>232</sup>Th measurements, we used an SEM ion counter equipped with an RPQ system on mass <sup>229</sup>Th. Our external precision and accuracy for elemental ratios determined by isotope dilution involving U and Th typically is better than ± 1% for both U/W and Th/W (2 SD). Total blanks during ID measurements were generally 1 – 66 pg/g (Th), 9 – 19 pg (U), and 50 – 65 pg/g (W). For W this translates to propagated errors of blank uncertainties ≤ ± 0.5%.

### *1.3.2 Ion exchange protocol for high precision W isotope measurements*

To improve existing protocols for separation of W from rock samples, we developed a new separation procedure that permits W isotope measurements on samples with W contents in the lower ppb range, where gram-sized amounts of sample need to be processed. In addition, we aim to better understand the origin of artificial mass independent isotope effects that were previously reported in the literature (Shirai and Humayun, 2011; Willbold et al., 2011; Kruijer et al., 2012; Cook and Schönbacher, 2016).

As reagents, we used blank tested Teflon-distilled HCl, HF and HNO<sub>3</sub> as well as commercial Suprapur<sup>®</sup> H<sub>2</sub>O<sub>2</sub> (Merck KGaA) throughout the chemistry. To prevent cross-contamination and associated isotope anomalies, all Savillex vials that were used for sample digestion, and during the separation procedures, have never been used for isotope dilution (ID) measurements. All beakers were cleaned with HNO<sub>3</sub>, reverse aqua regia, concentrated HF, and DTPA/HCl. Sample splits of  $\geq 1$ g were digested in several steps, starting with dissolution in a 1:1 cHNO<sub>3</sub> – cHF mixture (30 ml) in closed Savillex vials on a hotplate at 120° C for 3-4 days. After evaporation to dryness, samples were treated 3 times with 5 ml cHNO<sub>3</sub> at 120° C to remove fluorides before dissolving the residues in 30 ml 6 M HCl at 120° to 150° C. In case of incomplete dissolution after 48 hours, the HCl digestion step was repeated. Usually, a visibly clear solution without precipitates was obtained after this repetition. Finally, the samples were dried down and dissolved in 20 ml 1 M HCl for  $\geq 12$  hours. Before loading onto ion exchange columns, the solution was centrifuged and occasionally occurring precipitates were washed repeatedly in 1 M HCl. The loading solution was adjusted to 1 M HCl – 1 vol% H<sub>2</sub>O<sub>2</sub> by adding 30% H<sub>2</sub>O<sub>2</sub>. The separation of W for high precision W isotope measurements follows a three-stage ion-exchange chromatography, which is outlined below and shown in Table 1.1.

Our separation protocol consists of three stages in the following order: A cation exchange stage after Patchett and Tatsumoto (1981), an anion exchange stage, and a final stage using TEVA resin after Peters et al. (2015). As for the first cation stage, we observed that conventional matrix separation on 7ml of AG 50W-X8 and loading in 1 M HCl – 0.1M HF, (Patchett and Tatsumoto, 1981) is insufficient for sample quantities exceeding 700 mg. For this amount of sample, incomplete matrix separation leads to overloading of the columns during the following ion exchange steps (particularly stage II, see Table 1.1), thus changing the elution behavior of the elements of interest. Increasing the column volume to 15ml of resin and loading sample solutions in 1 M HCl – 1 vol% H<sub>2</sub>O<sub>2</sub> causes the HFSE along with W and Ti to not adsorb on the resin, while most matrix elements and trace elements including REE are efficiently retained. Moreover, similar to HF, H<sub>2</sub>O<sub>2</sub> serves as a complexing agent and promotes the quantitative dissolution of W in form of peroxy complexes, similar to the formation of fluoride complexes (see Korkisch, 1989). The big advantage by making use of H<sub>2</sub>O<sub>2</sub> is, that it lacks the unfavorable property to form fluoride-precipitates with alkaline-earth metals that may lead to co-precipitation of trace elements of interest (Yokoyama et al.,

1999). Admittedly, the presence of  $\text{H}_2\text{O}_2$  can lead to hydrolysis and precipitation of other HFSE (Münker, 1998) if the solution step is prolonged. Low yields of other HFSE, however, were not observed in our protocol. Subsequently, separation of matrix elements from REE is achieved by rinsing with different HCl molarities. The W-bearing cut in HCl –  $\text{H}_2\text{O}_2$  can now be directly loaded onto an anion exchange column (2 ml BioRad AG 1-X8 in Poly-Prep® columns) to further remove potentially remaining matrix elements and to isolate W from Ti and the other HFSE. The HFSE and Ti immediately pass through the columns, and after 3 rinsing steps with HCl –  $\text{H}_2\text{O}_2$  absolute yields of nearly 100% were obtained for these elements. Subsequently, remaining matrix elements, in particular Fe and Zn, are eluted in 2 M HF. After this step, W is eluted together with Mo and Sn in 3 M  $\text{HNO}_3$  – 0.2 M HF. Peters et al. (2015) already utilized the capability of Eichrom™ TEVA resin to separate Hf, Ti, and Zr from W at high efficiency. Additionally, the elution of W in HCl media allows for a separation of W from Mo (Komori et al., 2015). We developed a slightly modified TEVA resin step as third stage column to further improve the separation of W from remaining Hf, Ti, and Zr. In contrast to the protocol by Peters et al. (2015), our columns have a different geometry, we slightly increased the resin volume (rv) to 0.65 ml and elute remaining HFSE in only 1 ½ rv of 6 M HCl, followed by the elution of W in further 9 rv of 6 M HCl and 9 rv of 4 M HCl. By employing this modified protocol, Mo and Sn are completely retained on the column and can subsequently be eluted in 12 rv 3M  $\text{HNO}_3$ . Our separation procedure was already successfully used in the study by Kurzweil et al. (2018) who performed high-precision stable W isotope measurements.

Stage	Resin volumes	Reagent
I Separation of HFSE & Ti from g-sized silicate matrix		
Column I (15 ml BioRad AG 50W-X8 in BioRad Econo-Pac® columns (ø 15mm))		
Preconditioning	4 x 1/3	1 M HCl - 1Vol% H <sub>2</sub> O <sub>2</sub>
Load, collect HFSE & Ti	1 1/3	1 M HCl - 1Vol% H <sub>2</sub> O <sub>2</sub>
Collect HFSE & Ti	2 x 1/3	1 M HCl - 1Vol% H <sub>2</sub> O <sub>2</sub>
Elute major element matrix	2 x 2 2/3	1.8 M HCl
Elute MREE - HREE & Sr	2 x 2	6 M HCl
Elute remaining LREE & Ba	2 2/3	6 M HCl
Elute Th	1 1/3	2 M HF
II Tungsten separation from other HFSE & Ti and purification from matrix		
Column II (2 ml BioRad AG 1-X8 in BioRad Poly-Prep® columns)		
Preconditioning	3 x 2 1/2	1 M HCl - 1Vol% H <sub>2</sub> O <sub>2</sub>
Load, elute HFSE & Ti	15	1 M HCl - 1Vol% H <sub>2</sub> O <sub>2</sub>
Elute HFSE & Ti	3 x 2 1/2	1 M HCl - 1Vol% H <sub>2</sub> O <sub>2</sub>
Elute remaining matrix	3 x 5	2 M HF
Collect W, Mo & Sn	3 x 2 1/2	3 M HNO <sub>3</sub> - 0.2 M HF
III Separation of W from Mo & Sn and purification from remaining HFSE		
Column III (0.65 ml Eichrom TEVA in Spectra/Chrom® 45µm PP MiniColumns)		
Preconditioning	10 3/4	6 M HCl
Load, elute remaining HFSE	3	6 M HCl
Elute remaining HFSE	1 1/2	6 M HCl
Collect W	2 x 4 3/5	6 M HCl
Collect W	2 x 4 3/5	4 M HCl
Collect Mo & Sn	2 x 6	3 M HNO <sub>3</sub>

**Table 1.1: Separation procedure of W from gram-sized samples (minimum 1 g per column) for measurements of <sup>182</sup>W in natural rock samples.**

Our absolute yields for W were mostly > 75%, which is within range of other studies (Rizo et al., 2016a of 60-90%, Cook and Schönbacher (2016) of 60-80%, Touboul et al. (2012) of ca. 80%). Exceptionally low yields below 50% (16 out of 131 measurements) occurred during the early stage of this study and were probably caused by the formation of insoluble W oxide compounds during re-dissolution after dry-down, as previously suggested by Willbold et al. (2011). Such a formation of insoluble compounds could be avoided by repeated dry-down in cHNO<sub>3</sub> – 30% H<sub>2</sub>O<sub>2</sub> (1:1), which consistently improved yields and, most importantly, also removed artificial effects on measured <sup>183</sup>W abundances (see below).

Total procedural blanks for W IC measurements were typically below 350 pg and usually contributed less than 1% of the total analyte. Some erratic blank values exceeded 4ng (ca. 5% of the total W). Most likely, these values are not representative. However, even if these erratic blank values were representative and had a  $\mu^{182}\text{W} = 0$ , the associated decrease in  $\mu^{182}\text{W}$  for typical excesses of 13 ppm in Isua samples would

propagate into the measured value by less than 1 ppm, which is still analytically insignificant.

### 1.3.3 Mass spectrometry for high precision $^{182}\text{W}$ isotope measurements

High precision measurements were performed over an eleven-month interval, using the Thermo-Fisher® Neptune MC-ICPMS at Cologne. The analytical protocol for high-precision W isotope measurement mainly followed Peters et al. (2015), with the exception that  $^{182}\text{W}$  was measured on the center cup to add  $^{177}\text{Hf}$  as an additional interference monitor for  $^{180}\text{W}$  measurements.

L4	L3	L2	L1	C	H1	H2	H3	H4
<b><math>^{177}\text{Hf}</math></b>	$^{178}\text{Hf}$	<b><math>^{180}\text{W}</math></b>	$^{181}\text{Ta}$	$^{182}\text{W}$	$^{183}\text{W}$	$^{184}\text{W}$	$^{186}\text{W}$	<b><math>^{188}\text{Os}</math></b>
		$^{180}\text{Hf}$				$^{184}\text{Os}$	$^{186}\text{Os}$	
		$^{180}\text{Ta}$						

**Table 1.2: Collector configurations on the Thermo-Fisher® Neptune MC-ICPMS at Cologne.** Faraday collectors connected to  $10^{13} \Omega$  are in bold text, interfering isotopes are shown in red.

The Thermo-Fisher® Neptune MC-ICPMS at the University of Cologne can simultaneously measure signals in 9 faraday collectors that each can be connected to one of ten amplifiers, three of which have a  $10^{13} \Omega$ , six that have  $10^{11} \Omega$  and one that has a  $10^{10} \Omega$  resistor. Table 1.2 lists the collector configurations used for our W isotope measurements including amplifiers. The low-abundance isotope  $^{180}\text{W}$  and the interference monitors  $^{177}\text{Hf}$  and  $^{188}\text{Os}$  were measured in Faraday collectors connected to  $10^{13} \Omega$  resistor amplifiers, while all other isotopes were measured using  $10^{11} \Omega$  resistor amplifiers. For  $10^{11} \Omega$  resistor amplifiers, the automated internal gain calibration routine of the mass spectrometer was used. Gain values for  $10^{13} \Omega$  resistor amplifiers were obtained by analysis of the synthetic reference material *JNdi-1* following Trinquier (2014). The associated reproducibility (2 SD) of the gains for the  $10^{13}$  amplifiers over the time period of our measurements was better than  $\pm 330$  ppm with an internal precision (2 SE) better than  $\pm 210$  ppm on each amplifier. The low precision is probably caused by individually differing response and decay times of high-ohm amplifiers (Hirata et al., 2003; Günther-Leopold et al., 2005; Cottle et al., 2009; Pfeifer et al., 2017). Note that our analytical routine expresses unknown isotope compositions relative to a terrestrial reference material (W NIST SRM 3136) or



terrestrial in-house rock standards that are analyzed at the same run conditions along with the samples. As we always alternate samples and standards at relatively short measurement periods (when compared to TIMS), any inaccuracy in gain values of amplifiers that are used for measuring isotopes of the element of interest cancels out. Moreover, inaccuracy in gain values at the level observed here is generally insignificant when associated with interference monitors for small magnitudes of interference correction. The magnet settling time was set to 1 s. Baselines of 1200 s were taken before every measurement session, following the gain calibration with a break of at least 10 minutes, in order to permit signal decay on the  $10^{13}$  Ohm amplifiers.

The solution was introduced into the MC-ICP-MS by a self-aspirating Cetac AridusII PFA nebulizer with an average uptake rate of 70  $\mu\text{l}/\text{min}$ . By installing a stable sample introduction dual quartz chamber between the desolvator system and the torch we increased the expansion volume of the inlet system, which significantly increased signal stability. A washout time of 300 s was interspersed between measurements.

Analyses were performed in static and low-resolution mode ( $M/\Delta M \sim 1850$ ), using a combination of an H-type sample and an X-type skimmer cone. Using  $10^{11}$  Ohm amplifiers, a signal of 5.3 V was typically obtained on  $^{182}\text{W}$  for a  $\sim 50$  ng/ml W sample solution at an uptake rate of ca. 70  $\mu\text{l}/\text{min}$ . High precision W isotope measurements were typically run at intensities of 2.7 – 22 V on  $^{182}\text{W}$ , corresponding to 32-161 ng/ml solutions. We found an optimized reproducibility (relative 2 SD) for 60 – 100 cycle analysis. Furthermore, shorter measurements at higher intensities resulted in better reproducibility than longer measurements at lower intensities, most likely due to instrumental drift. Therefore, a single high precision W isotope measurement typically comprised 60 cycles of 8.39 s integration time each. All samples were measured at least five times and  $\mu^{182}\text{W}$  values are reported with corresponding 95% confidence intervals (95% CI). To perform multiple measurements on samples with lower ppb-level W concentrations, up to ten powder aliquots per sample were dissolved, individually passed through our separation procedure, and individually measured. During the course of measurements, samples were always bracketed by a reference material (W NIST SRM 3136). Results for  $^{182}\text{W}$  isotope compositions are always reported in the  $\mu$  notation (equivalent to ppm) relative to NIST SRM 3136.

For W isotope analysis, small isobaric Os interferences on mass 184 and 186 were monitored by measuring  $^{188}\text{Os}$ . Corrections for Hf and Ta interferences on mass 180

were done monitoring  $^{177}\text{Hf}$ ,  $^{178}\text{Hf}$ , and  $^{181}\text{Ta}$ . Corrections for isobaric  $^{180}\text{Hf}$  always used the  $^{177}\text{Hf}$  monitor, because erratic  $^{178}\text{Hf}$  results have previously been observed (e.g. Sprung et al., 2010). Final W cuts had  $^{177}\text{Hf}/^{183}\text{W} \leq 6 \cdot 10^{-5}$ , allowing for accurate interference corrections for  $^{180}\text{W}$  (Schulz et al., 2013). Mass bias corrections used the exponential law (Russell et al., 1978), normalizing either to  $^{186}\text{W}/^{184}\text{W} = 0.92767$  (denoted '6/4') (Völkening et al., 1991) or  $^{186}\text{W}/^{183}\text{W} = 1.9859$  (denoted ('6/3')). As these ratios are both affected by Os interferences, the final mass bias correction for all isotope ratios of W is done after first subtracting Os interferences from  $^{186}\text{W}/^{184}\text{W}$  and  $^{186}\text{W}/^{183}\text{W}$  and using their measured ratios for an initial estimate of the mass bias. Using two isotope ratios ( $^{186}\text{W}/^{184}\text{W}$  and  $^{186}\text{W}/^{183}\text{W}$ ) for mass bias correction allows to check for analytical artifacts, e.g., mass independent fractionation effects (e.g. Shirai and Humayun, 2011) or interferences by organic species. In section 5.1 we show, that several of our samples are affected by a mass-independent fractionation of the odd isotope  $^{183}\text{W}$  relative to the even isotopes  $^{182}\text{W}$ ,  $^{184}\text{W}$ , and  $^{186}\text{W}$ , as previously described by Willbold et al. (2011) and Kruijer et al. (2012). This observation can be described by what is predicted for a nuclear field shift (NFS) effect (Cook and Schönbacher, 2016). It has recently been demonstrated for MC-ICP-MS measurements, that correcting for the instrumental mass bias by using an internal normalization to  $^{186}\text{W}/^{183}\text{W}$  can create analytical artifacts (Kruijer and Kleine, 2018). Therefore, we initially make use of the  $^{186}\text{W}/^{184}\text{W}$  ratio to correct for instrumental mass bias. After applying a correction for  $^{183}\text{W}$  however, measurements normalized to 6/4 and 6/3, respectively, agree within uncertainty. Typical deficits of  $\mu$   $^{183}\text{W}$  after normalization to 6/4 were always smaller than -16 ppm. By modifying the dry-down protocol during the course of the study (cHNO<sub>3</sub> – 30% H<sub>2</sub>O<sub>2</sub>) the mass independent effects on  $^{183}\text{W}$  could be completely removed within typical analytical uncertainty ( $\pm$  3ppm).

Average external reproducibilities achieved for samples are  $\pm$  10.9 ppm (2 SD). Given that each sample was analyzed 5 – 18 times, this translates to 95% CI from  $\pm$  2.7 to  $\pm$  6.8 ppm, on average  $\pm$  4.3 ppm. The high accuracy and reproducibility of our analytical routine is further demonstrated by repeated measurements (18 sessions) of two in-house reference materials that were individually passed through our separation protocol (historical La Palma basalt "LP1" and a 3455 Ma grey gneiss from the Mtimane river, southwest Swaziland, labeled "AGC 351", Kröner et al., 2014). Despite variable procedural yields during separation and analyses at different beam intensities (2.8 –

27.2 Volts on  $^{182}\text{W}$ ), the session averages for  $\mu^{182}\text{W}$  for LP 1 ( $n = 8$ ) and AGC 351 ( $n = 10$ ), 181 single measurements if taken together, perfectly overlap within their 95% CI ( $+0.3 \pm 0.7$  ppm and  $+0.3 \pm 0.8$  ppm, respectively) and are indistinguishable from the NIST reference material (Fig. 1.1). The reproducibility of our two in-house rock standards relative to the NIST reference material is given by the 2 SD of the pooled average  $\mu^{182}\text{W}$  of 0.3 ppm for all LP 1 and AGC 351 analyses which amounts to  $\pm 2$  ppm. The high level of accuracy of our analytical approach is given by the corresponding 95% CI of  $\pm 0.5$  ppm ( $n = 18$ ). All single measurements ( $n = 181$ ) are confined by a 2 SD of  $\pm 12.1$  ppm and give a mean  $\mu^{182}\text{W}$  of  $+0.1$  ppm with a corresponding 95% CI of  $\pm 0.9$  ppm.

## 1.4 Geological background and samples

As opposed to many remnants of Paleo- to Mesoarchean terranes, the 3890-3650 Ma old IGC (e.g., Nutman et al., 1996; Horie et al., 2010; Næraa et al., 2012) in Southern

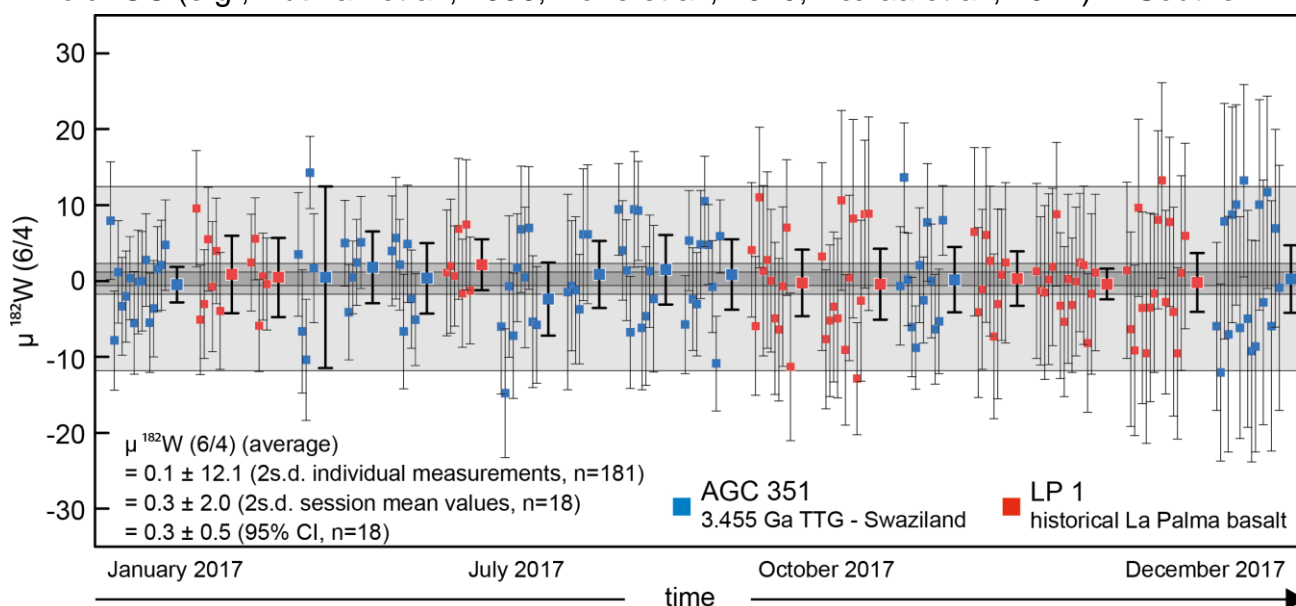


**Fig. 1.1: Long-term reproducibility for  $\mu^{182}\text{W}$  (6/4), inferred from the repeated analysis of multiple digestions for our in-house rock standards LP1 and AGC 351 reported relative to W NIST SRM 3136.** Small symbols refer to single measurements and larger symbols give the corresponding session mean values. Error bars for single measurements and session mean values refer to the internal error (2se) and the corresponding 95% CI, respectively. The long-term reproducibility for rock samples with variable composition (mafic LP1 and felsic AGC 351) passed through our chemical separation and exhibit modern mantle-like  $^{182}\text{W}$  isotope composition is given by the 2 SD of the session mean values. With proceeding time individual measurements show larger scatter, as samples with low W concentrations were run at the end of our study, and internal precision depend on beam intensities

West Greenland underwent a less complex tectono-metamorphic history, resulting in good preservation potential of primary textural and geochemical features (Moorbath et al., 1977; Nutman et al., 1984; Appel et al., 1998; Nutman et al., 1999; Polat et al., 2002; Polat and Hofmann, 2003; Hoffmann et al., 2014). The IGC was formed by several terrane assembly events and is subdivided into the Isukasia and Færingehavn terranes (Friend and Nutman, 2005). Volumetrically, the IGC is dominated by polyphase TTG gneisses that are intercalated with supracrustal fragments of various sizes (Nutman and Friend, 2009), of which the Isua Supracrustal Belt (ISB) is the largest (Figs. 1.2 and 1.3). This arcuate association of meta-volcanic and meta-sedimentary rocks has been suggested to consist of two unrelated packages, an older ca. 3800 Ma outer part, and a younger 3720-3690 Ma inner sequence (Nutman et al., 1997). These ages are given by two generations of meta-tonalites adjacent to the ISB, which form intrusive sheets into the supracrustal assemblage (Nutman et al., 1997; Nutman et al., 1999). Therefore, Nutman and Friend (2009) subdivided the Isua region into a southern ca. 3800 Ma and a northern ca. 3700 Ma terrane, with a tectonic boundary located within the belt.

We have analyzed the W isotope composition from a variety of representative samples from the Isua- and Nuuk region and discuss their W elemental behavior, in order to better constrain the geochemical significance of previously reported  $^{182}\text{W}$  isotope anomalies. For this study, (1) three tholeiitic amphibolites, (2) one TTG, (3) three Ameralik dikes, (4) a variety of samples from a mafic-felsic magma mingling association within the western limb towards the outer arc of the ISB and (5) various types of ultramafic rocks were selected for W isotope composition and concentration analysis. Most samples are from the northern and southern belt within the ISB, from South of the ISB (Isukasia terrane), and a few samples originate from the southwestern coast of the Færingehavn terrane. Figure 1.2 provides a simplified overview of the geology of southern west Greenland and the sampling areas. Figures 1.3 a-c show detailed sample localities.

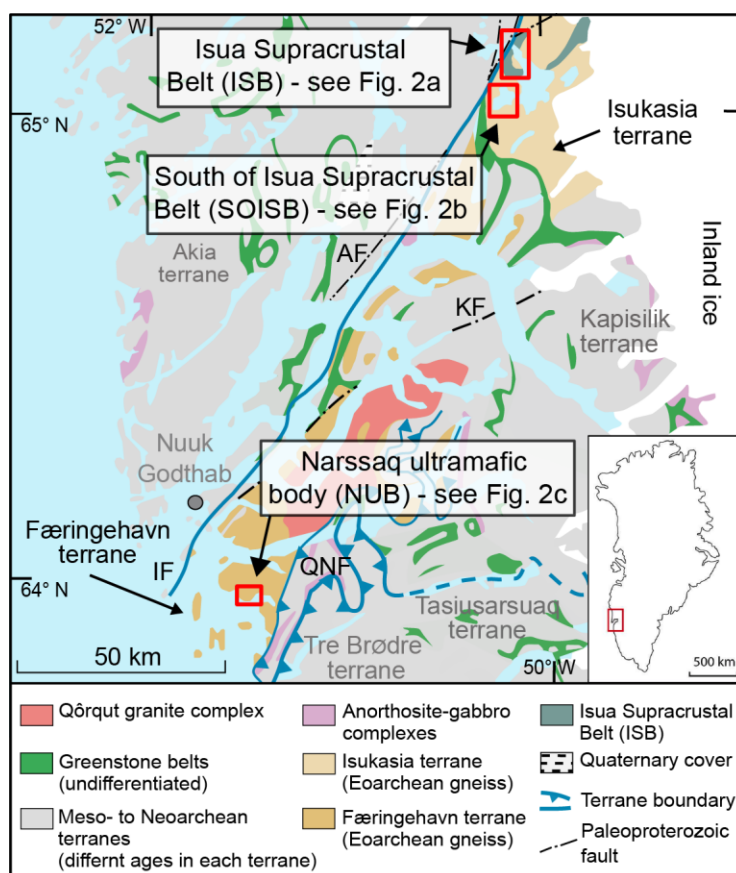


**Fig. 1.2: Simplified geological map of southern west Greenland** Sample localities are indicated by black boxes and shown in detail in Figs. 1.3 a-c. Taken from van de Löcht et al. (2018a) and modified after Naeraa et al. (2012).

(1) Sample 2000-10, previously described in studies by Polat and Hofmann (2003) and Hoffmann et al. (2011), was collected in the SW part of the ISB and is representative for ~3720 Ma amphibolites (Nutman and Friend, 2009) from the northern terrane. Samples 10-17 and 10-37 (Fig. 1.3b), described by van de Löcht et al. (2018b) were sampled from amphibolite enclaves within the ca. 3800 Ma gneiss area south of the ISB. The emplacement of their protoliths is dated to  $\geq 3800$  Ma, as inferred from crosscutting relationships with younger tonalite dikes (Nutman et al., 1996; Nutman et al., 2002; Crowley, 2003).

(2) Sample 10-38 (Fig. 1.3b) is a homogeneous TTG from a low-strain domain southwest of the ISB and representative for the TTG suite of the IGC. Similar TTGs nearby the sample locality have been dated at 3806 Ma (Nutman et al., 1999). For more details of this sample see Hoffmann et al. (2014).

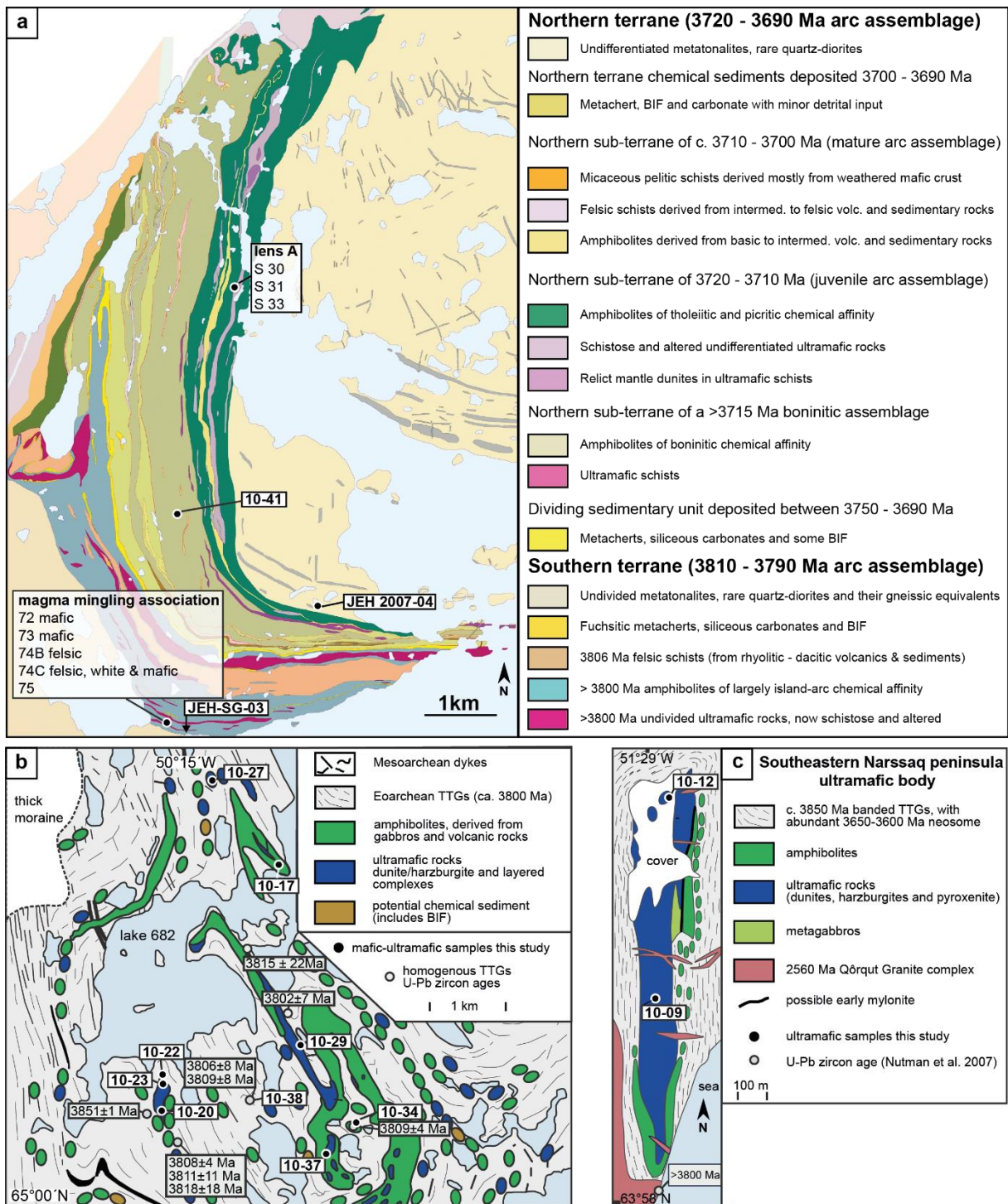


**Fig. 1.3: Simplified geological maps of (a) the western limb of the Isua Supracrustal Belt ISB, (b) the area South of the Isua Supracrustal Belt SOISB, and (c) the Narssaq Ultramafic Body NUB, showing the sample localities of this study. Sample JEH-SG-03 is located approx. 1km south of Fig. 1.3a. There is no GPS data available for sample 2000-10. Map (a) taken from Szilas et al. (2015) and modified after Nutman and Friend (2009), map (b) taken from Hoffmann et al. (2014) and modified after Nutman et al. (2009), (c) taken from van de Löcht et al. (2018a) and modified after Nutman et al. (2007). Age data in (b) and (c) are compiled from Amelin et al. (2010) and Nutman et al. (1996, 1999, 2007, 2009).**

(3) Samples from the Ameralik dike swarm postdate all rock types of the ISB and the adjacent Itsaq gneisses. As revealed by U-Pb zircon ages the emplacement of the basic dikes span a time period of ca. 250 Ma (3500 Ma to 3260 Ma, Nutman et al., 2004) and show a diversity in composition, ranging from noritic, doleritic to ultramafic. Noritic dikes mainly intrude the IGC and show trace element systematics that suggest an origin from mantle sources that had assimilated crust-like material (Gill and Bridgwater, 1979; Chadwick, 1981) or underwent metasomatism by fluid phases that were released from tonalitic host rocks (Rizo et al., 2016b). Rizo et al., (2016b) analyzed one doleritic dike from within the ISB (*00-015*) and one noritic dike intruding the gneisses north of the belt (*AM019*). They found positive  $^{182}\text{W}$  isotope anomalies for both types of Ameralik dikes, whereas Dale et al., (2017) could not confirm the presence of  $^{182}\text{W}$  excesses in doleritic dikes. The heterogeneous  $^{182}\text{W}$  isotope composition likely reflects the diverse petrogenesis of the dike swarm as indicated by their variable composition and intrusion ages (Gill and Bridgwater, 1979; Chadwick, 1981; Nutman et al., 2004). We took a comparative approach and analyzed three doleritic Ameralik dikes for cross reference (Fig. 1.3a). All three samples have similar major and trace element compositions when compared to the metadolerite dikes that were analyzed by Rizo et al. (2016b) and Dale et al. (2017) (see Fig. A1, appendix A) and show retrograde greenschist facies mineral assemblages that are dominated by amphibole and plagioclase. Samples JEH-2007-04 and JEH-SG-03 are medium-grained dikes, which intrude the adjacent orthogneisses of the IGC in the northern and southern periphery of the belt, respectively. Sample 10-41 is a medium-grained dike with that was collected within the ISB.

(4) We analyzed various rock types from a newly discovered low deformation outcrop within the outer periphery of the western limb of the ISB, where mafic-felsic magma mingling textures were observed (Fig. 1.3a). The outcrop and all rock samples have been described in Boyd (2018). The authors interpret this suite as a well-preserved mafic-felsic magma mingling-zone, indicating that mafic mantle melts and crustal melts were coeval during the formation of the ISB. Moreover, the Boyd (2018) study demonstrates that there is a petrogenetic relationship to other felsic rocks in the ISB, and that felsic rocks from the magma mingling association are analogues to the protoliths of the prominent central massive felsic unit, which occurs along the central part of the ISB. This unit has yielded U-Pb zircon ages constraining the minimum age of the ISB as ca. 3800 Ma (e.g. Baadsgaard, 1976; Michard-Vitrac et al., 1977;

Baadsgaard et al., 1984). Samples that were investigated in this study are three granular felsic rocks (*74B felsic*, *74C felsic*, and *75*), three mafic enclaves (*72*, *73*, and *74C mafic*) and one leucosome at a mafic-felsic contact (*74C white*) that is interpreted as an anatectic melt that formed due to reheating associated with mafic melt intrusion (Boyd, 2018). Samples from the magma mingling association were differently affected by secondary W enrichment, and therefore could be of great significance for assessing the impact of elemental W redistribution in rocks from the Isua region.

(5) Samples S30, S31, and S33 are dunites interpreted to be 3710 to 3720 Ma old (Friend and Nutman, 2010) from the northwestern part of the ISB (Fig. 1.3a). These ultramafic rocks were sampled from a locality referred to as “lens A” (after Friend and Nutman, 2011) one of two large ultramafic slivers that are associated with tholeiitic basalts and boninite-like volcanic rocks in the ISB. Szilas et al. (2015) have shown that the protoliths of these ultramafic rocks rather represent igneous cumulates of the local subduction-related volcanic rocks than tectonic slivers of subarc mantle, as suggested by previous studies (e.g. Friend and Nutman, 2011). For samples S31 and S33 Rizo et al. (2016b) already performed W isotope measurements on the same sample powder splits and only found slightly enriched  $\mu^{182}\text{W}$  values that could not be resolved from the present day terrestrial W isotope composition ( $\mu^{182}\text{W} = 0$ ). Beside these dunitic samples, there are only three other Archean samples from the Isua region not showing an anomalous W isotope composition (cf. Rizo et al., 2016b; Dale et al., 2017).

In addition to the samples described above, we analyzed ultramafic rocks from (A) the > 3800 Ma (Nutman et al., 2007) Narssaq ultramafic body (NUB), which is located in the southwest of the Færingehavn terrane (Figs. 2 and 3b), and (B) from ca. 3800 Ma old (Nutman et al., 1996; Friend et al., 2002) enclaves 15 km south of the ISB (SOISB), which is part of the Isukasia terrane (Figs. 1.2 and 1.3b). As recently described by van de Löcht et al. (2018a), these dunites and harzburgites can be divided into two subgroups, based on their Iridium-like Platinum Group Elements (IPGE = Os, Ir, and Ru), Platinum-like Platinum Group Elements (PPGE = Pt and Pd), and Re contents. Group 1 peridotites share similarities with residual upper mantle peridotites (strong depletion of PPGEs relative to IPGEs), whereas group 2 peridotites underwent metasomatic enrichment processes (higher PPGE concentrations). Both groups partially preserved their primary mineralogy. According to van de Löcht et al. (2018a), the HSE systematics of group 1 peridotites demonstrate that the Isua mantle was



virtually fully replenished by a putative late veneer prior to the time of their formation. Our study includes both group 1 and group 2 peridotites.

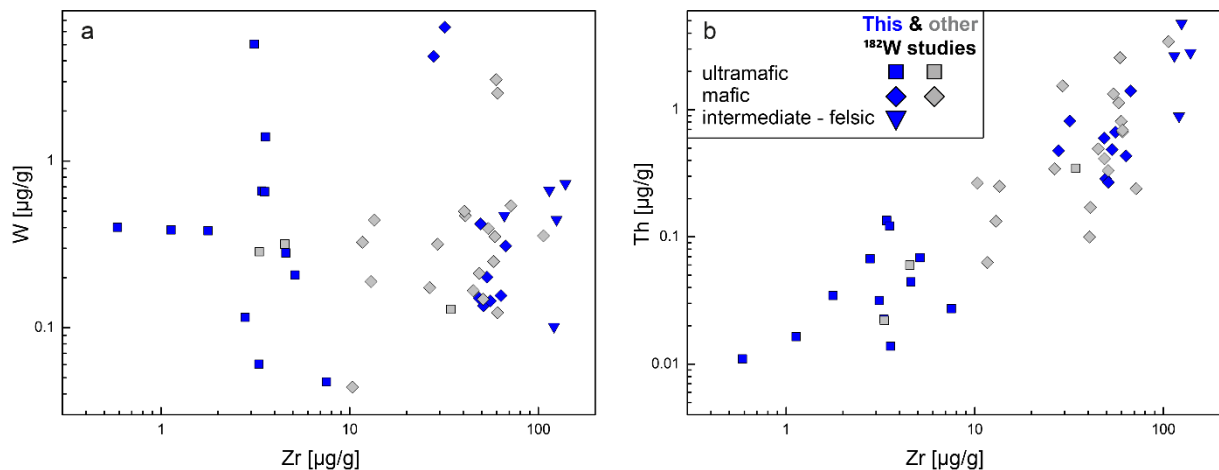
## 1.5 Results

The measured elemental concentrations for W, Th & U together with average  $^{182}\text{W}$  isotope compositions are given in Table 1.3, other high precision HFSE and conventional trace element data are given in Table A1 (appendix A). Tungsten concentrations are highly variable ranging from 0.0473 to 5.05  $\mu\text{g/g}$ . With reference to the canonical W/Th range for MORB (0.09 to 0.24) and OIB (0.04 to 0.23) (König et al., 2011), most of the samples show highly elevated W/Th ratios of up to 160, which is even higher than W/Th ratios found in arc lavas (W/Th up to 1.9, König et al., 2011). In particular, the ultramafic samples from SOISB, NUB and lens A from the western limb of the ISB show the strongest W enrichments. One mafic sample from the magma mingling association (*73 mafic*), all felsic samples and the amphibolites from the ISB and SOISB have preserved near canonical W/Th. Tungsten whole-rock concentrations do not show a correlation with Zr abundances as it would be expected for magmatic systems (Fig. 1.4a), arguing for secondary disturbance. As shown in Figure 1.5a and 1.5b, ratios of W/Th display clear negative correlations with Th contents and less pronounced positive co-variations with W contents. In this regard, elevated W/Th ratios may either be explained by secondary W enrichment or by the variable depletions of Th. In section 1.6.2 we further address this issue and combine W and Th systematics with those of Ta and Zr, as these elements show markedly lower solubilities than W in hydrothermal environments (McCulloch and Gamble, 1991; Pearce and Peate, 1995; Keppler, 1996; Münker et al., 2004; Bali et al., 2012).

Locality Sample	Unit	Age (Ma)	$\mu^{182}\text{W}$ (6/4) ( $\pm$ 95% CI)	n	W ( $\mu\text{g/g}$ )	Th ( $\mu\text{g/g}$ )	U ( $\mu\text{g/g}$ )	W/Th	W/W*
<b>Ameralik dikes</b>									
JEH-2007-04	Ameralik dike	3500 - 3260 [1]	+14.7 $\pm$ 5.7	5	0.419	0.287	0.126	1.46	6.09
JEH-SG-03	Ameralik dike	3500 - 3260 [1]	+11.8 $\pm$ 3.3	5	0.135	0.269	0.0718	0.504	2.10
010-41	Ameralik dike	3500 - 3260 [1]	+15.0 $\pm$ 2.9	5	0.156	0.432	0.0881	0.360	1.50
<b>Isua Supracrustal Belt</b>									
72 mafic	Mingling associator	3800 [2]	+10.7 $\pm$ 3.0	8	4.26	0.476	0.284	8.94	37.2
73 mafic	Mingling associator	3800 [2]	+11.4 $\pm$ 4.9	15	0.310	1.40	0.264	0.220	0.919
74B felsic	Mingling associator	3800 [2]	+13.0 $\pm$ 5.4	7	0.668	2.64	0.683	0.253	1.05
74C felsic	Mingling associator	3800 [2]	+9.5 $\pm$ 5.3	8	0.446	4.76	0.687	0.0936	0.390
74C white	Mingling associator	3800 [2]	+9.7 $\pm$ 3.4	12	0.471	7.35	2.88	0.0641	0.267
74C mafic	Mingling associator	3800 [2]	+11.7 $\pm$ 2.8	12	6.36	0.816	0.253	7.79	32.5
75	Mingling associator	3800 [2]	+11.7 $\pm$ 4.4	12	0.732	2.81	0.828	0.261	1.09
S 30	Lens A Peridotite	3720 [3]	+11.1 $\pm$ 4.0	16	0.383	0.0347	0.0108	11.0	46.0
S 31	Lens A Peridotite	3720 [3]	+10.5 $\pm$ 3.0	14	0.662	0.134	0.106	4.92	20.5
S 33	Lens A Peridotite	3720 [3]	+15.2 $\pm$ 1.9	16	0.657	0.122	0.144	5.39	22.5
2000-10	Amphibolite	> 3718 [4]	+13.3 $\pm$ 3.2	18	0.145	0.666	0.131	0.217	0.906
<b>South of Isua Supracrustal Belt</b>									
10-17	Amphibolite	> 3800 [5]	+14.1 $\pm$ 3.9	8	0.201	0.486	0.144	0.414	1.72
10-37	Amphibolite	> 3800 [5]	+14.1 $\pm$ 5.1	10	0.150	0.598	0.158	0.251	1.05
10-38	TTG	3806 [6]	+9.5 $\pm$ 3.5	10	0.102	0.887	0.380	0.114	0.477
10-20C	Type 1 Peridotite	> 3800 [5]	+15.5 $\pm$ 7.1	6	0.281	0.0444	0.0368	6.33	26.4
10-22	Type 1 Peridotite	> 3800 [5]	+14.9 $\pm$ 3.7	10	0.401	0.0110	0.0314	36.5	152
10-23	Type 1 Peridotite	> 3800 [5]	+11.3 $\pm$ 3.8	8	0.387	0.0165	0.0221	23.5	97.9
10-34	Type 1 Peridotite	> 3800 [5]	+13.0 $\pm$ 4.1	8	5.05	0.0316	0.0319	160	666
10-29A	Type 2 Peridotite	> 3800 [5]	+11.8 $\pm$ 2.0	18	1.40	0.0139	0.0796	101	420
10-29B	Type 2 Peridotite	> 3800 [5]	+10.9 $\pm$ 3.3	12	0.207	0.0688	0.179	3.01	12.5
10-27	Cumulate	> 3800 [5]	+19.9 $\pm$ 4.1	10	0.0473	0.0273	0.00753	1.73	7.21
<b>Narssaq Ultramafic Body</b>									
10-09	Type 1 Peridotite	$\geq$ 3800 [7]	+15.2 $\pm$ 7.2	8	0.0604	0.0226	0.0163	2.67	11.1
10-12B	Type 1 Peridotite	$\geq$ 3800 [7]	+15.2 $\pm$ 10.0	7	0.115	0.0675	0.0624	1.71	7.12

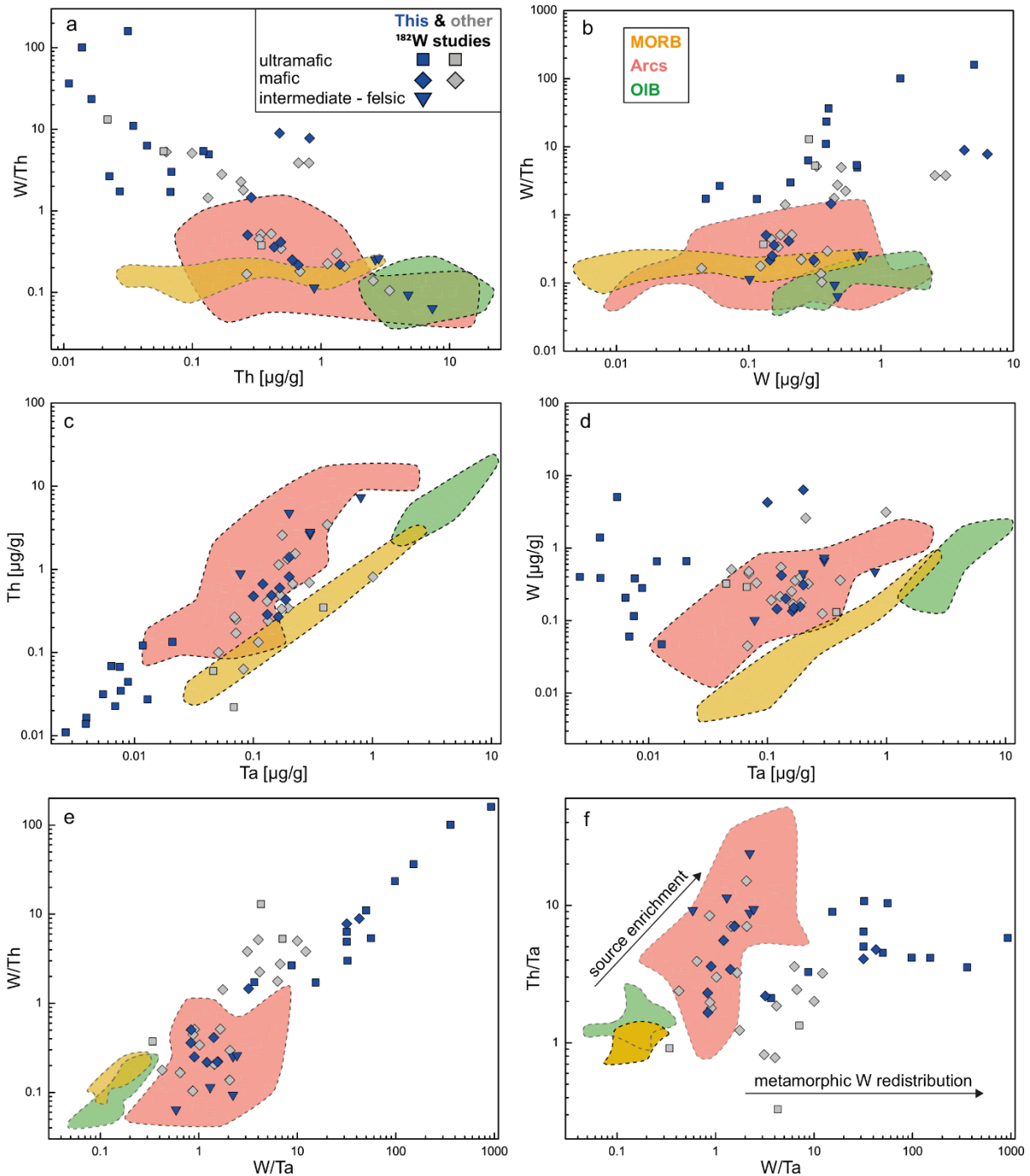
**Table 1.3: Measured  $^{182}\text{W}$  isotope compositions and concentrations for W, Th, and U obtained by high precision measurements.** All concentration measurements for W, Th, and U were performed by isotope dilution except for samples S30, S31, and S33 from lens A. The W-enrichment factor  $W/W^*$  ( $W/\text{Th}_{\text{sample}}/W/\text{Th}_{\text{canonical}}$ ) gives the deviation from the max. W/Th ratio observed in unaltered MORB glasses ( $W/\text{Th} = 0.24$  (König et al., 2011)). Age data for the lithostratigraphic units are taken from [1] Nutman et al. (2004), [2] Baadsgaard et al. (1976), [3] Friend and Nutman, (2010), [4] Nutman and Friend (2009), [5] Nutman et al. (1996), [6] Nutman et al. (1999), [7] Nutman et al. (2007).

Table 1.4 lists measured W isotope ratios that were corrected for instrumental mass bias by applying the exponential law, either involving the measured  $^{186}\text{W}/^{184}\text{W}$  (6/4) or  $^{186}\text{W}/^{183}\text{W}$  (6/3). Many samples show significantly different  $\mu^{182}\text{W}/^{184}\text{W}$  (6/4) and  $\mu^{182}\text{W}/^{183}\text{W}$  (6/3) values, usually with larger apparent excesses when 6/3 is used for normalization (Fig. 1.6a). Such samples are characterized by negative  $^{183}\text{W}/^{184}\text{W}$  (6/4) (Fig. 1.7), probably indicating a mass-independent deficiency of the odd isotope  $^{183}\text{W}$  relative to the even isotopes  $^{182}\text{W}$ ,  $^{184}\text{W}$ , and  $^{186}\text{W}$  (Cook and Schönbacher, 2016). If the NFS effect is corrected the  $^{182}\text{W}$  results for both normalization schemes (6/4 and 6/3) become indistinguishable (Fig. 1.6b, see discussion for details). Below, we always quote our  $^{182}\text{W}$  isotope compositions using the 6/4 normalization scheme.



**Fig. 1.4: Bulk rock W (Fig. 1.4a) and Th (Fig 1.4b) concentrations ( $\mu\text{g/g}$ ) plotted versus bulk rocks Zr contents ( $\mu\text{g/g}$ ).** The absence of a correlation in Fig. 1.4a argues for second stage W mobility. Data for other mafic and ultramafic rocks from the Isua region taken from Rizo et al. (2011, 2012, 2013, 2016b), and Dale et al. (2017).

As shown in Table 1.3 and illustrated in Fig. 1.8, all samples from the Isua and Nuuk regions are characterized by similarly elevated  $\mu^{182}\text{W}$  values relative to the present-day mantle, ranging from  $\mu^{182}\text{W} +9.5 \pm 3.5$  ppm to  $+19.9 \pm 4.1$  ppm. Figure A2 (appendix A) also comprises the results for  $^{182}\text{W}$  isotope analysis of individual digestions. The multiple measurements ( $n = 5$  to 18) for all samples allow for  $^{182}\text{W}$  isotope measurements at uncertainties typically better than  $\pm 5$  ppm (95% CI). Even at this high level of analytical precision, the results for all analyzed subgroups reveal no statistical difference and constitute a mean  $\mu^{182}\text{W}$  of  $+12.8 \pm 1$  ppm (95% CI), which is in accordance with previous studies (Willbold et al., 2011; Rizo et al., 2016b; Dale et al., 2017). Only sample 10–27, a peridotite cumulate sample south of the ISB displays a significantly higher  $^{182}\text{W}$  excess of  $+19.9 \pm 4.1$  ppm as compared to the average  $\mu^{182}\text{W}$ . Figure A3 (appendix A) provides a supplementary compilation of  $^{182}\text{W}$  isotope data that combines previous results with our study.



**Fig. 1.5: Combined *element-concentration* and *element-ratio* diagrams (using W, Th, and Ta) for rock samples from this study (blue symbols) and previous studies that report <sup>182</sup>W isotope systematics for rocks from SW Greenland (grey symbols).** Compared to modern mantle-derived rocks (MORB and OIB) Th (Fig. 1.5c) and W (Fig. 1.5d) are relatively enriched compared to Ta, presumably reflecting their derivation from a subduction-modified mantle source. Beyond this source enrichment the elemental W budgets were subject to post-emplacement W redistribution, probably during late-stage metamorphism and/or alteration (Fig. 1.5f). As a result W/Th ratios are systematically enriched (Fig. 1.5e).

Data for other mafic and ultramafic rocks from the Isua area were taken from Rizo et al. (2011, 2012, 2013, 2016b) and Dale et al. (2017). Data for MORB, OIB and Arc fields were taken from König et al. (2011 and references therein).

sample	Normalized to $^{186}\text{W}/^{184}\text{W} = 0.92767$		Normalized to $^{186}\text{W}/^{183}\text{W} = 1.9859$		
	$\mu^{182}\text{W} (\pm 95\% \text{ CI})$	$\mu^{183}\text{W} (\pm 95\% \text{ CI})$	$\mu^{182}\text{W} (\pm 95\% \text{ CI})$	$\mu^{184}\text{W} (\pm 95\% \text{ CI})$	$\mu^{182}\text{W}_{\text{corr}} (\pm 95\% \text{ CI})$
<b>Ameralik dikes</b>					
JEH-2007-04	14.7 ± 5.7	0.2 ± 7.9	18.5 ± 3.5	-0.2 ± 5.3	18.9 ± 8.3
JEH-SG-03	11.8 ± 3.3	-14.1 ± 7.4	29.4 ± 10.2	9.4 ± 4.9	11.0 ± 4.4
010-41	15.0 ± 2.9	-9.3 ± 6.6	29.6 ± 8.8	6.2 ± 4.4	17.5 ± 2.8
<b>Isua Supracrustal Belt</b>					
72 mafic	10.7 ± 3.0	-5.4 ± 2.7	15.9 ± 1.5	3.6 ± 1.8	8.9 ± 2.7
73 mafic	11.4 ± 4.9	-6.0 ± 3.2	19.6 ± 2.7	4.0 ± 2.1	11.8 ± 4.0
74B felsic	13.0 ± 5.4	-1.1 ± 4.6	12.1 ± 6.6	0.8 ± 3.1	10.7 ± 6.8
74C felsic	9.5 ± 5.3	-7.6 ± 4.8	20.8 ± 4.5	5.1 ± 3.2	10.9 ± 4.0
74C white	9.7 ± 3.4	-11.5 ± 3.5	24.4 ± 2.7	7.6 ± 2.3	9.5 ± 3.0
74C mafic	11.7 ± 2.8	-7.4 ± 2.1	21.2 ± 3.3	4.9 ± 1.4	11.5 ± 3.0
75	11.7 ± 4.4	-7.4 ± 2.9	20.5 ± 2.6	4.9 ± 1.9	10.8 ± 4.5
S 30*	10.1 ± 4.0	0.6 ± 3.0	9.0 ± 3.6	-0.4 ± 2.0	9.8 ± 4.4
S 31*	10.5 ± 3.0	-0.9 ± 2.0	11.8 ± 2.7	0.6 ± 1.4	10.7 ± 3.1
S 33*	15.2 ± 1.9	2.1 ± 3.0	9.8 ± 2.3	-1.4 ± 2.0	12.5 ± 3.0
2000-10*	13.3 ± 3.2	-1.1 ± 4.0	13.2 ± 3.5	0.7 ± 2.7	11.8 ± 3.5
<b>South of Isua Supracrustal Belt</b>					
10-17*	14.1 ± 3.9	1.6 ± 3.4	12.0 ± 5.4	-1.1 ± 2.3	14.1 ± 4.4
10-37*	14.1 ± 5.1	1.9 ± 4.1	11.4 ± 3.5	-1.3 ± 2.7	13.9 ± 5.3
10-38*	9.5 ± 3.5	0.6 ± 7.3	12.0 ± 7.4	-0.4 ± 4.9	12.7 ± 6.9
10-20C	15.5 ± 7.1	-13.5 ± 4.9	33.9 ± 6.8	9.0 ± 3.3	16.3 ± 11.7
10-22	14.9 ± 3.7	-7.8 ± 3.4	23.7 ± 5.1	5.2 ± 2.3	13.5 ± 2.8
10-23	11.3 ± 3.8	-7.9 ± 3.7	22.6 ± 3.1	5.2 ± 2.5	12.3 ± 4.5
10-34	13.0 ± 4.1	-5.4 ± 2.7	18.6 ± 3.3	3.6 ± 1.8	11.5 ± 4.7
10-29A	11.8 ± 2.0	-6.8 ± 1.0	21.5 ± 2.5	4.6 ± 0.6	12.6 ± 2.2
10-29B	10.9 ± 3.3	-10.1 ± 4.2	23.3 ± 4.6	6.7 ± 2.8	10.1 ± 3.7
10-27*	19.9 ± 4.1	0.6 ± 4.0	21.3 ± 5.6	-0.4 ± 2.7	22.1 ± 4.7
<b>Narssaq Ultramafic Body</b>					
10-09*	15.2 ± 7.2	1.2 ± 7.2	12.7 ± 7.2	-0.8 ± 7.2	14.3 ± 7.2
10-12B	15.2 ± 10.0	-12.3 ± 7.0	27.5 ± 6.0	8.2 ± 4.7	11.5 ± 10.7
<b>In-house rock standards (session means)</b>					
LP 1	0.9 ± 5.1	-16.1 ± 2.0	21.8 ± 8.1	10.7 ± 1.3	0.7 ± 7.0
LP 1	0.5 ± 5.2	-9.2 ± 7.7	11.5 ± 8.0	6.1 ± 5.1	-0.4 ± 4.4
LP 1	2.2 ± 3.4	-13.9 ± 5.6	23.6 ± 6.3	9.3 ± 3.7	5.5 ± 4.4
LP 1*	-0.3 ± 4.4	-1.2 ± 4.3	2.4 ± 4.0	0.8 ± 2.9	0.8 ± 4.5
LP 1*	-0.4 ± 4.7	2.5 ± 5.1	-3.7 ± 3.7	-1.7 ± 3.4	-0.4 ± 4.9
LP 1*	0.3 ± 3.6	-0.9 ± 2.2	3.6 ± 4.8	0.6 ± 1.5	2.4 ± 3.5
LP 1*	-0.4 ± 2.0	-1.2 ± 1.9	0.6 ± 3.1	0.8 ± 1.2	-1.0 ± 2.6
LP 1*	-0.2 ± 3.9	-2.8 ± 3.6	4.1 ± 3.8	1.9 ± 2.4	0.4 ± 4.3
AGC 351	-0.5 ± 2.3	0.3 ± 1.5	-1.3 ± 1.5	-0.2 ± 1.0	-0.8 ± 2.0
AGC 351	0.5 ± 8.9	-1.0 ± 5.3	-0.3 ± 10.4	0.7 ± 3.5	-1.6 ± 11.0
AGC 351	1.8 ± 4.7	-2.9 ± 6.2	6.2 ± 4.8	2.0 ± 4.1	2.3 ± 4.8
AGC 351	0.4 ± 4.6	-3.9 ± 5.3	4.4 ± 4.8	2.6 ± 3.6	-0.8 ± 4.7
AGC 351	-2.4 ± 4.8	-2.5 ± 4.6	3.9 ± 3.7	1.7 ± 3.1	0.7 ± 4.6
AGC 351	0.9 ± 4.4	-4.3 ± 6.1	6.2 ± 7.0	2.8 ± 4.1	0.6 ± 10.0
AGC 351*	1.5 ± 4.6	0.7 ± 2.9	1.5 ± 3.2	-0.4 ± 1.9	2.3 ± 3.5
AGC 351*	0.8 ± 4.6	-0.9 ± 4.4	1.1 ± 3.1	0.6 ± 2.9	-0.1 ± 5.1
AGC 351*	0.2 ± 4.3	1.5 ± 2.5	-2.8 ± 2.6	-1.0 ± 1.7	-0.8 ± 3.9
AGC 351*	0.3 ± 4.4	-3.5 ± 5.4	5.9 ± 6.3	2.3 ± 3.6	1.4 ± 6.0

**Table 1.4: Tungsten isotope composition of Greenland samples and in-house rock standards.**

\*These samples have been treated with the strong dry-down procedure involving  $\text{cHNO}_3 - 30\%\text{H}_2\text{O}_2$

## 1.6 Discussion

### 1.6.1 Methodology

Our newly developed three-stage ion exchange chromatography has the capability to separate W from large sample quantities exceeding 1g per column. This is of particular importance for high precision W isotope measurements on rocks such as peridotites or depleted basalts, where W whole rock concentrations are only in the range of several ng/g. Our procedure ensures a robust purification of W from interfering elements (basaltic matrix:  $\text{Hf}/\text{W} < 10^{-5}$ , and  $\text{Ta}/\text{W} < 10^{-2}$ ) and from elements that exert a strong influence on the mass bias behavior of W during mass spectrometry (basaltic matrix:  $\text{Zr}/\text{W} < 10^{-4}$ , and  $\text{Ti}/\text{W} < 10^{-3}$ ) (cf. Peters et al., 2015). Unlike previously used analytical protocols, our method only comprises three column steps, circumvents loading in HF media and also avoids repeated dry down steps between individual ion exchange columns, which improves absolute column yields, and largely avoids the formation of insoluble W-rich compounds. Furthermore, our procedure has the advantage to provide matrix-free cuts for elements that are of interest for further element and isotope analysis (REEs, Ti, Zr, Nb, Mo, Sn, Hf, Ta).

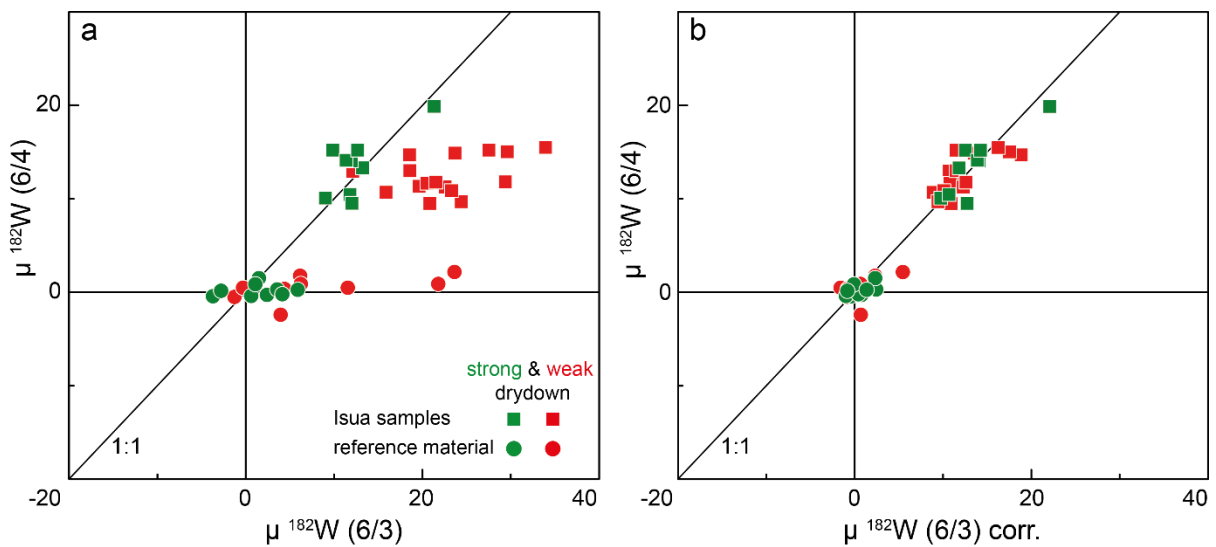


**Fig. 1.6: Measured  $\mu^{182}\text{W}$  (6/4) versus (a) measured  $\mu^{182}\text{W}$  (6/3) and (b) NFS corrected  $\mu^{182}\text{W}$  (6/3).** After correction for the NFS following Cook and Schönbacher (2016), samples and in-house rock standards that show NFS affected  $\mu^{182}\text{W}$  (6/3) (see Fig. 1.7) fall on a 1:1 correlation line (see Fig. 1.7b). Strong dry-down (green color coding) refers to a threefold treatment with 80  $\mu\text{l}$  of  $\text{cHNO}_3 - 30\%\text{H}_2\text{O}_2$  at max. 60°C before re-dissolution steps. The weak dry-down procedure (red color coding) made use of a single treatment with 1ml 6 M  $\text{HNO}_3 - 0.2$  M  $\text{HF} : \text{H}_2\text{O}_2$  (9:1). Error bars are omitted for visual clarity, but uncertainties are given in Table 1.4

We confirm a mass-independent fractionation effect of the odd isotope  $^{183}\text{W}$  from the even isotopes  $^{182}\text{W}$ ,  $^{184}\text{W}$ , and  $^{186}\text{W}$ , as first suggested by Willbold et al. (2011) and Kruijer et al. (2012). Measured  $^{183}\text{W}/^{184}\text{W}$  values (6/4) for both samples and reference materials that passed through the separation procedure reveal strong  $^{183}\text{W}$  deficits, relative to NIST SRM 3136 ( $\mu^{183}\text{W}$  (6/4) as low as -16.1 ppm, see Table 1.4). This observation has been ascribed to a nuclear field shift (NFS) effect that is consistent with available nuclear charge radii for W (Angeli, 2004; Cook and Schönbachler, 2016). In a  $\mu^{184}\text{W}$  (6/3) -  $\mu^{182}\text{W}$  (6/3) diagram, most measured samples and reference materials fall on a line with a slope of  $\sim 2$  (dashed lines in Fig. 1.7), as previously described by Kruijer et al. (2012) and predicted for samples that are affected by the NFS ((Cook and Schönbachler, 2016), solid line in Fig. 1.7). This correlation allows to correct for the NFS by using the measured  $\mu^{184}\text{W}$  (6/3) and  $\mu^{182}\text{W}$  (6/3) values and the relation  $\mu^{182}\text{W}$  (6/3)<sub>corr</sub> =  $\mu^{182}\text{W}$  (6/3)<sub>meas</sub> - (1.962 x  $\mu^{184}\text{W}$  (6/3)) (Cook and Schönbachler, 2016). After correcting for the NFS effect,  $\mu^{182}\text{W}$  (6/3)<sub>corr</sub> are in good agreement with measured  $\mu^{182}\text{W}$  (6/4) values. In a  $\mu^{182}\text{W}$  (6/3)<sub>corr</sub> -  $\mu^{182}\text{W}$  (6/4) diagram samples and reference materials now fall on a 1:1 correlation line (see Fig. 1.6b). Reference material AGC 351 seems to be less affected by the NFS effect (see Table 1.4). This could be explained by its high whole rock W concentration (11.02  $\mu\text{g/g}$ ) which buffers the NFS effect. However, other samples with high W concentrations in the range of 4.26 – 6.36  $\mu\text{g/g}$  (72 mafic, 74C mafic, 10-34) display significant offsets for  $\mu^{183}\text{W}$  (6/4) as low as -7.4 ppm (see Table 1.4).

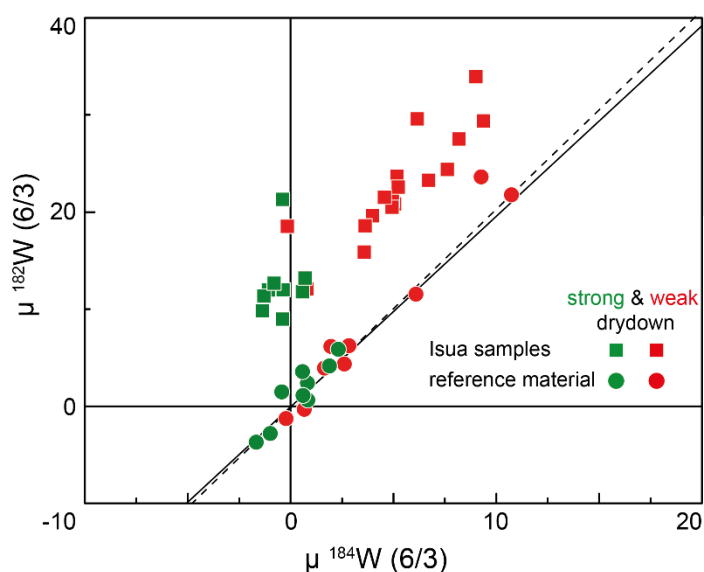


**Fig. 1.7: Measured  $\mu^{182}\text{W}$  (6/3) and  $\mu^{184}\text{W}$  (6/3) for samples and in-house reference materials.** Including one outlier the measured values for our reference materials show a correlation (indicated by dashed line) that is similar to what has previously been described by Kruijer et al., (2012) and predicted for samples that are affected by the nuclear field shift (NFS) effect (Cook and Schönbachler, 2012, solid line).

Before correcting for the NFS effect, the average  $\mu^{182}\text{W}$  (6/3) value for all Isua samples is  $+19.1 \pm 2.7$  ppm (95% CI). The NFS corrected value of  $+12.5 \pm 1.1$  ppm (95% CI) is in perfect agreement with the average  $\mu^{182}\text{W}$  (6/4) of  $+12.8 \pm 1.0$  ppm (95% CI). It has been demonstrated that the observed NFS effect is introduced during the chemical separation of W and can be explained best by isotope fractionation during incomplete re-dissolution of insoluble compounds that formed during dry-down steps (Willbold et al., 2011; Kruijer et al., 2012; Cook and Schönbacher, 2016). We can now confirm these conclusions, as stronger NFS effects, as expressed by highly negative  $\mu^{183}\text{W}$  (6/4) ratios, tend to be associated with lower procedural yields of the W purification process (see Fig. 1.9). To reduce NFS effects, we changed our dry-down procedures during the course of our study. The dry-down step between columns II and III as well as for the final W cut now involved a threefold treatment with 80  $\mu\text{l}$  of  $\text{cHNO}_3 - 30\%\text{H}_2\text{O}_2$ . This threefold dry-down was done at max.  $60^\circ\text{C}$  to prevent vigorous disproportionation of  $\text{H}_2\text{O}_2$ , which would increase cross contamination. This modification dramatically improved yields and, most importantly, also removed NFS effects on measured  $^{183}\text{W}$  abundances. Before we applied our new dry-down protocol with concentrated  $\text{HNO}_3$  and  $\text{H}_2\text{O}_2$  (strong dry-down),  $\mu^{183}\text{W}$  (6/4) reached negative values up to  $-16.1$  ppm when samples were dried down with only 6 M  $\text{HNO}_3 - 0.2$  M  $\text{HF} : \text{H}_2\text{O}_2$  (weak dry-down, see Fig. 1.10), which is in the range of previous studies (Willbold et al., 2011; Dale et al., 2017; Kruijer and Kleine, 2018). By applying our new dry-down procedure, we were able to remove the mass independent effects on  $^{183}\text{W}$  completely within typical analytical uncertainty ( $\pm 4.2$  ppm). Our new dry-down procedure allows us to directly employ measured  $^{183}\text{W}$  for high-precision  $^{182}\text{W}$  isotope analysis. This is justified by  $\mu^{182}\text{W}$  (6/3) values for samples and reference materials that now overlap within uncertainty with measured  $\mu^{182}\text{W}$  (6/4) values (see table 1.4). Average yields after modifying our dry-down procedure were 81% and are thus significantly higher than before (60%).



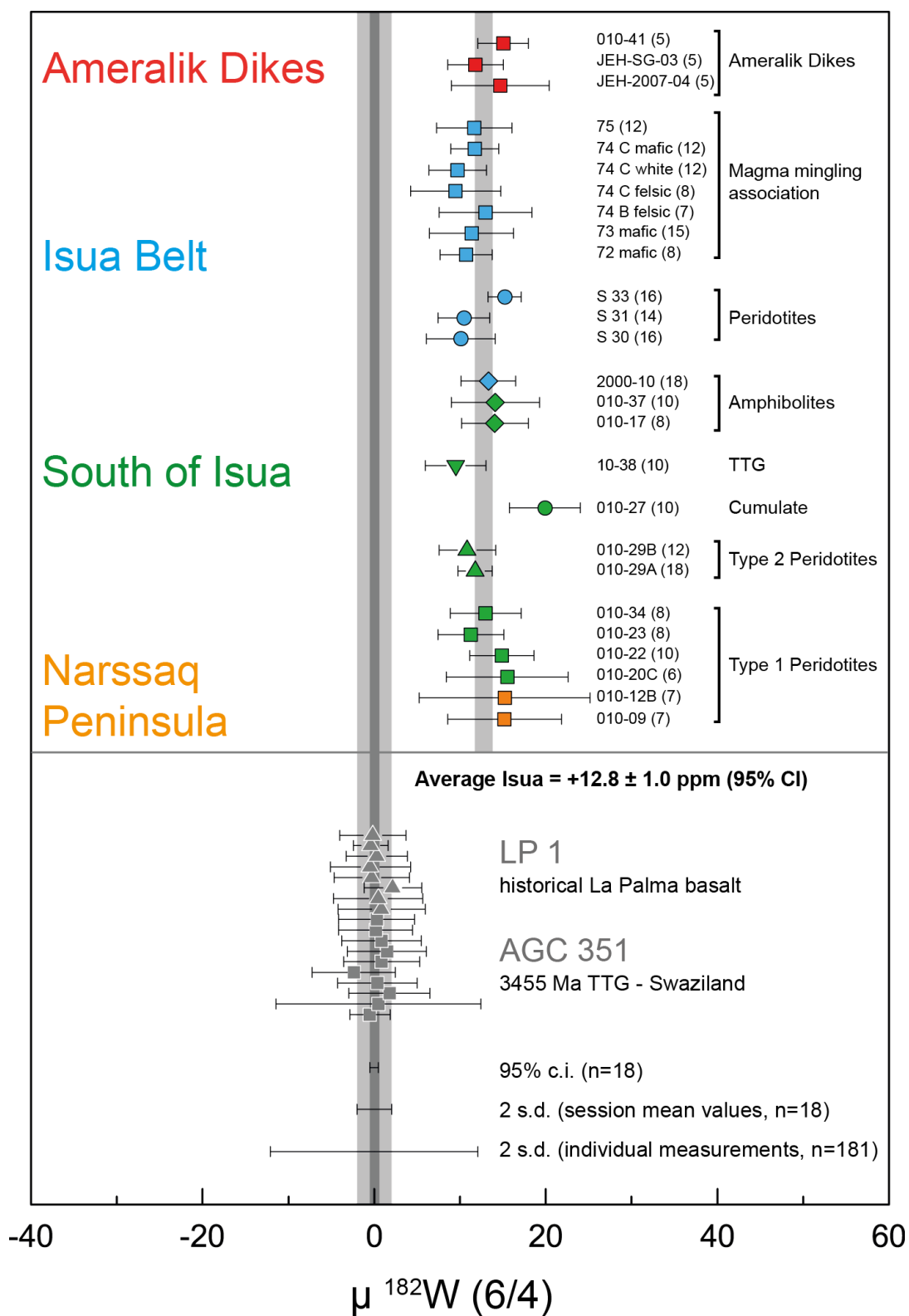


**Fig. 1.8: High precision  $\mu^{182}\text{W}$  isotope measurements for rocks from southern West Greenland (upper panel) and our in-house rock standards (lower panel).** Each datapoint corresponds to the average for repeated measurements (n) of multiple digestions. Uncertainties are given by the corresponding 95% CI. The grey shaded areas defined by the rock standards correspond to the 2 SD and 95% CI of the repeated analysis of our in-house rock standards LP1 and AGC 351. The grey bar defined by the Greenland samples defines the average  $\mu^{182}\text{W}$  for Eoarchean rocks and Paleoarchean Ameralik dikes and gives the corresponding 95% CI for all 26 samples (+12.8 ± 1.0 ppm).

We can exclude that the extremely high W concentrations found in our samples (in particular in ultramafic rocks) are the result of contamination introduced during sample preparation with the steel jaw crusher at the University of Cologne. Trace element measurements of the jaw crusher at the University of Cologne revealed a concentration of  $13.14 \mu\text{g/g}$  W, and 2.42 wt. % Cr: During sample preparation, we usually process at least 1 kg of sample. If we assume a whole rock W concentration of  $0.5 \mu\text{g/g}$  and attribute higher concentrations (e.g. sample 72 mafic with  $4.3 \mu\text{g/g}$  W) to contamination by the jaw crusher (i.e., contamination by a factor of  $\sim 9$ ), about 350g of the jaw crusher would have been abraded. This amount would shift the Cr whole rock concentration to 0.85 % (which is not observed) and the blade of the jaw crusher (6.6 kg) would completely disappear after 19 runs. Therefore, we argue that W concentrations in the jaw crusher material are too low to have an effect on the whole rock W concentrations. Moreover, we analyzed the  $^{182}\text{W}$  isotope composition of our jaw crusher and found a modern mantle like  $^{182}\text{W}$  isotope composition of  $\mu^{182}\text{W} = 0.9 \pm 1.4 \text{ ppm}$  (see Fig. A4, appendix A). Any samples that were affected by a W contamination would therefore lack measurable  $^{182}\text{W}$  isotope excesses. In fact, extremely high W concentrations in Isua samples were previously reported by Rizo et al. (2016b), who found W concentrations up to  $3.084 \mu\text{g/g}$  (3.8 Ga old amphibolite 460219). Tungsten concentrations in the range of  $\mu\text{g/g}$  were also reported in other  $^{182}\text{W}$  isotope studies on Archean rocks (Touboul et al., 2014; Willbold et al., 2015; Liu et al., 2016; Puchtel et al., 2016a).

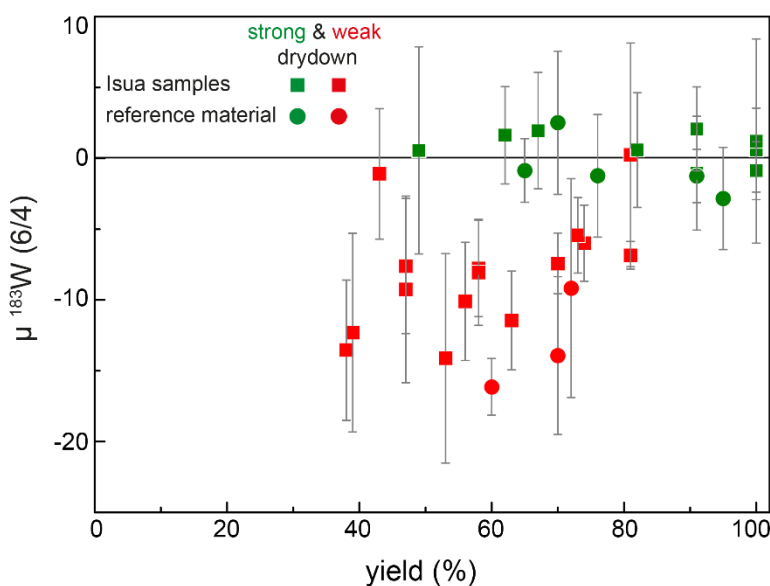


**Fig. 1.9: Measured  $\mu^{183}\text{W} (6/4)$  versus procedural yields.** Before we applied our strong dry-down protocol using  $\text{CHNO}_3 - 30\%\text{H}_2\text{O}_2$ , procedural yields were always below 80% and affected by the NFS as a function of the yield. This dependence is not observed for samples that were exposed to the strong dry-down procedure, even in cases of exceptionally low yields.

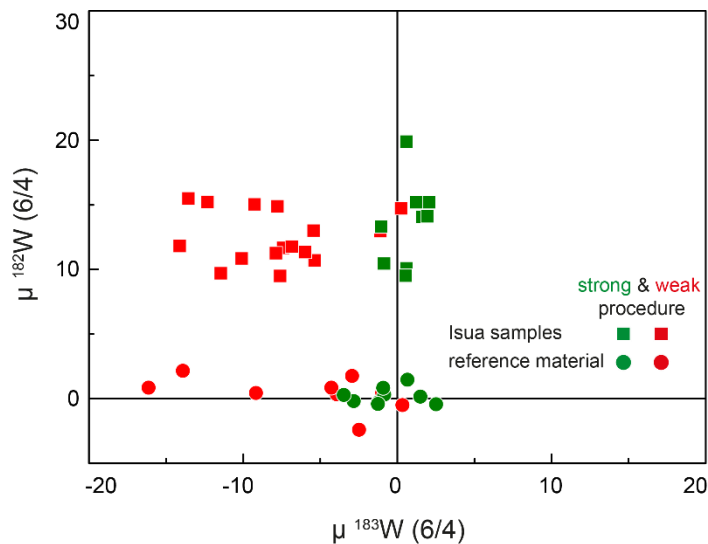


**Fig. 1.10: Measured  $\mu^{182}\text{W}$  (6/4) versus  $\mu^{183}\text{W}$  (6/4), clearly illustrating that our strong dry-down procedure is able to remove the mass independent effects on  $^{183}\text{W}$  within typical uncertainty ( $\pm 4.2\text{ppm}$ , 95% CI). Error bars are omitted for visual clarity, but uncertainties are given in Table 1.4.**

### 1.6.2 Elemental behavior of W in rocks from the Isua region

Understanding the origin of  $^{182}\text{W}$  isotope anomalies requires samples of which the elemental W budget is pristine, i.e., it was solely controlled by silicate crystal-liquid partitioning and was not affected by secondary W enrichments. The strong modification of W concentrations in samples that underwent alteration or metamorphism has been described in detail in studies by König et al. (2008) and König et al. (2011). During crystal-liquid fractionation in silicate systems, W behaves highly incompatible, similar to Th and U (e.g. Palme and Rammensee, 1981; Adam and Green, 2006; König et al., 2011). Hence, W/Th ratios in both, fresh OIB and MORB samples, are confined to a canonical range between 0.04 and 0.23 (OIB) and between 0.09 and 0.24 (MORB) (König et al., 2011; Jenner and O'Neill, 2012). In arc lavas, W/Th ratios can range to higher values of up to 1.9 by the selective addition of W-rich subduction components (König et al., 2011). The majority of samples analyzed in this study, in particular the ultramafic samples from SOISB, NUB and lens A from the western limb of the ISB, reveal highly elevated W/Th ratios that fall outside the range for silicate melting as described above, in many cases even significantly above values for young arc lavas. Samples with unusually high W/Th ratios systematically exhibit lower concentrations of Th and higher concentrations of W (Figs. 1.5a and 1.5b) being clearly the result of preferential W mobilization during second stage processes. For comparison we included previously published data (Rizo et al., 2011; Rizo et al., 2012; Rizo et al., 2013; Dale et al., 2017) for mafic and ultramafic rock samples from the Isua region, which were previously target of  $^{182}\text{W}$  isotope measurements (Willbold et al., 2011; Rizo et al., 2016b; Dale et al., 2017). Moreover, we grouped our samples in Figs. 1.4 and

1.5 (*ultramafic*, *mafic*, and *intermediate-felsic*) to provide a better overview. Generally, the literature data for the Isua region display broadly similar elemental W systematics as our samples, although these trace element data are of lower accuracy. Trace element variation diagrams versus Zr (Fig. 1.4) clearly demonstrate the conservative and non-conservative behavior of Th and W, respectively. While Th correlates with fertility indicators, such as Zr content (Fig. 1.4b), W does not (Fig. 1.4a). This non-conservative behavior of W also becomes evident when Th and W concentrations of the samples are plotted against Ta contents (Figs. 1.5c and 1.5d). Tantalum is regarded as one of the most immobile elements in fluid-dominated regimes (e.g. McCulloch and Gamble, 1991; Keppler, 1996; Münker et al., 2004) and displays a similar compatibility than W and Th (e.g. König et al., 2011). A comparison of W and Th contents with those of Ta can therefore reveal fluid-controlled overprints that superimpose magmatic processes. To better illustrate the elemental behavior of W, Th, and Ta, we included the arrays defined by MORB, OIB, and arc lavas in Fig. 1.5 (König et al., 2011 and references therein). In Th-Ta space (Fig. 1.5c), most of the samples from SW Greenland fall within the array of modern arc rocks that runs parallel to the MORB-OIB arrays at lower Ta concentrations. Such a selective enrichment of Th in the vast majority of present-day arc rocks is usually explained by magma-felsic crust interaction or by derivation from a subduction-modified mantle source (Pearce and Peate, 1995). Indeed, many rocks from Isua have island arc affinities and their origin can be plausibly explained by melting metasomatized mantle that has been modified in a supra-subduction zone-like setting (Polat et al., 2002; Polat and Hofmann, 2003; Nutman et al., 2007; Jenner et al., 2009). The variations in degree of melting and subsequent fractional crystallization then define the elevated array at constant Th/Ta ratios in Fig. 1.5c. Collectively, the preservation of this Th-Ta array provides independent evidence that (1) the inventory of Th and Ta was little affected by metamorphism and (2) mafic rocks from the Isua region likely originate from mantle sources overprinted by subduction-like processes.

Opposite to Th-Ta patterns, however, variations in W-Ta space (Fig. 1.5d) provide evidence that at least the ultramafic rocks have been affected by an additional process that significantly increased W concentrations while Th and Ta remained largely unaffected. This effect is more pronounced in the depleted residual mantle peridotites (highest W/Th), whereas it is somewhat buffered by higher W concentrations in more differentiated rocks (lower W/Th). Importantly, none of the samples from SW

Greenland that were subject of  $^{182}\text{W}$  isotope measurements displays an elemental W budget that has solely been controlled by mantle melting. This is because as W/Th and, more important, W/Ta ratios are always systematically higher than observed for mantle melts (Fig. 1.5e). This demonstrates the absence of pristine, unmetasomatized mantle sources, and a subduction-like modified mantle is the most plausible source for metavolcanic rocks from SW Greenland. An additional, post-magmatic W enrichment is required for the samples that display extremely modified elemental W budgets (Fig. 1.5f). The enrichment factor  $W/W^*$  ( $W/\text{Th}_{\text{sample}}/W/\text{Th}_{\text{canonical}}$ ) can provide an estimate for the secondary W re-distribution subsequent to the source enrichment. This enrichment factor is only a minimum estimate as it makes use of the maximum W/Th ratio observed for MORB (0.24) (König et al., 2011). Ratios of W/Th in samples from this study range up to 160, corresponding to an enrichment factor  $W/W^*$  of up to 666 (Table 1.3), much higher than found in Phanerozoic arc lavas.

In summary, our high precision isotope dilution data for W, Th, U, and Ta can clearly demonstrate that W is selectively enriched relative to elements of similar incompatibility. Disturbed elemental W patterns in all of our samples, therefore, hamper a straightforward linkage of measured W isotope compositions to their respective mantle sources. Similar observations were already tentatively described in previous studies that investigated W isotope compositions in Archean rocks (Touboul et al., 2014; Willbold et al., 2015; Liu et al., 2016; Rizo et al., 2016b; Dale et al., 2017).

Liu et al. (2018) have shown that mineral reactions of W-bearing phases during metamorphism and metasomatism may exert a strong influence on the elemental W bulk composition, whereby the formation of secondary grain-boundary mineral assemblages, the presence of sub-micron W-rich phases, or break-down reactions affect elemental W-systematics differently. Therefore, a clear assignment of the secondary W enrichment in samples from the Isua region to a distinct geological process is difficult. The elemental overprint could either have taken place during initial, subduction-related mantle source metasomatism, or during younger metamorphic overprint. For Isua, Rizo et al. (2016b) have attributed the secondary W-enrichment to late-stage metamorphic events, during which W-rich fluids overprinted the elemental W budgets and may now dominate the W isotope budget. According to their study, abundant scheelite mineralizations could tap representative metamorphic fluid compositions in Isua. In their  $^{182}\text{W}$  isotope study, a scheelite from the southern part of

the ISB did indeed reveal an excess of  $+15.5 \text{ ppm} \pm 3.6 \text{ ppm}$ , consistent with excesses found in samples that are characterized by secondary W enrichments. However, Rizo et al. (2016b) also reported the absence of  $^{182}\text{W}$  excesses for samples, in which pristine whole rock W concentrations were clearly overprinted. Therefore, Rizo et al. (2016b) came to the conclusion that different metasomatic agents must have been present with both anomalous and modern mantle-like  $^{182}\text{W}$  isotope signatures.

In further evaluating the  $^{182}\text{W}$  isotope record of secondary scheelite, it is important to note that these mineralizations are spatially related to mafic-ultramafic rocks and they are thought to be the product of post-emplacement alteration within the subseafloor crust (Appel, 1986; Appel, 1994). We might also consider the possibility that the scheelite mineralizations are linked to one or more of the late Archean metamorphic and metasomatic events that caused the  $^{147}\text{Sm}$ - $^{143}\text{Nd}$  system to re-equilibrate in many lithologies in the region at around 2900-2800 Ma during a regional thermal overprint at amphibolite-facies conditions (Gruau et al., 1996; Blichert-Toft and Frei, 2001; Frei et al., 2002; Polat et al., 2003; Rizo et al., 2011). In this case the W could be derived from the regional TTG as well as from the supracrustal assemblages. Several sources of W in the scheelite are therefore possible. If W was derived solely from the supracrustal assemblages, it was either locally derived from the sea-floor host-rocks, or, alternatively, from Archean seawater. In the case of a seawater origin, its W budget could be dominated by either submarine volcanic exhalations or by continental weathering. In modern seawater W is regarded as being conservative, which means that its oceanic residence time exceeds the mixing time of the oceans, the reaction with particles is not very strong and its solubility is relatively independent of salinity (e.g. Bruland et al., 2014). If submarine volcanic exhalations were the major contributor of W in Archean seawater, scheelites would therefore likely reflect the global  $^{182}\text{W}$  isotope composition of the convective mantle at the time of their formation. If continental weathering dominated the W budget of the Archean seawater the isotopic composition would provide integrated information about the exposed Archean lithosphere. Therefore,  $^{182}\text{W}$  isotope anomalies in rocks from southern west Greenland that were affected by secondary W re-distribution might be a vestige of average crust-mantle composition rather than a signature of the ambient mantle. These considerations clearly call for a better understanding of the behavior of W in Archean seawater and the elemental W cycle during sea-floor alteration or weathering.

### 1.6.3 Significance of uniform $^{182}\text{W}$ isotope compositions

All measured samples (N=26) reveal positive  $^{182}\text{W}$  anomalies between +9.5 and +19.9 ppm with most samples clustering in their composition from  $+9.5 \pm 5.3$  ppm to  $+15.5 \pm 7.1$  ppm. Eoarchean samples from the Isua region (n = 21) display a uniform  $^{182}\text{W}$  excess of +12.5 ppm ( $\pm 1.2$  ppm, 95% CI). This is broadly in accordance with previously reported  $^{182}\text{W}$  isotope anomalies for Eo- to Paleoarchean samples from the Isua region (Willbold et al., 2011; Rizo et al., 2016b; Dale et al., 2017). All three Paleoarchean Ameralik dikes display similar  $^{182}\text{W}$  isotope excesses and yielded a mean  $\mu^{182}\text{W}$  of +13.9 ppm ( $\pm 1.8$  ppm, 2 SD), confirming the results from Rizo et al. (2016b). Our multiple measurements for samples S30, S31, and S33 from *lens A* reveal uniform excesses for  $^{182}\text{W}$  between +10.1 and +15.2 ppm which overlap within uncertainty. These results stand in marked contrast to those of Rizo et al. (2016b), who performed measurements on the same powder splits of samples S31 and S33. They only found minor excesses that could not be resolved from the present-day mantle composition. Our data for Lens A peridotites from Rizo et al. (2016b) and this study does not overlap within uncertainty. However, our multiple measurements for our Lens A samples (N  $\geq$  14) have a significant statistical power (95% CI  $\leq \pm 4$  ppm) and yield consistent results with other samples that were affected by secondary W enrichment.

There is no correlation between  $^{182}\text{W}$  isotope compositions and W/Th ratios (Fig. 1.11). The  $^{182}\text{W}$  isotope composition of samples that show a selective W enrichment are strongly dominated by their contaminant. This feature can be illustrated by a simple two endmember mixing-model (see dashed curves in Fig. 1.11). Hypothetically, one can assume that the elemental W budget of a sample initially characterized by modern mantle-like  $^{182}\text{W}$  isotope composition would be contaminated by an agent with excess  $^{182}\text{W}$  of +15.5 ppm. In such a model, an increase in W concentration by 100% would raise the  $\mu^{182}\text{W}$  to +7.7 ppm. Therefore, when considering the average uncertainty for our multiple  $^{182}\text{W}$  measurements ( $\pm 4.3$  ppm, 95% CI), samples with a W/W\* of only 2 would already be analytically indistinguishable from the  $\mu^{182}\text{W}$  of the metasomatizing agent. Hence, the possibility cannot be ruled out that samples with elevated W/Th ratios had modern mantle-like, or even lower  $^{182}\text{W}$  isotope composition before they were affected by secondary W enrichment. Alternatively, a homogeneous  $^{182}\text{W}$  isotope composition could already have prevailed prior to elemental W disturbance, i.e., the

two mixing endmembers both carried the  $^{182}\text{W}$  excess. This scenario is very plausible, as samples with canonical W/Th ratios show no discernible variations in their W isotope composition, when compared to samples that are strongly enriched in W (Fig. 1.11).

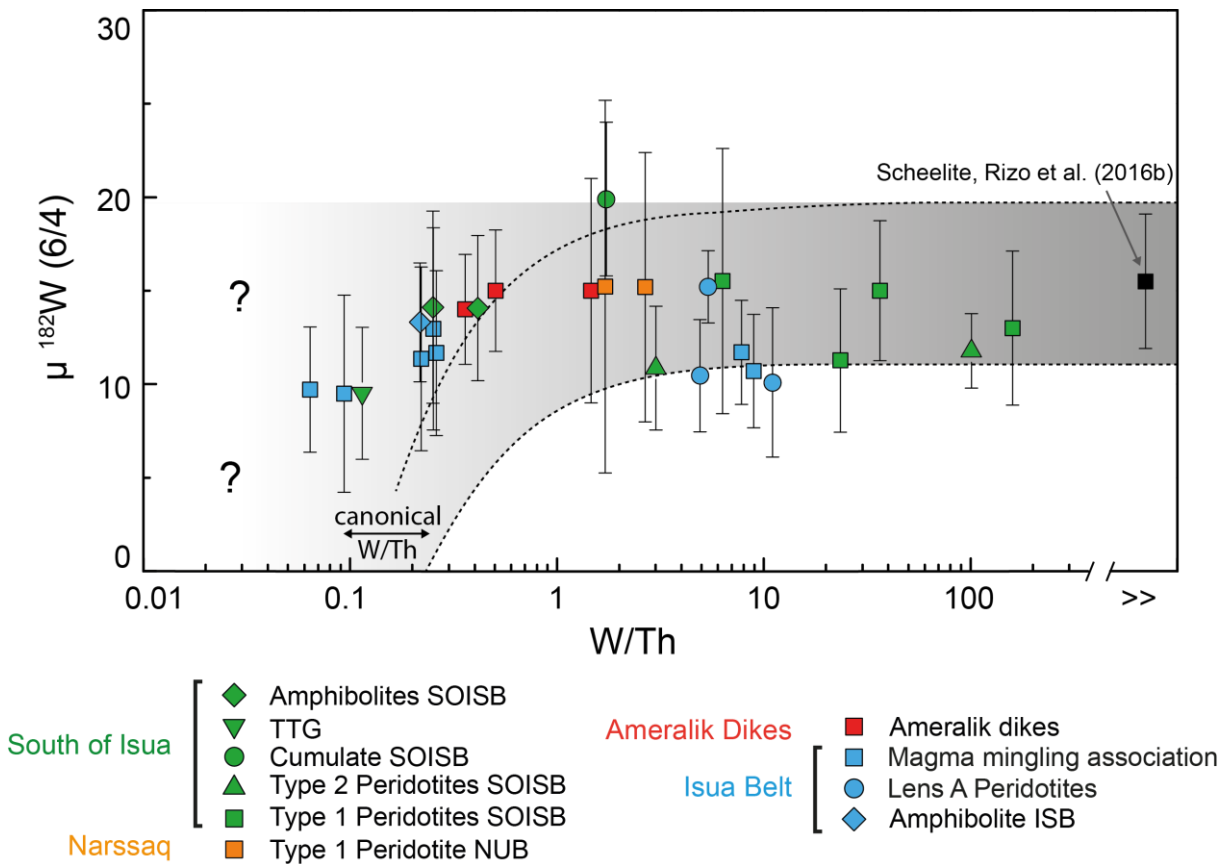


**Fig. 1.11:  $\mu^{182}\text{W}$  (6/4) versus W/Th ratios for samples analyzed in this study.** Error bars correspond to the 95% CI for multiple measurements. High W/Th are indicative of secondary W-enrichment. There is no correlation between  $\mu^{182}\text{W}$  and W/Th ratios. Also included is a scheelite that is representative for the W isotope composition of local metasomatic agents (Rizo et al., 2016b). These metasomatic agents might account for the disturbed elemental W budgets and the uniform  $^{182}\text{W}$  isotope composition in rocks from the Isua- and Nuuk regions. The primary W isotope composition of samples that show a selective W enrichment remains ambiguous (see text for discussion).

Dashed lines indicate the range of  $^{182}\text{W}$  isotope composition expected for a two endmember mixing-model between modern mantle-like  $^{182}\text{W}$  isotope composition and a metasomatic agent carrying a  $\mu^{182}\text{W}$  of +15.5 ppm.

The uniform  $^{182}\text{W}$  excesses found here for rocks from the Isua region calls for an inspection of previous data, based on which a heterogeneity of  $^{182}\text{W}$  isotope excesses was claimed. Disregarding the controversial ultramafic rock samples S31 & S33 from lens A, the presence of heterogeneous  $^{182}\text{W}$  sources appears to be indicated by 3.7 Ga amphibolites with  $\mu^{182}\text{W}$  ranging from +5.4 to +21.3 ppm (Rizo et al., 2016b). Other rocks with modern mantle-like  $^{182}\text{W}$  isotope compositions include a 3.8 Ga amphibolite



(Rizo et al., 2016b) and a Paleoaarchean Ameralik dike (Dale et al., 2017). However, the modern mantle-like  $\mu^{182}\text{W}$  of  $+5.4 \pm 7.2$  ppm for the 3.7 Ga amphibolite 00-008 (Rizo et al., 2016b) also overlaps with our proposed average for rocks from the Isua region ( $+12.8 \pm 1.0$  ppm). Likewise, the 3.8 Ga amphibolite (sample 460217 of Rizo et al., 2016b) and the Paleoproterozoic Ameralik dike (sample 242774 of Dale et al., 2017) are only barely resolvable from our average ( $+3.7 \pm 6.9$  ppm and  $+5 \pm 6$  ppm, respectively) and overlap within uncertainty with 3.8 Ga amphibolites and Ameralik dikes measured in our study. This clearly demonstrates that the previously reported heterogeneity of  $^{182}\text{W}$  isotope compositions in rocks from the Isua area are most likely only a result of a larger scatter in previously published datasets.

Based on  $^{142}\text{Nd}$  anomalies, it has been suggested, that primordial heterogeneities in the Isua mantle progressively disappeared from the Eo- to the Paleoaarchean, between  $\sim 3.7$ -3.8 Ga and 3.4 Ga (Bennett et al., 2007; Saji et al., 2018) and diminish between 3.4 Ga and 3.3 Ga (Rizo et al., 2012; Rizo et al., 2013). Unfortunately, 3.3 Ga old amphibolites that are the oldest rocks in the region not showing resolvable  $^{142}\text{Nd}$  excesses (Rizo et al., 2013) exhibit disturbed elemental W systematics (cf. Rizo et al., 2013; Rizo et al., 2016b) and are still characterized by positive  $^{182}\text{W}$  excesses (Rizo et al., 2016b). So, in summary, there is presently no sufficient evidence for decreasing  $^{182}\text{W}$  isotope excesses with age in rocks from the Isua region, as shown for  $^{142}\text{Nd}$ . We conclude that the widespread  $^{182}\text{W}$  excess in rocks from the Isua region, which is independent of W enrichment, can be regarded as an intrinsic feature of Eoaarchean and possibly younger units. This finding calls for high precision  $^{182}\text{W}$  isotope investigations on younger (i.e.,  $< 3.3$  Ga old) rocks from the Isua region with undisturbed elemental W systematics.

#### 1.6.4 Significance of the $^{182}\text{W}$ and W/Th signatures in mantle-like peridotites

The mantle-like peridotites from the Isukasia and F eringehavn terranes (Friend et al., 2002; Bennett et al., 2002; van de L ocht et al., 2018a) provide a unique opportunity to directly combine the information from both  $^{182}\text{W}$  isotope compositions and HSE systematics. It has been previously shown that these mantle-like peridotites from the Isukasia and F eringehavn terranes display the full inventory of HSE and chondritic Os isotope compositions (Bennett et al., 2002; Friend et al., 2002; van de L ocht et al., 2018a). Previous estimates on HSE abundances in the mantle sources for rocks from

Isua were only indirect, as they were based on compositions of metabasalts (Rizo et al., 2016b; Creech et al., 2017; Dale et al., 2017). Our mantle-like peridotites can now provide direct information on HSE systematics, which avoids uncertainties induced by extrapolating back from the metabasalts. In the original study of van de Löcht et al. (2018a), two groups of peridotites were discriminated, with group 1 peridotites representing compositions depleted in PPGE and group 2 peridotites representing metasomatized composition replenished in PPGE. Importantly, both group 1 and 2 peridotites described by van de Löcht et al. (2018a) show indistinguishable excesses for  $^{182}\text{W}$  that also overlap those of other mafic rocks from the Isua region (between +10.9 and +15.5 ppm). However, both groups exhibit manifold W enrichments with  $W/W^*$  ranging from 7.12 to 666. This feature illustrates that the records of  $^{182}\text{W}$  and HSE are clearly decoupled in these rocks. The excesses in  $^{182}\text{W}$  in the peridotites may therefore be inherited from the surrounding lithologies, mainly TTGs and amphibolites (e.g. Nutman and Friend, 2009).

#### *1.6.5 Origin of $^{182}\text{W}$ isotope anomalies in SW Greenland*

Although we have shown above that HSE and  $^{182}\text{W}$  isotope systematics are clearly decoupled in the mantle-like peridotites, the study by van de Löcht et al. (2018a) reveals that the ambient mantle in the Isua region was nearly fully replenished with HSE. As for modern mantle peridotites, however, the scatter of IPGEs (Os-Ir) in the Greenland peridotites allows for a deficit in HSE of up to 40% to be accommodated within this scatter. There are other estimates on the contribution of the late veneer in the Isua region (Rizo et al., 2016b; Creech et al., 2017; Dale et al., 2017) that are substantially lower, but overlap with the lower bound of the estimate by van de Löcht et al. (2018a). However, unlike in the van de Löcht et al. (2018a) study, these previous estimates are based on extrapolations from mafic rocks or ultramafic suites that are definitively not mantle peridotites (cf. Szilas et al., 2015) and therefore have an even larger uncertainty. Likewise, propagated uncertainties of the primitive upper mantle abundances of HSE (Becker et al., 2006) and for rock types that are taken for reference (e.g., modern dunites and harzburgites, Becker and Dale, 2015) need to be considered. Hence, it cannot unambiguously be ruled out that somewhat less than 100% of the late veneer was indeed present in the ambient Eoarchean mantle at Isua. Consequently, it cannot be excluded, that small proportions of the late veneer were

missing in the Archean Isua mantle and thereby part of the  $^{182}\text{W}$  excess could be explained this way. However, due to the complete overlap in PGE concentrations between the Isua peridotites and Phanerozoic peridotites, the extent of this contribution can only be very small, which limits missing late veneer effects on  $^{182}\text{W}$  isotope excesses in the Isua region. Even if the lower estimates for late veneer contribution to the Isua mantle are taken into consideration (Creech et al., 2017; Dale et al., 2017) the excess of 12.8 ppm  $^{182}\text{W}$  cannot be explained by the incomplete addition of material with bulk carbonaceous chondritic composition (Fig. 1.12). The maximum excess expected in  $\mu^{182}\text{W}$  for a mantle that is missing 50% of a chondritic late veneer (with W concentrations up to 200 ng/g and a  $^{182}\text{W}$  deficit of -190ppm) would not exceed +7.5 ppm. To account for the relatively high  $^{182}\text{W}$  isotope excess found in Isua rocks that evidently formed from mantle sources rich in HSEs, the late veneer must have had a rather extreme composition with a significant portion of iron meteorites with high W concentrations and even larger  $^{182}\text{W}$  deficits than chondrites (Dale et al., 2017). Instead of simple missing late veneer models that are clearly not plausible, formation of the  $^{182}\text{W}$  excess by silicate differentiation in an early depleted reservoir appears to be more plausible. This putative depletion event must have occurred within the lifetime of  $^{182}\text{Hf}$  (i.e., during the first ca. 60 Myrs after solar system evolution). Such an early silicate differentiation event is also supported by rather uniform  $^{142}\text{Nd}$  excesses found in Eoarchean and old Paleoarchean (>3.4 Ga old) rocks from the Isua region (Caro et al., 2003; Boyet and Carlson, 2006; Caro et al., 2006; Bennett et al., 2007; Rizo et al., 2011; Rizo et al., 2012; Rizo et al., 2013; Rizo et al., 2016b; Saji et al., 2018) and by the fact that elevated initial  $\epsilon\text{Hf}$  values in some Isua rocks are in support of a depleted Hadean mantle reservoir (Hoffmann et al., 2010). Typically, the short-lived  $^{146}\text{Sm} - ^{142}\text{Nd}$  (half-life between 68 and 103 Ma, Meissner et al., 1987; Kinoshita et al., 2012) and  $^{182}\text{Hf} - ^{182}\text{W}$  (half-life 8.9 Ma, Vockenhuber et al., 2004) should be coupled during early silicate differentiation as in both cases the parent isotope is more compatible than the daughter isotope. Indeed, Bennett et al. (2007) calculated a  $^{142}\text{Nd}$ - $^{143}\text{Nd}$  model age of >4.50 Ga based on Nd isotopes, in line with  $^{182}\text{W}$  considerations. A decoupling of  $^{142}\text{Nd}$ - $^{182}\text{W}$  patterns, however, would be expected for silicate differentiation events younger than 60 Myrs after solar system formation, when  $^{182}\text{Hf}$  was extinct, but  $^{146}\text{Sm}$  was not.

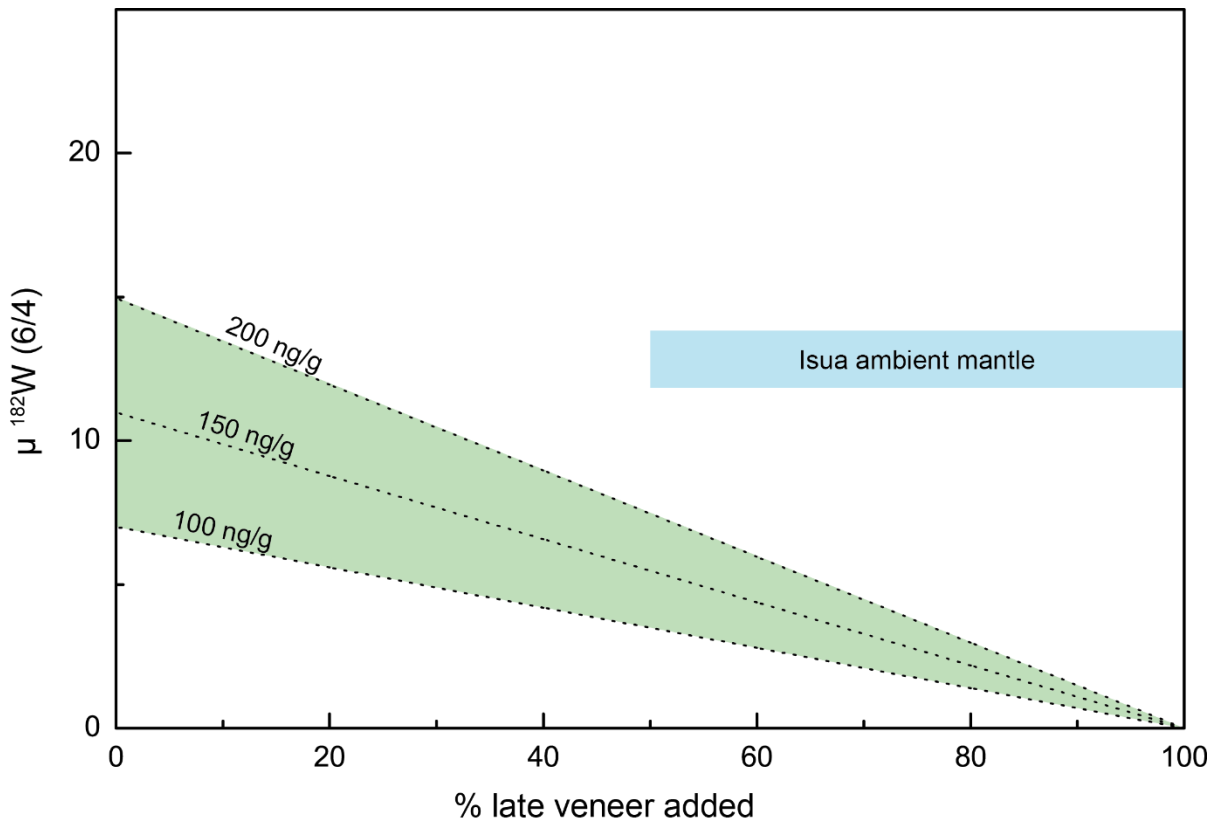


**Fig. 1.12: Model calculation illustrating the evolution of the  $^{182}\text{W}$  isotope composition of the BSE as a function of late veneer contribution during the final stages of Earth's accretion.** The relative late veneer addition reports the fraction of the mass that was added to the mantle (0.5 mass-% of the present-day mantle) after core formation. The evolution lines give the  $\mu^{182}\text{W}$  of the BSE after admixing of different proportions of late veneer material with bulk carbonaceous chondritic composition, i.e.  $\mu^{182}\text{W} = -190$  (Kleine et al., 2002; Kleine et al., 2004) and estimated chondritic W concentrations that range from ~100 to 200 ppb (Wasson and Kallemeyn, 1988; Anders and Grevesse, 1989; Kleine et al., 2004). An updated estimate for the composition of the ambient mantle in the Isua region is illustrated by the blue box, being defined by the  $^{182}\text{W}$  isotope composition reported in this study, and the range of late veneer contributions to the Isua region ambient mantle, as previously estimated by other studies ((Rizo et al., 2016b; Creech et al., 2017; Dale et al., 2017; van de Löcht et al., 2018a).

When looking at a recent compilation of  $^{182}\text{W}$  and  $^{142}\text{Nd}$  data (Rizo et al., 2016b) it becomes obvious, that samples older than 3.4 Ga exhibit coupled excesses in both isotopes, once the typical  $^{182}\text{W}$  excess of ca. +12 ppm is used for samples S31 and S33 (this study) and the 3.8 Ga old amphibolite analyzed by Rizo et al. (2016b). A decoupling between  $^{142}\text{Nd}$  and  $^{182}\text{W}$  patterns is observed for rocks younger than 3.4 Ga (Rizo et al., 2016b). This can be explained twofold. First, these rocks may originate from mantle sources that underwent differentiation after  $^{182}\text{Hf}$  became extinct. Secondly, the strongly disturbed elemental W systematics in many lithostratigraphic units may mirror W redistribution that might have homogenized the  $^{182}\text{W}$  but not the  $^{142}\text{Nd}$  isotopic patterns. For  $^{142}\text{Nd}$ , a recent study (Saji et al., 2018) now demonstrated

that anomalies decreased from the Eo – to Paleoproterozoic rocks and began to diminish between 3.4 Ga and 3.3 Ga (Rizo et al., 2012; Rizo et al., 2013). Correspondingly, a decrease of  $^{182}\text{W}$  excesses in these rocks (Ameralik dikes) would be expected, but this is not evident from our data for Ameralik dikes. As one explanation, the preservation of an evolution trend for  $^{182}\text{W}$  in rocks from southern west Greenland may have been obscured by second stage alteration, resulting in a pervasive homogenization of the  $^{182}\text{W}$  isotope signatures in Eoarchean and Paleoproterozoic rocks. Even though the REE are considered to be largely immobile during alteration (Ludden et al., 1982; Arndt, 1994), modeling calculations by Rosing (1990) and geochemical studies of metamorphic systems (e.g. Marshall and Futa, 1991; Frost and Frost, 1995) demonstrated that metasomatism can cause REE mobility and may therefore also have an impact on the Sm-Nd decay systems. The susceptibility of the Sm-Nd system to secondary disturbances has also been demonstrated for poly-metamorphic rock assemblages from the Isua area (e.g. Gruau et al., 1996; Blichert-Toft et al., 1999; Polat et al., 2003). In contrast, it has been demonstrated by Polat et al. (2002), and Polat and Hofmann (2003), that the REE in some of the rocks from the ISB were not significantly disturbed by alteration. Accordingly, subsequent  $^{142}\text{Nd}$  studies on rocks from the Isua area combined their results with  $^{147}\text{Sm}$ - $^{143}\text{Nd}$  systematics to assess the possible re-equilibration of the radiogenic  $^{142}\text{Nd}$ - $^{143}\text{Nd}$  budgets (Caro et al., 2006; Rizo et al., 2011; Rizo et al., 2012) and to demonstrate that in spite of open system behavior  $\epsilon^{143}\text{Nd}$  and  $\mu^{142}\text{Nd}$  values do decrease similarly with time (Rizo et al., 2013). As positive  $^{182}\text{W}$  isotope anomalies were found in our study in 3.7 - 3.8 Ga old rocks with canonical W/Th ratios, it can be confidently assumed that the  $^{182}\text{W}$  excess was ubiquitous in the Eoarchean units of the Isua region, as previously demonstrated for  $^{142}\text{Nd}$  (Saji et al., 2018). This is less certain for the Paleoproterozoic units, and future W isotope investigations on samples with near canonical W/Th are required to evaluate this issue further. In summary, there now appears to be growing evidence, that the  $^{182}\text{W}$  isotope excesses in the ambient Isua mantle is to a large extent a vestige of early silicate differentiation, particularly when considering the coupling with  $^{142}\text{Nd}$  excesses and the PGE systematics in 3.8 Ga old mantle- like peridotites.

## 1.7 Conclusion

Our study presents a high precision dataset combining  $^{182}\text{W}$  isotope measurements and elemental W, Th, U, Ta systematics obtained from isotope dilution measurements for several lithostratigraphic units from the Eoarchean Isukasia and F eringehavn terranes and for the Paleoarchean Ameralik dikes. The dataset also includes samples with W abundances in the lower ppb range, that now could be analyzed following the development of a new ion exchange separation scheme for gram-sized samples. This separation procedure allows for high precision  $^{182}\text{W}$  isotope measurements with uncertainties typically better than  $\pm 5$  ppm (95% CI,  $n > 5$ ). Factors that particularly affect the accuracy of high precision  $^{182}\text{W}$  isotope measurements are mass independent fractionation effects during chemical separation, such as nuclear field shift (NFS) effects for  $^{183}\text{W}$ . We can circumvent this analytical artifact by applying a new ion exchange protocol also involving modified dry-down procedures prior to re-dissolution during the chemical separation and immediately after final W purification. This now allows involving  $^{183}\text{W}$  in order to correct for the instrumental mass bias by using an internal normalization to  $^{186}\text{W}/^{183}\text{W}$ . As demonstrated by Kruijer and Kleine (2018) this can be important for high precision  $^{182}\text{W}$  isotope measurements by NTIMS when  $^{183}\text{W}$  is used for oxygen fractionation correction (Touboul and Walker, 2012).

Our study reveals that  $^{182}\text{W}$  isotope excesses amongst rocks from the Isua region display a homogenous  $\mu^{182}\text{W}$  composition of  $+12.8 \pm 1$  ppm (95% CI). The magnitude of this excess is in line with previous studies (Willbold et al., 2011; Rizo et al., 2016b; Dale et al., 2017). The ubiquitous  $^{182}\text{W}$  isotope excesses are most plausibly explained by the redistribution of W, as shown by non-canonical W-Th and W-Ta in most samples. Importantly, rocks in which elevated W abundances were mainly controlled by source enrichment also carry the characteristic  $^{182}\text{W}$  excess, now suggesting that the Eoarchean ambient mantle in SW Greenland originally carried the  $^{182}\text{W}$  excess.

Amongst the units analyzed here for the first time are mantle-like peridotite enclaves from the region south of the ISB that exhibit HSE patterns similar to Phanerozoic peridotites but they still carry the characteristic  $^{182}\text{W}$  excess. Based on combined trace element and isotope information, HSE and  $^{182}\text{W}$  isotope systematics are clearly decoupled in these peridotites. Even within uncertainties, their HSE systematics illustrate that missing late veneer additions are unlikely to be the only cause of the  $^{182}\text{W}$  excesses in Isua rocks. Rather, the formation of an early silicate reservoir by  $>4.50$  Ga

is a more plausible explanation, as previously suggested by  $^{142}\text{Nd}$  studies in the Isua region (Boyet et al., 2003; Caro et al., 2003; Boyet and Carlson, 2006; Caro et al., 2006; Bennett et al., 2007; Rizo et al., 2011; Rizo et al., 2012; Rizo et al., 2013; Rizo et al., 2016b; Saji et al., 2018) and also by highly radiogenic initial  $\epsilon\text{Hf}$  values in igneous rocks from SW Greenland (Hoffmann et al., 2010).

# Chapter 2

## 2 Convective isolation of Hadean mantle reservoirs through Archean time

### 2.1 Abstract

Although Earth is a convecting planet with active plate tectonics, ancient mantle reservoirs that formed within the first hundred million years of Earth's history (Hadean Eon) appear to have been preserved through geologic time. Evidence for this is based on small anomalies of isotopes such as  $^{182}\text{W}$ ,  $^{142}\text{Nd}$  and  $^{129}\text{Xe}$  that are decay products of short-lived nuclide systems which were together only active during the first ca. 100 million years of Earth's history. Studies of such short-lived isotopes have typically focused on geological units with a limited age range and therefore only provide snapshots of regional mantle heterogeneities. Here we present for the first time a dataset for short-lived  $^{182}\text{Hf}$ - $^{182}\text{W}$  (half life = 9 million years) in a rock suite that covers a longer geological record and that provides a better understanding of timescales of convective homogenization in Earth's early mantle. Our study focuses on rocks from the Pilbara Craton, Western Australia that preserve a unique geological archive covering 800 million years of Archean history. Pristine  $^{182}\text{W}$  signatures are only preserved in unaltered samples with near canonical W/Th (0.07-0.26). Early Paleoarchean, juvenile, igneous rocks from the East Pilbara Terrane display a uniform pristine  $\mu^{182}\text{W}$  excess of  $12.6 \pm 1.4$  ppm. From ca. 3.3 billion years onwards, the pristine  $^{182}\text{W}$  signatures progressively vanish and are only preserved in younger igneous rocks of the craton that tap stabilized ancient lithosphere. Given that the anomalous  $^{182}\text{W}$  signature must have formed by ca. 4.5 billion years, the mantle domain that was tapped by magmatism in the Pilbara Craton must have been convectively isolated for nearly 1.2 billion years. This finding puts lower bounds on timescale estimates for convective homogenization in early Earth's interior and on the widespread emergence of plate tectonics that are important input parameters in many physical models.



## 2.2 Introduction

Among the terrestrial planets, Earth is unique in that plate tectonic processes efficiently mix and homogenize its silicate mantle. Surprisingly, however, recent geochemical studies have revealed that both Archean and Phanerozoic mantle reservoirs still carry primordial geochemical signatures, thus escaping efficient convective homogenization as also predicted by geodynamic models (Labrosse et al., 2007; Ballmer et al., 2017). The main evidence for such ancient geochemical heterogeneities stems from noble gas systematics (Craig and Lupton, 1976) and from short-lived nuclide decay-series that became extinct after the Hadean eon (>4.0 Ga) (Bennett et al., 2007; Willbold et al., 2011). For instance, the relative abundance of daughter isotopes from short-lived nuclide-series such as  $^{142}\text{Nd}$  and  $^{182}\text{W}$  show significant variations in ancient rocks when compared to the Earth's modern mantle composition (Bennett et al., 2007; Willbold et al., 2011). From these short-lived isotope systems, the  $^{182}\text{Hf} - ^{182}\text{W}$  decay system has proven particularly useful in constraining the timing of planetary core formation (Kleine et al., 2002), timescales of late accretion, and silicate differentiation (Kruijer et al., 2015; Touboul et al., 2015).

There are two competing explanations for the origin of  $^{182}\text{W}$  isotope anomalies found in the terrestrial rock record, arising from the markedly different geochemical behavior of Hf and W during both core formation and silicate differentiation in planetary bodies. As primitive meteorites exhibit strong  $^{182}\text{W}$  isotope deficits ( $\mu^{182}\text{W} = -190$ , Kleine et al., (2002)), the observation of positive anomalies in Eoarchean rocks was interpreted as evidence that these rocks lacked a late veneer component (Willbold et al., 2011). Conversely, the presence of late accreted material was inferred to explain the elevated abundances of highly siderophile elements (HSE) in Earth's modern silicate mantle (Chou, 1978). However, Archean rocks with apparent pre-late veneer like  $^{182}\text{W}$  isotope excesses were shown to display HSE concentrations that are indistinguishable from modern mantle abundances (Touboul et al., 2012), which is difficult to reconcile with the missing late veneer hypothesis. An alternative suggestion is that early silicate differentiation during the lifetime of  $^{182}\text{Hf}$  might have caused the formation of mantle reservoirs with anomalous  $^{182}\text{W}$  signatures (Touboul et al., 2012; Rizo et al., 2016b). In addition, recent studies have revealed variable  $^{182}\text{W}$  isotope deficits in the mantle plume sources of ocean island basalts (OIBs, Mundl et al., (2017)). In line with noble gas systematics and seismic properties of such deep-rooted mantle plumes, these  $^{182}\text{W}$  anomalies have been taken as evidence for the presence of mantle domains that

have been convectively isolated since Earth's earliest history (Mundl et al., 2017). This requires interpreting the temporal evolution of the terrestrial  $^{182}\text{W}$  isotope composition as a bimodal distribution, with increasing homogenization via mantle convection through geologic time.

Surprisingly few studies have assessed the  $^{182}\text{W}$  record of lithostratigraphic successions that span a relatively long time frame of Archean geodynamic evolution. Rather, most studies have only provided snapshots within the  $^{182}\text{W}$  isotope evolution of individual Archean cratons (see method section). In order to allow for a more comprehensive understanding of Archean geodynamic evolution, studies are required to assess the  $^{182}\text{W}$  isotope evolution of a particular region over a long time period. An apparently successful example of this approach is from the Acasta Gneiss Complex (AGC) of Northern Canada, where  $^{182}\text{W}$  excesses appear to diminish throughout the Eoarchean (Willbold et al., 2015). However, it was later proposed that some of this variability may result from metamorphic overprint of primordial W isotope signatures (Reimink et al., 2018). Similar observations were made for rocks from the Isua region (southern W-Greenland) that span an age range from 3.8 – 3.4 Ga. These rocks show uniform  $^{182}\text{W}$  excesses but decreasing  $^{142}\text{Nd}$  anomalies through time in the same lithostratigraphic successions (Rizo et al., 2016b; Tusch et al., 2019), suggesting that an original decrease in  $^{182}\text{W}$  may have been obscured by secondary W redistribution during metamorphism (Tusch et al., 2019), as also shown for other Archean rocks from the North Atlantic Craton (Liu et al., 2016) and the Superior Province (Touboul et al., 2014). These examples illustrate that robust information on the  $^{182}\text{W}$  isotope evolution of the Archean mantle with time is scarce and often ambiguous due to secondary disturbance. In fact, only 16 percent of all available samples previously analyzed for  $^{182}\text{W}$  display pristine W abundances (see method section).

### **2.3 Geological background and samples**

Here we present for the first time a nearly continuous  $^{182}\text{W}$  isotope record for an Archean craton that spans an age range of 800 Ma, from the Paleo- to the Neoproterozoic. We investigated the  $^{182}\text{W}$  isotope evolution of the exceptionally well preserved 3.58 – 2.76 Ga old Pilbara Craton (Western Australia). Since much of this craton is only little affected by metamorphism (Van Kranendonk et al., 2007), many units within the lithostratigraphic successions are more likely to have preserved their primary W

systematics than other more deformed cratons of similar age. Therefore, our new data may allow a much more robust assessment of  $^{182}\text{W}$  isotope evolution through the Archean. A detailed outline of the geologic evolution of the Pilbara Craton is provided in the method section. In short, mantle-derived (mafic and ultra-mafic) magmatic sequences in the east [East Pilbara Terrane (EPT); Warrawoona, Kelly, and Sulphur Springs groups] and west [West Pilbara Superterrane (WPS); Ruth Well Formation] of the craton cover an age range from 3.52 – 3.23 Ga and tapped rather undepleted mantle sources that were emplaced during distinct mantle plume events, similar to modern plateau basalts (Smithies et al., 2007). Burial of these mafic sequences, together with older protocrust, caused melting to form four supersuites of sodic (tonalites, trondhjemites and granodiorites) and potassic granitoids (felsic rocks) that can be regarded as probes of early mafic crust. The younger evolution of the EPT involved plume-initiated rifting (Soanesville Group) at 3.18 Ga and subsequent accretion (3.07 Ga) of the younger WPS that also includes ~3.1 Ga subduction related mafic lithologies (Whundo Group, Smithies et al., (2005); Van Kranendonk et al., (2010)). After amalgamation, post-orogenic, lithosphere-derived magmatism included mafic rocks from the Bookingarra Group (Opaline Well Intrusion, Loudon -, and Mount Negri Volcanics) and crust-derived post-tectonic granites (e.g., Split Rock Supersuite, Van Kranendonk et al., (2007)).

We employed two strategies in selecting our samples. Firstly, we analyzed mafic volcanic rocks that tapped the ambient asthenospheric mantle of the EPT (plume-derived) and the WPS (subduction related). Secondly, to understand the evolution of the lithospheric mantle and to obtain average crustal compositions we analyzed mafic dikes, sediments and granitoids of different ages. We studied a total of 56 samples from more than ten major stratigraphic units of the two different terranes (see Fig. 2.4, method section), also covering different tectonic regimes (vertical tectonics in the EPT and horizontal tectonics in the WPS). For all these samples, selected trace element abundances (Zr, Hf, Nb, Ta, W, Th & U) were obtained by isotope dilution measurements (details in the method section). Ten ultra-mafic (komatiite) samples were also previously analyzed for HSE (Maier et al., 2009). For high-precision W isotope measurements on a subset of 30 mostly pristine samples, we followed a slightly modified analytical protocol of Tusch et al. (2019). Results for high-precision  $^{182}\text{W}$  isotope analysis are given in Table 2.1, major- and trace-element composition and

isotope dilution measurements are reported in Table B3 (appendix B).

Locality Sample	Group/ Supersuite	Subgroup	Formation	Age [Ma]	Normalized to $^{186}\text{W}/^{184}\text{W} = 0.92767$		Normalized to $^{186}\text{W}/^{183}\text{W} = 1.9859$				
					$\mu^{182}\text{W}$ ( $\pm$ 95% CI)	$\mu^{183}\text{W}$ ( $\pm$ 95% CI)	$\mu^{182}\text{W}$ ( $\pm$ 95% CI)	$\mu^{184}\text{W}$ ( $\pm$ 95% CI)	$\mu^{182}\text{W}_{\text{corr}}$ ( $\pm$ 95% CI)	N	
<b>Mantle-derived rocks</b>											
<b>East Pilbara Terrane</b>											
Pil 17-07	Mount Webber			3578	6.7 $\pm$ 2.6	-3.7 $\pm$ 2.1	10.6 $\pm$ 2.8	2.5 $\pm$ 1.4	5.7 $\pm$ 3.2	16	
Pil 16-54a	Coonterunah	Tabletop		3525	7.0 $\pm$ 1.6	-2.8 $\pm$ 2.3	10.2 $\pm$ 2.4	1.9 $\pm$ 1.5	6.5 $\pm$ 2.2	13	
Pil 16-54b				3525	7.8 $\pm$ 2.0	-1.3 $\pm$ 2.1	8.4 $\pm$ 2.1	0.8 $\pm$ 1.4	6.8 $\pm$ 2.6	15	
Pil 16-56	Warrawoona	Coucal		3515	12.0 $\pm$ 3.0	-1.0 $\pm$ 2.6	13.2 $\pm$ 2.2	0.7 $\pm$ 1.7	11.9 $\pm$ 3.2	15	
Pil 16-44a		Talga Talga	North Star	3490	9.1 $\pm$ 2.0	-1.1 $\pm$ 1.7	10.2 $\pm$ 2.2	0.8 $\pm$ 1.1	8.7 $\pm$ 2.7	13	
Pil 16-37a				3490	10.0 $\pm$ 2.8	-5.8 $\pm$ 2.1	16.8 $\pm$ 2.6	3.8 $\pm$ 1.4	9.3 $\pm$ 3.3	23	
Pil 16-28		Coongan	Mount Ada	3475	13.2 $\pm$ 4.7	2.2 $\pm$ 7.5	11.5 $\pm$ 4.8	-1.6 $\pm$ 4.9	14.6 $\pm$ 6.0	11	
Pil 17-10			3475	11.1 $\pm$ 2.6	-6.2 $\pm$ 4.8	19.7 $\pm$ 5.2	4.1 $\pm$ 3.2	11.6 $\pm$ 4.8	14		
Pil 16-24	Salgash	Apex Basalt		3465	7.4 $\pm$ 2.2	-2.3 $\pm$ 2.0	10.5 $\pm$ 2.0	1.5 $\pm$ 1.4	7.5 $\pm$ 2.3	19	
Pil 16-25				3465	14.3 $\pm$ 4.6	-1.2 $\pm$ 3.2	15.9 $\pm$ 5.4	0.8 $\pm$ 2.1	14.3 $\pm$ 5.4	10	
179738				3465	11.9 $\pm$ 2.9	-7.1 $\pm$ 3.3	15.7 $\pm$ 5.0	4.7 $\pm$ 2.2	6.5 $\pm$ 6.3	12	
Pil 16-39a	Kelly	Euro Basalt		3340	8.5 $\pm$ 2.1	-1.7 $\pm$ 2.1	9.9 $\pm$ 2.1	1.1 $\pm$ 1.4	7.6 $\pm$ 3.2	16	
Pil 16-53a				3340	5.2 $\pm$ 2.6	-1.3 $\pm$ 2.6	6.6 $\pm$ 2.8	0.9 $\pm$ 1.7	4.9 $\pm$ 4.0	10	
Pil 16-51	Soanesville	Honeyeater Basalt		3180	1.1 $\pm$ 3.9	-2.2	5.0	7.8 $\pm$ 4.5	1.5 $\pm$ 3.3	4.9 $\pm$ 6.6	12
Pil 16-51 (repl.)				3180	-0.3 $\pm$ 4.8	-3.7	7.6	6.4 $\pm$ 8.7	2.4 $\pm$ 5.0	1.7 $\pm$ 5.5	14
Pil 16-51 (ave)				3180	0.4	-3.0		7.1	2.0	3.2	
<b>West Pilbara Terrane</b>											
Pil 16-66b	Roeboume	Ruth Well		3270	11.6 $\pm$ 2.0	-0.8 $\pm$ 2.0	12.2 $\pm$ 1.7	0.5 $\pm$ 1.3	11.2 $\pm$ 2.2	15	
160245				3270	6.8 $\pm$ 2.3	-3.2 $\pm$ 1.4	12.7 $\pm$ 1.3	2.1 $\pm$ 0.9	8.5 $\pm$ 1.9	19	
Pil 16-67	Whundo	Bradley Basalt		3120	5.3 $\pm$ 4.8	-8.2 $\pm$ 2.6	16.6 $\pm$ 4.7	5.5 $\pm$ 1.8	5.9 $\pm$ 4.8	12	
Pil 16-74				3120	5.9 $\pm$ 3.2	-3.3 $\pm$ 3.2	11.3 $\pm$ 3.4	2.2 $\pm$ 2.1	7.1 $\pm$ 2.8	14	
<b>Lithosphere-derived rocks</b>											
Pil 16-63	Bookingarra	Opaline Well Intrusion		2990	8.0 $\pm$ 3.7	-0.2 $\pm$ 3.4	8.3 $\pm$ 2.2	0.1 $\pm$ 2.2	8.0 $\pm$ 3.6	13	
Pil 16-65		Louden Volcanics		2990	11.1 $\pm$ 2.8	-0.3 $\pm$ 3.0	12.0 $\pm$ 2.4	0.2 $\pm$ 2.0	11.6 $\pm$ 2.9	12	
Pil 16-75		Mount Negri Volcanics		2990	8.0 $\pm$ 2.7	0.0 $\pm$ 2.5	8.8 $\pm$ 2.7	0.0 $\pm$ 1.7	8.8 $\pm$ 2.2	16	
Pil 16-31	Fortescue	Black Range Dyke		2775	7.6 $\pm$ 3.1	-1.5 $\pm$ 2.6	9.0 $\pm$ 2.3	1.0 $\pm$ 1.7	7.0 $\pm$ 2.5	12	
<b>Shales</b>											
Pil 16-38b	Fortescue	Hardey		2756 - 2766	7.1 $\pm$ 1.9	0.0 $\pm$ 1.6	6.3 $\pm$ 1.8	0.0 $\pm$ 1.1	6.3 $\pm$ 1.8	16	
Pil 16-50b	Soanesville	Paddy Market		3190	7.4 $\pm$ 1.6	-1.0 $\pm$ 1.5	8.9 $\pm$ 1.4	0.7 $\pm$ 1.0	7.6 $\pm$ 2.1	20	
<b>BIF</b>											
Pil 16-62b	Warrawoona	Coongan	Duffer	3461 - 3471	9.0 $\pm$ 3.3	1.2 $\pm$ 2.8	8.5 $\pm$ 2.8	-0.8 $\pm$ 1.9	10.0 $\pm$ 3.0	16	
<b>Granitoids</b>											
Pil 16-12	Callina	North Pole Monzogranite		3450	7.2 $\pm$ 2.9	-0.6 $\pm$ 2.0	8.4 $\pm$ 2.4	0.4 $\pm$ 1.3	7.7 $\pm$ 3.0	16	
Pil 16-34		North Shaw Tonalite		3468	10.4 $\pm$ 3.3	-0.2 $\pm$ 3.9	9.5 $\pm$ 5.0	0.1 $\pm$ 2.6	9.2 $\pm$ 3.0	11	
Pil 16-35				3468	10.1 $\pm$ 2.6	-1.3 $\pm$ 3.1	13.5 $\pm$ 1.3	0.9 $\pm$ 2.1	11.8 $\pm$ 4.1	9	
Pil 16-41		Homeward Bound Granite		3466	8.1 $\pm$ 3.4	-0.5 $\pm$ 1.7	9.7 $\pm$ 1.8	0.3 $\pm$ 1.1	9.1 $\pm$ 1.4	11	
Pil 16-36a	Split Rock	Spearhill Monzogranite		2850	6.4 $\pm$ 4.0	-0.4 $\pm$ 3.1	7.4 $\pm$ 2.4	0.3 $\pm$ 2.1	6.9 $\pm$ 4.3	12	
<b>In-house rock standards</b>											
LP 1					-3.2 $\pm$ 2.5	-2.9 $\pm$ 3.2	1.0 $\pm$ 2.5	1.9 $\pm$ 2.1	-2.8 $\pm$ 3.5	11	
LP 1					-3.5 $\pm$ 2.6	-1.3 $\pm$ 2.5	-3.5 $\pm$ 2.7	0.9 $\pm$ 1.7	-5.2 $\pm$ 3.8	12	
LP 1					-2.1 $\pm$ 3.2	-3.9 $\pm$ 4.7	6.0 $\pm$ 4.6	2.6 $\pm$ 3.1	0.9 $\pm$ 4.0	19	
LP 1					3.2 $\pm$ 2.9	-0.1 $\pm$ 2.9	3.3 $\pm$ 3.1	0.1 $\pm$ 1.9	3.2 $\pm$ 3.8	19	
LP 1					-2.5 $\pm$ 3.4	-1.0 $\pm$ 2.2	-1.9 $\pm$ 4.1	0.7 $\pm$ 1.5	-3.2 $\pm$ 2.9	11	
LP 1					-3.3 $\pm$ 7.0	3.2 $\pm$ 4.9	-6.3 $\pm$ 7.2	-2.1 $\pm$ 3.3	-2.1 $\pm$ 7.9	15	
LP 1					-2.3 $\pm$ 3.3	1.2 $\pm$ 2.9	-0.9 $\pm$ 4.4	-0.8 $\pm$ 1.9	0.6 $\pm$ 3.1	8	
LP 1					-2.4 $\pm$ 4.2	-1.2 $\pm$ 4.2	-2.6 $\pm$ 2.9	0.8 $\pm$ 2.8	-4.2 $\pm$ 3.9	8	
LP 1					2.1 $\pm$ 3.9	2.1 $\pm$ 2.5	0.6 $\pm$ 3.5	-1.4 $\pm$ 1.6	3.3 $\pm$ 3.7	19	
LP 1					0.2 $\pm$ 2.3	0.5 $\pm$ 2.5	-0.6 $\pm$ 3.5	-0.3 $\pm$ 1.6	0.0 $\pm$ 3.3	15	
LP 1					-3.4 $\pm$ 4.0	-2.9 $\pm$ 3.5	0.7 $\pm$ 3.1	1.9 $\pm$ 2.3	-3.0 $\pm$ 3.9	17	
LP 1					2.0 $\pm$ 4.6	-2.8 $\pm$ 3.5	7.0 $\pm$ 3.1	1.8 $\pm$ 2.3	3.4 $\pm$ 4.4	11	
LP 1					-0.7 $\pm$ 4.7	0.5 $\pm$ 3.8	-2.7 $\pm$ 3.6	-0.3 $\pm$ 2.5	-2.0 $\pm$ 4.9	11	
LP 1					-2.1 $\pm$ 2.8	-2.6 $\pm$ 2.5	0.6 $\pm$ 2.7	1.7 $\pm$ 1.7	-2.7 $\pm$ 2.6	17	
LP 1					-1.6 $\pm$ 3.8	-0.8 $\pm$ 1.8	1.4 $\pm$ 3.0	0.5 $\pm$ 1.2	0.4 $\pm$ 3.3	19	
LP 1					-0.9 $\pm$ 3.1	-2.5 $\pm$ 2.6	1.1 $\pm$ 2.4	1.7 $\pm$ 1.7	-2.2 $\pm$ 2.8	23	
AGC 351					2.5 $\pm$ 2.4	1.9 $\pm$ 1.6	-0.8 $\pm$ 3.0	-1.3 $\pm$ 1.1	1.7 $\pm$ 2.9	13	
AGC 351					-2.4 $\pm$ 4.6	-5.9 $\pm$ 2.7	5.5 $\pm$ 2.5	3.9 $\pm$ 1.8	-2.1 $\pm$ 3.9	13	
AGC 351					-2.2 $\pm$ 2.2	-0.9 $\pm$ 1.8	-1.9 $\pm$ 1.8	0.6 $\pm$ 1.2	-3.0 $\pm$ 2.1	14	
AGC 351					-1.0 $\pm$ 2.5	1.5 $\pm$ 1.7	-3.0 $\pm$ 1.7	-1.0 $\pm$ 1.1	-1.1 $\pm$ 2.2	14	
AGC 351					0.1 $\pm$ 2.7	1.0 $\pm$ 2.1	-1.1 $\pm$ 2.6	-0.6 $\pm$ 1.4	0.2 $\pm$ 2.9	13	
AGC 351					0.9 $\pm$ 1.6	-2.3 $\pm$ 3.3	3.3 $\pm$ 3.4	1.5 $\pm$ 2.2	0.3 $\pm$ 3.3	12	
AGC 351					0.0 $\pm$ 2.2	0.8 $\pm$ 1.9	-0.9 $\pm$ 1.9	-0.5 $\pm$ 1.3	0.2 $\pm$ 2.3	13	
AGC 351					2.1 $\pm$ 1.8	-0.3 $\pm$ 1.3	2.4 $\pm$ 1.5	0.2 $\pm$ 0.8	2.0 $\pm$ 2.2	15	
AGC 351					0.2 $\pm$ 1.3	0.4 $\pm$ 1.7	-1.8 $\pm$ 1.3	-0.3 $\pm$ 1.1	-1.2 $\pm$ 2.0	17	
AGC 351					1.5 $\pm$ 1.9	1.1 $\pm$ 1.4	-0.2 $\pm$ 2.0	-0.8 $\pm$ 0.9	1.3 $\pm$ 2.1	13	
AGC 351					-2.4 $\pm$ 2.3	-3.4 $\pm$ 1.6	2.5 $\pm$ 2.1	2.2 $\pm$ 1.0	-1.9 $\pm$ 1.0	14	

**Table 2.1: Tungsten isotope composition of Pilbara samples and in-house rock reference materials.** Values for  $\mu^{182}\text{W}_{\text{corr}}$  were corrected for the nuclear field shift (NFS) effect on  $^{183}\text{W}$ , when normalized to  $^{186}\text{W}/^{183}\text{W}$  (6/3), using the measured  $\mu^{184}\text{W}$  (6/3) and  $\mu^{182}\text{W}$  (6/3) values and the relation  $\mu^{182}\text{W}$  (6/3) $_{\text{corr}} = \mu^{182}\text{W}$  (6/3) $_{\text{measured}} - (1.962 \times \mu^{184}\text{W}$  (6/3)) (Cook and Schönbacher, 2016). Notably, our analytical protocol (Tusch et al., 2019) ensures that in most of the cases (93%), NFS effects for  $\mu^{182}\text{W}$  in our study were within the range of the analytical uncertainty (for  $\mu^{182}\text{W}$  (6/3) on average  $\pm$  3.0ppm) as opposed to previous studies that reported massive NFS effects during  $^{182}\text{W}$  isotope measurements with MC-ICP-MS (Kruijer and Kleine, 2018; Archer et al., 2019).

High-precision concentration measurements are required to identify samples with primary W abundances, because W is strongly fluid-mobile when compared to elements of similar incompatibility (e.g. Th, U, Ta, König et al., (2011)). Thus, W mobility during fluid alteration results in non-canonical W/Th ratios (König et al., 2011) whereas in undisturbed magmatic systems, the similarly high incompatibility of W and Th results in canonical W/Th ratios between 0.09 and 0.24 over a wide range of mafic to felsic melts (König et al., 2011). Our Archean rock samples display pristine trends for Th versus Zr (Fig. 2.1a), but not for W versus Zr, as W was enriched in many samples (Fig. 2.1b). Samples with canonical W/Th ratios, however, define a pristine magmatic trend (Fig. 2.1b) allowing us to restrict further consideration primarily to samples with  $^{182}\text{W}$  isotope composition unmodified by secondary processes.

## 2.4 Results

The oldest plume-related mafic volcanic samples from the EPT (Warrawoona Group) all display resolvable  $^{182}\text{W}$  excesses. However, Warrawoona Group rocks, and a slightly older gabbroic enclave from the Shaw Granitic Complex (Mount Webber Gabbro; Pil 17-07), with supracanonical W/Th ratios, display markedly lower  $\mu^{182}\text{W}$  compositions when compared to samples with undisturbed elemental W budgets. Pristine samples display an average of  $\mu^{182}\text{W} = +12.6 \pm 1.4$  ppm [95% confidence interval (CI),  $n=8$ , also including previously published data for two samples from the Apex basalt (Rizo et al., 2019), red bar in Fig. 2.2], whereas rocks affected by secondary W-enrichment display resolvably lower excesses of  $\sim +8.1 \pm 1.4$  ppm (95% CI,  $n=8$ ; grey bar in Fig. 2.2). Interestingly, the average  $^{182}\text{W}$  excess in the metasomatized samples is indistinguishable from the long-term lithospheric average (see Fig. 2.2 and below). Samples from the younger, plume-derived  $\sim 3.35$  Ga Kelly Group (Euro Basalt) exhibit a contrasting pattern. The altered sample Pil 16-39a displays a  $\mu^{182}\text{W}$  value of  $+8.5 \pm 2.1$  ppm, again indistinguishable from the long-term lithospheric average. However, the unaltered sample Pil 16-53a shows a remarkably lower excess of  $\mu^{182}\text{W} = +5.2 \pm 2.6$  ppm. The youngest sample from the EPT, a 3.18 Ga Honeyeater basalt, displays no  $^{182}\text{W}$  isotope excess, overlapping the modern upper mantle value (Pil 16-51,  $\mu^{182}\text{W} = +1.1 \pm 3.9$  ppm). The eruption of the Honeyeater Basalt marks extension at the onset of clear plate tectonic style processes (the earliest recorded Wilson Cycle)

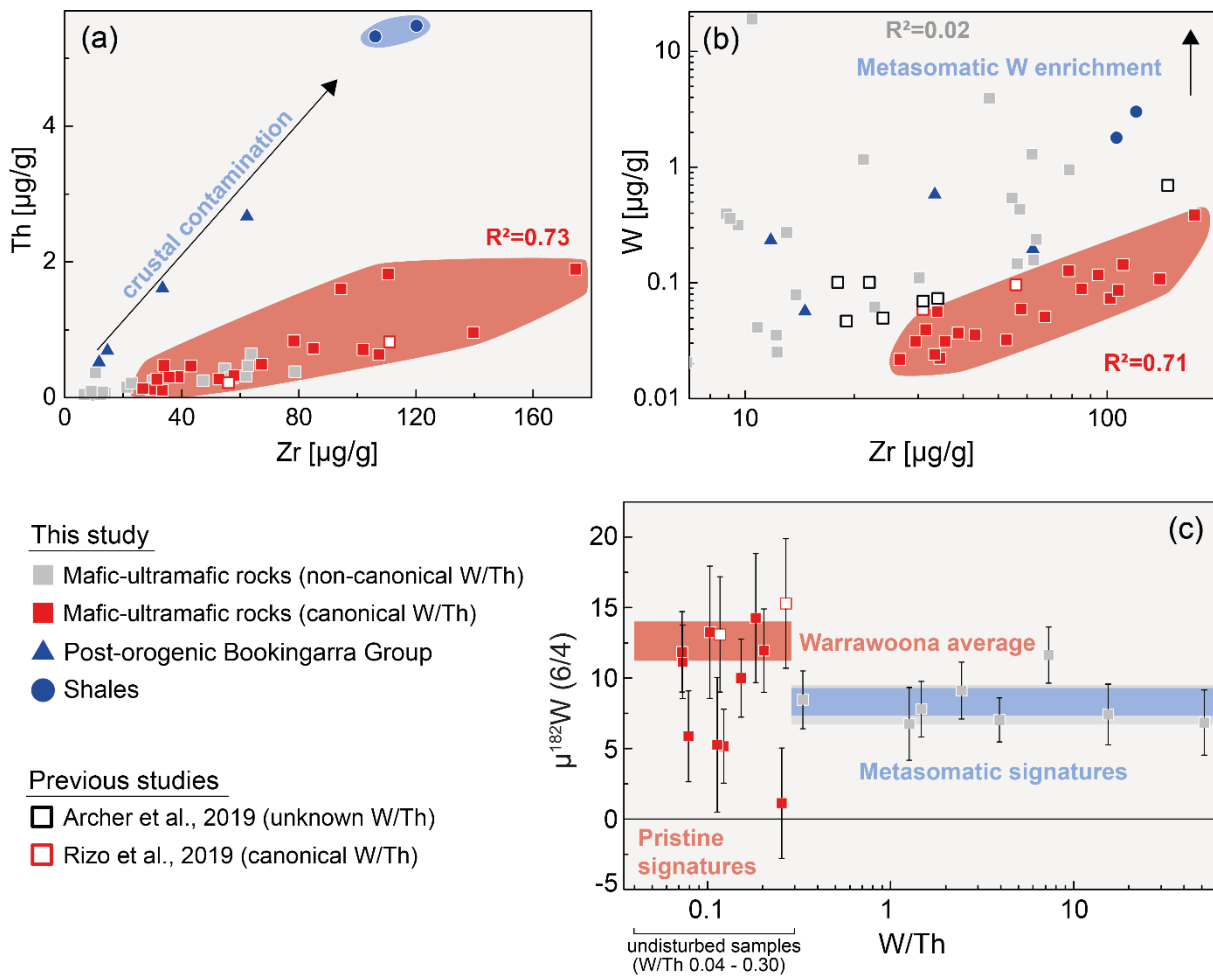


**Fig. 2.1:** Trace element variation diagrams showing Th and W vs. Zr contents in mafic-ultramafic rocks from the Pilbara craton (a & b) and high-precision  $\mu^{182}\text{W}$  data for rocks from the Pilbara Craton versus W/Th ratios (c). All concentration measurements were conducted by isotope dilution. Also included are Pilbara samples that were previously analyzed for their  $^{182}\text{W}$  isotope composition (Archer et al., 2019; Rizo et al., 2019). **(a)** Nearly all Pilbara samples have preserved robust magmatic differentiation trends for Th vs. Zr, indicating that Th was not significantly affected by secondary processes. Only the post-orogenic samples from the Bookingarra Group were contaminated by crustal components, in line with previous studies (Smithies et al., 2004). **(b)** In contrast to Th, the scattered concentrations of W mirror post-magmatic W enrichment by secondary processes. Pristine differentiation trends are preserved in samples with canonical W/Th ratios. Notably, all samples from ref 26 display strongly elevated W concentrations that indicate post-magmatic W enrichment. **(c)** Samples with undisturbed elemental W budgets (red squares, W/Th lower than 0.30, see method section) display variable  $^{182}\text{W}$  isotope excesses that constitute a progressive diminishing with time (see Fig. 2.2). Samples with elevated W/Th ratios (grey squares) were affected by secondary W enrichment by metasomatic agents that integrate the  $^{182}\text{W}$  isotope composition of the whole Pilbara Craton. Accordingly, these samples display intermediate  $^{182}\text{W}$  isotope excesses yielding the same average as lithosphere derived samples (grey and blue bars, respectively).

in the Pilbara Craton (Van Kranendonk et al., 2010). Thus, decreasing  $\mu^{182}\text{W}$  values in the unaltered samples indicate a diminishing  $^{182}\text{W}$  isotope excess with time during a change in the tectonic regime. Additional evidence for change in geodynamic pattern is manifested in rocks from the 3.13-3.11 Ga Whundo Group (WPS), a sequence with geochemical characteristics that are consistent with derivation from a depleted mantle source that was variably affected by subduction components in an arc-like setting (Smithies et al., 2005). Samples from the Whundo Group exhibit consistently lower  $\mu^{182}\text{W}$  (Pil 16-67:  $\mu^{182}\text{W} = +5.3 \pm 4.8$  and Pil16-74:  $\mu^{182}\text{W} = +5.9 \pm 3.2$ ). Beside data for 3.48 Ga komatiites from the Komati Formation of the Kapvaal Craton (Touboul et al., 2012), our data provides the oldest evidence for modern upper mantle-like W isotope compositions in the early Archean rock record.

The  $^{182}\text{W}$  isotope excesses also slightly decrease in granitoids, from  $\sim +10$  ppm in sodic granites (Pil 16-34 & -35, 3.47 Ga North Shaw Tonalite) to  $\sim +7$  ppm in younger and more evolved potassic granitoids (Pil 16-41, 3.47 Ga Homeward Bound Granite) and highly fractionated post-orogenic monzogranites (Pil 16-36A, 2.85 Ga Spearhill Monzogranite; blue squares in Fig. 2.2). Hence, the granitoids in the EPS mimic the  $^{182}\text{W}$  isotopic evolution of the ambient mantle. Given that the oldest and most pristine sodic granites are directly derived from mafic protocrust, this protocrust must have had  $^{182}\text{W}$  isotope excesses similar to those of the Warrawoona Group samples. Lower  $^{182}\text{W}$  isotope excesses in younger and more evolved granitoids mirror the temporal decrease in  $^{182}\text{W}$  as also observed for mantle-derived mafic rocks. This trend is also manifested by lower  $^{182}\text{W}$  excesses ( $\mu^{182}\text{W}$  between +7.1 and +7.6 ppm) in Meso- to Neoproterozoic shales (Pil 16-50B, 3.19 Ga Paddy Market Formation and Pil 16-38b, 2.76 Ga Hardey Formation), a rift-related lithospheric-derived dolerite from the Fortescue Group ( $\mu^{182}\text{W} = +7.6 \pm 3.1$  ppm Pil 16-31, 2.78 Ga Black Range dolerite) and mafic rocks from the Bookingarra Group (ca. 2.95 Ga; Pil 16-63, -65 & -75), which derived from a metasomatized, lithospheric mantle source that was refertilized by subducted sediments in a subduction zone-like setting (Smithies et al., 2004) ( $\mu^{182}\text{W}$  between +8 and +11 ppm; Fig. 2.2). The shales provide an average of the  $^{182}\text{W}$  isotope composition of the upper crust, and the lithosphere-derived mafic intrusion probes the composition of the subcontinental lithospheric keel. Unlike the shales, a Paleoproterozoic Algoma-type Banded Iron Formation (BIF) from the EPT (Pil 16-62B, 3.47 Ga Duffer Formation) has negligible detrital components (0.4%  $\text{Al}_2\text{O}_3$ ), and carries a  $^{182}\text{W}$  excess of  $+9.0 \pm 3.3$  ppm. We interpret this signature as being seawater-derived and reflecting the average

composition of the ambient hydrothermal input provided by local volcanism with similar W isotope composition.

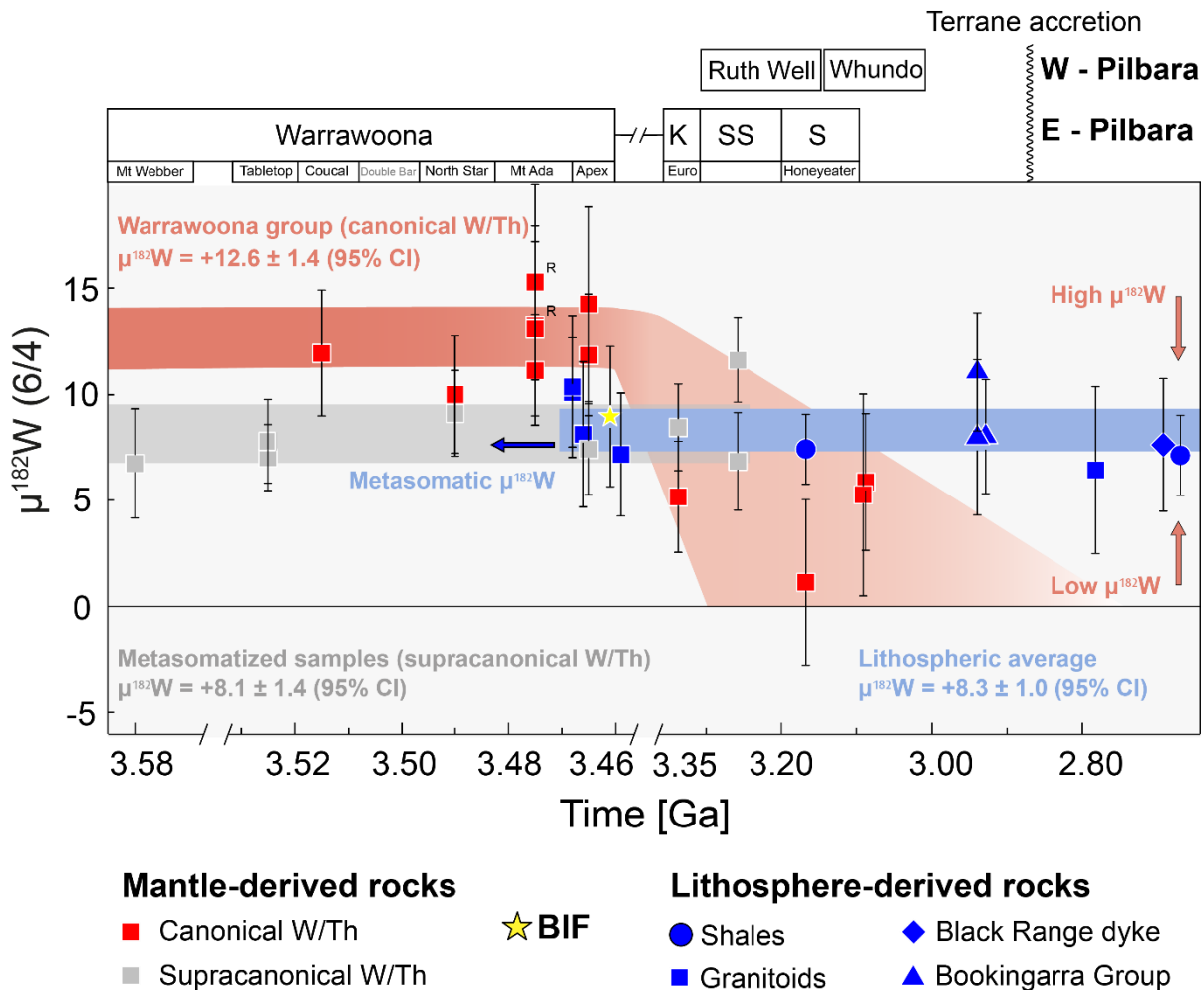


**Fig. 2.2: High-precision  $\mu^{182}\text{W}$  analyses for rocks from the Pilbara Craton presented in stratigraphic order.** Associated uncertainties refer to the corresponding 95% confidence intervals of multiple digestions (95% CI). Mantle-derived samples with undisturbed elemental W budgets (having canonical W/Th ratios) are represented by red squares, mantle-derived samples that were affected by secondary W-enrichment (supracanonical W/Th ratios) are shown as grey squares. Undisturbed Warrawoona Group samples display an average of  $\mu^{182}\text{W} = +12.6 \pm 1.4$  ppm (95% confidence interval (CI),  $n=8$ , red bar), whereas rocks that were affected by secondary W-enrichment display resolvable lower excesses of  $\sim +8.1 \pm 1.4$  ppm (95% CI,  $n=8$ ; grey bar). Younger mantle derived rocks with undisturbed W budgets display significantly lower  $^{182}\text{W}$  excesses. Lithosphere-derived rocks are shown as blue symbols. Granitoid rocks (blue squares) include non-gneissic tonalites and more fractionated and post-orogenic granitoids. Shales (blue circles) provide information about the upper continental crust, whereas lithospheric mafic magmatism is recorded in samples from the Bookingarra and Fortescue Groups. The lithospheric samples provide an average  $\mu^{182}\text{W}$  of  $+8.3 \pm 1.0$  ppm (blue bar) which is significantly lower than the average  $\mu^{182}\text{W}$  of  $+12.6 \pm 1.4$  ppm for Warrawoona group samples with canonical W/Th (red bar). Notably, samples that were affected by secondary W enrichment (grey bar) display the same average as the lithosphere-derived rocks (blue bar). R = previously published data for two samples from the Apex basalt (Rizo et al., 2019)



## 2.5 Discussion

Altogether, the integrated  $^{182}\text{W}$  isotope compositions recorded in granitoids, shales and lithosphere-derived rocks provide a lithospheric average  $\mu^{182}\text{W}$  of  $+8.3 \pm 1.0$  ppm (N = 11, blue bar in Fig. 2.2), which is significantly lower than the average  $\mu^{182}\text{W}$  of  $+12.6 \pm 1.4$  ppm for Warrawoona group samples with canonical W/Th (N = 8, red bar in Fig. 2.2) but higher than the modern upper mantle-like  $\mu^{182}\text{W}$  of  $+1.1 \pm 3.9$  ppm for the Honeyeater Basalt. Thus, the lithospheric average seems to carry the integrated  $^{182}\text{W}$  isotope composition of different mantle reservoirs. Samples from the EPT that were affected by secondary W enrichment (grey bar in Fig. 2.2) show a similar average as the lithosphere-derived rocks, which is evidence for a craton wide homogenization of ambient  $^{182}\text{W}$  isotope compositions and the partial homogenization of primary  $^{182}\text{W}$  isotope variability. Hence, using elemental W-Th systematics is a key tool, as this can unambiguously clarify the origin of  $^{182}\text{W}$  isotope variability. In contrast to a previous study (Archer et al., 2019), where this tool has not been applied and altered samples were studied, we can now distinguish between diminishing  $^{182}\text{W}$  isotope anomalies in the ambient mantle and secondary processes that re-distribute  $^{182}\text{W}$  isotope anomalies (Fig. 2.1c).

Our study demonstrates that the oldest mantle-derived rocks from the Pilbara Craton with canonical W/Th display  $^{182}\text{W}$  isotope excesses of a magnitude similar to other Archean cratons. As outlined above, however, there is no uniformly accepted explanation for the origin of these  $^{182}\text{W}$  excesses. For the Pilbara craton, the missing late veneer hypothesis provides a plausible explanation, as decreasing depletions of Platinum Group Elements (PGE) in komatiites with decreasing age are consistent with a progressive in-mixing of late veneer material (Maier et al., 2009). Amongst the ten komatiite samples previously analyzed for HSE (Maier et al., 2009) we found only one sample (179738) that preserved its primary W budget. This confirms previous evidence that ultramafic rocks are extremely susceptible to (fluid mediated) second stage enrichment of W (Tusch et al., 2019), which causes decoupling of HSE and  $^{182}\text{W}$  systematics. The pristine komatiite sample 179738 (3.46 Ga Apex Basalt of the Warrawoona Group) analyzed in this study is strongly depleted in PGE and displays an elevated  $^{182}\text{W}$  of  $+11.9 \pm 2.9$  ppm, consistent with a model assuming an incomplete late veneer contribution to the mantle source of this sample. Such an interpretation is also in line with the absence of  $^{142}\text{Nd}$  anomalies in Pilbara rock samples that show significant PGE depletions (Archer et al., 2019), thereby negating early silicate

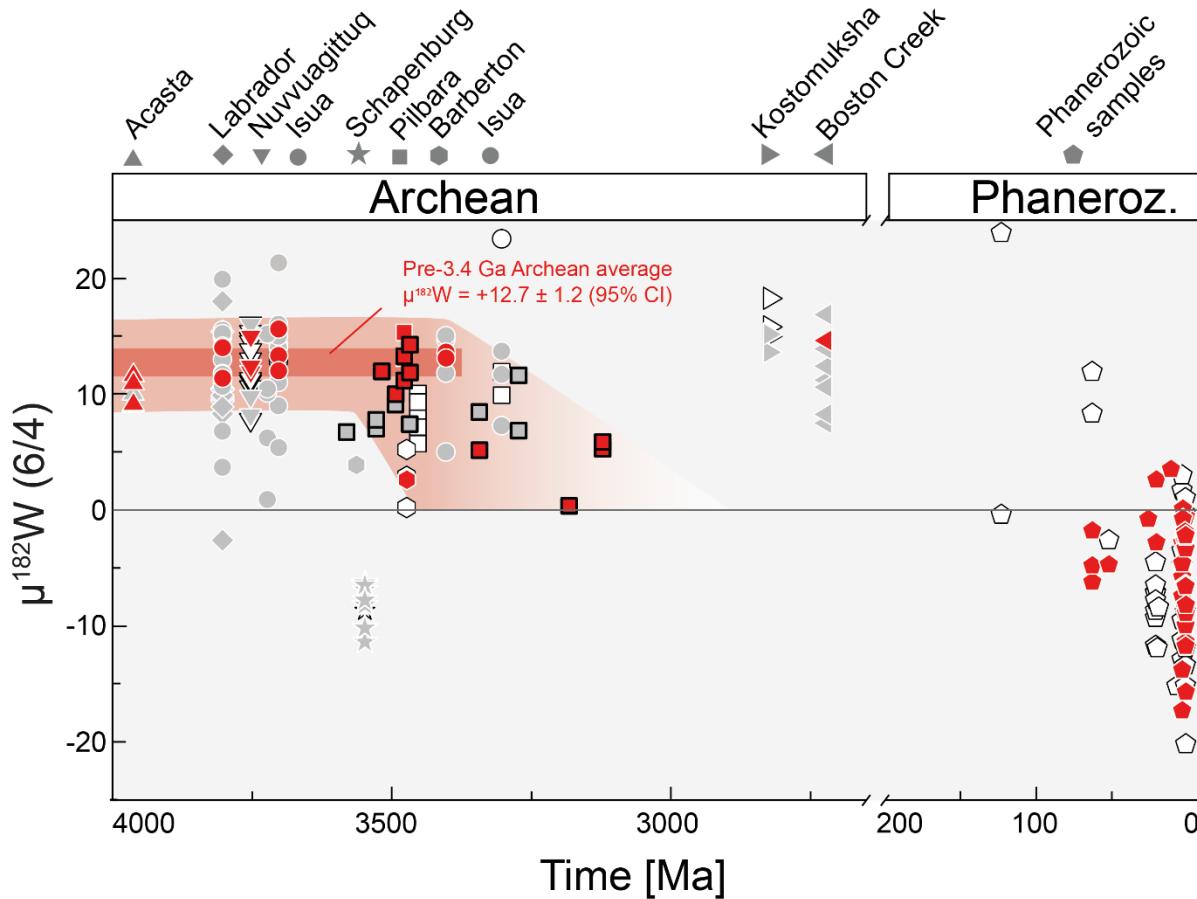


**Fig. 2.3: Compilation illustrating the secular  $^{182}\text{W}$  isotope evolution of the terrestrial mantle.** This dataset includes all available  $^{182}\text{W}$  isotope literature data for mantle-derived rocks. For Nuvvuagittuq we assume a minimum emplacement age of 3.75 Ga (Cates and Mojzsis, 2007), being well aware that it might be older (O’Neil et al., 2008). The literature data are subdivided into samples with overprinted elemental W budgets (grey) and samples with canonical W/Th (red). Symbols with no color fill refer to samples with unknown W/Th ratios. Data for Pilbara rocks presented in this study are squares with thick black frames. References and information on the data compilation are provided in the method section and Table B2 (appendix B). Error bars are omitted for visual clarity, but uncertainties are given in Table B2 (appendix B).

differentiation as an additional explanation for the occurrence of  $^{182}\text{W}$  isotope excesses. Collectively, our data indicate that Hadean, pre-late veneer mantle was preserved in the mantle sources of Pilbara igneous rocks until ca. 3.3-3.1 Ga, much longer than evident from other cratons (Touboul et al., 2014; Rizo et al., 2016b). The long-standing apparent mismatch between virtually constant  $^{182}\text{W}$  isotope excesses and progressively vanishing  $^{142}\text{Nd}$  anomalies through Archean time (Rizo et al., 2016b) is therefore well explained by the larger mobility of W compared to Nd and its redistribution during secondary processes. By only considering samples with strictly canonical W/Th ratios, we show that the prevalence of  $^{182}\text{W}$  isotope excesses even in the younger Archean rock record (Fig. 2.3) may be a vestige of older rocks, from which

W was progressively redistributed. Hence, we rather argue that mantle convection homogenized primordial  $^{182}\text{W}$  isotope anomalies during the Paleo- and Mesoarchean (Fig. 2.3) at the same timescales as  $^{142}\text{Nd}$  systematics (Debaille et al., 2013).

## 2.6 Conclusion

Our  $^{182}\text{W}$  results for the Pilbara Craton have important implications for understanding timescales of geodynamic processes on the early Earth and provide a future reference parameter for geodynamic models addressing mantle mixing in the early Earth. Geodynamic models addressing the Pilbara data have to account for the observations that (1) a Hadean pre-late veneer signature remains isolated for over more than 1 billion years and (2) such an isotopically isolated mantle domain continuously triggered prolonged plume-driven magmatism with a distinct isotopic signature, most likely in a stagnant lid regime (Bédard, 2018). In contrast to present-day mantle plumes with negative  $^{182}\text{W}$  signatures (Mundl et al., 2017), Archean mantle plumes beneath the Pilbara Craton appear to have carried rather uniform  $^{182}\text{W}$  isotope excesses that were similar to the shallower mantle, thus arguing that compositionally distinct deep mantle sources such as LLSVPs or ULVZs may not have been involved or, alternatively, even may not have formed (Bédard, 2018; Mei et al., 2020).

The marked geodynamic transition at 3.3 – 3.1 Ga in the Pilbara Craton with influx of modern-like, upper mantle material without  $^{182}\text{W}$  excess coincides with models claiming a global transition from stagnant lid-type regimes to modern plate tectonics. This transition is, for instance, postulated from crustal growth curves based on the zircon record (Belousova et al., 2010), from the increased occurrence of subduction-like magmatism in the Archean (Pearce, 2008), the change of composition in the subcontinental lithospheric mantle (Shirey and Richardson, 2011), and from increasingly larger volumes of exposed felsic crust (Dhuime et al., 2015). It is therefore tempting to postulate that the initiation of plate tectonics caused a more efficient homogenization of Earth's mantle than vertical, plume-driven dynamics that prevailed in a stagnant lid regime as proposed for the older units of the Pilbara Craton. Indeed, geodynamic models for a stagnant lid regime show that, contrary to expectation, the timescales of mantle mixing in the Archean were not accelerated due to a hotter thermal state of the mantle but were rather prolonged (Debaille et al., 2013). The Archean regime was possibly characterized by small, isolated convection cells and

episodic mantle overturn events that vertically homogenized discrete regions of the mantle (O'Neill et al., 2007; Bédard, 2018) but maintained lateral heterogeneities for billions of years (Ballmer et al., 2017). In summary, our study demonstrates that the Pilbara Craton preserved a natural laboratory for Archean geodynamics that may serve as a future test case for interdisciplinary studies assessing timescales of mantle dynamics through deep time. In particular, the rock record of the Pilbara Craton provides important observational constraints on the Archean mantle which are indispensable for numerical simulations as such input parameters define the evolutionary pathway of computational convection models (Weller and Lenardic, 2012).

## 2.7 Method Section

### 2.7.1 Analytical protocol

Concentration measurements for high-field-strength elements (HFSE), W, U, and Th were conducted by isotope dilution, using mixed isotope tracers that are enriched in  $^{229}\text{Th}$ - $^{233}\text{U}$ - $^{236}\text{U}$  and  $^{183}\text{W}$ - $^{180}\text{Ta}$ - $^{180}\text{Hf}$ - $^{94}\text{Zr}$ , respectively. Around 120 mg of sample powder were spiked and digested using a previously described protocol (Tusch et al., 2019). After sample-spike equilibration, we separated our sample solution (30% aliquot for U, Th, and W analyses and 70% for HFSE analyses). The chemical separation for HFSE followed a previously published protocol (Thiemens et al., 2019). The 30% aliquot for U, Th and W analyses was loaded onto BioRad Poly-Prep® columns filled with 1.6ml Eichrom TRU-Spec® resin (200-400 mesh) atop 0.4ml Eichrom prefilter® material. Tungsten and most matrix components of the 30% aliquot were eluted during loading (1.5N  $\text{HNO}_3$ ) and subsequent rinsing (2 x 5/8 resin volumes (rv) of 1.5 M  $\text{HNO}_3$ ). The subsequent separation of U and Th on TRU-Spec® resin followed a previously published protocol (Luo et al., 1997). In previous protocols (Thiemens et al., 2019; Tusch et al., 2019), U and Th were first separated during an HFSE protocol in 2 M HF prior to loading onto TRU-Spec® resin. By first loading our 30% aliquot onto TRU-Spec® resin, we avoid the formation of insoluble Th bearing fluorides. Tungsten was subsequently separated from residual matrix components using BioRad Poly-Prep® columns filled with 2ml AG-1-X8 resin (Kleine et al., 2004). Tungsten concentration measurements for granites were performed differently, using a  $^{180}\text{W}$ - $^{183}\text{W}$  double-spike technique (Kurzweil et al., 2017). All high-precision isotope dilution

analyses were performed on a Thermo Fisher® Neptune Plus Multicollector ICP-MS at Cologne (Weyer et al., 2002; Kleine et al., 2004; Thiemens et al., 2019). For measurements of other trace elements we used the analytical protocol described by Tusch et al. (2019). Trace element concentrations were measured using a quadrupole ICP-MS at the Institut für Geowissenschaften at CAU Kiel (Garbe-Schönberg, 1993).

The chemical purification of W for high-precision isotope composition analyses follows a previously published analytical protocol (Tusch et al., 2019) that was only slightly modified to be able to process up to 1.6 g rock powder per column. The final W bearing cut after the third stage column (Eichrom™ TEVA resin) was directly loaded onto TODGA resin (1ml TODGA resin in Spectra/Chrom® 45µm PP MiniColumns) that purifies W more efficiently from remaining matrix elements and Ti (Pourmand and Dauphas, 2010). During loading in 5 M HCl and subsequent rinsing with 2 x 6.5 rv 3 M HNO<sub>3</sub> the remaining Ti and most other remaining matrix elements pass through the resin. By subsequently rinsing with 3 x 6.5 rv 8 M HNO<sub>3</sub> residual Ca is also eluted. During these washing steps W is completely retained on the column and can be finally eluted in 3 x 5 rv 0.56 M HNO<sub>3</sub> – 0.24 M HF. Remaining impurities in our final W cut after processing 1.6 g rock powder (felsic matrix) were 5 ng/ml Na, 11 ng/ml Mg, 4 ng/ml Al, 2 ng/ml K, 21 ng/ml Ca, 0.1 ng/ml Ti, 1.2 ng/ml Ta, 2 ng/ml Nb and 0.5 ng/ml Mo. Considering the initial weight of sample material (1.6 g) this translates to fractions in the ppt range.

The setup for high-precision <sup>182</sup>W isotope measurements has also been described in detail in a previous study (Tusch et al., 2019). In short, the analyses of the Pilbara samples were run over a period of 22 months (February 2018 – November 2019) at an average signal sensitivity of 4.5 V on <sup>182</sup>W (using 10<sup>11</sup> Ohm amplifiers) for a ~50 ng/ml W sample solution at an uptake rate of ca. 60 µl/min. The measurements of sample solutions were run at intensities between 2.0 and 27.5 V on <sup>182</sup>W, corresponding to 23 – 274 ng/ml solutions. Samples were always bracketed by a concentration-matched certified reference material (NIST SRM 3163) to report relative <sup>182</sup>W isotope compositions. For all samples we performed multiple measurements (n = 9-23) to obtain a statistically significant population, and uncertainties for average  $\mu^{182}\text{W}$  values are correspondingly reported as 95% confidence intervals (95% CI). The 95% CI for repeatedly measured samples (n = 9-23) ranged between ±1.6 ppm and ± 4.8 ppm (average of ±3.0 ppm). Differences in the 95% CI mainly result from differences in

beam intensities.

Our long-term reproducibility is inferred from repeated measurements of two in-house rock reference materials (historical La Palma basalt “LP1” and a 3455 Ma gneiss from Swaziland, labeled “AGC 351” (Kröner et al., 2014)). Along with our samples, the in-house rock standards were always passed individually through our separation protocol and measured in every session at different run-conditions (variable procedural yields at different signal intensities). In total, we performed 16 measurements for sample LP1 (235 single measurements) and 11 measurements for sample AGC 351 (151 single measurements). The session averages for  $\mu^{182}\text{W}$  of both samples overlap within their 95% CI (LP1 =  $-1.3 \pm 1.1$  ppm and AGC 351 =  $-0.1 \pm 1.2$  ppm) and are indistinguishable from the NIST reference material (Fig. 2.5) and previously reported long-term averages for the same sample powders (Tusch et al., 2019). The reproducibility of both in-house rock reference materials relative to NIST SRM 3163 is given by the 2 SD of the corresponding average  $\mu^{182}\text{W}$  ( $-1.3 \pm 4.3$  ppm for LP1 and  $-0.1 \pm 3.5$  ppm for AGC 351). The somewhat poorer reproducibility of sample LP 1 stems from lower signal intensities (2.1 – 15.0 volts on  $^{182}\text{W}$ ) when compared to sample AGC 351 (8.2 – 27.5 volts on  $^{182}\text{W}$ ).

Our average procedural yields were 77% (70% of samples above 70%, 24% between 60% and 70%) with only three samples below 60% (7% of all samples). Total procedural W blanks were measured on a Thermo Fisher® Neptune Plus Multicollector ICP-MS at the University of Cologne after adding a  $^{180}\text{W}$ - $^{183}\text{W}$  double-spike tracer (Kurzweil et al., 2017). Blanks were typically below 500 pg (137-471 pg) which corresponds to less than 1 % blank contribution. Three erratic blank values were higher (1401, 1804 and 3427 pg) but only contributed up to 4.5 % to the total analyte. Considering the average excess for undisturbed samples from the Warrawoona Group ( $\mu^{182}\text{W} = +12.6 \pm 1.4$  ppm) and our average uncertainty on the sample averages ( $\pm 3.0$  ppm) a blank contribution of 4.5% carrying modern upper mantle like  $^{182}\text{W}$  isotope composition ( $\mu^{182}\text{W} = 0$ ) would propagate into our  $\mu^{182}\text{W}$  values to less than 1ppm.

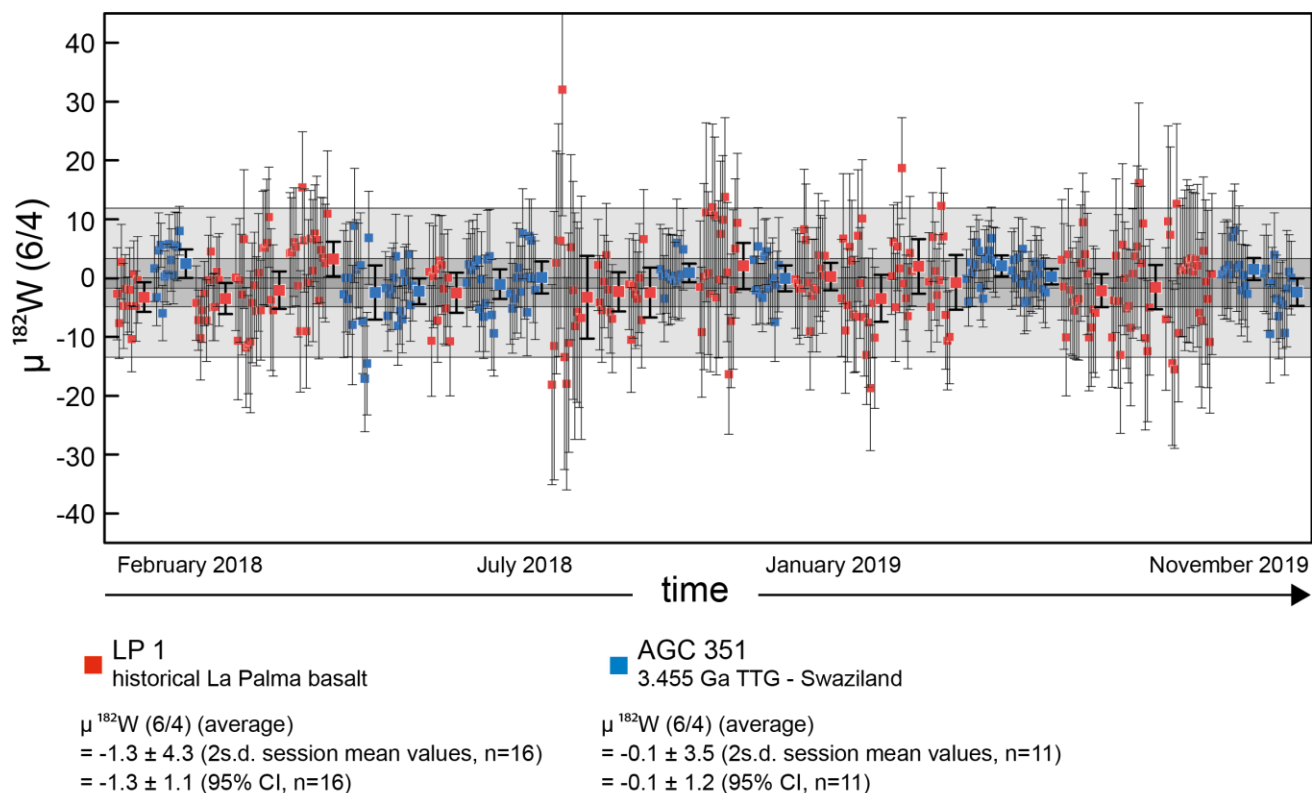


**Fig. 2.5: Long-term reproducibility for  $\mu^{182}\text{W} (6/4)$ , inferred from the repeated analysis of multiple digestions for our in-house reference materials AGC 351 and LP1 reported relative to W NIST SRM 3136.** Small symbols refer to single measurements and larger symbols give the average for the corresponding analytical session. For the single measurements, error bars refer to the internal run statistic (2 SE). The uncertainty for the session mean values are given by the corresponding 95% CI. The long-term reproducibility for our two in-house reference materials with variable composition (mafic LP1 and felsic AGC 351) are given by the 2 SD of the session mean values. The poorer reproducibility and larger scatter of sample LP 1 stems from lower signal intensities when compared to sample AGC 351.

### 2.7.2 Geological background

The Pilbara Craton of Western Australia has been subdivided into the East Pilbara Terrane (EPT), West Pilbara Superterrane (WPS, comprised of three separate terranes), and the Kuranna Terrane (Van Kranendonk et al., 2007). Rocks from the EPT and WPS display dissimilar geochemical, geochronological, and structural characteristics, reflecting markedly different processes of crust formation (Smithies et al., 2018). The 3.52-3.18 Ga East Pilbara Terrane is the ancient nucleus of the craton and a global type example for the dome-and-keel geometry that is unique to many Archean terranes (Van Kranendonk et al., 2004). Granitoid domes are ovoid, multi-component intrusive complexes that are separated by narrow, mostly steeply dipping cusped greenstone belts, and encircled by ring faults (Van Kranendonk et al., 2002). EPT greenstones comprise 3.52 – 3.18 Ga old, predominantly tholeiitic and lesser

komatiitic volcanic rocks, with minor interbedded sediments, of the Pilbara Supergroup that is subdivided into four unconformity-bound groups (Warrawoona, Kelly, Sulphur Springs and Soanesville). The lower three volcanic groups were derived from undepleted mantle sources (R. H. Smithies et al., 2005) and emplaced during distinct mantle plume events (Arndt et al., 2001) similar to modern plateau basalts (Condie, 2005; Van Kranendonk et al., 2007). The Honeyeater Basalt of the youngest Soanesville Group is interpreted as the product of plume-initiated rifting that caused intra-continental extension and magmatism at the start of a Wilson cycle (Van Kranendonk et al., 2010).

A rifted fragment of the EPT is inferred in the WPS (Karratha Terrane) that, together with MORB-like rocks of the Regal Terrane, and subduction-related rocks of the Sholl Terrane, accreted to form the WPS at c. 3.07 Ga (Smithies et al., 2005; Van Kranendonk et al., 2007). The Sholl Terrane comprises the 3.13-3.11 Ga Whundo Group, a sequence with geochemical characteristics that are consistent with their derivation from a depleted mantle source that was variably affected by metasomatic enrichment in an arc-like setting (Smithies et al., 2005).

The Pilbara Supergroup of the EPT erupted on a > 3.53 Ga proto-continental basement that was most likely a heterogeneous mix of mafic and felsic lavas and TTGs (tonalites, trondhjemites and granodiorites) with a common tholeiitic parental magmatic source (Smithies et al., 2019). Multiple lines of evidence for the presence of an older basement (Van Kranendonk et al., 2002) include the presence of older gabbroic-anorthositic enclaves (Mount Webber Gabbro) embedded in granitic rocks of the Shaw Granitic Complex (McNaughton et al., 1988; Petersson et al., 2019), older TTG enclaves, and abundant inherited zircons (Van Kranendonk et al., 2002). The burial of heat-producing ancient TTGs into the middle crust, together with conductive and convective heat brought by excessive mantle melting events, caused re-melting of early TTGs, which resulted in thermal softening of the middle crust (Sandiford et al., 2004). This led to diapirism of granitoid melts ascending from the middle crust, and to the sinking of the dense volcanic rocks from the greenstone successions during partial convective overturn, which led to the observed dome-and-keel geometry (Van Kranendonk et al., 2004).

Granitic rocks of the EPT have been divided into five supersuites that were emplaced during discrete intervals between 3.49 and 3.22 Ga (Van Kranendonk et al. (2007),



3.49-3.46 Ga Callina, 3.45-3.42 Tambina, 3.33-3.29 Emu Pool, 3.27-3.22 Ga Cleland supersuites). The large-scale granitoid domes are polyphase complexes that initially derived through melting from a mafic (tholeiitic) protocrust and earlier TTG rocks (Bickle et al., 1993; Smithies et al., 2019) and subsequently evolved to more evolved high-K granitic compositions (predominantly monzogranites) through successive melting events. Younger granitic phases were emplaced into the cores of the developing domes (Smithies et al., 2003) during partial convective overturn.

After c. 3.07 Ga, when accretion of the WPS onto the EPT took place, volcanic and sedimentary rocks of the De Grey Supergroup were deposited from 3.02 Ga in several basins that formed in response to lithospheric extension (Van Kranendonk et al., 2007). Mafic volcanic rocks of the Bookingarra Group and associated intrusive rocks were emplaced between ~3.0 and 2.95 Ga. The Bookingarra Group unconformably overlies volcano-sedimentary rocks of the Whim Creek and Croydon Groups at the western end of the late-tectonic Mallina Basin. These older rocks derived from a metasomatized, lithospheric mantle source that was refertilized by subducted sediments during the formation of the Whundo Group in a subduction zone-like setting ca. 150 Ma earlier (Smithies et al., 2004). The tectono-magmatic history of the Pilbara Craton was completed by the emplacement of ca. 2.85 Ga post-tectonic granites of the Split Rock Supersuite (Van Kranendonk et al., 2007). Emplacement of ca. 2.78 Ga (Wingate, 1999) lithosphere-derived rift-related dikes of the Black Range Dolerite Suite record the onset of rifting and deposition of the unconformably overlying Fortescue Group.

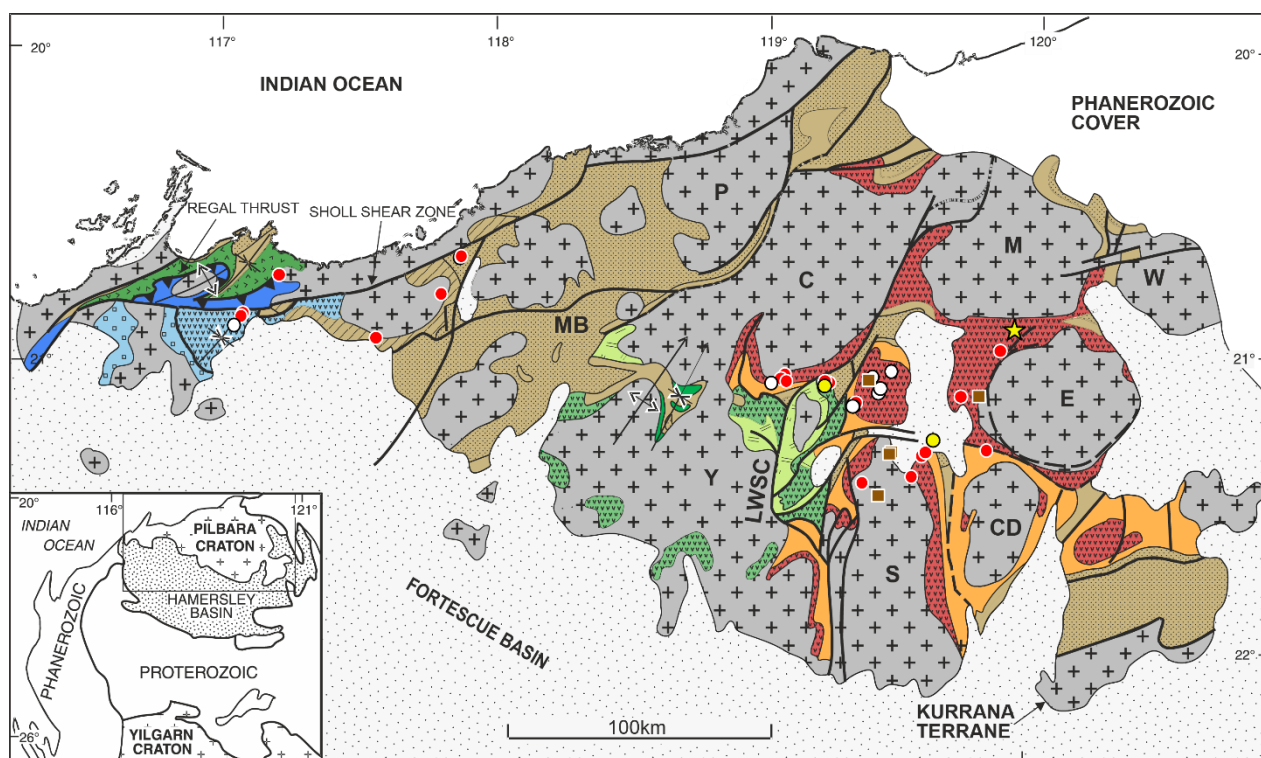
### *2.7.3 Sample selection*

Most mantle-derived samples from the EPT were collected in the Marble Bar greenstone belt and in the North Pole Dome area (Panorama greenstone belt) where rocks were only affected by low grade metamorphism and low strain (Van Kranendonk et al., 2007). Samples from the oldest Coonterunah Subgroup of the Warrawoona Group were collected in the East Strelley greenstone belt and samples from the Honeyeater Basalt from the Soanesville greenstone belt (see Fig. 2.4). The low metamorphic grade is most promising for preservation of primary elemental W budgets.

To expand our dataset for mantle-derived rocks from the EPT we also sampled a recently described 3.59 Ga magmatic suite (Mount Webber Gabbro, Pil 17-07) that was shown to predate the oldest rocks from the Warrawoona Group and that are thought to represent remnants of an early proto-crust (McNaughton et al., 1988; Petersson et al., 2019). Our sample was collected in an outcrop on the eastern bank of the Shaw River where anorthositic host rocks within the tonalites contain gabbroic enclaves (McNaughton et al., 1988).



Mantle-derived rocks from the WPS comprise samples from the Sholl Terrane (Whundo Group, Pil 16-67, -74, -75) and Karratha Terrane (Ruth Well Formation, Pil 16-66b). Our samples from the Whundo Group were collected in the same outcrop area as previously described in detail by pioneering studies on the Whundo Group (Smithies et al., 2005).

Granitoid samples from the multi-phase dome complexes of the EPT include those from the low-strain North Shaw Suite (3.49-3.46 Ga Callina Supersuite) in the northern part of the Shaw Granitic Complex, which comprises exceptionally well preserved tonalites that still display igneous textures (Bickle et al., 1983). We sampled two undeformed to weakly-foliated tonalites from the North Shaw Suite (Pil 16-34 & -35), as well as younger (Pil 16-36a) and more fractionated gneissic TTGs (Pil 16-12, -36a, -41) to cover a suite of rocks that represent lithostratigraphic and petrological end-members of the long-lived granitic complexes. Additionally, we sampled lithosphere-derived mafic rocks from the Bookingarra (Pil 16-63, -65 & -75) and Fortescue Group (Black Range dolerite, Pil 16-31) to better constrain the  $^{182}\text{W}$  isotope composition of the subcontinental lithosphere within the Pilbara Craton.




### West Pilbara Superterrane

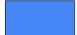
#### Sholl Terrane


-  Railway Supersuite (3130-3090 Ma)
-  Whundo Group (3130-3110 Ma)

#### Regal Terrane


-  Regal Terrane (3200 Ma)

#### Karratha Terrane

-  Roebourne Group (3280 Ma)

-  Soanesville Group (3220-3165 Ma)

### East Pilbara Terrane


-  Sulphur Springs Group (3250 Ma)

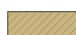
-  Kelly Group (3350-3300 Ma)

-  Warrawoona Group (3525-3426 Ma)


-  Undivided Granitoid Rocks (3500-2830 Ma)



### De Grey Supergroup

-  Croydon and Nullagine Group (3015-2930 Ma)






-  Whim Creek Group (3010-2990 Ma)

-  Gorge Creek Group (3050-3015 Ma)

-  Folds, Synclines, Anticlines

-  Faults, exposed (2.94 Ga) & concealed (3.3 Ga)
-  Thrust faults (3070 Ma)

### Samples

-  Mafic-Ultramafic rocks measured for  $^{182}\text{W}$
-  Shales
-  BIF
-  Mafic-Ultramafic rocks
-  Granitoids

**Fig. 2.4: Simplified geological map of the Pilbara Craton, NW Australia showing the sample localities covered in this study.** The map is modified from previous studies (Van Kranendonk et al., 2007; Van Kranendonk et al., 2010). Shown are the main groups of the West Pilbara Superterrane and East Pilbara Terrane. Both terranes are unconformably overlain by sedimentary rocks of the De Grey Supergroup. LWSZ = Lalla Rookh-Western Shaw structural corridor; MB = Mallina Basin. The older greenstones are intruded by diverse granitoid complexes: M = Muccan; W = Warrawagine; E = Mount Edgar; CD = Corunna Downs; S = Shaw; Y = Yule; C = Carlindie; P = Pippingarra.

#### 2.7.4 Secular evolution of $^{182}\text{W}$ isotope anomalies

To better understand the secular evolution of  $^{182}\text{W}$  isotope anomalies in Earth's mantle, we compiled all literature data for  $^{182}\text{W}$  isotope compositions measured in mantle-derived rocks. Supplementary Table B2 (appendix B) provides an overview and lists all references for  $^{182}\text{W}$  data and elemental concentrations of W and Th. In total, 19 studies reported 191  $^{182}\text{W}$  isotope compositions for mantle-derived rocks, with 122 samples from the Archean, only 1 sample from the Proterozoic (Puchtel et al., 2016b) and 68 samples of Phanerozoic age. It becomes apparent that most studies have only provided snapshots within the  $^{182}\text{W}$  isotope evolution of individual Archean cratons (Touboul et al., 2012; Touboul et al., 2014; Liu et al., 2016; Puchtel et al., 2016a; Puchtel et al., 2018). We further screened this compilation for samples that were not substantially affected by secondary W-enrichment. Indeed, 95% of the Phanerozoic samples in our compilation that report elemental concentrations for W and Th display canonical W/Th ratios. Only two samples have slightly supracanonical W/Th ratios of 0.26 and 0.27, respectively. The Phanerozoic samples with canonical W/Th ratios are characterized by an average deficit in  $\mu^{182}$  of  $-5.4 \pm 1.7$  ppm and display an average W/Th of 0.152, which perfectly overlaps with the combined average for fresh MORB and OIB samples (W/Th = 0.150, König et al., 2011). It has been argued that elevated W/Th ratios in mantle-derived rocks from the Archean might be a non-uniformitarian Archean feature (Willbold et al., 2015). However, as demonstrated in this study the Archean suite analysed here comprises many rocks with primary W budgets as present day MORB and OIB.

After screening the global dataset, it becomes apparent, that Archean rocks with canonical W/Th ratios display uniform excesses before  $\sim 3.4$  Ga 13 ppm. Exceptions are two  $\sim 3.7$  Ga old amphibolites from Isua (sample 00-044:  $\mu^{182}\text{W} = +21.3 \pm 5.3$  ppm; sample 00-008:  $\mu^{182}\text{W} = +5.4 \pm 7.2$  ppm, Rizo et al., 2016b). We regard these two samples as outliers for two reasons. First, it was not possible to reproduce results for  $^{182}\text{W}$  isotope compositions on the same powder splits for other rocks that displayed markedly different  $^{182}\text{W}$  isotope compositions than typically observed for Isua rocks (samples S31 & S33, Tusch et al., 2019). Second, other  $\sim 3.7$ - $3.8$  Ga old amphibolites and metabasalts from Isua with canonical W/Th ratios display homogeneous excesses of ca. +13 ppm (Willbold et al., 2011; Dale et al., 2017; Tusch et al., 2019). As demonstrated by our study on rocks from the Pilbara Craton, the  $^{182}\text{W}$  isotope composition of mantle-derived rocks with supracanonical W/Th ratios are dominated

by metasomatic agents that re-mix reservoirs of variable  $^{182}\text{W}$  isotope compositions. If not taken into consideration, this can lead to ambiguous models on the origin of early formed mantle heterogeneities and on the time-scales of mantle convection. Moreover, overprinted elemental W budgets caused a decoupling of  $^{182}\text{W}$  isotope and HSE systematics, thereby also biasing conclusions on the late-accretion history of the Earth (Touboul et al., 2012; Archer et al., 2019).

# Chapter 3

## 3 Long-term preservation of Hadean protocrust in Earth's mantle

### 3.1 Abstract

Due to plate tectonics operating on Earth, the preservation potential for mantle reservoirs from the Hadean Eon (>4.0 Ga) has been regarded as very small. The quest for such early remnants has been spurred by the observation that many Archean rocks exhibit excesses of  $^{182}\text{W}$ , which is the decay product of short-lived  $^{182}\text{Hf}$ . The exact causes for these  $^{182}\text{W}$  excesses, however, have remained ambiguous and proposed models involve missing late veneer additions or early silicate differentiation. Hence, it remains speculative, if the Archean isotope anomalies and also  $^{182}\text{W}$  deficits found in many young ocean island basalts (OIBs) mirror primordial Hadean mantle differentiation or just incomplete mixing of older meteorite building blocks delivered to the growing Earth. Here, we present a coherent high precision  $^{182}\text{W}$  isotope dataset for 3.22-3.55 Ga old mafic and felsic rocks from the Kaapvaal Craton, Southern Africa. Some mafic rocks from the Schapenburg Greenstone Belt of the Kaapvaal Craton were the first Archean rocks reported to exhibit negative  $^{182}\text{W}$  anomalies, in fact similar to modern ocean island basalts. Our study reveals widespread  $^{182}\text{W}$  deficits in different rock units from the Kaapvaal Craton and also the very first discovery of an anti-correlation between short-lived  $^{182}\text{W}$  and long-lived  $^{176}\text{Hf}$ - $^{143}\text{Nd}$  patterns. The only plausible model to explain these patterns is the presence of recycled mafic restites from Hadean protocrust in the ancient mantle beneath the Kaapvaal Craton. Hence, the data provide unambiguous evidence for the operation of silicate differentiation processes on Earth during the lifetime of  $^{182}\text{Hf}$ , i.e., the first 60 million years after solar system formation, thereby also providing a firm lower bound for the age of the Earth-Moon system. The striking isotopic similarity between recycled protocrust and the low  $^{182}\text{W}$  endmember of modern OIBs might also be the missing link bridging  $^{182}\text{W}$  isotope systematics in Archean and young mantle-derived rocks. This finding offers important

constraints on the geodynamic evolution of Earth's mantle through time, indicating inefficient homogenization of Hadean silicate reservoirs.

## 3.2 Introduction

Due to plate tectonic processes, the accessible silicate reservoirs on Earth have lost most of their memory of the first ca. 500 Ma of Earth's history. Hence, our understanding of this time period comes from indirect evidence, e.g., from geochemical tracers such as short-lived nuclide series that were active during the first ca. hundred million years after solar system formation (Harper and Jacobsen, 1992; Willbold et al., 2011; Mukhopadhyay, 2012). The detection of terrestrial variability in the relative abundances of short lived nuclide decay products such as  $^{129}\text{Xe}$ ,  $^{142}\text{Nd}$ , and  $^{182}\text{W}$  provided firm evidence that primordial reservoirs were not fully homogenized by mantle-dynamics, and played a significant role during the formation of the first continental crust (Allègre et al., 1987; Caro et al., 2003; Willbold et al., 2011). The very recent discovery of  $^{182}\text{W}$ ,  $^{142}\text{Nd}$ , and  $^{129}\text{Xe}$  anomalies in modern mantle-derived rocks (Mukhopadhyay, 2012; Mundl et al., 2017; Peters et al., 2018) demonstrate that primordial reservoirs are still accessible. Whereas anomalous  $^{129}\text{Xe}$  and  $^{142}\text{Nd}$  isotope compositions in mantle-derived rocks can primarily be assigned to early planetary outgassing and early silicate differentiation, respectively, the presence of  $^{182}\text{W}$  isotope anomalies can mirror multiple processes. While some interpret the prevalence of positive  $^{182}\text{W}$  anomalies in Archean rocks as a result of disproportional accretion of late veneer (Archer et al., 2019), others have pointed out that this view may be a simplification as observations from other isotope systematics suggest other processes to be involved, such as metal-silicate segregation or silicate differentiation in an early magma ocean, or during crust-mantle differentiation (Touboul et al., 2012; Puchtel et al., 2016a). Isotope anomalies of  $^{142}\text{Nd}$  in Archean rocks that are coupled with  $^{182}\text{W}$  anomalies (Puchtel et al., 2016a; Rizo et al., 2016b) clearly provide evidence that early silicate differentiation must have operated during the first ca. 60 Ma. However, it has been demonstrated that pristine  $^{142}\text{Nd}$ - $^{182}\text{W}$  records are often obscured, either by multistage processes within the lifetime of  $^{142}\text{Nd}$ , while  $^{182}\text{W}$  was extant, or via fluid-controlled second stage metasomatic overprint of primordial  $^{182}\text{W}$  patterns (Tusch et al., 2019).

### 3.3 Geological and methodological overview

To further evaluate the processes that account for  $^{182}\text{W}$  anomalies in Archean rocks, we investigated samples from the eastern Kaapvaal Craton, southern Africa that are well suited to search for vestiges of early silicate differentiation, because they were shown to display both heterogeneous  $^{142}\text{Nd}$  and  $^{182}\text{W}$  compositions (Touboul et al., 2012; Puchtel et al., 2016a; Schneider et al., 2018). We performed high-precision  $^{182}\text{W}$  isotope analyses on a comprehensive suite of 17 samples that range from mantle-derived lithologies of mafic-ultramafic composition to different types of granitoids. These samples span an age range from ca. 3.55-3.22 Ga, represent the main lithological units of the Ancient Gneiss Complex (AGC) and also comprise the oldest rocks of the Barberton Granite-Greenstone terrain (BGGT). Moreover, most of these samples have previously been analyzed for their  $^{142}\text{Nd}$  compositions (Schneider et al., 2018). More information about the regional geology and samples is provided in the method section. By combining  $^{182}\text{W}$  isotope analysis with high-precision isotope dilution measurements for high field strength elements (HFSE), U, and Th, we assessed the source budget of W in these samples. Measurements of  $^{182}\text{W}$  isotope compositions followed protocols (Tusch et al., 2019) that were slightly modified to yield strongly purified solutions for high-precision isotope measurements using a Thermo Fisher Neptune Plus MC-ICP-MS at Cologne. Uncertainties for averages of repeated analysis of sample solutions (95% confidence interval,  $n = 6-11$ ) range between  $\pm 1.4$  ppm and  $\pm 5.1$  ppm (average  $\pm 2.7$  ppm). Our long-term external reproducibility is inferred from repeated analyses of in-house rock reference materials, here also including a 3.27 Ga old Komatiite from the Pilbara Craton (sample 160245, Ruth Well Formation), Western Australia that displays an excess of  $^{182}\text{W}$ . All in-house rock reference materials were always passed through our separation protocol and measured in every session, yielding 2 SD between  $\pm 1.5$  ppm and  $\pm 2.7$  ppm (Fig. 3.8, method section). More information about the analytical protocol is provided in the method section.

### 3.4 Results

Our results for  $^{182}\text{W}$  isotope analysis are summarized in Table 3.1. Major and trace element compositions are provided in Table C1 (appendix C). Irrespective of petrology and provenance (AGC or BGGT), all rock types display  $^{182}\text{W}$  isotope compositions that



range from modern mantle values ( $\mu^{182}\text{W} = 0$ ) to deficits as low as  $-9.2 \pm 3.2$  ppm. Most of the mantle-derived rocks from the BGGT display moderate  $\mu^{182}\text{W}$  deficits, in some cases overlapping with the modern mantle value, whereas mantle-derived rocks from the AGC display  $\mu^{182}\text{W}$  deficits throughout, in most cases not overlapping with the modern mantle. The distribution and the range of isotope compositions for  $^{182}\text{W}$  in rocks from the Kaapvaal craton is similar to that for  $^{142}\text{Nd}$ , displaying both, negative and modern isotope composition (Schneider et al., 2018). However, combined  $^{182}\text{W}$ - $^{142}\text{Nd}$  data for rocks from the eastern Kaapvaal Craton, also including literature data from the Schapenburg Greenstone Remnant (SGR) adjacent to the BGGT (Puchtel et al., 2016a), only reveal a vague co-variation (Fig. C1, appendix C), even when only considering samples with pristine W concentrations (i.e., canonical W/Th ratios). Interestingly, our dataset reveals a co-variation of  $\mu^{182}\text{W}$  with initial  $\epsilon^{143}\text{Nd}_{(t)}$  and  $\epsilon^{176}\text{Hf}_{(t)}$  for mantle-derived rocks and some granitoid gneisses (Fig. 3.1). To our knowledge, this is the first discovery of a co-variation between  $^{182}\text{W}$  compositions and long-lived radiogenic nuclides. The observed co-variation for our samples is further strengthened by literature data for komatiites from the SGR adjacent to the BGGT (Puchtel et al., 2016a) and the Komati Formation from the BGB (Touboul et al., 2012; Puchtel et al., 2013). Interestingly, co-variations with  $^{182}\text{W}$  compositions are also observed for incompatible trace element ratios, in particular Zr/Sm (Fig. 3.7. method section).

### 3.5 Discussion

As the observed co-variations of  $\mu^{182}\text{W}$  with  $\epsilon^{143}\text{Nd}_{(t)}$  and  $\epsilon^{176}\text{Hf}_{(t)}$  are largely defined by ultramafic-mafic samples, it is obvious that the observed trend reflects mixing between different mantle-source reservoirs. It is in fact surprising that felsic samples plot on the same trend. This finding suggests short residence times between emplacement of the protolith and formation of felsic orthogneisses. One mantle endmember exhibits no resolvable  $^{182}\text{W}$  isotope anomalies at near chondritic initial  $\epsilon^{143}\text{Nd}_{(t)}$  and  $\epsilon^{176}\text{Hf}_{(t)}$  values, most likely representing near primitive mantle. The other endmember is best characterized by komatiites from the SGR that exhibit the largest  $^{182}\text{W}$  isotope deficits of up to  $-11.4$  ppm and strongly elevated initial  $\epsilon^{143}\text{Nd}_{(t)}$  and  $\epsilon^{176}\text{Hf}_{(t)}$  values of up to  $+2.6$  and  $+6.2$   $\epsilon$  units, respectively (Puchtel et al., 2016a). In the following discussion, we will largely focus on the origin of this low  $^{182}\text{W}$  endmember. As we will show, the

low  $^{182}\text{W}$  endmember in rocks from the Kaapvaal Craton may provide novel insights into the secular evolution of the  $^{182}\text{W}$  isotope composition of Earth's mantle.

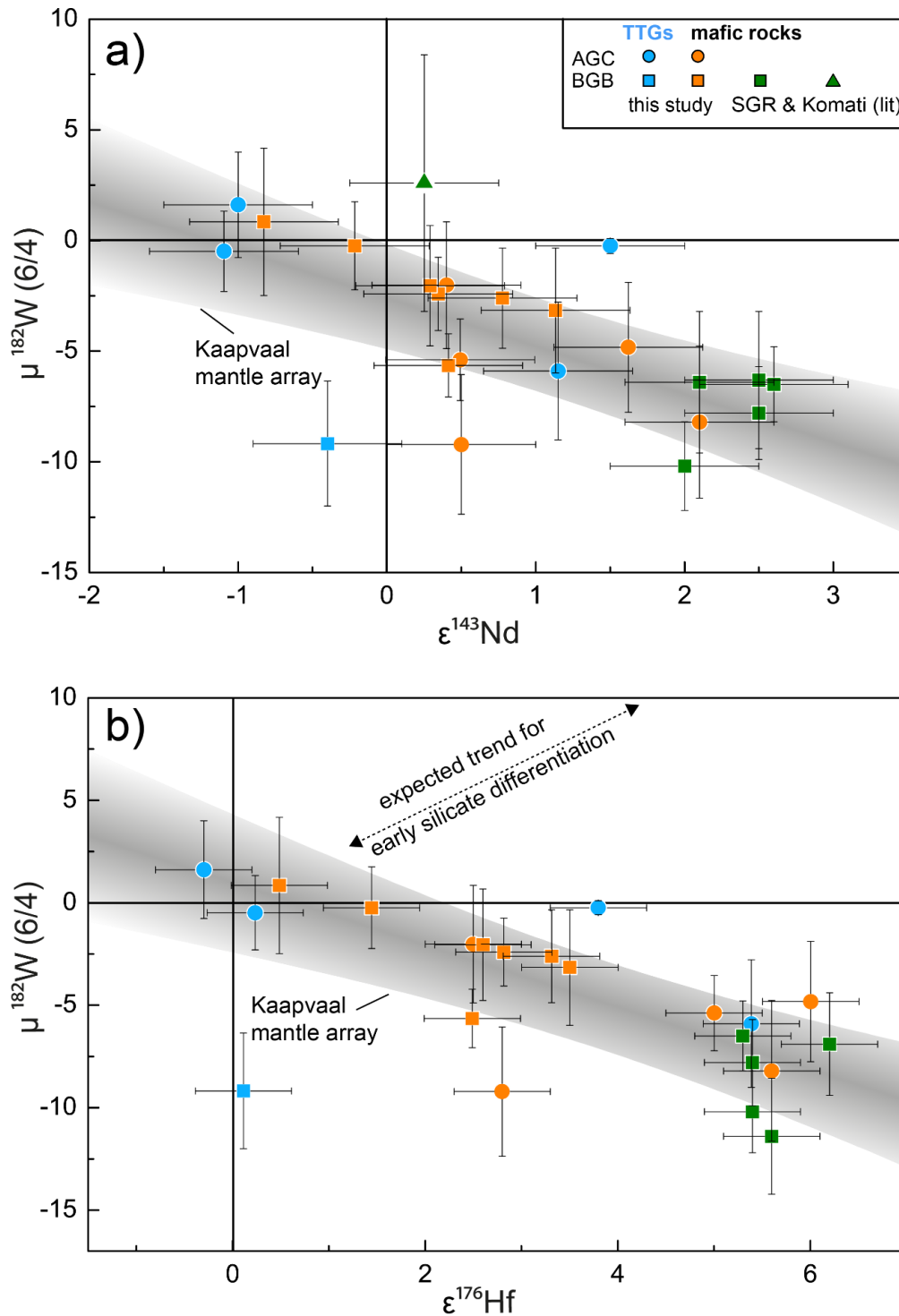


**Fig. 3.1: Measured  $\mu^{182}\text{W}$  vs.  $\epsilon^{143}\text{Nd}_{(t)}$  (a) and  $\mu^{182}\text{W}$  vs.  $\epsilon^{176}\text{Hf}_{(t)}$  (b) for mantle derived and TTG-like mafic rock samples from the Kaapvaal Craton including literature data.** The literature data include previously published data for komatiites from the Schapenburg Greenstone Remnant (SGR, Puchtel et al., 2016a) and the Komatii Formation (Touboul et al., 2012). The shaded field, referred to as Kaapvaal mantle array, is the 95% confidence interval in which all mantle derived samples are expected to fall. Note, that the anti-correlation displayed by the Kaapvaal mantle array does not follow the expected trend for early silicate differentiation (indicated by dashed line in panel 3.1b).

sample	Normalized to $^{186}\text{W}/^{184}\text{W} = 0.92767$		Normalized to $^{186}\text{W}/^{183}\text{W} = 1.9859$			N
	$\mu^{182}\text{W}$ ( $\pm$ 95% CI)	$\mu^{183}\text{W}$ ( $\pm$ 95% CI)	$\mu^{182}\text{W}$ ( $\pm$ 95% CI)	$\mu^{184}\text{W}$ ( $\pm$ 95% CI)	$\mu^{182}\text{W}_{\text{corr}}$ ( $\pm$ 95% CI)	
<b>Ancient Gneiss Complex</b>						
AGC 351	-0.2 $\pm$ 0.3	-0.1 $\pm$ 0.5	-0.5 $\pm$ 0.8	0.1 $\pm$ 0.3	-0.6 $\pm$ 0.5	20
AGC 352	-5.9 $\pm$ 3.1	17.5 $\pm$ 3.1	-28.6 $\pm$ 1.6	-11.6 $\pm$ 2.0	-5.8 $\pm$ 3.9	9
AGC 445	-0.4 $\pm$ 1.8	-5.2 $\pm$ 3.9	6.0 $\pm$ 3.8	3.5 $\pm$ 2.6	-0.8 $\pm$ 5.6	6
AGC 445 replicate	-0.6 $\pm$ 2.5	1.7 $\pm$ 3.1	-4.9 $\pm$ 3.1	-1.1 $\pm$ 2.0	-2.7 $\pm$ 4.0	10
AGC 473	1.6 $\pm$ 2.4	6.8 $\pm$ 5.6	-7.4 $\pm$ 4.9	-4.5 $\pm$ 0.0	1.5 $\pm$ 6.6	6
AGC 83	-8.2 $\pm$ 3.4	-1.8 $\pm$ 1.6	-4.6 $\pm$ 3.0	1.2 $\pm$ 5.3	-6.9 $\pm$ 3.0	8
AGC 86	-5.4 $\pm$ 1.8	0.0 $\pm$ 5.1	-5.9 $\pm$ 4.9	0.0 $\pm$ 4.0	-5.9 $\pm$ 2.4	11
AGC 38	-2.0 $\pm$ 2.9	-0.6 $\pm$ 2.2	-0.8 $\pm$ 2.1	0.4 $\pm$ 4.8	-1.6 $\pm$ 2.3	11
AGC 350	-9.2 $\pm$ 3.2	-1.1 $\pm$ 3.2	-8.2 $\pm$ 3.1	0.8 $\pm$ 4.0	-9.7 $\pm$ 3.2	11
AGC 222	-4.7 $\pm$ 5.1	-0.1 $\pm$ 1.6	-6.7 $\pm$ 4.2	0.1 $\pm$ 5.1	-6.9 $\pm$ 4.2	9
AGC 222 replicate	-5.0 $\pm$ 2.9	4.3 $\pm$ 1.9	-10.9 $\pm$ 1.9	-2.9 $\pm$ 5.0	-5.3 $\pm$ 2.3	11
<b>Barberton Greenstone Belt</b>						
BA 132	-9.2 $\pm$ 2.8	-5.6 $\pm$ 1.7	-1.1 $\pm$ 3.9	3.7 $\pm$ 1.2	-8.3 $\pm$ 3.9	11
KS-BA 189	-3.2 $\pm$ 2.8	0.5 $\pm$ 2.6	-3.2 $\pm$ 3.2	-0.3 $\pm$ 1.8	-2.6 $\pm$ 4.0	11
KS-BA 171	-2.4 $\pm$ 1.7	3.5 $\pm$ 2.7	-7.7 $\pm$ 1.8	-2.3 $\pm$ 1.8	-1.1 $\pm$ 2.9	9
KS-BA 181	0.8 $\pm$ 3.3	-0.1 $\pm$ 3.2	1.3 $\pm$ 2.6	0.0 $\pm$ 2.1	1.2 $\pm$ 4.8	10
KS-BA 182	-0.2 $\pm$ 2.0	2.3 $\pm$ 1.8	-1.1 $\pm$ 2.1	-1.5 $\pm$ 1.2	1.9 $\pm$ 1.9	10
ZA 32a	-2.0 $\pm$ 2.7	-0.9 $\pm$ 2.1	-2.3 $\pm$ 2.5	0.6 $\pm$ 1.4	-3.5 $\pm$ 3.0	10
ZA 31a	-5.6 $\pm$ 1.4	-1.5 $\pm$ 2.0	-3.2 $\pm$ 2.1	1.0 $\pm$ 1.3	-5.2 $\pm$ 2.2	11
ZA 38	-2.6 $\pm$ 2.3	4.5 $\pm$ 2.4	-10.3 $\pm$ 3.0	-3.0 $\pm$ 1.6	-4.4 $\pm$ 3.4	7
<b>In-house rocks standards</b>						
<b>La Palma Basalt</b>						
LP 1	1.2 $\pm$ 4.0	2.0 $\pm$ 4.4	-3.1 $\pm$ 4.3	-1.4 $\pm$ 2.9	-0.5 $\pm$ 4.6	14
LP 1	-0.5 $\pm$ 2.7	1.1 $\pm$ 4.3	-1.7 $\pm$ 5.9	-0.7 $\pm$ 2.8	-0.3 $\pm$ 5.8	9
LP 1	-0.1 $\pm$ 3.3	1.2 $\pm$ 4.2	-2.3 $\pm$ 3.0	-0.8 $\pm$ 2.8	-0.8 $\pm$ 3.8	9
LP 1	-1.4 $\pm$ 2.5	0.4 $\pm$ 2.3	-3.1 $\pm$ 3.0	-0.3 $\pm$ 1.5	-2.5 $\pm$ 2.5	9
LP 1	-1.3 $\pm$ 2.2	-0.1 $\pm$ 3.0	0.3 $\pm$ 4.1	0.1 $\pm$ 2.0	0.2 $\pm$ 3.1	6
LP 1	-2.0 $\pm$ 1.8	0.4 $\pm$ 2.1	-2.1 $\pm$ 2.7	-0.3 $\pm$ 1.4	-1.6 $\pm$ 3.0	7
LP 1	2.0 $\pm$ 2.0	0.8 $\pm$ 2.0	0.2 $\pm$ 4.8	-0.5 $\pm$ 1.3	1.3 $\pm$ 2.3	7
LP 1	0.2 $\pm$ 2.5	0.9 $\pm$ 3.7	-2.8 $\pm$ 2.5	-0.6 $\pm$ 2.5	-1.6 $\pm$ 3.7	8
LP 1	-1.8 $\pm$ 2.5	-0.7 $\pm$ 2.3	-0.9 $\pm$ 2.4	0.5 $\pm$ 1.5	-1.8 $\pm$ 1.6	10
<b>AGC Gneiss</b>						
AGC 351	-0.8 $\pm$ 3.6	0.6 $\pm$ 2.1	-0.4 $\pm$ 2.4	-0.4 $\pm$ 1.4	0.3 $\pm$ 3.8	11
AGC 351	1.4 $\pm$ 3.7	-2.8 $\pm$ 2.5	4.2 $\pm$ 2.3	1.8 $\pm$ 1.7	0.6 $\pm$ 3.4	13
AGC 351	-0.8 $\pm$ 2.1	0.8 $\pm$ 1.8	-1.4 $\pm$ 2.6	-0.5 $\pm$ 1.2	-0.3 $\pm$ 2.4	11
AGC 351	-0.7 $\pm$ 2.4	-0.2 $\pm$ 2.8	-0.4 $\pm$ 3.9	0.1 $\pm$ 1.9	-0.7 $\pm$ 4.1	8
AGC 351	-0.5 $\pm$ 2.3	0.1 $\pm$ 4.5	-1.8 $\pm$ 4.3	-0.1 $\pm$ 3.0	-1.6 $\pm$ 4.1	12
AGC 351	-0.3 $\pm$ 1.6	-0.8 $\pm$ 1.7	0.3 $\pm$ 1.9	0.5 $\pm$ 1.1	-0.8 $\pm$ 2.6	10
AGC 351	-0.1 $\pm$ 1.8	0.5 $\pm$ 1.7	-0.8 $\pm$ 2.5	-0.3 $\pm$ 1.1	-0.2 $\pm$ 1.9	9
AGC 351	-1.6 $\pm$ 2.1	-0.6 $\pm$ 2.2	-1.4 $\pm$ 1.9	0.4 $\pm$ 1.5	-2.2 $\pm$ 2.3	20
AGC 351	0.6 $\pm$ 2.4	-0.3 $\pm$ 2.4	1.5 $\pm$ 2.0	0.2 $\pm$ 1.6	1.2 $\pm$ 3.3	11
AGC 351	0.5 $\pm$ 1.8	0.9 $\pm$ 5.0	-1.6 $\pm$ 5.7	-0.6 $\pm$ 3.3	-0.4 $\pm$ 4.0	7
AGC 351	0.2 $\pm$ 2.3	-0.3 $\pm$ 1.9	0.7 $\pm$ 3.2	0.2 $\pm$ 1.3	0.2 $\pm$ 2.3	18
AGC 351	-1.3 $\pm$ 3.2	0.8 $\pm$ 1.9	-2.8 $\pm$ 1.2	-0.5 $\pm$ 1.3	-1.8 $\pm$ 2.4	12
AGC 351	0.2 $\pm$ 2.5	1.3 $\pm$ 2.7	-1.3 $\pm$ 2.5	-0.9 $\pm$ 1.8	0.4 $\pm$ 3.8	13
AGC 351	0.1 $\pm$ 2.7	0.1 $\pm$ 2.9	-0.7 $\pm$ 4.0	-0.1 $\pm$ 1.9	-0.6 $\pm$ 2.8	9
AGC 351	-0.4 $\pm$ 3.9	-2.1 $\pm$ 2.5	1.7 $\pm$ 3.3	1.4 $\pm$ 1.7	-1.0 $\pm$ 3.9	9
AGC 351	-0.6 $\pm$ 2.0	-0.2 $\pm$ 1.8	-1.7 $\pm$ 2.0	0.2 $\pm$ 1.2	-2.0 $\pm$ 2.4	19
AGC 351	-0.3 $\pm$ 3.1	-1.0 $\pm$ 3.9	-1.1 $\pm$ 6.9	0.6 $\pm$ 2.6	-2.2 $\pm$ 4.1	12
AGC 351	0.8 $\pm$ 1.7	1.0 $\pm$ 2.4	-1.4 $\pm$ 3.1	-0.7 $\pm$ 1.6	-0.1 $\pm$ 2.6	13
AGC 351	-0.9 $\pm$ 1.9	-1.7 $\pm$ 3.0	1.5 $\pm$ 5.2	1.1 $\pm$ 2.0	-0.8 $\pm$ 3.5	7
AGC 351	-0.4 $\pm$ 2.8	1.3 $\pm$ 1.9	-2.2 $\pm$ 2.3	-0.8 $\pm$ 1.2	-0.6 $\pm$ 2.7	11
<b>West Pilbara Komatiite</b>						
160245	5.6 $\pm$ 1.9	-3.7 $\pm$ 3.2	9.9 $\pm$ 4.4	2.5 $\pm$ 2.1	5.0 $\pm$ 1.6	9
160245	5.6 $\pm$ 3.2	-0.4 $\pm$ 2.1	6.9 $\pm$ 2.3	0.3 $\pm$ 1.4	6.4 $\pm$ 2.9	12
160245	7.3 $\pm$ 2.3	-1.1 $\pm$ 1.4	8.4 $\pm$ 1.9	0.8 $\pm$ 0.9	6.9 $\pm$ 2.6	10
160245	8.8 $\pm$ 3.0	-0.1 $\pm$ 2.7	6.6 $\pm$ 2.4	0.0 $\pm$ 1.8	6.5 $\pm$ 2.7	11
160245	9.1 $\pm$ 1.4	-0.7 $\pm$ 1.3	8.5 $\pm$ 2.1	0.4 $\pm$ 0.8	7.7 $\pm$ 1.8	11
160245	6.4 $\pm$ 2.8	-1.1 $\pm$ 3.4	8.3 $\pm$ 2.8	0.7 $\pm$ 2.2	6.9 $\pm$ 3.0	10
160245	7.1 $\pm$ 3.2	-3.8 $\pm$ 2.3	12.1 $\pm$ 2.6	2.5 $\pm$ 1.5	7.1 $\pm$ 2.9	13
160245	8.5 $\pm$ 3.4	1.0 $\pm$ 1.7	7.1 $\pm$ 1.7	-0.6 $\pm$ 1.2	8.4 $\pm$ 2.4	13
160245	8.8 $\pm$ 3.6	0.3 $\pm$ 3.1	9.0 $\pm$ 2.0	-0.2 $\pm$ 2.1	9.4 $\pm$ 4.3	11
160245	8.6 $\pm$ 5.4	-0.6 $\pm$ 2.7	12.2 $\pm$ 3.1	0.4 $\pm$ 1.8	11.4 $\pm$ 4.3	11
160245	9.6 $\pm$ 4.6	-1.4 $\pm$ 4.3	11.6 $\pm$ 3.9	0.9 $\pm$ 2.8	9.8 $\pm$ 5.0	10
160245	8.5 $\pm$ 2.3	1.2 $\pm$ 1.5	7.7 $\pm$ 1.7	-0.8 $\pm$ 1.0	9.2 $\pm$ 1.6	10
160245	7.5 $\pm$ 2.1	-0.9 $\pm$ 1.9	8.7 $\pm$ 2.7	0.6 $\pm$ 1.3	7.5 $\pm$ 1.9	11
160245	8.4 $\pm$ 3.0	-2.2 $\pm$ 3.0	10.1 $\pm$ 2.2	1.5 $\pm$ 2.0	7.3 $\pm$ 3.3	13
160245	8.8 $\pm$ 3.5	-4.6 $\pm$ 1.6	12.3 $\pm$ 2.9	3.1 $\pm$ 1.1	6.3 $\pm$ 2.1	10

**Table 3.1: Tungsten isotope composition of Kaapvaal samples and in-house rock reference materials.** Values for  $\mu^{182}\text{W}_{\text{corr}}$  were corrected for the nuclear field shift (NFS) effect on  $^{183}\text{W}$ , when normalized to  $^{186}\text{W}/^{183}\text{W}$  (6/3), using the measured  $\mu^{184}\text{W}$  (6/3) and  $\mu^{182}\text{W}$  (6/3) values and the relation  $\mu^{182}\text{W}$  (6/3) $_{\text{corr}} = \mu^{182}\text{W}$  (6/3) $_{\text{measured}} - (1.962 \times \mu^{184}\text{W}$  (6/3)) (Cook and Schönbächler, 2016).

In particular, we evaluate, if present-day mantle plumes with their characteristic  $^{182}\text{W}$  deficit may be modern analogues of the low  $^{182}\text{W}$  endmember from the Kaapvaal Craton.

The presence of negative  $^{182}\text{W}$  isotope anomalies within rocks from the Kaapvaal Craton could be the consequence of several processes. These processes include (1) equilibration of the mantle source with anomalously large amounts of late accretionary material (late accretion hypothesis), (2) early fractionation of Hf from W by silicate crystal-liquid fractionation, e.g., in an early magma ocean, or (3) core-mantle interaction.

The late accretion hypothesis has been postulated to explain the relative and absolute abundances of highly siderophile elements (HSE) in the bulk silicate earth (BSE) by the addition of about 0.5% of chondritic material after core formation (Chou, 1978; Mann et al., 2012), likely with CI or CM like composition (Wang and Becker, 2013; Braukmüller et al., 2019). Late accretion would not only have affected the HSE budget of the BSE but also its  $^{182}\text{W}$  isotope composition (Willbold et al., 2011). Accordingly, even after the addition of the late veneer, some portions of the Archean mantle could have remained in disequilibrium (Marchi et al., 2018), and mantle domains that did not fully equilibrate with late accretionary components, would be characterized by positive  $^{182}\text{W}$  isotope anomalies coupled with HSE abundances that are lower than the modern BSE. Consequently, negative  $^{182}\text{W}$  isotope anomalies would imply additional late accreted contributions that would be reflected in unusually high HSE contents. The absolute HSE abundances in the mantle source of the SGR-like endmember with its large  $^{182}\text{W}$  deficits, however, were estimated to be only ca. 30% of those in the present-day BSE (Puchtel et al., 2009; Puchtel et al., 2016a), and, accordingly, a late accretion model can therefore be ruled out. If  $^{182}\text{W}$  isotope systematics were coupled to the HSE systematics by late accretion one would expect  $^{182}\text{W}$  isotope excesses and not deficits. Direct addition of core material to the source of the SGR komatiites also seems an unlikely explanation, as this would likely result in elevated PGE concentrations (Brandon and Walker, 2005). Again, the low absolute HSE abundances in the source of the SGR-like endmember rule out such a scenario and may be better explained by second-stage melting of an already sulfide exhausted mantle source (Puchtel et al., 2009).

An alternative explanation for negative  $^{182}\text{W}$  isotope anomalies in Archean rocks like those from the Kaapvaal craton may be offered by insights from recent studies on OIBs. It has been proposed that the prevalent negative  $^{182}\text{W}$  isotope anomalies in modern, plume-derived OIBs result from chemical and isotopic equilibration between their mantle sources and the outer core (Mundl-Petermeier et al., 2019; Mundl-Petermeier et al., 2020). Notably, it has been argued that Archean mafic-ultramafic sequences like those in the BGB also originate from mantle plumes (Robin-Popieul et al., 2012). Additional work from noble gas systematics in modern mantle-derived rocks provide evidence that the source reservoirs must have had differentiated from the convecting mantle very early (pre 4.45 Ga) (Allègre et al., 1987; Parai et al., 2012; Tucker and Mukhopadhyay, 2014). The concurrent  $^{182}\text{W}$  isotope anomalies in the modern mantle could therefore also have been produced early by in-situ decay of  $^{182}\text{Hf}$  (i.e., during the first ca. 60 Ma after solar system formation). The presence of such ancient mantle reservoirs and the role of mantle plumes in the past, in particular their contribution to the secular evolution of the  $^{182}\text{W}$  isotope composition in the BSE has so far only poorly been constrained. In this regard, mantle derived rocks from the Kaapvaal Craton offer the possibility to combine insights from isotope constraints on the origin and preservation of ancient mantle heterogeneities through deep time.

It has been postulated that Hadean protocrust or delaminated restites of early differentiated Hadean protocrust are responsible for the geochemical and isotopic variability of modern mantle plumes (Hofmann, 1997). In the case of the Kaapvaal craton, direct recycling of ancient protocrust formed during the first ca. 60 Ma appears unlikely, because in this case the negative  $^{182}\text{W}$  and  $^{142}\text{Nd}$  anomalies should be coupled with negative  $^{143}\text{Nd}$  and  $^{176}\text{Hf}$  anomalies. In this regard, the coupled depletions of  $^{182}\text{W}$  and  $^{142}\text{Nd}$  led a previous study (Puchtel et al., 2016a) to conclude that the komatiites from the SGR derived from a mantle domain that was enriched very early (ca. 30 Ma after solar system formation) in highly incompatible elements as a result of silicate crystal-liquid fractionation in an early magma ocean. Such an early enrichment in highly incompatible trace elements, however, should have resulted in negative initial  $\epsilon^{143}\text{Nd}_{(t)}$  and  $\epsilon^{176}\text{Hf}_{(t)}$  values in the parental source regions of the SGR komatiites, which is not observed (Puchtel et al., 2016a). Puchtel et al. (2016a) therefore suggested that this parental source must have experienced subsequent melt depletion, after  $^{182}\text{Hf}$  went extinct, to account for the observed radiogenic initial  $^{143}\text{Nd}$  and  $^{176}\text{Hf}$  in SGR

komatiites. However, this model cannot easily account for the trace element patterns of the SGR komatiites, as these are not depleted and relatively flat.

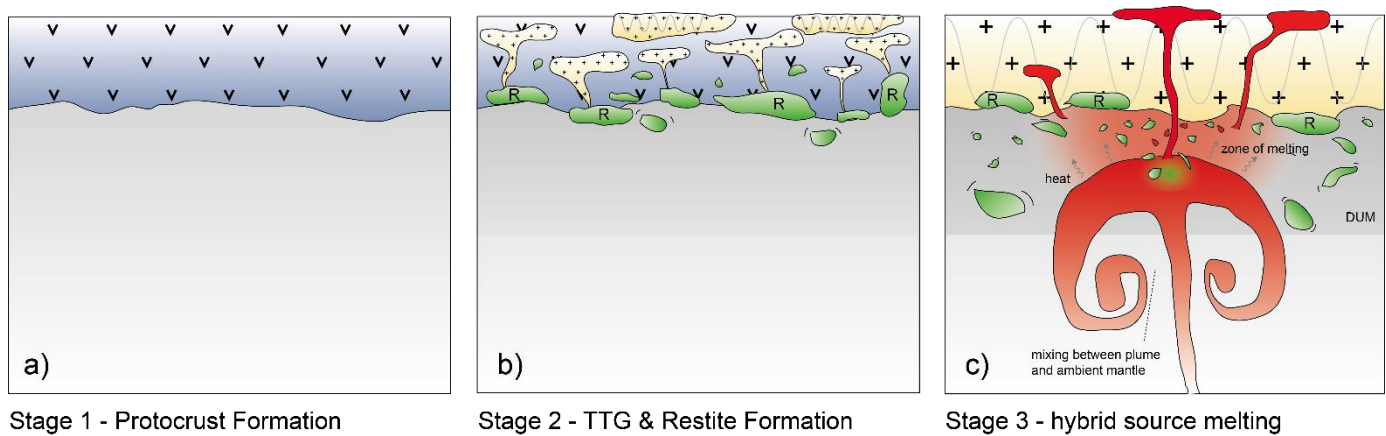


**Fig. 3.2: Preferred geodynamic model for the origin of crustal and mantle-derived rocks from the Kaapvaal Craton. (a)** Formation of a mafic protocrust by ca. 50 Ma after solar system formation. **(b)** Formation of TTG-like batoliths (orange) and residual garnet – rich restites (green, labelled „R“) after partial protocrustal anatexis between ca. 4.35 and 4.25 Ga. **(c)** Recycling of lower crustal restites and plume initiated volcanism lead to melting of hybrid sources that involved delaminated restites, depleted ambient upper mantle and primitive mantle supplied by the ascending plume. Shades of grey visualize depleted upper mantle (DUM) and lower mantle (light grey).

Based on the considerations above, a two-stage process is clearly required where the negative  $^{182}\text{W}$  and  $^{142}\text{Nd}$  anomalies formed early and the radiogenic  $^{143}\text{Nd}$  and  $^{176}\text{Hf}$  compositions were established after the short-lived systems went extinct. Our preferred geodynamic model is illustrated in Fig. 3.2 and a detailed description is given in the method section. Our model is inspired by pioneering studies on the formation mechanisms of early continental crust (Zegers, 2001; Bédard, 2006), where after formation of mafic protocrust (Fig. 3.2a) intra-crustal fractionation lead to the formation of a felsic, TTG-like crust and mafic lower crustal restites that are recycled into the upper mantle (Fig. 3.2b). This process can account for hybrid mantle reservoirs, where ambient upper mantle mixes with lower crustal restites (Fig. 3.2c). Melting of such hybrid reservoirs might be triggered by ascending plume-like material from the lower mantle that might also account for the compositional trend observed for mafic rocks from the Kaapvaal Craton. In this scenario, the lower mantle endmember is characterized by the Barberton komatiites and the hybrid upper mantle endmember is characterized by the SGR komatiites. Hence, such mixing relationships are a plausible explanation for the anti-correlation between the short- and long-lived radiogenic

systems. Moreover, our model can also explain the incompatible trace element systematics in our samples and the SGR komatiites (see method section).

The model described above can also explain the somewhat obscured  $^{142}\text{Nd}$  patterns of the Kaapvaal craton samples. Following constraints from phase equilibrium and trace element modeling, melting of Archean TTG suites from mafic protocrust leaves behind residual assemblages of amphibolitic, garnet-amphibolitic or eclogitic composition (Zhang et al., 2013). Figure 3.3a illustrates that during a first stage mafic protocrust that formed 50 Ma after solar system formation developed strongly unradiogenic isotope compositions, in particular for the short-lived decay products  $^{182}\text{W}$  and  $^{142}\text{Nd}$ . Subsequent TTG melting (stage 2 in Fig 3.3a) leaves behind garnet-rich restites (Zhang et al., 2013), and depending on the timing of this second event, the residual restites will develop towards markedly different  $^{142}\text{Nd}$  isotope compositions with time. In contrast, the  $^{182}\text{W}$  isotope composition will be insensitive to the timing of TTG extraction, because  $^{182}\text{Hf}$  went extinct shortly after formation of the protocrust. Evidence for the presence of such ancient TTG precursors in the Kaapvaal Craton comes from Hf-in-zircon isotope data (Compston and Kröner, 1988; Zeh et al., 2011; Kröner et al., 2014) that suggest formation of a first felsic protocrust already by the Eoarchean or late Hadean. Due to the longer half-lives of their parent nuclides,  $^{143}\text{Nd}$  and  $^{176}\text{Hf}$  isotope compositions in the restites integrate a larger time span and develop much more homogenous with time than that of  $^{142}\text{Nd}$ , which can only be formed over a smaller time interval until  $^{146}\text{Sm}$  becomes extinct. These considerations explain, why  $^{142}\text{Nd}$  signatures could become quite variable, depending on the time of TTG extraction, unlike long-lived Hf-Nd compositions which would develop towards slightly radiogenic values over time.

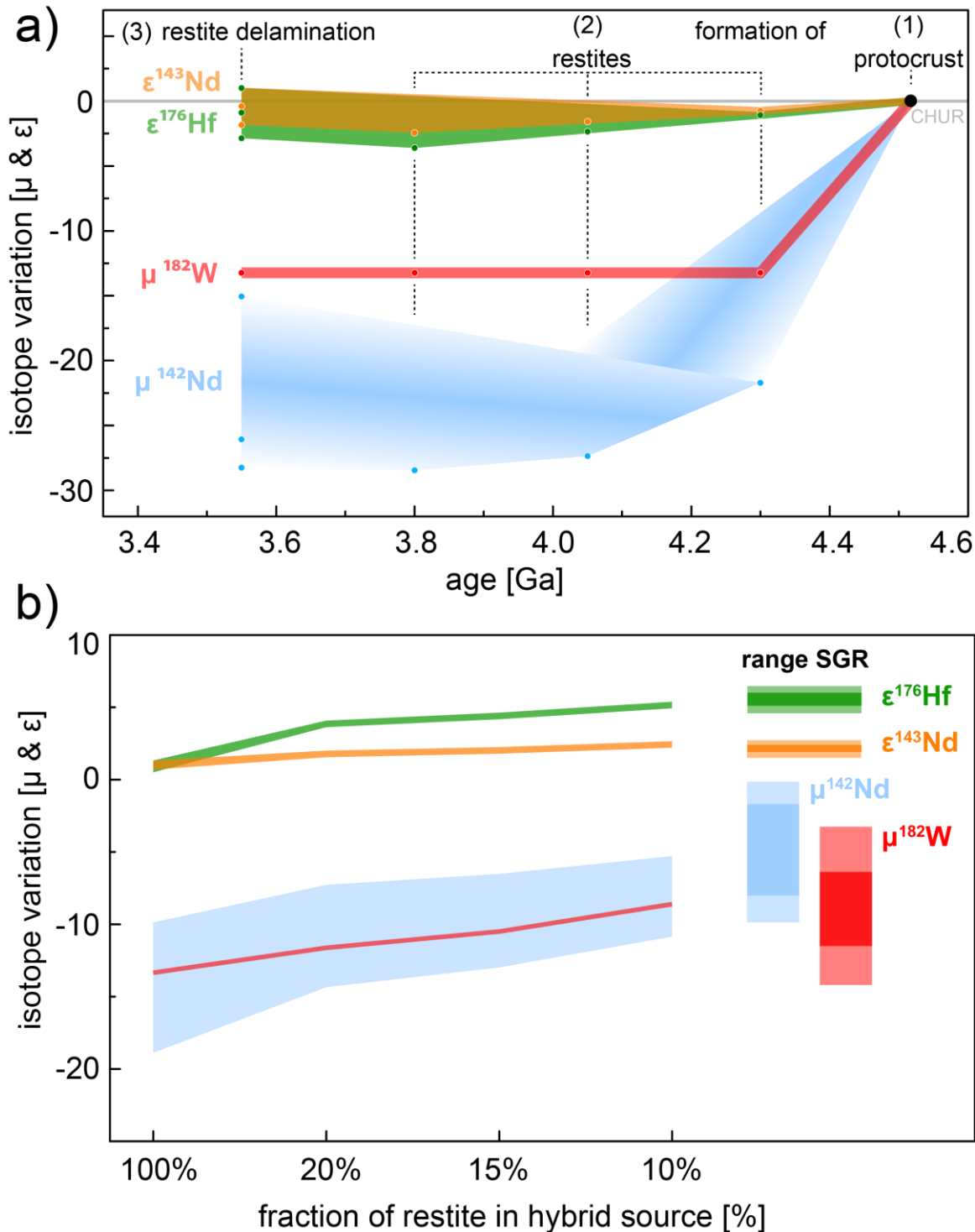


**Fig. 3.3: Isotope evolution graphs for the proposed geodynamic model, involving mantle recycling of lower crustal restites.** (a) During stage (1), mafic protocrust formed ca. 50 Ma after solar system formation developed strongly unradiogenic isotope compositions, in particular for  $^{182}\text{W}$  and  $^{142}\text{Nd}$ . Stage (2) is set by restite formation during TTG extraction from mafic protocrust. The dashed lines illustrate how prolonged TTG extraction (between 4.3 and 3.8 Ga) affects the isotope compositions of residual restites. Accordingly, the restites develop to markedly variable  $^{142}\text{Nd}$  isotope composition with time. In contrast,  $^{182}\text{W}$  is insensitive to the timing of TTG extraction, because  $^{182}\text{Hf}$  went extinct shortly after formation of the mafic protocrust. Due to the longer half lives and enriched composition of the parental source the variation for the long-lived radionuclides will be negligible. (b) Mixing calculations between delaminated restites and ambient depleted mantle, both forming a hybrid source. Ca. 10-20% of admixed restite to a ambient depleted mantle reproduces the isotope compositions found in the SGR endmember. This hybrid source mixed with primitive material supplied by the mantle plume which is reflected in the *Kaapvaal mantle array* for  $^{182}\text{W}$  and long-lived radiogenic nuclides (see Fig. 3.1).



It becomes apparent from Fig. 3.3a that lower crustal restites from ancient protocrust in the sources of the SGR komatiites can explain why the  $^{143}\text{Nd}$  and  $^{176}\text{Hf}$  isotope compositions are so tightly correlated with  $^{182}\text{W}$  but not with  $^{142}\text{Nd}$ . Recycling into the upper mantle (stage 3) formed a hybrid source that is best approximated by the source of Schapenburg komatiites, which formed through high-degree melting. We found that 10-20% of admixed restite to an ambient depleted upper mantle already reproduces the radiogenic isotope compositions found in the SGR endmember (Fig. 3.3b). Once this hybrid upper mantle source is mixed with primitive material supplied by ascending mantle plumes, it can account for the entire compositional spectrum and for the negative correlations between  $^{182}\text{W}$  and the long-lived radiogenic isotopes (Fig. 3.1). Our proposed model can also reproduce the incompatible trace element compositions and reconcile distinct trace element systematics that are diagnostic for the SGR komatiites. As shown in Fig. 3.6 (method section) our modelling results are in good agreement with the SGR komatiites originating from 20-30% batch melting of a hybrid source that consists of ambient depleted mantle and 10-20% lower crustal restites. Moreover, our model can reproduce distinctive Zr/Sm ratios prominent within SGR komatiites and its correlation with  $^{182}\text{W}$  isotope compositions (Fig. 3.7, method section). However, we attribute the highly variable absolute trace element abundances of the SGR komatiite suite to olivine accumulation, as indicated by co-variations between MgO content and incompatible trace element concentrations (not shown). The hybrid source model can also explain the Re-Os isotope data for the SGR komatiites (Puchtel et al., 2009). As shown in the method section the positive initial  $\gamma^{187}\text{Os}$  of the SGR komatiites ( $\gamma^{187}\text{Os} = +3.7 \pm 0.3$ , Puchtel et al., 2009) is in accord with the addition of 10-20 % of garnet-rich restites from Hadean protocrust to a depleted mantle source that was previously exhausted in sulfides.

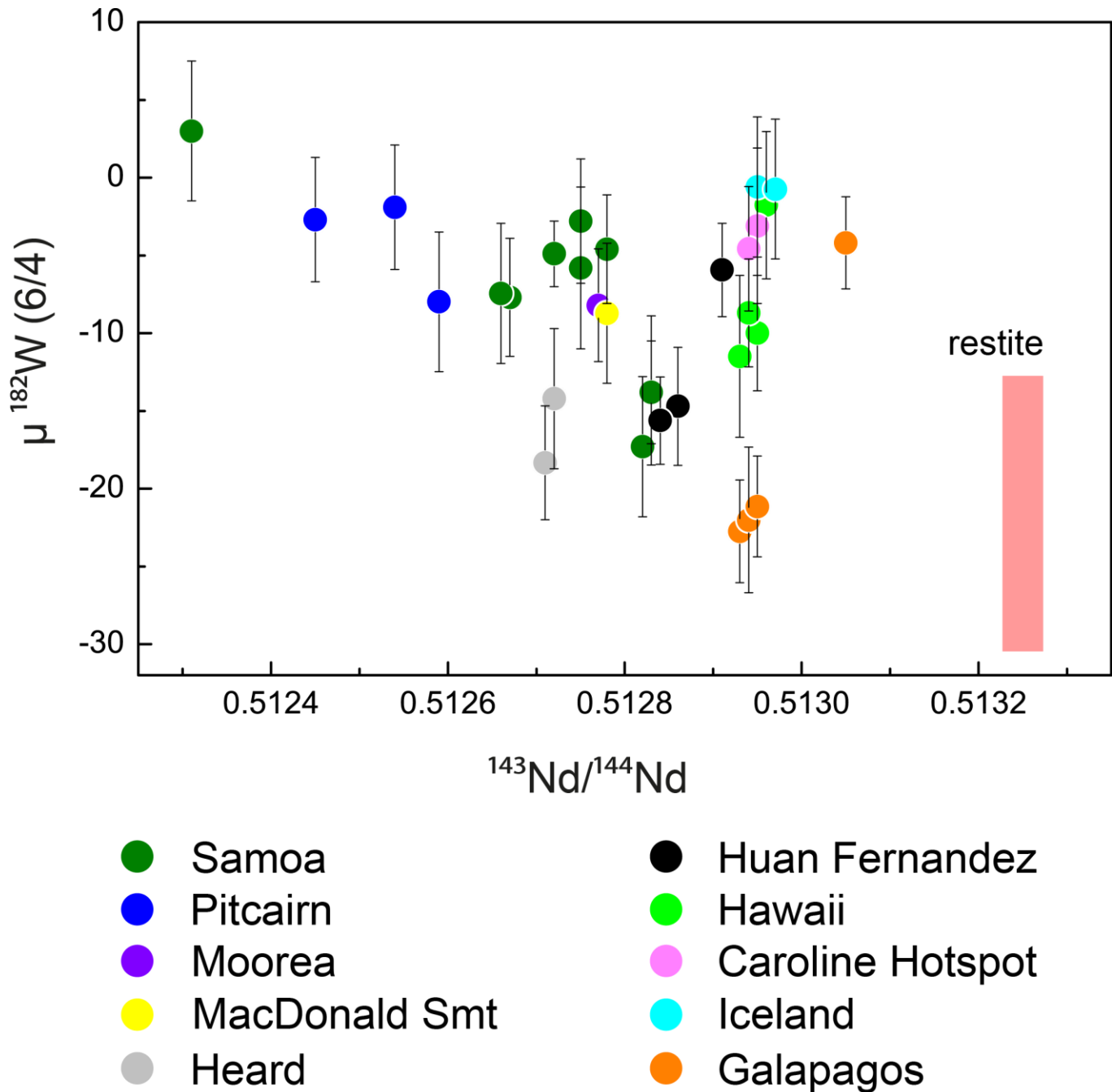


**Fig. 3.4: Compilation of combined  $^{182}\text{W}$  and  $^{143}\text{Nd}$  isotope data available for modern OIBs.** Data were compiled from Mundl-Petermeier et al. (2020) and references therein. Notably, the global compilation for modern OIBs displays a similar trend than the Archean mantle-derived rock assemblage from the Kaapvaal Craton. Also shown is the present  $^{182}\text{W}$  and  $^{143}\text{Nd}$  isotope composition calculated for Hadean restites that remained isolated in the mantle (red pale field). A similar OIB compilation for  $^{182}\text{W}$  and  $^{176}\text{Hf}$  is limited by the availability of  $^{176}\text{Hf}$  isotope data but shown for comparison in Fig. C2 (appendix C).

## 3.6 Conclusions

Our proposed lower crustal restite model for the Kaapvaal craton also provides an intriguing explanation of  $^{182}\text{W}$  isotope variations in modern OIBs. Interestingly, a global compilation of combined  $\mu^{182}\text{W}$  vs.  $^{143}\text{Nd}/^{144}\text{Nd}$  data for modern OIBs (Mundl-Petermeier et al. (2020) and references therein) displays a similar trend in  $\mu^{182}\text{W}$  vs.  $^{143}\text{Nd}/^{144}\text{Nd}$  space than the Archean mantle-derived rock assemblage from the Kaapvaal Craton (Fig. 3.4). Remarkably, lower crustal restites, formed between 4.35 and 4.25 Ga after partial melting of a mafic protocrust that formed between 40-50 Ma after solar system formation, constitute a viable endmember in the global OIB array (Fig. 3.4). We therefore speculate, that lower crustal restites from Hadean protocrust were delaminated and ultimately recycled into the lower mantle where they might be part of large low shear-wave velocity provinces (LLSVPs) in the present day mantle that were interpreted to contribute to rising mantle plumes (Burke et al., 2008). Indeed, geophysical studies demonstrated that LLSVPs represent mixtures of recycled dense material that accumulated at the core mantle boundary (Jones et al., 2019; Jones et al., 2020). In this regard, our model provides an alternative explanation for the origin of negative  $^{182}\text{W}$  isotope anomalies in modern OIBs and bridges  $^{182}\text{W}$  isotope systematics in Archean mantle derived rocks with observations from modern-day mantle plumes.

Our discovery of long-term preservation of Hadean protocrust in Earth's mantle has far-reaching implications as this requires silicate reservoirs on Earth to have already differentiated during the lifetime of  $^{182}\text{Hf}$  (Touboul et al., 2012). Hence, this finding is in support of previous studies (Barboni et al., 2017; Thiemens et al., 2019) that argued the Earth-Moon system to have formed within the first ~60 Ma of our solar system, much earlier than previously thought.

## 3.7 Method section

### 3.7.1 Geological background of our sample selection

We analyzed a comprehensive set of rocks from the Kaapvaal craton that range from different types of grey orthogneisses (TTGs and more evolved granitoids) to mantle-derived lithologies of mafic-ultramafic composition. This representative suite of 17 samples span an age range from 3.55 to 3.22 Ga and represent the main lithological

units of the Ancient Gneiss Complex (AGC), also comprising the oldest mafic rocks (lower Onverwacht Group, 3.55 to 3.45 Ga) of the Barberton Granite-Greenstone Terrane (BGGT).

The AGC is located in Swaziland and is a typical high-grade gneiss terrain that comprises 3.66-3.20 Ga old rocks (Hoffmann and Kröner, 2019). The oldest part of the AGC are polydeformed granitoid gneisses, heterogeneous in age and composition (Kröner et al., 1989; Kröner et al., 2014), that are interbanded with amphibolites. Together, they formed layered grey gneiss sequences in response to ductile deformation under high strain conditions (Hoffmann and Kröner, 2019). The different varieties of rocks from this sequence have been summarized as the Ngwane Gneiss (NG) (Wilson, 1982). The oldest generation of NG (NG *sensu stricto*) are 3.66 Ga to 3.5 Ga granitoid gneisses (Compston and Kröner, 1988; Kröner et al., 1989; Schoene et al., 2008; Zeh et al., 2011; Kröner et al., 2014) that mainly belong to the tonalite-trondhjemite-granodiorite (TTG) suite but also comprise granitic rocks. As indicated by trace element systematics (Compston and Kröner, 1988), whole rock Nd isotope systematics (Kröner et al., 1993) and Hf-in-zircon isotope data (Compston and Kröner, 1988; Zeh et al., 2011; Kröner et al., 2014) the protoliths of the orthogneisses resulted, at least in part, from melting of a LREE enriched source with considerable residence time, most likely older continental crust of Eoarchean to late Hadean age. Younger generations of grey gneisses, which are mapped as NG, were emplaced after 3.45 Ga. These show the same field appearance as the 3.66-3.45 Ga NG but are as young as 3.2 Ga (Kröner et al., 1993; Kröner, 2007). The oldest NG hosts scattered remnants of supracrustal assemblages with greenstone belts (e.g. Dwalile Supracrustal Suite, DSS (Jackson, 1984)). These remnants postdate the oldest NG, vary in size and are either infolded, occur as tectonically intercalated xenoliths of a few centimeters or even represent coherent blocks of several kilometers (Jackson, 1984; Kröner and Tegtmeier, 1994). The origin of these remnants remains contentious. They were interpreted either as strongly flattened dikes (Hunter et al., 1984; Jackson, 1984) or as dismembered portions of the Dwalile Greenstone Remnant (DGR), which represents the largest of the greenstone remnants of the AGC (Kröner and Tegtmeier, 1994; Kröner et al., 2014; Hoffmann and Kröner, 2019; Kröner et al., 2019). The DGR is located in SW Swaziland and the supracrustal rock assemblage (metavolcanics, metasediments) were shown to be extruded between 3.44 and 3.46 Ga, therefore postdating the oldest generation of NG (Kröner and Tegtmeier, 1994; van Schijndel et

al., 2017; Hoffmann et al., 2020). Interestingly, the metavolcanic rocks from the DGR share geochemical similarities with volcanic assemblages from the Onverwacht Group which hints at a genetic link between the DGR and the BGB (Hunter et al., 1984; Kröner and Tegtmeyer, 1994; Hoffmann et al., 2020). Based on trace element systematics and variable whole-rock initial  $\epsilon\text{Nd}$  and  $\epsilon\text{Hf}$  values it has been argued that the mafic and ultramafic DGR rocks were derived from a mildly depleted mantle source and were in part contaminated by rocks from an ancient continental source, presumably crustal material of NG-like composition (Kröner and Tegtmeyer, 1994; Hoffmann et al., 2020). The oldest NG and intercalated members of the DSS were intruded by the texturally and compositionally distinct Tsawela Gneiss between 3.48-3.43 Ga (Jackson, 1984; Kröner, 2007; Zeh et al., 2011; Mukasa et al., 2013; Hoffmann et al., 2016) and younger generations of grey gneisses that date back to ca. 3.2 Ga (Kröner, 2007).

All sample localities are shown in Fig. 3.5. We have analyzed two grey gneisses from the >3.45 Ga NG suite that were collected along the Mtimane River in the Mankayane area in central Swaziland, where granitoid gneisses of different ages were variably affected by intensive regional migmatization at ca. 3.2 Ga (Kröner and Tegtmeyer, 1994; Kröner et al., 2018; Moyen et al., 2018). Both samples (AGC 351 and AGC 352) were previously described (Kröner et al., 2014; Hoffmann et al., 2016). AGC 351 is a 3.455 Ga old, strongly migmatized grey gneiss of near granitic composition and interpreted to be derived from felsic crustal precursors that mixed with juvenile, depleted-mantle derived melts (Kröner et al., 2014; Kröner et al., 2018). AGC 352 is a 3.442 Ga very homogeneous fine grained grey gneiss (Hoffmann et al., 2016).

We have analyzed several samples from greenstone remnants that are interlayered with grey gneisses of the AGC. We investigated two komatiites and one amphibolite from the DGR (AGC 83, AGC 86 and AGC 38), one typical amphibolite fragment as found in the AGC (AGC 222) and a 3.455 Ga gabbroic enclave (AGC 350) from central Swaziland. The mafic-ultramafic rock samples from the DGR were previously characterized (Kröner and Tegtmeyer, 1994; Hoffmann et al., 2020). Sample AGC 222 is a fragmented amphibolite enclave from Kubuta in central Swaziland with a minimum age of 3.4 Ga (Suhr et al., 2014). It is similar in composition to other greenstone remnants found in the AGC (Kröner et al., 2014; Hoffmann et al., 2016). Gabbroic enclaves like AGC 350 can be found along the Mtimane River in the Mankayane area close to the sample localities of AGC 351 and AGC 352. As described by Kröner et al.

(2018) the precursors of the gabbroic enclaves were emplaced together with granitoid gneisses at 3.455 Ga. At about 3.2 Ga, a tectono-magmatic-metamorphic event reworked the grey gneisses and greenstones (Moyen et al., 2018) which led to boudinage and local anatexis of the gabbros and migmatization of the grey gneisses (e.g. sample locality of AGC 351).

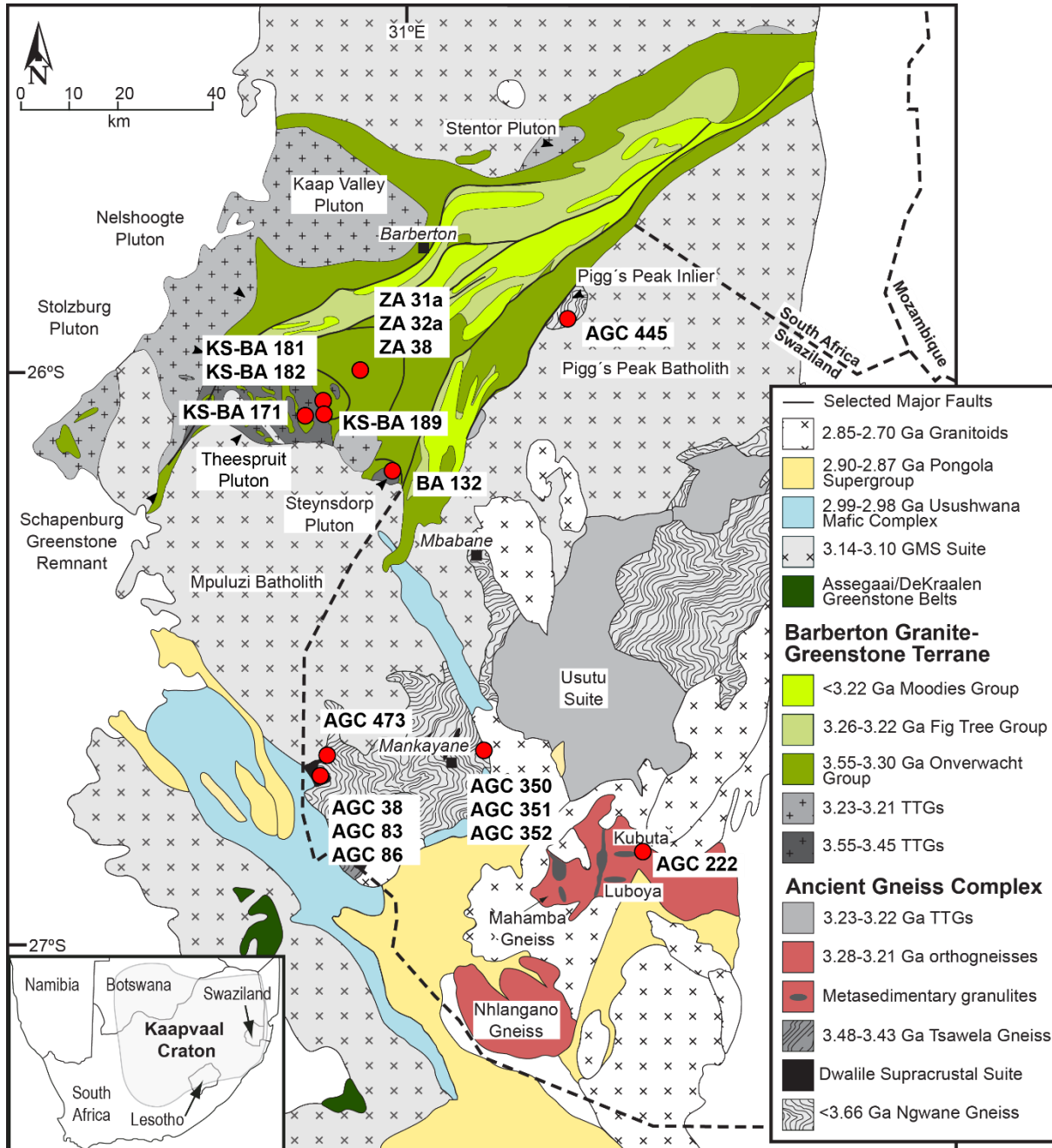


**Fig. 3.5: Simplified geological map of the Kaapvaal Craton, Southern Africa, showing the sample localities covered in this study.** The map is taken from Schneider et al. (2018) and modified after van Schijndel et al. (2017).

The youngest samples from the AGC are two ca. 3.2 Ga gneisses. Sample AGC 473 is a 3.24 Ga grey gneiss of trondhjemitic composition, which intruded into the oldest generation of NG northwest of the DGR. Based on structural considerations, the adjacent NG were interpreted as basement for the volcanic sequences of the DGR (Jackson, 1984). Our younger grey gneiss sample AGC 473 belongs to the youngest generation of NG but contains inherited zircon grains of 3.49 Ga and ca. 3.64 Ga (Schneider et al., 2018). This young generation of grey gneisses belongs to a 3.2 Ga magmatic event that is typically associated with indicators for strong deformation and high-grade metamorphism and therefore suggested to be the result of migmatization and crustal melting of older generations of crustal rocks (Kröner et al., 2018; Kröner et al., 2019). Sample AGC 445 is a 3.216 Ga old grey gneiss from the Pigg's Peak area also belonging to the former 3.2 Ga NG generation (Kröner et al., 2019).

The AGC is in faulted contact with the BGGT along the ca. > 3.2 Ga old Phophonyane shear zone northwest of Pigg's Peak town (Schoene et al., 2008) and is spatially separated by sheet-like intrusions of the Mpuluzi and Pigg's Peak batoliths. Rocks from the BGGT comprise a complex association of greenstone sequences and grey gneisses. The greenstone sequences in the BGGT (referred to as the Barberton Greenstone Belt, BGB) comprise a complex association of volcanic-sedimentary rocks that were deposited over more than 300 million years from < 3547 to > 3219 Ga (Byerly et al., 2018). The volcano-sedimentary sequence of the BGB (known as the Barberton Supergroup) has traditionally been divided (from base to top) into three main lithostratigraphic units: The Onverwacht, Fig Tree, and Moodies groups. The Onverwacht Group (OG) is the oldest greenstone succession of the BGB and comprises voluminous mafic to ultramafic metavolcanics successions with sparsely interbedded metasediments. As we only analyzed samples from the lower OG, we only provide a short overview about the lowest stratigraphy of the BGB. The OG is subdivided into the lower and upper Onverwacht Group, marked by a chert layer, known as the Middle Marker. The lower OG comprises the Sandspruit, Theespruit, and Komati Formations, the upper OG includes the Hoggenoeg, Noisy, Mendon, and Kromberg Formations (Armstrong et al., 1990). The oldest magmatic events preserved in the lithostratigraphic succession of the BGB are mafic-ultramafic and felsic metavolcanic rocks. This bimodal sequence (originally assigned to the Sandspruit and Theespruit Formations) comprises the oldest rocks of the lower Onverwacht Group. The metavolcanic rocks of the Sandspruit and Theespruit Formations were shown to

be time-equivalent and deposited during one single volcanic event at ca. 3530 Ma and therefore constitute a single lithostratigraphic unit (Kröner et al., 2016). The record of the somewhat younger 3.482 Ga Komati Formation (Armstrong et al., 1990) bears witness to a period of prolonged volcanic activity, as it comprises a continuous succession of alternating komatiitic, komatiitic basalt, and tholeiitic basalt lava flows without any intercalated sedimentary layers that would reflect a hiatus in the stratigraphy (Dann, 2000).

The BGB is surrounded by 3.521 to 3.197 Ga old granitoid gneisses (Kröner et al., 2019) that form a cluster of 12 diapiric plutons with a wide variety of compositional types that intruded into the lowermost formations of the BGB (Anhaeusser, 2010). They can be subdivided into two major compositionally families that were emplaced during two periods: The older (3.45-3.2 Ga) TTG group that was coeval with deposition of supracrustal sequences in the BGB, and the much younger (ca. 3.1 Ga) GMS group (granite-monzonite-syenite) which intruded after sedimentation and stabilization of the crust through continued deformation of the TTG basement and greenstone sequences at ca. 3.2 Ga (Byerly et al., 2018).

Our samples were collected at the southwestern margin of the BGGT southeast of the town of Badplaas, in an area around the settlement of Tjakastad (see Fig. 3.5). Here a significant proportion of the metavolcanic rocks from the Sandspruit and Theespruit Formations occur as dismembered rafts and xenoliths in tonalitic-trondhjemitic gneisses of the Badplaas, Stolzburg and Theespruit Plutons in the southern part of the Barberton Mountain Land (Anhaeusser, 2010; Van Kranendonk et al., 2014).

### 3.7.2 *Lower protocrust delamination model*

In our model we assumed batch melting throughout (Shaw, 1970). Isotope compositions for  $^{143}\text{Nd}$  and  $^{176}\text{Hf}$  were modelled by using parent-daughter ratios from the calculated sources, the appropriate decay constants (Lugmair and Marti, 1977; Scherer et al., 2001; Söderlund et al., 2004) and assuming CHUR composition for the BSE (Bouvier et al., 2008). The isotope compositions for  $^{142}\text{Nd}$  and  $^{182}\text{W}$  were back calculated by using the appropriate decay constants (Meissner et al., 1987; Vockenhuber et al., 2004), present-day isotope composition for the BSE (Caro et al., 2006; Kleine et al., 2009), elemental Hf/W and Sm/Nd ratios for the BSE (König et al., 2011; Palme and O'Neill, 2014), and solar-system initials for the parent-daughter ratios



(Kleine et al., 2009; Marks et al., 2014). Formation of a mafic protocrust is stage 1 of our model (Fig. 3.2a). The older boundary for the timing of protocrust formation is set by core formation, which could have been completed as early as 38 Ma after solar system formation (König et al., 2011). We extract a mafic protocrust 50 Ma after solar system formation from a mantle with BSE composition (Palme and O'Neill, 2014). The timing of protocrust formation affects in particular the isotope compositions of the short-lived isotope systems during further evolution of the protocrust (Fig. 3.3a). For protocrust formation, we applied partition coefficients for REE, HFSE, and Th that were experimentally conducted and, according to the experiments, assumed 20% batch melting at 2 GPa (Salters and Stracke, 2004). Partition coefficients for W are often incomplete in the literature. If not available, we calculated partition coefficients for W by using partition coefficients for mineral phases from experiments on garnet lherzolite (Adam and Green, 2006) that were adjusted to the melt conditions in our model by using appropriate partition coefficients for Th. Both elements were shown to behave similarly incompatible during silicate crystal-liquid fractionation (König et al., 2011). Hence, the W/Th ratio of our modelled melts extracted from the primitive mantle ( $W/Th = 0.14$ ) is indistinguishable from the canonical range reported in the literature (König et al., 2011). During stage 2 (Fig. 3.2b) we remelt our modeled mafic protocrust and calculate (based on an experimental study (Zhang et al., 2013)) the composition of a typical garnet-rich restite that remained after lower crustal anatexis of a metamorphosed basaltic assemblage (estimated to be representative for the Hadean protocrust) at 12 kbar, in equilibrium with ca. 21% tonalitic melt. The timing of TTG formation as well as the residual mineral assemblage exerts a strong influence on the  $^{142}\text{Nd}$  evolution. In contrast, the  $^{182}\text{W}$  isotope composition will not change because the  $^{182}\text{Hf}$ - $^{182}\text{W}$  system went functionally extinct shortly after protocrust formation at ca. 60 Ma. Due to the enriched composition of the precursor and the long half lives of their parent isotopes, prolonged tonalite formation will only cause small ingrowths in the  $^{143}\text{Nd}$  and  $^{176}\text{Hf}$  isotope compositions in the lower crustal restites (Fig. 3.3a). Therefore, prolonged tonalite formation caused decoupling of  $^{142}\text{Nd}$  from the other isotope systems in the residual garnet-rich restites and provide an explanation why  $^{143}\text{Nd}$  and  $^{176}\text{Hf}$  correlate so tightly with  $^{182}\text{W}$  but not  $^{142}\text{Nd}$ . Indeed, Hf isotope data in zircon reported for Paleoproterozoic grey gneisses of the eastern Kaapvaal Craton reveal incorporation of older continental crustal rocks with Eoarchean to late Hadean age (Compston and Kröner, 1988; Zeh et al., 2011; Kröner et al., 2014). Assuming

prolonged tonalite formation initiated at ca. 4.35 Ga and continued for 100 Ma the variation of  $^{142}\text{Nd}$  isotope composition within their restites would be ca. 9  $\mu$  units at 3.55 Ga. In contrast,  $^{143}\text{Nd}$  and  $^{176}\text{Hf}$  would not vary more than 1  $\epsilon$  unit.

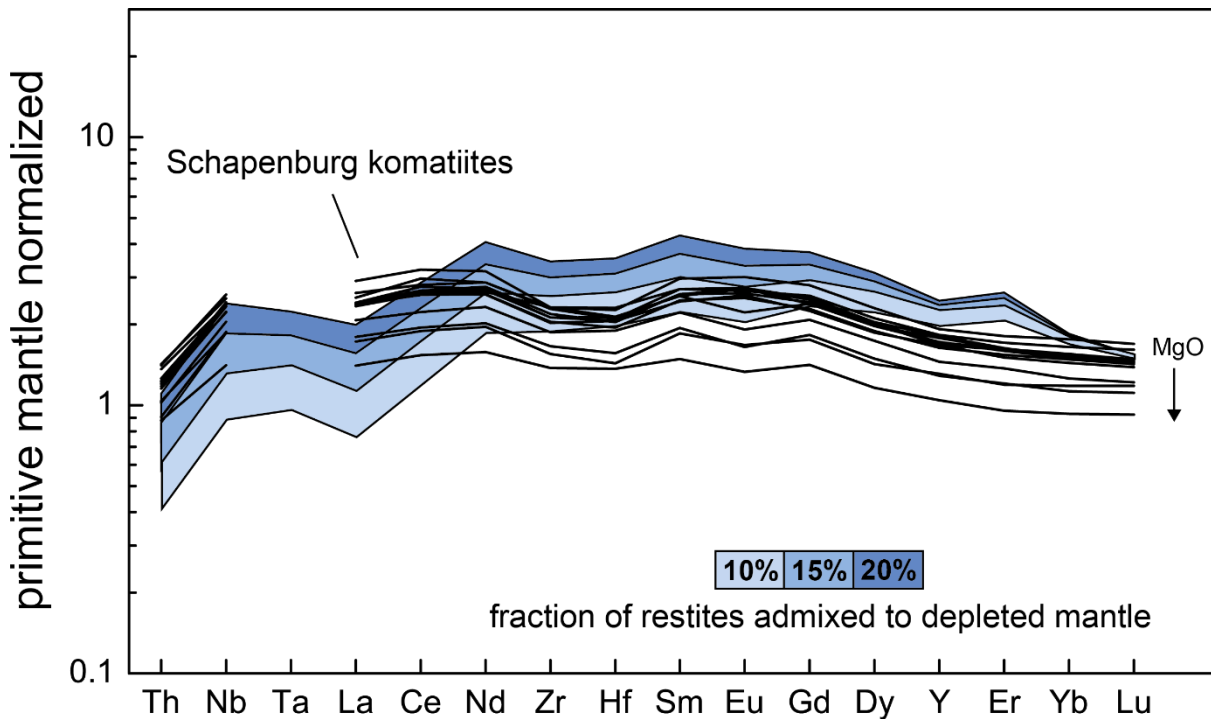


**Fig. 3.6: Incompatible trace element compositions for komatiites from the Schapenburg Greenstone Remnant (black lines) in comparison to our modeled hybrid sources (blue shaded arrays).** Data for the SGR komatiites are taken from Puchtel et al. (2016a). In our model calculations 10 – 20 % of garnet – rich lower crustal restite admixed to an ambient depleted mantle at 3.55 Ga and subsequent 20 – 30% batch melting of this hybrid source can reproduce the trace element compositions of the SGR komatiites. We attribute the variation within the SGR komatiite suite and their more depleted trace element compositions, compared to the modelled patterns, to olivine accumulation as indicated by covariations between MgO content and incompatible trace element concentrations (not shown).

It has previously been shown that delamination of crustal restites into depleted mantle can cause melting of a hybrid source and that the resulting trace element signatures resemble typical komatiites (Bédard, 2006). Similarly, the mechanical introduction of 10-20 % of the garnet-rich restite into an ambient depleted mantle at ca. 3.55 Ga and subsequent 20-30% batch melting of the hybrid source can reproduce the trace element compositions of the SGR komatiites (Fig. 3.6). We attribute the variation within the SGR komatiite suite and their partially more depleted trace element compositions, compared to the modelled patterns, to olivine accumulation as indicated by covariations between MgO content and incompatible trace element concentrations (not

shown). For the ambient mantle we assume 10% melt depletion at ca. 3.9 Ga, using coherent parameters during experimentally constrained melt conditions (Salters and Stracke, 2004) to calculate the isotope and trace element composition at 3.55 Ga. The modelled ambient mantle displays initial  $\epsilon^{143}\text{Nd}$  and  $\epsilon^{176}\text{Hf}$  values of +4.6 and +7.8, respectively, which is in perfect agreement with the modern terrestrial Hf-Nd array (Vervoort et al., 2011), within the range of the modelled DMM composition at 3.55 Ga (Griffin et al., 2000) and consistent with observational constraints from mantle derived rocks from the Kaapvaal Craton (Hoffmann and Wilson, 2017). The isotope compositions for  $^{182}\text{W}$ ,  $^{142}\text{Nd}$ ,  $^{143}\text{Nd}$ , and  $^{176}\text{Hf}$  of 20-30% melt extracted from a hybrid source, composed of 10-20% restite and appropriate fractions of ambient depleted mantle, is in accord with the range observed for SGR komatiites (see Fig. 3.3b). It is noteworthy that the  $^{182}\text{W}$  isotope composition of the melt is controlled by the restite because high modal abundances of garnet and amphibole, together with refractory Ti-rich phases (rutile/ilmenite), result in high bulk partition coefficients. This buffers the  $^{182}\text{W}$  isotope composition against possible variations in the Archean mantle (on average ca. +10 ppm, Archer et al., 2019). Considering rutile or ilmenite in the restites as a residual Ti-rich phase does not significantly affect the results of our model. Ratios of Nb/Ta have been proven to be valuable indicators to discriminate between rutile and ilmenite (Hoffmann et al., 2011a). Unfortunately, no Ta concentrations exist for the SGR komatiites. We expect ilmenite being present in the restites as this results in reasonable Nb/Th ratios that are similar (Nb/Th = 15.1-15.4) to the range observed in the SGR komatiites (Nb/Th = 11.2-14.6). Evidence for the presence of a restite in the source of the SGR komatiites also come from Zr/Sm ratios that are best explained by fractionation of garnet. The correlation of Zr/Sm with  $^{182}\text{W}$  isotope composition is perfectly reproduced by our model (Fig. 3.7).

The hybrid source model can also explain the Re-Os isotope data for the SGR komatiites. The positive initial  $\gamma^{187}\text{Os}$  of the SGR komatiites ( $\gamma^{187}\text{Os} = +3.7 \pm 0.3$ ) reveal that their mantle source evolved with a time-integrated suprachondritic Re/Os (Puchtel et al., 2009). In our model, the early formation of an enriched protocrust (at ca. 4.52 Ga) with elevated Re/Os ratios caused strongly radiogenic ingrowth of  $^{187}\text{Os}$  for ca. 150-250 Ma. As a result, the garnet-rich restites had strongly elevated initial  $\gamma^{187}\text{Os}$  values at the time of TTG genesis (4.35-4.25 Ga). For Re/Os, the depletion of the restite during TTG melt formation is buffered by the high modal abundance of garnet that was shown to display high compatibility for Re (Righter and Hauri, 1998;

Westrenen et al., 2000). Therefore, the radiogenic  $^{187}\text{Os}$  isotope composition will be retained by relatively high Re/Os ratios in the garnet-rich restite. Moreover, overall PGE abundances should be low as sulfides are expected have melted out during TTG extraction. These conceptual assumptions are in good agreement with previous estimates that calculated the effects of incorporation of Hadean crust or restites into the source of the SGR komatiites on its Os isotopic composition (Puchtel et al., 2009; Aulbach et al., 2011).

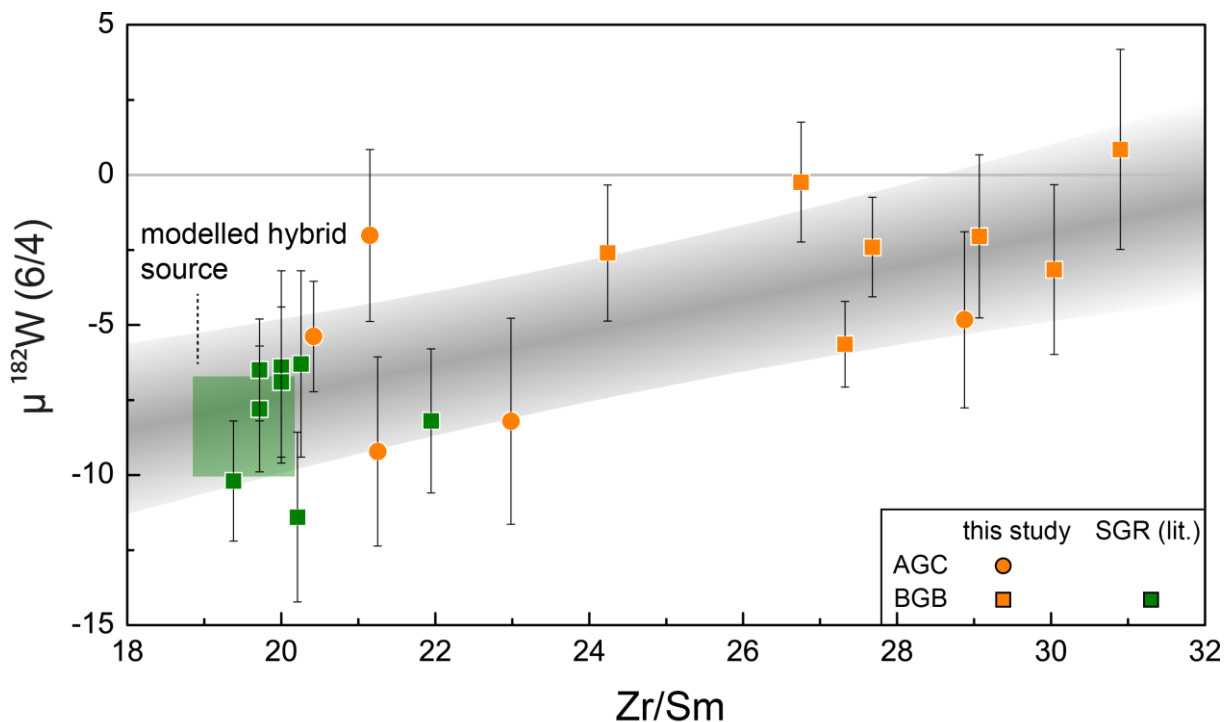


**Fig. 3.7: Plot of  $\mu^{182}\text{W}$  vs. Zr/Sm for rocks from the Kaapvaal craton.** Data for komatiites from the Schapenburg Greenstone Remnant (SGR) are taken from Puchtel et al. (2016a). The combined data indicate a systematic correlation between  $^{182}\text{W}$  isotope composition and Zr/Sm ratios with one endmember defined by the SGR komatiites. The negative  $\mu^{182}\text{W}$  anomalies and low Zr/Sm ratios prominent in the SGR komatiites can be attributed to the presence of 10 – 20% garnet rich restites within a hybrid source that underwent 20 – 30% batch melting (green box). The grey shaded array refers to the 95% confidence interval in which of all samples are expected to fall.

### 3.7.3 Analytical protocol

Our analytical protocol for isotope dilution analysis follows procedures that were described in detail by previous studies (Thiemens et al., 2019; chapter 2). High-precision  $^{182}\text{W}$  isotope analysis mainly follows established analytical protocols (Tusch et al., 2019; chapter 2) that were slightly modified to yield highly purified W solutions from large sample loads (up to 18g) and to improve our analytical uncertainty. Our protocol for the chemical purification of W for high-precision isotope composition analysis comprises four columns. During a cation (AG 50 W-X8 resin, column I) and

anion exchange stage (AG 1-X8 resin, column II) W is separated from matrix elements and HFSE & Ti, respectively. Columns III (TEVA resin) and IV (TODGA resin) are clean up columns to that yield purified W cuts. In this regard, the iteration of the final stage column during the chemical separation of W (chapter 2) improves the purification from remaining matrix elements. The final W-bearing eluate was directly loaded onto BioRad Poly-Prep® columns filled with 0.8ml Eichrom prefilter® material to hold back organic compounds. This, together with threefold treatments with 80 µl of  $\text{cHNO}_3$ -30% $\text{H}_2\text{O}_2$  at max. 60°C after dry-down steps during and after the chemical separation, strongly improved yields and removed mass independent effects on  $^{183}\text{W}$  (Tusch et al., 2019). Prior to loading onto our final stage column, we combined (up to 10) cuts in case sample powders were split up into aliquots (up to 1.3g) during matrix separation. The combination of sample solutions during chemical separation does not affect the accuracy of our high precision  $^{182}\text{W}$  isotope analysis as demonstrated by indistinguishable results for sample solutions of our in-house rock reference material LP 1 (historical La Palma Basalt), that were either obtained from single column cuts (up to 1.3g) or combined solutions from 10 column cuts (in total 11.3 g). The purpose of combining the final cuts is to efficiently measure the cuts by reducing the cumulative volume of leftovers after multiple measurements of individual solutions. This allows to measure at the highest beam intensities possible and, together with our refined separation procedure, significantly improves the analytical uncertainty of our measurements. This is also reflected by our long-term external reproducibility of our in-house rock reference materials LP 1 and AGC 351 that were always measured in every session, yielding markedly improved 2 SD of  $\pm 1.5$  ppm and  $\pm 2.7$  ppm, respectively (see Fig. 3.8). The  $\mu^{182}\text{W}$  session averages for LP 1 (1480 OIB from La Palma) and AGC 351 (3455 Ma gneiss from Swaziland) overlap within their 95% CI (LP1 =  $-0.4 \pm 1.0$  ppm and AGC 351 =  $-0.2 \pm 0.5$  ppm) and are indistinguishable from the NIST reference material and previously reported long-term averages for the same sample powders (Tusch et al., 2019; chapter 2). Additionally, we also performed repeated analyses ( $n = 15$ ) of a 3.27 Ga old Komatiite (sample 160245, Ruth Well Formation) from the Pilbara Craton Western Australia that exhibits highly elevated W concentrations of 19.1 µg/g (chapter 2). The  $\mu^{182}\text{W}$  session average for sample 160245 ( $\mu^{182}\text{W} = +7.9 \pm 0.7$  ppm, 95% CI) is in agreement with previous results (chapter 2) and shows a good long-term reproducibility (2 SD of  $\pm 2.5$  ppm). This, together with the elevated  $^{182}\text{W}$  isotope composition and high W concentration of sample 160245

validates the method for analytical campaigns that address  $^{182}\text{W}$  isotope systematics in Archean mantle derived rocks that often display anomalous  $^{182}\text{W}$  isotope compositions and elevated W concentrations.

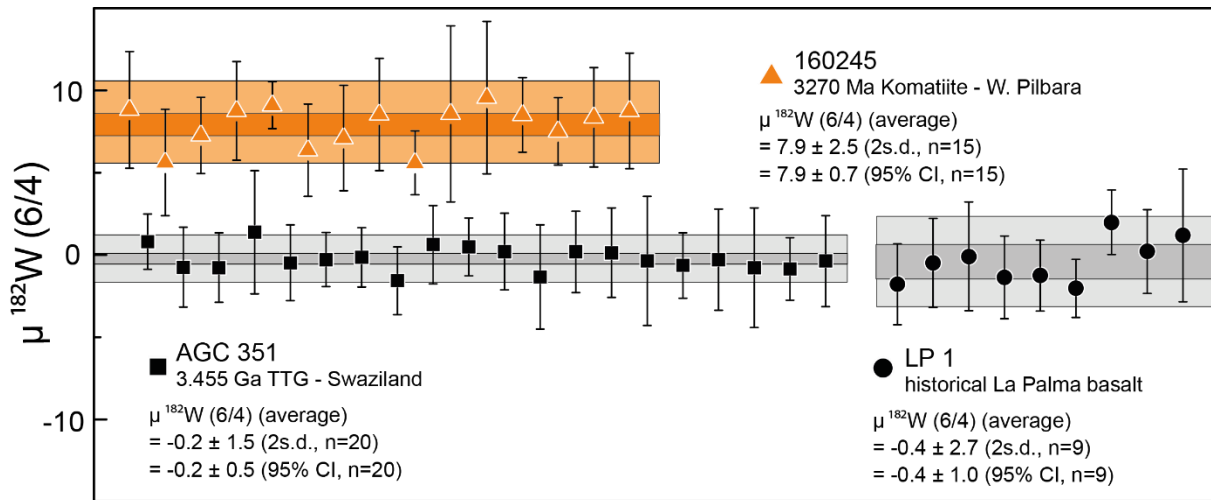


**Fig. 3.8: Long-term reproducibility for  $\mu^{182}\text{W} (6/4)$ , inferred from the repeated analysis of multiple digestions for our in-house reference materials AGC 351, LP 1, and 160245 that are reported relative to W NIST SRM 3136.** Each symbol refers to the average value of multiple measurements conducted during an analytical session. The uncertainties for the session mean values are given by the corresponding 95% CI. The long-term reproducibility for our in-house reference materials are given by the 2 SD of the session mean values.

## References

- Adam J. and Green T. (2006) Trace element partitioning between mica- and amphibole-bearing garnet lherzolite and hydrous basanitic melt: 1. Experimental results and the investigation of controls on partitioning behaviour. *Contrib. to Mineral. Petrol.* **152**, 1–17.
- Allègre C. J. (2008) *Isotope Geology.*, Cambridge University Press.
- Allègre C., Staudacher T. and Sarda P. (1987) Rare gas systematics: formation of the atmosphere, evolution and structure of the Earth's mantle. *Earth Planet. Sci. Lett.* **81**, 127–150.
- Alvarado G. E., Denyer P. and Sinton C. W. (1997) The 89 Ma Tortugal komatiitic suite, Costa Rica: Implications for a common geological origin of the Caribbean and Eastern Pacific region from a mantle plume. *Geology* **25**, 439–442.
- Anders E. and Grevesse N. (1989) Abundances of the elements: Meteoritic and solar. *Geochim. Cosmochim. Acta* **53**, 197–214.
- Angeli I. (2004) A consistent set of nuclear rms charge radii: Properties of the radius surface  $R(N,Z)$ . *At. Data Nucl. Data Tables* **87**, 185–193.
- Anhaeusser C. R. (2010) Magmatic and structural characteristics of the ca. 3440 ma theespruit pluton, barberton mountain land, South Africa. *Am. J. Sci.* **310**, 1136–1167.
- Appel P. W. U. (1986) Strata bound scheelite in the Archean Malene supracrustal belt, West Greenland. *Miner. Depos.* **21**, 207–215.
- Appel P. W. U. (1994) Stratabound scheelite in altered Archaean komatiites, West Greenland. *Miner. Depos.* **29**, 341–352.
- Appel P. W. U., Fedo C. M., Moorbath S. and Myers J. S. (1998) Recognizable primary volcanic and sedimentary features in a low-strain domain of the highly deformed, oldest known (~ 3.7-3.8 Gyr) Greenstone Belt, Isua, West Greenland. *Terra Nov.* **10**, 57–62.
- Archer G. J., Brennecka G. A., Gleißner P., Stracke A., Becker H. and Kleine T. (2019) Lack of late-accreted material as the origin of 182 W excesses in the Archean mantle : Evidence from the Pilbara Craton , Western Australia. *Earth Planet. Sci. Lett.* **528**, 115841.
- Arevalo R. and McDonough W. F. (2008) Tungsten geochemistry and implications for understanding the Earth's interior. *Earth Planet. Sci. Lett.* **272**, 656–665.
- Armstrong R. A., Compston W., de Wit M. J. and Williams I. S. (1990) The stratigraphy of the 3.5-3.2 Ga Barberton Greenstone Belt revisited: a single zircon ion microprobe study. *Earth Planet. Sci. Lett.* **101**, 90–106.
- Arndt N. (2003) Komatiites, kimberlites, and boninites. *J. Geophys. Res. Solid Earth* **108**, 1–11.
- Arndt N. R., Bruzak G. and Reischmann T. (2001) The oldest continental and oceanic

- plateaus: geochemistry of basalts and komatiites of the Pilbara craton, Australia. *Geol. Soc. Am.* **352**, 359–387.
- Arndt N. T. (1994) Archean komatiites. In *Archean Crustal Evolution* (ed. K. C. Condie). Elsevier. pp. 11–44.
- Arndt N. T. and Nisbet E. G. (1982) What is a komatiite? In *Komatiites* (eds. N. T. Arndt and E. G. Nisbet). Allen and Unwin. pp. 19–28.
- Audi G., Kondev F. G., Wang M., Huang W. J. and Naimi S. (2017) The NUBASE2016 evaluation of nuclear properties. *Chinese Phys. C* **41**, 1–138.
- Aulbach S., Stachel T., Heaman L. M., Creaser R. A. and Shirey S. B. (2011) Formation of cratonic subcontinental lithospheric mantle and complementary komatiite from hybrid plume sources. *Contrib. to Mineral. Petrol.* **161**, 947–960.
- Baadsgaard H. (1976) Further U-Pb dates on zircons from the early Precambrian rocks of the Godthaabsfjord area, West Greenland. *Earth Planet. Sci. Lett.* **33**, 261–267.
- Baadsgaard H., Nutman A. P., Bridgwater D., Rosing M., McGregor V. R. and Allaart J. H. (1984) The zircon geochronology of the Akilia association and Isua supracrustal belt, West Greenland. *Earth Planet. Sci. Lett.* **68**, 221–228.
- Bali E., Keppler H. and Audetat A. (2012) The mobility of W and Mo in subduction zone fluids and the Mo-W-Th-U systematics of island arc magmas. *Earth Planet. Sci. Lett.* **351–352**, 195–207. Available at:
- Ballmer M. D., Houser C., Hernlund J. W., Wentzcovitch R. M. and Hirose K. (2017) Persistence of strong silica-enriched domains in the Earth's lower mantle. *Nat. Geosci.* **10**, 236–240.
- Barboni M., Boehnke P., Keller B., Kohl I. E., Schoene B., Young E. D. and McKeegan K. D. (2017) Early formation of the Moon 4.51 billion years ago. *Sci. Adv.* **3**, 1–9.
- Barnes S. J. and Arndt N. T. (2019) Distribution and Geochemistry of Komatiites and Basalts Through the Archean. In *Earth's Oldest Rocks* (eds. M. J. Van Kranendonk, V. C. Bennett, and J. E. Hoffmann). Elsevier, Amsterdam. pp. 103–132.
- Becker H. and Dale C. W. (2015) Re–Pt–Os Isotopic and Highly Siderophile Element Behavior in Oceanic and Continental Mantle Tectonites. *Rev. Mineral. Geochemistry* **81**, 369–440.
- Becker H., Horan M. F., Walker R. J., Gao S., Lorand J. P. and Rudnick R. L. (2006) Highly siderophile element composition of the Earth's primitive upper mantle: Constraints from new data on peridotite massifs and xenoliths. *Geochim. Cosmochim. Acta* **70**, 4528–4550.
- Bédard J. H. (2006) A catalytic delamination-driven model for coupled genesis of Archaean crust and sub-continental lithospheric mantle. *Geochim. Cosmochim. Acta* **70**, 1188–1214.
- Bédard J. H. (2013) How many arcs can dance on the head of a plume? A “comment” on: A critical assessment of neorchaean “plume only” geodynamics: Evidence from the superior province, by Derek Wyman, precambrian research, 2012. *Precambrian Res.* **229**, 189–197.



- Bédard J. H. (2018) Stagnant lids and mantle overturns: Implications for Archaean tectonics, magmagenesis, crustal growth, mantle evolution, and the start of plate tectonics. *Geosci. Front.* **9**, 19–49.
- Belousova E. A., Kostitsyn Y. A., Griffin W. L., Begg G. C., O'Reilly S. Y. and Pearson N. J. (2010) The growth of the continental crust: Constraints from zircon Hf-isotope data. *Lithos* **119**, 457–466.
- Bennett V. C., Brandon A. D. and Nutman A. P. (2007) Coupled  $^{142}\text{Nd}$  -  $^{143}\text{Nd}$  Isotopic Evidence for Hadean Mantle Dynamics. *Science (80- )*. **318**, 1907–1910.
- Bennett V. C., Nutman A. P. and Esat T. M. (2002) Constraints on mantle evolution from  $^{187}\text{Os}$  /  $^{188}\text{Os}$  isotopic compositions of Archean ultramafic rocks from southern West Greenland ( 3 . 8 Ga ) and Western Australia ( 3 . 46 Ga ). *Geochemica Cosmochem. Acta* **66**, 2615–2630.
- Bickle M. J., Bettenay L. F., Barley E., Chapman H. J., Groves D. I., Campbell I. H. and Laeter J. R. De (1983) A 3500 Ma Plutonic and Volcanic Calc-Alkaline Province in the Archaean East Pilbara Block. *Contrib. to Mineral. Petrol.* **84**, 25–35.
- Bickle M. J., Bettenay L. F., Chapman H. J., Groves D. I., McNaughton N. J., Campbell I. H. and de Laeter J. R. (1993) Origin of the 3500-3300 Ma calc-alkaline rocks in the Pilbara Archaean: isotopic and geochemical constraints from the Shaw Batholith. *Precambrian Res.* **60**, 117–149.
- Bindeman I. N., Eiler J. M., Yogodzinski G. M., Tatsumi Y., Stern C. R., Grove T. L., Portnyagin M., Hoernle K. and Danyushevsky L. V. (2005) Oxygen isotope evidence for slab melting in modern and ancient subduction zones. *Earth Planet. Sci. Lett.* **235**, 480–496.
- Black L. P., Williams I. S. and Compston W. (1986) Four zircon ages from one rock: the history of a 3930 Ma-old granulite. *Contrib to Mineral. Petrol.* **94**, 427–437.
- Bleeker W. (2003) The late Archean record: A puzzle in ca. 35 pieces. *Lithos* **71**, 99–134.
- Blichert-Toft J., Albarède F., Rosing M., Frei R. and Bridgwater D. (1999) The Nd and Hf isotopic evolution of the mantle through the Archean. results from the Isua supracrustals, West Greenland, and from the Birimian terranes of West Africa. *Geochim. Cosmochim. Acta* **63**, 3901–3914.
- Blichert-Toft J. and Frei R. (2001) Complex Sm-Nd and Lu-Hf isotope systematics in metamorphic garnets from the Isua supracrustal belt , West Greenland. *Geochemica Cosmochem. Acta* **65**, 3177–3187.
- Bouvier A., Vervoort J. D. and Patchett P. J. (2008) The Lu-Hf and Sm-Nd isotopic composition of CHUR: Constraints from unequilibrated chondrites and implications for the bulk composition of terrestrial planets. *Earth Planet. Sci. Lett.* **273**, 48–57.
- Bouvier A. and Wadhwa M. (2010) The age of the Solar System redefined by the oldest Pb-b age of a meteoritic inclusion. *Nat. Geosci.* **3**, 637–641.
- Bowring S. A. and Williams I. S. (1999) Priscoan (4.00-4.03 Ga) orthogneisses from northwestern Canada. *Contrib. to Mineral. Petrol.* **134**, 3–16.
- Boyd A. J. (2018) Geochemical Dynamics of the Isua Supracrustal Belt and the

- Eoarchean Earth. Ph.D. Thesis, University of Copenhagen.
- Boyet M., Blichert-toft J., Rosing M., Storey M., Telouk P. and Albarede F. (2003) Nd evidence for early Earth differentiation. *Earth Planet. Sci. Lett.* **214**, 427–442.
- Boyet M. and Carlson R. W. (2006) A new geochemical model for the Earth ' s mantle inferred from 146 Sm – 142 Nd systematics. **250**, 254–268.
- Brandon A. D. and Walker R. J. (2005) The debate over core-mantle interaction. *Earth Planet. Sci. Lett.* **232**, 211–225.
- Braukmüller N., Wombacher F., Funk C. and Münker C. (2019) Earth's volatile element depletion pattern inherited from a carbonaceous chondrite-like source. *Nat. Geosci.* **12**, 564–568.
- Brown M. (2010) Paired metamorphic belts revisited. *Gondwana Res.* **18**, 46–59.
- Bruland K. W., Middag R. and Lohan M. C. (2014) *Controls of Trace Metals in Seawater*. 2nd ed., Elsevier Ltd.
- Burke K., Steinberger B., Torsvik T. H. and Smethurst M. A. (2008) Plume Generation Zones at the margins of Large Low Shear Velocity Provinces on the core-mantle boundary. *Earth Planet. Sci. Lett.* **265**, 49–60.
- Byerly G. R., Lowe D. R. and Heubeck C. (2018) Geologic evolution of the Barberton Greenstone Belt - A unique record of crustal development, surface processes, and early life 3.55 - 3.20 Ga. In *Earth ' s Oldest Rocks* (eds. M. J. Van Kranendonk, V. C. Bennett, and J. E. Hoffmann). Elsevier, Amsterdam. pp. 569–613.
- Cameron A. G. W. (1997) The origin of the Moon and the single impact hypothesis V. *Icarus* **126**, 126–137.
- Cameron A. G. W. and Ward W. R. (1976) The origin of the Moon. *Lunar Planet. Sci.* **VII**, 120–122.
- Canup R. M. (2012) Forming a Moon with an Earth-like Composition via a Giant Impact. *Science* **338**, 1052–1056.
- Canup R. M. and Asphaug E. (2001) Origin of the Moon in a giant impact near the end of the Earth's formation. *Nature* **412**, 708–712.
- Capitanio F. A., Nebel O., Cawood P. A., Weinberg R. F. and Chowdhury P. (2019) Reconciling thermal regimes and tectonics of the early Earth. *Geology* **47**, 923–927.
- Carlson R. W., Boyet M., O'Neil J., Rizo H. and Walker R. J. (2015) Early Differentiation and Its Long-Term Consequences for Earth Evolution. In *The Early Earth: Accretion and Differentiation* (eds. J. Badro and M. Walter). John Wiley & Sons, Inc., Hoboken, New Jersey. pp. 143–173.
- Caro G., Bourdon B. and Birck J. (2003) 146Sm – 142 Nd evidence from Isua metamorphosed sediments for early differentiation of the Earth ' s mantle. *Nature* **423**, 428–431.
- Caro G., Bourdon B., Birck J. L. and Moorbath S. (2006) High-precision 142Nd/144Nd measurements in terrestrial rocks: Constraints on the early differentiation of the Earth's mantle. *Geochim. Cosmochim. Acta* **70**, 164–191.

- Cates N. L. and Mojzsis S. J. (2007) Pre-3750 Ma supracrustal rocks from the Nuvvuagittuq supracrustal belt, northern Québec. *Earth Planet. Sci. Lett.* **255**, 9–21.
- Chadwick B. (1981) Field relations, petrography and geochemistry of Archaean amphibolite dykes and malene supracrustal amphibolites, northwest Buksefjorden, southern West Greenland. *Precambrian Res.* **14**, 221–259.
- Chambers J. E. (2004) Planetary accretion in the inner Solar System. *Earth Planet. Sci. Lett.* **223**, 241–252.
- Champion D. C. and Smithies R. H. (2019) Geochemistry of Paleoarchean Granites of the East Pilbara Terrane, Pilbara Craton, Western Australia: Implications for Early Archean Crustal Growth. In *Earth's Oldest Rocks* (eds. M. J. Van Kranendonk, V. C. Bennett, and J. E. Hoffmann). Elsevier, Amsterdam. pp. 487–518.
- Chou C.-L. (1978) Fractionation of siderophile elements in the earth's upper mantle. *Proc. Lunar Planet. Sci. Conf. 9th*, 219–230.
- Compston W. and Kröner A. (1988) Multiple zircon growth within early Archaean tonalitic gneiss from the Ancient Gneiss Complex, Swaziland. *Earth Planet. Sci. Lett.* **87**, 13–28.
- Condie K. C. (2005) High field strength element ratios in Archean basalts: A window to evolving sources of mantle plumes? *Lithos* **79**, 491–504.
- Cook D. L. and Schönbächler M. (2016) High-precision measurement of W isotopes in Fe–Ni alloy and the effects from the nuclear field shift. *J. Anal. At. Spectrom.*
- Cottle J. M., Horstwood M. S. A. and Parrish R. R. (2009) A new approach to single shot laser ablation analysis and its application to in situ Pb/U geochronology. *J. Anal. At. Spectrom.* **24**, 1355.
- Craig H. and Lupton J. E. (1976) Primordial neon, helium, and hydrogen in oceanic basalts. *Earth Planet. Sci. Lett.* **31**, 369–385.
- Creech J. B., Baker J. A., Handler M. R., Lorand J.-P., Storey M., Wainwright A. N., Luguët A., Moynier F. and Bizzarro M. (2017) Late accretion history of the terrestrial planets inferred from platinum stable isotopes. *Geochemical Perspect. Lett.*, 94–104.
- Crowley J. L. (2003) U-Pb geochronology of 3810–3630 Ma granitoid rocks south of the Isua greenstone belt, southern West Greenland. *Precambrian Res.* **126**, 235–257.
- Ćuk M. and Stewart S. T. (2012) Making the moon from a fast-spinning earth: A giant impact followed by resonant despinning. *Science* (80- ). **338**, 1047–1052.
- Dale C. W., Kruijjer T. S. and Burton K. W. (2017) Highly siderophile element and 182W evidence for a partial late veneer in the source of 3.8 Ga rocks from Isua, Greenland. *Earth Planet. Sci. Lett.* **458**, 394–404.
- Dann J. C. (2000) The 3.5 Ga Komati Formation, Barberton Greenstone Belt, South Africa, Part I: New maps and magmatic architecture. *South African J. Geol.* **103**, 47–68.
- Day J. M. D., Pearson D. G., Macpherson C. G., Lowry D. and Carracedo J. C. (2010)

- Evidence for distinct proportions of subducted oceanic crust and lithosphere in HIMU-type mantle beneath El Hierro and La Palma, Canary Islands. *Geochim. Cosmochim. Acta* **74**, 6565–6589.
- Debaille V., O'Neill C., Brandon A. D., Haenecour P., Yin Q. Z., Mattielli N. and Treiman A. H. (2013) Stagnant-lid tectonics in early Earth revealed by  $^{142}\text{Nd}$  variations in late Archean rocks. *Earth Planet. Sci. Lett.* **373**, 83–92.
- Debaille V., Trønnes R. G., Brandon A. D., Waight T. E., Graham D. W. and Lee C. T. A. (2009) Primitive off-rift basalts from Iceland and Jan Mayen: Os-isotopic evidence for a mantle source containing enriched subcontinental lithosphere. *Geochim. Cosmochim. Acta* **73**, 3423–3449.
- Dhuime B., Wuestefeld A. and Hawkesworth C. J. (2015) Emergence of modern continental crust about 3 billion years ago. *Nat. Geosci.* **8**, 552–555.
- Echevarria L. M. (1980) Tertiary or mesozoic komatiites from Gorgona Island, Colombia: field relation and geochemistry. *Contrib. to Mineral. Petrol.* **73**, 253–266.
- Ellam R. M., Upton B. G. J. and Fitton J. G. (1998) Petrogenesis of late stage magmatism at Hold with Hope, East Greenland. *Contrib. to Mineral. Petrol.* **133**, 51–59.
- Faure F., Arndt N. I. and Libourel G. (2006) Formation of spinifex texture in komatiites: An experimental study. *J. Petrol.* **47**, 1591–1610.
- Fischer-Gödde M., Elfers B. M., Münker C., Szilas K., Maier W. D., Messling N., Morishita T., Van Kranendonk M. and Smithies H. (2020) Ruthenium isotope vestige of Earth's pre-late-veener mantle preserved in Archaean rocks. *Nature* **579**, 240–244.
- Frei R., Rosing M. T., Waight T. E. and Ulfbeck D. (2002) Hydrothermal-metasomatic and tectono-metamorphic processes in the Isua supracrustal belt ( West Greenland ): A multi-isotopic investigation of their effects on the Earth ' s oldest oceanic crustal sequence. *Geochemica Cosmochem. Acta* **66**, 467–486.
- Friend C. R. L. and Nutman a. P. (2005) New pieces to the Archaean terrane jigsaw puzzle in the Nuuk region, southern West Greenland: steps in transforming a simple insight into a complex regional tectonothermal model. *J. Geol. Soc. London.* **162**, 147–162.
- Friend C. R. L. and Nutman A. P. (2011) Dunites from Isua, Greenland: A ca. 3720 Ma window into subcrustal metasomatism of depleted mantle. *Geology* **39**, 663–666.
- Friend C. R. L. and Nutman A. P. (2010) Eoarchean ophiolites? New evidence for the debate on the ISUA supracrustal belt, southern west greenland. *Am. J. Sci.* **310**, 826–861.
- Friend C. R. L., Nutman A. P. and McGregor V. R. (1988) Late Archean terrane accretion in the Godthab region, southern West Greenland. *Nature* **335–538**, 535.
- Friend L., Bennett C. and Nutman P. (2002) Abyssal peridotites > 3,800 Ma from southern West Greenland: field relationships , petrography , geochronology , whole-rock and mineral chemistry of dunite and harzburgite inclusions in the Itsaq Gneiss Complex. *Contrib. to Mineral. Petrol.* **143**, 71–92.

- Frost C. D. and Frost B. R. (1995) Open-System Dehydration of Amphibolite , Morton Pass , Wyoming : Elemental and Nd and Sr Isotopic Effects '. *J. Geol.* **103**, 269–284.
- Füri E., Hilton D. R., Murton B. J., Hémond C., Dymant J. and Day J. M. D. (2011) Helium isotope variations between Réunion Island and the Central Indian Ridge (17°-21°S): New evidence for ridge-hot spot interaction. *J. Geophys. Res. Solid Earth* **116**, 1–17.
- Garapić G., Jackson M. G., Hauri E. H., Hart S. R., Farley K. A., Blusztajn J. S. and Woodhead J. D. (2015) A radiogenic isotopic (He-Sr-Nd-Pb-Os) study of lavas from the Pitcairn hotspot: Implications for the origin of EM-1 (enriched mantle 1). *Lithos* **228–229**, 1–11.
- Garbe-Schönberg C.-D. (1993) Simultaneous Determination of Thirty-Seven Trace Elements in Twenty-Eight International Rock Standards By Icp-MS. *Geostand. Newsl.* **17**, 81–97.
- Gerya T. (2019) Geodynamics of the early Earth: Quest for the missing paradigm. *Geology* **47**, 1006–1007.
- Gill R. C. O. and Bridgwater D. (1979) Early archaean basic magmatism in West Greenland: The geochemistry of the ameralik dykes. *J. Petrol.* **20**, 695–726.
- Green D. H. (1975) Genesis of archaean peridotitic magmas and constraints on archaean geothermal gradients and tectonics. *Geology* **3**, 15–18.
- Green D. H. (1981) Petrogenesis of Archaean Ultramafic Magmas and Implications for Archaean Tectonics. In *Precambrian Plate Tectonics. Developments in Precambrian Geology* (ed. A. Kröner). Elsevier, Amsterdam. pp. 469–489.
- Griffin W. L., Pearson N. J., Belousova E., Jackson S. E., Van Acherbergh E., O'Reilly S. Y. and Shee S. R. (2000) The Hf isotope composition of cratonic mantle: LAM-MC-ICPMS analysis of zircon megacrysts in kimberlites. *Geochim. Cosmochim. Acta* **64**, 133–147.
- Gruau G., Rosing M., Bridgwater D. and Gill R. C. O. (1996) Resetting of Sm-Nd systematics during metamorphism of > 3.7-Ga rocks: implications for isotopic models of early Earth differentiation. *Chem. Geol.* **133**, 225–240.
- Günther-Leopold I., Waldis J. K., Wernli B. and Kopajtic Z. (2005) Measurement of plutonium isotope ratios in nuclear fuel samples by HPLC-MC-ICP-MS. *Int. J. Mass Spectrom.* **242**, 197–202.
- Harley S. L., Kelly N. M. and Kusiak M. A. (2019) Ancient Antarctica: The Archaean of the East Antarctic Shield. In *Earth's Oldest Rocks* (eds. M. J. Van Kranendonk, V. C. Bennett, and J. E. Hoffmann). Elsevier, Amsterdam. pp. 865–897.
- Harper C. L. J. and Jacobsen S. B. (1992) Evidence from coupled  $^{147}\text{Sm}$ - $^{143}\text{Nd}$  and  $^{146}\text{Sm}$ - $^{142}\text{Nd}$  systematics for very early (4.5-Gyr) differentiation of the Earth's mantle. *Nature* **360**, 728–732.
- Harper C. L. and Jacobsen S. B. (1996) Evidence for  $^{182}\text{Hf}$  in the early Solar System and constraints on the timescale of terrestrial accretion and core formation. *Geochim. Cosmochim. Acta* **60**, 1131–1153.
- Hartmann W. K. and Davis D. R. (1975) Satellite-Sized Planetesimals and Lunar

- Origin. *Icarus* **24**, 504–515.
- Hawkesworth C. J., Dhuime B., Pietranik A. B., Cawood P. A., Kemp A. I. S. and Storey C. D. (2010) The generation and evolution of the continental crust. *J. Geol. Soc. London*. **167**, 229–248.
- Helz R. T. and Taggart Jr. J. E. (2012) Trace-Element Analyses of Core Samples from the 1967–1988 Drillings of Kilauea Iki Lava Lake, Hawaii. *U.S. Geol. Surv. Open-File Rep. 2010-1093*, 47 p.
- Herzberg C. (1992) Depth and degree of melting of komatiites. *J. Geophys. Res.* **97**, 4521–4540.
- Herzberg C., Cabral R. A., Jackson M. G., Vidito C., Day J. M. D. and Hauri E. H. (2014) Phantom Archean crust in Mangaia hotspot lavas and the meaning of heterogeneous mantle. *Earth Planet. Sci. Lett.* **396**, 97–106.
- Herzberg C. and O'hara M. J. (2002) Plume-Associated Ultramafic Magmas of Phanerozoic Age MODEL FOR CALCULATING. *J. Petrol.* **43**, 1857–1883.
- Hirata T., Hayano Y. and Ohno T. (2003) Improvements in precision of isotopic ratio measurements using laser ablation-multiple collector-ICP-mass spectrometry: reduction of changes in measured isotopic ratios. *J. Anal. At. Spectrom.* **18**, 1283.
- Hoffmann J. E. and Kröner A. (2019) Early Archean crustal evolution in southern Africa - an updated record of the Ancient Gneiss Complex of Swaziland. In *Earth's Oldest Rocks* (ed. M. J. Van Kranendonk). Elsevier, Amsterdam. pp. 553–567.
- Hoffmann J. E., Kröner A., Hegner E., Viehmann S., Xie H., Iaccheri L. M., Schneider K. P., Hofmann A., Wong J., Geng H. and Yang J. (2016) Source composition, fractional crystallization and magma mixing processes in the 3.48-3.43 Ga Tsawela tonalite suite (Ancient Gneiss Complex, Swaziland) - Implications for Palaeoarchean geodynamics. *Precambrian Res.* **276**, 43–66.
- Hoffmann J. E., Münker C., Naeraa T., Rosing M. T., Herwartz D., Garbe-Schönberg D. and Svahnberg H. (2011a) Mechanisms of Archean crust formation inferred from high-precision HFSE systematics in TTGs. *Geochim. Cosmochim. Acta* **75**, 4157–4178.
- Hoffmann J. E., Münker C., Polat A., König S., Mezger K. and Rosing M. T. (2010) Highly depleted Hadean mantle reservoirs in the sources of early Archean arc-like rocks, Isua supracrustal belt, southern West Greenland. *Geochim. Cosmochim. Acta* **74**, 7236–7260.
- Hoffmann J. E., Münker C., Polat A., Rosing M. T. and Schulz T. (2011b) The origin of decoupled Hf-Nd isotope compositions in Eoarchean rocks from southern West Greenland. *Geochim. Cosmochim. Acta* **75**, 6610–6628.
- Hoffmann J. E., Musese E., Kröner A., Schneider K. P., Wong J., Hofmann A., Hegner E., Kasper U. and Münker C. (2020) Hafnium-Neodymium isotope, trace element and U-Pb zircon age constraints on the petrogenesis of the 3.44-3.46 Ga Dwalile greenstone remnant, Ancient Gneiss Complex, Swaziland. *Precambrian Res.* **in Review**.
- Hoffmann J. E., Nagel T. J., Münker C., Naeraa T. and Rosing M. T. (2014) Constraining the process of Eoarchean TTG formation in the Itsaq Gneiss

- Complex, southern West Greenland. *Earth Planet. Sci. Lett.* **388**, 374–386.
- Hoffmann J. E. and Wilson A. H. (2017) The origin of highly radiogenic Hf isotope compositions in 3.33 Ga Comondale komatiite lavas (South Africa). *Chem. Geol.* **455**, 6–21.
- Hoffmann J. E., Zhang C., Moyen J. F. and Nagel T. J. (2019) The Formation of Tonalites - Trondjemite - Granodiorites in Early Continental Crust. In *Earth's Oldest Rocks* (eds. M. J. Van Kranendonk, V. C. Bennett, and J. E. Hoffmann). Elsevier, Amsterdam. pp. 133–168.
- Hofmann A. W. (1997) Mantle geochemistry: the message from oceanic magmatism. *Nature* **385**, 219–229.
- Hopkins M. D., Harrison T. M. and Manning C. E. (2010) Constraints on Hadean geodynamics from mineral inclusions in >4Ga zircons. *Earth Planet. Sci. Lett.* **298**, 367–376.
- Hopkins M., Harrison T. M. and Manning C. E. (2008) Low heat flow inferred from >4 Gyr zircons suggests Hadean plate boundary interactions. *Nature* **456**, 493–496.
- Horie K., Nutman A. P., Friend C. R. L. and Hidaka H. (2010) The complex age of orthogneiss protoliths exemplified by the Eoarchaean Itsaq Gneiss Complex (Greenland): SHRIMP and old rocks. *Precambrian Res.* **183**, 25–43.
- Huang S. and Frey F. A. (2003) Trace element abundances of Mauna Kea basalt from phase 2 of the Hawaii Scientific Drilling Project: Petrogenetic implications of correlations with major element content and isotopic ratios. *Geochemistry, Geophys. Geosystems* **4**.
- Hunter D. R., Barker F. and Millard H. T. (1984) Geochemical investigation of Archaean Bimodal and Dwalile metamorphic suites, Ancient Gneiss Complex, Swaziland. *Precambrian Res.* **24**, 131–155.
- Iizuka T., Horie K., Komiya T., Maruyama S., Hirata T., Hidaka H. and Windley B. F. (2006) 4.2 Ga zircon xenocryst in an Acasta gneiss from northwestern Canada: Evidence for early continental crust. *Geology* **34**, 245–248.
- Iizuka T., Nakai S., Sahoo Y. V., Takamasa A., Hirata T. and Maruyama S. (2010) The tungsten isotopic composition of Eoarchean rocks: Implications for early silicate differentiation and core-mantle interaction on Earth. *Earth Planet. Sci. Lett.* **291**, 189–200.
- Ireland T. J., Arevalo R., Walker R. J. and McDonough W. F. (2009) Tungsten in Hawaiian picrites: A compositional model for the sources of Hawaiian lavas. *Geochim. Cosmochim. Acta* **73**, 4517–4530.
- Jackson M. G., Hart S. R., Konter J. G., Kurz M. D., Blusztajn J. and Farley K. A. (2014) Helium and lead isotopes reveal the geochemical geometry of the Samoan plume. *Nature* **514**, 355–358.
- Jackson M. P. A. (1984) Archean structural styles in the Ancient Gneiss Complex of Swaziland, South Africa. In *Precambrian Tectonics Illustrated* (eds. A. Kröner and R. Greiling). Schweizerbart'sche Verlagsbuchhandlung. pp. 1–18.
- Jahn B. M., Glikson A. Y., Peucat J. J. and Hickman A. H. (1981) REE geochemistry and isotopic data of Archean silicic volcanics and granitoids from the Pilbara

- Block, Western Australia: implications for the early crustal evolution. *Geochim. Cosmochim. Acta* **45**, 1633–1652.
- Jenner F. E., Bennett V. C., Nutman A. P., Friend C. R. L., Norman M. D. and Yaxley G. (2009) Evidence for subduction at 3.8 Ga: Geochemistry of arc-like metabasalts from the southern edge of the Isua Supracrustal Belt. *Chem. Geol.* **261**, 82–97.
- Jenner F. E. and O'Neill H. S. C. (2012) Analysis of 60 elements in 616 ocean floor basaltic glasses. *Geochemistry, Geophys. Geosystems* **13**, 1–11.
- Jochum K. P., Nohl U., Herwig K., Lammel E., Stoll B. and Hofmann A. W. (2005) GeoReM: A New Geochemical Database for Reference Materials and Isotopic Standards. *Geostand. Geoanalytical Res.* **29**, 333–338.
- Johnson T. E., Brown M., Gardiner N. J., Kirkland C. L. and Smithies R. H. (2017) Earth's first stable continents did not form by subduction. *Nature*.
- Jones T. D., Davies D. R. and Sossi P. A. (2019) Tungsten isotopes in mantle plumes: Heads it's positive, tails it's negative. *Earth Planet. Sci. Lett.* **506**, 255–267.
- Jones T. D., Maguire R., van Keken P., Ritsema J. and Koelemeijer P. (2020) Subducted oceanic crust as the origin of seismically slow lower-mantle structures. *EarthArXiv* **1**, 1–16.
- Keppler H. (1996) Constraints from partitioning experiments on the composition of subduction-zone fluids. *Nature* **380**, 237–240.
- Kimura K., Lewis R. S. and Anders E. (1974) Distribution of gold and rhenium between nickel-iron and silicate melts: implications for the abundance of siderophile elements on the Earth and Moon. *Geochim. Cosmochim. Acta* **38**, 683–701.
- Kinoshita N., Paul M., Kashiv Y., Collon P., Deibel C. M., DiGiovine B., Greene J. P., Henderson D. J., Jiang C. L., Marley S. T., Nakanishi T., Pardo C. R., Rehm K. E., Robertson D., Scott R., Schmitt C., Tang X. D., Vondrasek R. and Yokohama A. (2012) A shorter <sup>146</sup>Sm half-life measured and implications for <sup>146</sup>Sm-<sup>142</sup>Nd chronology in the solar system. *Science (80- )*. **335**, 1614–1617.
- Kleine T., Mezger K., Münker C., Palme H. and Bischoff a. (2004) <sup>182</sup>Hf-<sup>182</sup>W isotope systematics of chondrites, eucrites, and martian meteorites: Chronology of core formation and early mantle differentiation in Vesta and Mars. *Geochim. Cosmochim. Acta* **68**, 2935–2946.
- Kleine T., Münker C., Mezger K. and Palme H. (2002) Rapid accretion and early core formation on asteroids and the terrestrial planets from Hf-W chronometry. *Nature* **418**, 952–955.
- Kleine T., Touboul M., Bourdon B., Nimmo F., Mezger K., Palme H., Jacobsen S. B., Yin Q. Z. and Halliday A. N. (2009) Hf-W chronology of the accretion and early evolution of asteroids and terrestrial planets. *Geochim. Cosmochim. Acta* **73**, 5150–5188.
- Komori Y., Yokokita T., Kasamatsu Y., Haba H., Toyoshima A., Toyomura K., Nakamura K., Kanaya J., Huang M., Kudou Y., Takahashi N. and Shinohara A. (2015) Solid-liquid extraction of Mo and W by Aliquat 336 from HCl solutions toward extraction chromatography experiments of Sg. *J. Radioanal. Nucl. Chem.*



- 303**, 1385–1388.
- König S., Münker C., Hohl S., Paulick H., Barth A. R., Lagos M., Pfänder J. and Büchl A. (2011) The Earth's tungsten budget during mantle melting and crust formation. *Geochim. Cosmochim. Acta* **75**, 2119–2136.
- König S., Münker C., Schuth S. and Garbe-Schönberg D. (2008) Mobility of tungsten in subduction zones. *Earth Planet. Sci. Lett.* **274**, 82–92.
- Konter J. G. and Jackson M. G. (2012) Large volumes of rejuvenated volcanism in Samoa: Evidence supporting a tectonic influence on late-stage volcanism. *Geochemistry, Geophys. Geosystems* **13**.
- Korkisch J. (1989) *Handbook of ion exchange resins, Volume IV.*
- Kramers J. D. (1998) Reconciling siderophile element data in the Earth and Moon, W isotopes and the upper lunar age limit in a simple model of homogeneous accretion. *Chem. Geol.* **145**, 461–478.
- Van Kranendonk M. J., Collins W. J., Hickman A. and Pawley M. J. (2004) Critical tests of vertical vs. horizontal tectonic models for the Archaean East Pilbara Granite-Greenstone Terrane, Pilbara Craton, Western Australia. *Precambrian Res.* **131**, 173–211.
- Van Kranendonk M. J., Hickman A. H., Smithes R. H. and Nelson D. R. (2002) Geology and tectonic evolution of the Archean North Pilbara Terrain, Pilbara Craton, Western Australia. *Econ. Geol.* **97**, 695–732.
- Van Kranendonk M. J., Hugh Smithies R., Hickman A. H. and Champion D. C. (2007) Review: Secular tectonic evolution of Archean continental crust: interplay between horizontal and vertical processes in the formation of the Pilbara Craton, Australia. *Terra Nov.* **19**, 1–38.
- Van Kranendonk M. J., Hugh Smithies R., Hickman A. H., Wingate M. T. D. and Bodorkos S. (2010) Evidence for Mesoarchean (~3.2 Ga) rifting of the Pilbara Craton: The missing link in an early Precambrian Wilson cycle. *Precambrian Res.* **177**, 145–161.
- Van Kranendonk M. J., Kröner A., Hoffman J. E., Nagel T. and Anhaeusser C. R. (2014) Just another drip: Re-analysis of a proposed mesoarchean suture from the Barberton mountain land, South Africa. *Precambrian Res.* **254**, 19–35.
- Kring D. A. and Cohen B. A. (2002) Cataclysmic bombardment throughout the inner solar system 3.9-4.0 Ga. *J. Geophys. Res. E Planets* **107**.
- Kröner A. (2007) Chapter 5.2 The Ancient Gneiss Complex of Swaziland and Environs: Record of Early Archean Crustal Evolution in Southern Africa. *Dev. Precambrian Geol.* **15**, 465–480.
- Kröner A., Anhaeusser C. R., Hoffmann J. E., Wong J., Geng H., Hegner E., Xie H., Yang J. and Liu D. (2016) Chronology of the oldest supracrustal sequences in the Palaeoarchaeon Barberton Greenstone Belt, South Africa and Swaziland. *Precambrian Res.* **279**, 123–143.
- Kröner A., Compston W. and Williams I. S. (1989) Growth of early Archaean crust in the Ancient Gneiss Complex of Swaziland as revealed by single zircon dating. *Tectonophysics* **161**, 271–298.

- Kröner A., Hoffmann J. E., Wong J. M., Geng H.-Y., Schneider K. P., Xie H., Yang J.-H. and Nhleko N. (2019) *Archaean Crystalline Rocks of the Eastern Kaapvaal Craton*.
- Kröner A., Hoffmann J. E., Xie H., Münker C., Hegner E., Wan Y., Hofmann A., Liu D. and Yang J. (2014) Generation of early Archaean grey gneisses through melting of older crust in the eastern Kaapvaal craton, southern Africa. *Precambrian Res.* **255**, 823–846.
- Kröner A., Nagel T. J., Hoffmann J. E., Liu X., Wong J., Hegner E., Xie H., Kasper U., Hofmann A. and Liu D. (2018) High-temperature metamorphism and crustal melting at ca. 3.2 Ga in the eastern Kaapvaal craton, southern Africa. *Precambrian Res.* **317**, 101–116.
- Kröner A. and Tegtmeier A. (1994) Gneiss-greenstone relationships in the Ancient Gneiss Complex of southwestern Swaziland, southern Africa, and implications for early crustal evolution. *Precambrian Res.* **67**, 109–139.
- Kröner A., Wendt J. I., Milisenda C., Compston W. and Maphalala R. (1993) Zircon geochronology and Nd isotopic systematics of the Ancient Gneiss Complex, Swaziland, and implications for crustal evolution. In *The Ancient Gneiss Complex: Overview papers and guidebook for excursion* (ed. A. Kröner). Swaziland Geological Survey and Mines Department. pp. 15–37.
- Kruijer T. ., Kleine T., Fischer-Gödde M. and Sprung P. (2015) Lunar tungsten isotopic evidence for the late veneer. *Nature* **520**, 534–537.
- Kruijer T. S. and Kleine T. (2018) No 182 W excess in the Ontong Java Plateau source. *Chem. Geol.* **485**, 24–31. Available at:
- Kruijer T. S., Sprung P., Kleine T., Leya I., Burkhardt C. and Wieler R. (2012) Hf-W chronometry of core formation in planetesimals inferred from weakly irradiated iron meteorites. *Geochim. Cosmochim. Acta* **99**, 287–304.
- Kurzweil F., Münker C., Grupp M., Braukmüller N., Fechtner L., Christian M., Hohl S. V. and Schoenberg R. (2019) The stable tungsten isotope composition of modern igneous reservoirs. *Geochim. Cosmochim. Acta* **251**, 176–191.
- Kurzweil F., Münker C., Tusch J. and Schoenberg R. (2017) Accurate stable tungsten isotope measurements of natural samples using a 180 W- 183 W double-spike. *Chem. Geol.* **476**, 407–417.
- Labrosse S., Hernlund J. W. and Coltice N. (2007) A crystallizing dense magma ocean at the base of the Earth's mantle. *Nature* **450**, 866–869.
- Larsen L. M. and Pedersen A. K. (2009) Petrology of the paleocene picrites and flood basalts on disko and nuussuaq, West Greenland. *J. Petrol.* **50**, 1667–1711.
- Lee C.-T. A., Luffi P. and Chin E. J. (2011) Building and Destroying Continental Mantle. *Annu. Rev. Earth Planet. Sci.* **39**, 59–90.
- Liu J., Pearson D. G., Chacko T. and Luo Y. (2018) A reconnaissance view of tungsten reservoirs in some crustal and mantle rocks: Implications for interpreting W isotopic compositions and crust-mantle W cycling. *Geochim. Cosmochim. Acta* **223**, 300–318.
- Liu J., Touboul M., Ishikawa A., Walker R. J. and Graham Pearson D. (2016)

- Widespread tungsten isotope anomalies and W mobility in crustal and mantle rocks of the Eoarchean Saglek Block, northern Labrador, Canada: Implications for early Earth processes and W recycling. *Earth Planet. Sci. Lett.* **448**, 13–23.
- van de Löcht J., Hoffmann J. E., Li C., Wang Z., Becker H., Rosing M. T. and Kleinschrodt R. (2018a) Earth's oldest mantle peridotites show full record of late accretion. **46**, 10–20.
- van de Löcht J., Münker C., Hoffmann J. E., Sprung P. and Rosing M. T. (2018b) Earth's oldest mantle peridotites may originate from a supra-subduction zone setting. *GeoBonn Conf. Abstract v*, 18.
- Ludden J., Gelin L. and Trudel P. (1982) Archean metavolcanics from the Rouyn-Noranda district, Abitibi Greenstone Belt, Quebec. 2. Mobility of trace elements and petrogenetic constraints 4. *Can. J. Earth Sci.* **19**, 2279–2287.
- Lugmair G. W. and Marti K. (1977) Sm-Nd-Pu timepieces in the Angra dos Reis meteorite. *Earth Planet. Sci. Lett.* **35**, 273–284.
- Luo X., Rehkämper M., Lee D.-C. and Halliday A. N. (1997) High precision  $^{230}\text{Th}/^{232}\text{Th}$  and  $^{234}\text{U}/^{238}\text{U}$  measurements using energyfiltered ICP magnetic sector multiple collector mass spectrometry. *Int. J. Mass Spectrom. Ion Process.* **171**, 105–117.
- Maier W. D., Barnes S. J., Campbell I. H., Fiorentini M. L., Peltonen P., Barnes S.-J. and Smithies R. H. (2009) Progressive mixing of meteoritic veneer into the early Earth's deep mantle. *Nature* **460**, 620–623.
- Mann U., Frost D. J., Rubie D. C., Becker H. and Audétat A. (2012) Partitioning of Ru, Rh, Pd, Re, Ir and Pt between liquid metal and silicate at high pressures and high temperatures - Implications for the origin of highly siderophile element concentrations in the Earth's mantle. *Geochim. Cosmochim. Acta* **84**, 593–613.
- Marchi S., Canup R. M. and Walker R. J. (2018) Heterogeneous delivery of silicate and metal to the Earth by large planetesimals. *Nat. Geosci.* **11**, 77–81.
- Marks N. E., Borg L. E., Hutcheon I. D., Jacobsen B. and Clayton R. N. (2014) Samarium-neodymium chronology and rubidium-strontium systematics of an Allende calcium-aluminum-rich inclusion with implications for  $^{146}\text{Sm}$  half-life. *Earth Planet. Sci. Lett.* **405**, 15–24.
- Marshall B. D. and Futa K. (1991) Lanthanide Element Mobility and Sm-Nd Systematics in a Contact Metamorphic Zone. *Radiochim. Acta* **52–53**, 405–412.
- McCulloch M. T. and Gamble J. A. (1991) Geochemical and geodynamical constraints on subduction zone magmatism. *Earth Planet. Sci. Lett.* **102**, 358–374.
- McDonough W. F. (2013) Compositional Model for the Earth's Core. In *Treatise on Geochemistry: Second Edition* Elsevier Ltd. pp. 559–577.
- McNaughton N. J., Green M. D., Compston W. and Williams I. S. (1988) Are anorthositic rocks basement to the Pilbara Craton? *Geol. Soc. Aust. Abstracts*, 272–273.
- Mei Q.-F., Yang J.-H., Wang Y.-F., Wang H. and Peng P. (2020) Tungsten isotopic constraints on homogenization of the Archean silicate Earth: Implications for the transition of tectonic regimes. *Geochim. Cosmochim. Acta* **278**, 51–64.

- Meissner F., Schmidt-Ott W. D. and Ziegeler L. (1987) Half-Life and alpha-Ray Energy of  $^{146}\text{Sm}$ . *Zeitschrift für Phys.* **174**, 171–174.
- Melosh H. J. (2014) New approaches to the Moon 's isotopic crisis. *Philos. Trans. R. Soc. A Math. Phys. Eng. Sci.* **372**.
- Michard-Vitrac A., Lancelot J., Allègre C. J. and Moorbath S. (1977) U-Pb ages on single zircons from the Early Precambrian rocks of West Greenland and the Minnesota River Valley. *Earth Planet. Sci. Lett.* **35**, 449–453.
- Miljković K., Wieczorek M. A., Collins G. S., Laneuville M., Neumann G. A., Melosh H. J., Solomon S. C., Phillips R. J., Smith D. E. and Zuber M. T. (2013) Asymmetric distribution of lunar impact basins caused by variations in target properties. *Science (80-. )*. **342**, 724–726.
- Mojzsis S. J., Cates N. L., Caro G., Trail D., Abramov O., Guitreau M., Blichert-Toft J., Hopkins M. D. and Bleeker W. (2014) Component geochronology in the polyphase ca. 3920Ma Acasta Gneiss. *Geochim. Cosmochim. Acta* **133**, 68–96.
- Mojzsis S. J., Harrison T. M. and Pidgeon R. T. (2001) Oxygen-isotope evidence from ancient zircons for liquid water at the Earth's surface 4,300 Myr ago. *Nature* **409**, 178–181.
- Moorbath S., Allaart J. H., Bridgwater D. and McGregor V. R. (1977) Rb-Sr ages of early Archaean supracrustal rocks and Amîtsoq gneisses at Isua. *Nature* **270**, 43–45.
- Moyen J. F. and Martin H. (2012) Forty years of TTG research. *Lithos* **148**, 312–336.
- Moyen J. F., Stevens G., Kisters A. F. M., Belcher R. W. and Lemirre B. (2018) TTG plutons of the Barberton granitoid-greenstone terrain, southern Africa. In *Earth's Oldest Rocks* (eds. M. J. Van Kranendonk, V. C. Bennett, and J. E. Hoffmann). Elsevier, Amsterdam. pp. 615–653.
- Mukasa S. B., Wilson A. H. and Young K. R. (2013) Geochronological constraints on the magmatic and tectonic development of the Pongola Supergroup (Central Region), South Africa. *Precambrian Res.* **224**, 268–286.
- Mukhopadhyay S. (2012) Early differentiation and volatile accretion recorded in deep-mantle neon and xenon. *Nature* **486**, 101–4.
- Mundl-Petermeier A., Walker R. J., Fischer R. A., Lekic V., Jackson M. G. and Kurz M. D. (2020) Anomalous  $^{182}\text{W}$  in high  $^3\text{He}/^4\text{He}$  ocean island basalts: Fingerprints of Earth's core? *Geochim. Cosmochim. Acta* **271**, 194–211.
- Mundl-Petermeier A., Walker R. J., Jackson M. G., Blichert-Toft J., Kurz M. D. and Halldórsson S. A. (2019) Temporal evolution of primordial tungsten-182 and  $^3\text{He}/^4\text{He}$  signatures in the Iceland mantle plume. *Chem. Geol.* **525**, 245–259.
- Mundl A., Touboul M., Jackson M. G., Day J. M. D., Kurz M. D., Lekic V., Helz R. T. and Walker R. J. (2017) Tungsten-182 heterogeneity in modern ocean island basalts. *Nature* **69**, 66–69.
- Münker C. (2010) A high field strength element perspective on early lunar differentiation. *Geochim. Cosmochim. Acta* **74**, 7340–7361.
- Münker C. (1998) Nb/Ta fractionation in a Cambrian arc/back arc system, New

- Zealand: source constraints and application of refined ICPMS techniques. *Chem. Geol.* **144**, 23–45.
- Münker C., Weyer S., Scherer E. and Mezger K. (2001) Separation of high field strength elements (Nb, Ta, Zr, Hf) and Lu from rock samples for MC-ICPMS measurements. *Geochemistry Geophys. Geosystems* **2**.
- Münker C., Wörner G., Yogodzinski G. and Churikova T. (2004) Behaviour of high field strength elements in subduction zones: Constraints from Kamchatka-Aleutian arc lavas. *Earth Planet. Sci. Lett.* **224**, 275–293.
- Næraa T., Scherstén A., Rosing M. T., Kemp A. I. S., Hoffmann J. E., Kokfelt T. F. and Whitehouse M. J. (2012) Hafnium isotope evidence for a transition in the dynamics of continental growth 3.2 Gyr ago. *Nature* **485**, 627–630.
- Nagel T. J., Hoffmann J. E. and Münker C. (2012) Generation of Eoarchean tonalite-trondhjemite-granodiorite series from a thickened mafic arc crust. *Geology* **40**, 375–378.
- Nair R. and Chacko T. (2008) Role of oceanic plateaus in the initiation of subduction and origin of continental crust. *Geology* **36**, 583–586.
- Nisbet E. G., Cheadle M. J., Arndt N. T. and Bickle M. J. (1993) Constraining the potential temperature of the Archaean mantle: A review of the evidence from komatiites. *Lithos* **30**, 291–307.
- Norman M. D. (2019) Origin of the Earth and the Late Heavy Bombardment. In *Earth's Oldest Rocks* (eds. M. J. Van Kranendonk, V. C. Bennett, and J. E. Hoffmann). Elsevier, Amsterdam. pp. 27–47.
- Norman M. D., Duncan R. A. and Huard J. J. (2010) Imbrium provenance for the Apollo 16 Descartes terrain: Argon ages and geochemistry of lunar breccias 67016 and 67455. *Geochim. Cosmochim. Acta* **74**, 763–783.
- Norman M. D. and Garcia M. O. (1999) Primitive magmas and source characteristics of the Hawaiian plume: Petrology and geochemistry of shield picrites. *Earth Planet. Sci. Lett.* **168**, 27–44.
- Nutman A., McGregor V. and Friend C. (1996) The Itsaq Gneiss Complex of southern West Greenland; the world's most extensive record of early crustal evolution. *Precambrian Res.* **78**, 1–39.
- Nutman A. P., Allaart J. H., Bridgwater D., Dimroth E. and Rosing M. (1984) Stratigraphic and geochemical evidence for the depositional environment of the early archaean Isua supracrustal belt, southern west Greenland. *Precambrian Res.* **25**, 365–396.
- Nutman A. P., Bennett V. C., Friend C. R. L. and Norman M. D. (1999) Meta-igneous (non-gneissic) tonalites and quartz-diorites from an extensive ca. 3800 Ma terrain south of the Isua supracrustal belt, southern West Greenland: Constraints on early crust formation. *Contrib. to Mineral. Petrol.* **137**, 364–388.
- Nutman A. P., Bennett V. C., Friend C. R. L. and Rosing M. T. (1997) ~ 3710 and > 3790 Ma volcanic sequences in the Isua (Greenland) supracrustal belt; structural and Nd isotope implications. *Chem. Geol.* **141**, 271–287.
- Nutman A. P. and Friend C. R. L. (2009) New 1:20,000 scale geological maps,

- synthesis and history of investigation of the Isua supracrustal belt and adjacent orthogneisses, southern West Greenland: A glimpse of Eoarchaeon crust formation and orogeny. *Precambrian Res.* **172**, 189–211.
- Nutman A. P., Friend C. R. L. and Bennett V. C. (2002) Evidence for 3650-3600 Ma assembly of the northern end of the Itsaq Gneiss Complex, Greenland: Implication for early Archaean tectonics. *Tectonics* **21**, 1005.
- Nutman A. P., Friend C. R. L., Bennett V. C. and MCGregor V. R. (2004) Dating of the Ameralik dyke swarms of the Nuuk district, southern West Greenland: mafic intrusion events starting from c. 3510 Ma. *J. Geol. Soc. London.* **161**, 421–430.
- Nutman A. P., Friend C. R. L., Horie K. and Hidaka H. (2007) The Itsaq Gneiss Complex of Southern West Greenland and the Construction of Eoarchaeon Crust at Convergent Plate Boundaries. *Dev. Precambrian Geol.* **15**, 187–218.
- O'Brien D. P., Morbidelli A. and Levison H. F. (2006) Terrestrial planet formation with strong dynamical friction. *Icarus* **184**, 39–58.
- O'Neil J., Carlson R. W., Paquette J. L. and Francis D. (2012) Formation age and metamorphic history of the Nuvvuagittuq Greenstone Belt. *Precambrian Res.* **220–221**, 23–44.
- O'Neil J., Francis D. and Carlson R. W. (2011) Implications of the Nuvvuagittuq greenstone belt for the formation of earth's early crust. *J. Petrol.* **52**, 985–1009.
- O'Neill C. and Debaille V. (2014) The evolution of Hadean-Eoarchaeon geodynamics. *Earth Planet. Sci. Lett.* **406**, 49–58.
- O'Neill C., Lenardic A., Moresi L., Torsvik T. H. and Lee C. T. A. (2007) Episodic Precambrian subduction. *Earth Planet. Sci. Lett.* **262**, 552–562.
- O'Neil J., Carlson R. W., Francis D. and Stevenson R. K. (2008) Neodymium-142 Evidence for Hadean Mafic Crust. *Science (80-. )*. **321**, 1828–1832.
- Ohtani E. (1984) Generation of komatiite magma and gravitational differentiation in the deep upper mantle. *Earth Planet. Sci. Lett.* **67**, 261–272.
- Palme H. and O'Neill H. (2014) Cosmochemical Estimates of Mantle Composition. In *Treatise on Geochemistry: Second Edition* Elsevier Ltd. pp. 1–39.
- Palme H. and Rammensee W. (1981) Tungsten and some other siderophile elements in meteoritic and terrestrial basalts. *Lunar Planet. Sci.* **XII**, 796–798.
- Parai R., Mukhopadhyay S. and Standish J. J. (2012) Heterogeneous upper mantle Ne, Ar and Xe isotopic compositions and a possible Dupal noble gas signature recorded in basalts from the Southwest Indian Ridge. *Earth Planet. Sci. Lett.* **359–360**, 227–239.
- Patchett P. J. and Tatsumoto M. (1981) A routine high-precision method for Lu-Hf isotope geochemistry and chronology. *Contrib. to Mineral. Petrol.* **75**, 263–267.
- Pearce J. A. (2008) Geochemical fingerprinting of oceanic basalts with applications to ophiolite classification and the search for Archean oceanic crust. **100**, 14–48.
- Pearce J. A. and Peate D. W. (1995) Tectonic implications of Volcanic Arc Magmas. *Annu. Rev. Earth Planet. Sci.* **23**, 251–285.

- Peters B. J., Carlson R. W., Day J. M. D. and Horan M. F. (2018) Hadean silicate differentiation preserved by anomalous  $^{142}\text{Nd}/^{144}\text{Nd}$  ratios in the Réunion hotspot source. *Nature* **555**, 89–93.
- Peters S. T. M., Münker C., Becker H. and Schulz T. (2014) Alpha-decay of  $^{184}\text{Os}$  revealed by radiogenic  $^{180}\text{W}$  in meteorites: Half life determination and viability as geochronometer. *Earth Planet. Sci. Lett.* **391**, 69–76.
- Peters S. T. M., Münker C., Wombacher F. and Elfers B. M. (2015) Precise determination of low abundance isotopes ( $^{174}\text{Hf}$ ,  $^{180}\text{W}$  and  $^{190}\text{Pt}$ ) in terrestrial materials and meteorites using multiple collector ICP-MS equipped with  $1012\Omega$  Faraday amplifiers. *Chem. Geol.* **413**, 132–145.
- Petersson A., Kemp A. I. S., Hickman A. H., Whitehouse M. J., Martin L. and Gray C. M. (2019) A new 3.59 Ga magmatic suite and a chondritic source to the east Pilbara Craton. *Chem. Geol.* **511**, 51–70.
- Pfeifer M., Lloyd N. S., Peters S. T. M., Wombacher F., Elfers B.-M., Schulz T. and Münker C. (2017) Tantalum isotope ratio measurements and isotope abundances determined by MC-ICP-MS using amplifiers equipped with 1010, 1012 and 1013 Ohm resistors. *J. Anal. At. Spectrom.* **32**, 130–143.
- Polat A. (2012) Growth of Archean continental crust in oceanic island arcs. *Geology* **40**, 383–384.
- Polat A. and Hofmann A. W. (2003) Alteration and geochemical patterns in the 3.7–3.8 Ga Isua greenstone belt, West Greenland. *Precambrian Res.* **126**, 197–218.
- Polat A., Hofmann A. W., Münker C., Regelous M. and Appel P. W. U. (2003) Contrasting geochemical patterns in the 3.7–3.8 Ga pillow basalt cores and rims, Isua greenstone belt, Southwest Greenland: Implications for postmagmatic alteration processes. *Geochemica Cosmochem. Acta* **67**, 441–457.
- Polat A., Hofmann A. W. and Rosing M. T. (2002) Boninite-like volcanic rocks in the 3.7–3.8 Ga Isua greenstone belt, West Greenland: geochemical evidence for intra-oceanic subduction zone processes in the early Earth. *Chem. Geol.* **184**, 231–254.
- Pourmand A. and Dauphas N. (2010) Distribution coefficients of 60 elements on TODGA resin: Application to Ca, Lu, Hf, U and Th isotope geochemistry. *Talanta* **81**, 741–753.
- Puchtel, Blichert-Toft J., Touboul M., Horan M. F. and Walker R. J. (2016a) The coupled  $^{182}\text{W}$ - $^{142}\text{Nd}$  record of early terrestrial mantle differentiation. *Geochemistry Geophys. Geosystems* **17**, 2168–2193.
- Puchtel I. S., Blichert-Toft J., Touboul M. and Walker R. J. (2018)  $^{182}\text{W}$  and HSE constraints from 2.7 Ga komatiites on the heterogeneous nature of the Archean mantle. *Geochim. Cosmochim. Acta* **228**, 1–26.
- Puchtel I. S., Blichert-Toft J., Touboul M., Walker R. J., Byerly G. R., Nisbet E. G. and Anhaeusser C. R. (2013) Insights into early Earth from Barberton komatiites: Evidence from lithophile isotope and trace element systematics. *Geochim. Cosmochim. Acta* **108**, 63–90.
- Puchtel I. S., Hofmann A. W., Mezger K., Jochum K. P., Shchipansky A. A. and

- Samsonov A. V. (1998) Oceanic plateau model for continental crustal growth in the Archaean: A case study from the Kostomuksha greenstone belt, NW Baltic Shield. *Earth Planet. Sci. Lett.* **155**, 57–74.
- Puchtel I. S., Walker R. J., Anhaeusser C. R. and Gruau G. (2009) Re-Os isotope systematics and HSE abundances of the 3.5 Ga Schapenburg komatiites, South Africa: Hydrous melting or prolonged survival of primordial heterogeneities in the mantle? *Chem. Geol.* **262**, 355–369.
- Puchtel, Touboul M., Blichert-Toft J., Walker R. J., Brandon A. D., Nicklas R. W., Kulikov V. S. and Samsonov A. V. (2016b) Lithophile and siderophile element systematics of Earth's mantle at the Archean-Proterozoic boundary: Evidence from 2.4 Ga komatiites. *Geochim. Cosmochim. Acta* **180**, 227–255.
- Rammensee W. and Wänke H. (1977) On the partition coefficient of tungsten between metal and silicate and its bearing on the origin of the moon. *Proc. Lunar Planet. Sci. Conf.* **8**, 399–409.
- Reimink J. R., Chacko T., Carlson R. W., Shirey S. B., Liu J., Stern R. A., Bauer A. M., Pearson D. G. and Heaman L. M. (2018) Petrogenesis and tectonics of the Acasta Gneiss Complex derived from integrated petrology and <sup>142</sup>Nd and <sup>182</sup>W extinct nuclide-geochemistry. *Earth Planet. Sci. Lett.* **494**, 12–22.
- Reimink Jesse R., Chacko T., Stern R. A. and Heaman L. M. (2016) The birth of a cratonic nucleus: Litho-geochemical evolution of the 4.02-2.94 Ga Acasta Gneiss Complex. *Precambrian Res.* **281**, 453–472.
- Reimink J. R., Davies J. H. F. L., Chacko T., Stern R. A., Heaman L. M., Sarkar C., Schaltegger U., Creaser R. A. and Pearson D. G. (2016) No evidence for Hadean continental crust within Earth's oldest evolved rock unit. *Nat. Geosci.* **9**, 777–780.
- Righter K. and Hauri E. H. (1998) Compatibility of rhenium in garnet during mantle melting and magma genesis. *Science (80- )*. **280**, 1737–1741.
- Rizo H., Andrault D., Bennett N. R., Humayun M., Brandon A., Vlastelic I., Moine B., Poirier A., Bouhifd M. A. and Murphy D. T. (2019) <sup>182</sup>W evidence for core-mantle interaction in the source of mantle plumes. *Geochemical Perspect. Lett.* **11**, 6–11.
- Rizo H., Boyet M., Blichert-toft J., Neil J. O., Rosing M. T. and Paquette J. (2012) The elusive Hadean enriched reservoir revealed by <sup>142</sup>Nd deficits in Isua Archaean rocks. *Nature* **490**, 96–100.
- Rizo H., Boyet M., Blichert-Toft J. and Rosing M. (2011) Combined Nd and Hf isotope evidence for deep-seated source of Isua lavas. *Earth Planet. Sci. Lett.* **312**, 267–279.
- Rizo H., Boyet M., Blichert-Toft J. and Rosing M. T. (2013) Early mantle dynamics inferred from <sup>142</sup>Nd variations in Archean rocks from southwest Greenland. *Earth Planet. Sci. Lett.* **377–378**, 324–335.
- Rizo, Walker R. J., Carlson R. W., Horan M. F., Mukhopadhyay S., Manthos V., Francis D. and Jackson M. G. (2016a) Preservation of Earth-forming events in the tungsten isotopic composition of modern flood basalts. *Science* **352**, 809–812.
- Rizo, Walker R. J., Carlson R. W., Touboul M., Horan M. F., Puchtel I. S., Boyet M. and Rosing M. T. (2016b) Early Earth Differentiation Investigated Through <sup>142</sup>Nd,



- 182W, and Highly Siderophile Element Abundances in Samples From Isua, Greenland. *Geochim. Cosmochim. Acta* **175**, 319–336.
- Robin-Popieul C. C. M., Arndt N. T., Chauvel C., Byerly G. R., Sobolev A. V. and Wilson A. (2012) A new model for barberton komatiites: Deep critical melting with high melt retention. *J. Petrol.* **53**, 2191–2229.
- Rosing M. T. (1990) The theoretical effect of metasomatism on Sm-Nd isotopic systems. *Geochemica Cosmochem. Acta* **54**, 1337–1341.
- Rubie D. C., Frost D. J., Mann U., Asahara Y., Nimmo F., Tsuno K., Kegler P., Holzheid A. and Palme H. (2011) Heterogeneous accretion, composition and core-mantle differentiation of the Earth. *Earth Planet. Sci. Lett.* **301**, 31–42.
- Rubie D. C., Nimmo F. and Melosh H. J. (2007) Formation of the Earth's core. Treatise on geophysics. In *Evolution of the Earth* (ed. D. Stevenson). Elsevier, Amsterdam. pp. 51–90.
- Rufu R., Aharonson O. and Perets H. B. (2017) A multiple-impact origin for the Moon. *Nat. Geosci.* **10**, 89–94.
- Russell W. A., Papanastassiou D. A. and Tombrello T. A. (1978) Ca isotope fractionation on the Earth and other solar system materials. *Geochim. Cosmochim. Acta* **42**, 1075–1090.
- Saji N. S., Larsen K., Wielandt D., Schiller M., Costa M. M., Whitehouse M. J., Rosing M. T. and Bizzarro M. (2018) Hadean geodynamics inferred from time-varying  $^{142}\text{Nd}/^{144}\text{Nd}$  in the early Earth rock record. *Geochemical Perspect. Lett.* **7**, 43–48.
- Salters V. J. M. and Stracke A. (2004) Composition of the depleted mantle. *Geochemistry, Geophys. Geosystems* **5**.
- Sandiford M., Van Kranendonk M. J. and Bodorkos S. (2004) Conductive incubation and the origin of dome-and-keel structure in Archean granite-greenstone terrains: A model based on the eastern Pilbara Craton, Western Australia. *Tectonics* **23**, 1–19.
- Scherer E., Münker C. and Mezger K. (2001) Calibration of the Lutetium-Hafnium Clock. *Science (80- )*. **293**, 683–687.
- van Schijndel V., Stevens G., Zeh A., Frei D. and Lana C. (2017) Zircon geochronology and Hf isotopes of the Dwalile Supracrustal Suite, Ancient Gneiss Complex, Swaziland: Insights into the diversity of Palaeoarchaeon source rocks, depositional and metamorphic ages. *Precambrian Res.* **295**, 48–66.
- Schneider K. P., Hoffmann J. E., Boyet M., Münker C. and Kröner A. (2018) Coexistence of enriched and modern-like  $^{142}\text{Nd}$  signatures in Archean igneous rocks of the eastern Kaapvaal Craton, southern Africa. *Earth Planet. Sci. Lett.* **487**, 54–66.
- Schoenberg R., Kamber B. S. and Collerson K. D. (2002a) Tungsten isotope evidence from for early meteorite bombardment of the Earth. *Nature* **418**, 403–405.
- Schoenberg R., Kamber B. S., Collerson K. D. and Eugster O. (2002b) New W-isotope evidence for rapid terrestrial accretion and very early core formation. *Geochim. Cosmochim. Acta* **66**, 3151–3160.

- Schoene B., de Wit M. J. and Bowring S. A. (2008) Mesoarchean assembly and stabilization of the eastern Kaapvaal craton: A structural-thermochronological perspective. *Tectonics* **27**, 1–27.
- Schulz T., Münker C. and Peters S. T. M. (2013) P-Process 180W anomalies in iron meteorites: Nucleosynthetic versus non-nucleosynthetic origins. *Earth Planet. Sci. Lett.* **362**, 246–257.
- Shaw D. M. (1970) Trace element fractionation during anatexis. *Geochim. Cosmochim. Acta* **34**, 237–243.
- Shirai N. and Humayun M. (2011) Mass independent bias in W isotopes in MC-ICP-MS instruments. *J. Anal. At. Spectrom.* **26**, 1414.
- Shirey S. B. and Richardson S. H. (2011) Start of the Wilson cycle at 3 Ga shown by diamonds from subcontinental mantle. *Science* (80-. ). **333**, 434–436.
- Siebert J. and Shahar A. (2015) An Experimentally Geochemistry Perspective on Earth's Core Formation. In *The Early Earth: Accretion and Differentiation* (eds. J. Badro and M. Walter). John Wiley & Sons, Inc., Hoboken, New Jersey. pp. 103–121.
- Sizova E., Gerya T., Brown M. and Perchuk L. L. (2010) Subduction styles in the Precambrian: Insight from numerical experiments. *Lithos* **116**, 209–229.
- Smit M. A., Scherstén A., Naeraa T., Emo R. B., Scherer E. E., Sprung P., Bleeker W., Mezger K., Maltese A., Cai Y., Rasbury E. T. and Whitehouse M. J. (2020) Boron isotopes: no “Arc” in Archean? In *Goldschmidt Conference Abstracts* p. 2409.
- Smithies, Champion D. C., Van Kranendonk M. J., Howard H. M. and Hickman A. H. (2005) Modern-style subduction processes in the Mesoarchaeon: Geochemical evidence from the 3.12 Ga Whundo intra-oceanic arc. *Earth Planet. Sci. Lett.* **231**, 221–237.
- Smithies R. H., Champion D. C. and Cassidy K. F. (2003) Formation of Earth's early Archaean continental crust. **127**, 89–101.
- Smithies R. H., Champion D. C. and Van Kranendonk M. J. (2019) The oldest well-preserved felsic volcanic rocks on Earth: Geochemical clues to the early evolution of the Pilbara Supergroup and Implications for the growth of a Paleoproterozoic protocontinent. In *Earth's Oldest Rocks* pp. 463–486.
- Smithies R. H., Champion D. C. and Sun S. S. (2004) Evidence for early LREE-enriched mantle source regions: Diverse magmas from the c. 3.0 Ga Mallina Basin, Pilbara Craton, NW Australia. *J. Petrol.* **45**, 1515–1537.
- Smithies R. H., Ivanic T. J., Lowrey J. R., Morris P. A., Barnes S. J., Wyche S. and Lu Y. J. (2018) Two distinct origins for Archean greenstone belts. *Earth Planet. Sci. Lett.* **487**, 106–116.
- Smithies R. H., Van Kranendonk M. J. and Champion D. C. (2005) It started with a plume - Early Archaean basaltic proto-continental crust. *Earth Planet. Sci. Lett.* **238**, 284–297.
- Smithies R. H., Van Kranendonk M. J. and Champion D. C. (2007) The Mesoarchean emergence of modern-style subduction. *Gondwana Res.* **11**, 50–68.

- Söderlund U., Patchett P. J., Vervoort J. D. and Isachsen C. E. (2004) The  $^{176}\text{Lu}$  decay constant determined by Lu-Hf and U-Pb isotope systematics of Precambrian mafic intrusions. *Earth Planet. Sci. Lett.* **219**, 311–324.
- Sossi P. A., Eggins S. M., Nesbitt R. W., Nebel O., Hergt J. M., Campbell I. H., O'Neill H. S. C., Kranendonk M. Van and Rhodri Davies D. (2016) Petrogenesis and geochemistry of Archean Komatiites. *J. Petrol.* **57**, 147–184.
- Sprung P., Scherer E. E., Upadhyay D., Leya I. and Mezger K. (2010) Non-nucleosynthetic heterogeneity in non-radiogenic stable Hf isotopes: Implications for early solar system chronology. *Earth Planet. Sci. Lett.* **295**, 1–11.
- Starkey N. A., Stuart F. M., Ellam R. M., Fitton J. G., Basu S. and Larsen L. M. (2009) Helium isotopes in early Iceland plume picrites: Constraints on the composition of high  $^3\text{He}/^4\text{He}$  mantle. *Earth Planet. Sci. Lett.* **277**, 91–100.
- Suhr N., Hoffmann J. E., Kröner A. and Schröder S. (2014) Archaean granulite-facies paragneisses from central Swaziland: Inferences on Palaeoarchean crustal reworking and a complex metamorphic history. *J. Geol. Soc. London.* **172**, 139–152.
- Szilas K., Kelemen P. B. and Rosing M. T. (2015) The petrogenesis of ultramafic rocks in the N 3 . 7 Ga Isua supracrustal belt , southern West Greenland : Geochemical evidence for two distinct magmatic cumulate trends. *Gondwana Res.* **28**, 565–580.
- Tera F., Papanastassiou D. A. and Wasserburg G. J. (1974) Isotopic Evidence For A Terminal Lunar Cataclysm. *Earth Planet. Sci. Lett.* **22**, 1–21.
- Thiemens M. M., Sprung P., Fonseca R. O. C., Leitzke F. P. and Münker C. (2019) Early Moon formation inferred from hafnium–tungsten systematics. *Nat. Geosci.* **12**.
- Thompson R. N., Morrison M. A., Hendry G. L. and Parry S. J. (1984) An assessment of the relative roles of crust and mantle in magma genesis: an elemental approach. *Philos. Trans. R. Soc. London* **310**, 549–590.
- Torsvik T. H., Steinberger B., Ashwal L. D., Doubrovine P. V. and Trønnes R. G. (2016) Earth evolution and dynamics—a tribute to Kevin Burke. *Can. J. Earth Sci.* **53**, 1073–1087.
- Touboul M., Liu J., O'Neil J., Puchtel I. S. and Walker R. J. (2014) New insights into the Hadean mantle revealed by  $^{182}\text{W}$  and highly siderophile element abundances of supracrustal rocks from the Nuvvuagittuq Greenstone Belt, Quebec, Canada. *Chem. Geol.* **383**, 63–75.
- Touboul M., Puchtel I. S. and Walker R. J. (2012)  $^{182}\text{W}$  Evidence for Long-Term Preservation of Early Mantle Differentiation Products. *Science (80-. )*. **335**, 1065–1070.
- Touboul M., Puchtel I. S. and Walker R. J. (2015) Tungsten isotopic evidence for disproportional late accretion to the Earth and Moon. *Nature* **520**, 530–533.
- Touboul M. and Walker R. J. (2012) High precision tungsten isotope measurement by thermal ionization mass spectrometry. *Int. J. Mass Spectrom.* **309**, 109–117.
- Trinquier A. (2014) Gain Calibration Protocol for 10  $^{13}\Omega$  Resistor Current Amplifiers

- using the Certified Neodymium Standard JNdi-1 on the TRITON Plus. *A Thermo Fish. Sci. Tech. note TN30285*, 1–2.
- Tucker J. M. and Mukhopadhyay S. (2014) Evidence for multiple magma ocean outgassing and atmospheric loss episodes from mantle noble gases. *Earth Planet. Sci. Lett.* **393**, 254–265.
- Tusch J., Sprung P., van de Löcht J., Hoffmann J. E., Boyd A. J., Rosing M. T. and Münker C. (2019) Uniform  $^{182}\text{W}$  isotope compositions in Eoarchean rocks from the Isua region, SW Greenland: the role of early silicate differentiation and missing late veneer. *Geochim. Cosmochim. Acta* **257**, 284–310.
- Valley J. W. (2008) The Origin of Habitats. *Geol. Soc. Am.* **36**, 911–912.
- Valley J. W., Cavosie A. J., Ushikubo T., Reinhard D. A., Lawrence D. F., Larson D. J., Clifton P. H., Kelly T. F., Wilde S. A., Moser D. E. and Spicuzza M. J. (2014) Hadean age for a post-magma-ocean zircon confirmed by atom-probe tomography. *Nat. Geosci.* **7**, 219–223.
- Vervoort J. D., Plank T. and Prytulak J. (2011) The Hf-Nd isotopic composition of marine sediments. *Geochim. Cosmochim. Acta* **75**, 5903–5926.
- Viljoen M. J. and Viljoen R. P. (1969) Evidence for the Existence for a Mobile Extrusive Peridotitic Magma from the Komati Formation of the Onverwacht Group. *Geol. Soc. South Africa* **2**, 87–112.
- Vlastélic I., Menard G., Gannoun A., Piro J. L., Staudacher T. and Famin V. (2013) Magma degassing during the April 2007 collapse of Piton de la Fournaise: The record of semi-volatile trace elements (Li, B, Cu, In, Sn, Cd, Re, Tl, Bi). *J. Volcanol. Geotherm. Res.* **254**, 94–107.
- Vockenhuber C., Oberli F., Bichler M., Ahmad I., Quitte G., Meier M., Halliday A. N., Lee D. C., Kutschera W., Steier P., Gehrke R. J. and Helmer R. G. (2004) New half-life measurement of  $^{182}\text{Hf}$ : Improved chronometer for the early solar system. *Phys. Rev. Lett.* **93**, 4–7.
- Völkening J., Köppe M. and Heumann K. G. (1991) Tungsten isotope ratio determinations by negative thermal ionization mass spectrometry. *Int. J. Mass Spectrom. Ion Process.* **107**, 361–368.
- Walker R. J. (2009) Highly siderophile elements in the Earth, Moon and Mars: Update and implications for planetary accretion and differentiation. *Chemie der Erde - Geochemistry* **69**, 101–125.
- Wang Z. and Becker H. (2013) Ratios of S, Se and Te in the silicate Earth require a volatile-rich late veneer. *Nature* **499**, 328–331.
- Wänke H., Dreibus G. and Jagoutz E. (1984) Mantle Chemistry and Accretion History of the Earth. *Archaean Geochemistry*, 1–24.
- Wasson J. T. and Kallemeyn G. W. (1988) Compositions of chondrites. *Philos. Trans. R. Soc. London. Ser. A, Math. Phys. Sci.* **325**, 535–544.
- Waterton P., Pearson D. G., Kjarsgaard B., Hulbert L., Locock A., Parman S. and Davis B. (2017) Age, origin, and thermal evolution of the ultra-fresh ~ 1.9 Ga Winnipegosis Komatiites, Manitoba, Canada. *Lithos* **268–271**, 114–130.

- Weller M. B. and Lenardic A. (2012) Hysteresis in mantle convection: Plate tectonics systems. *Geophys. Res. Lett.* **39**, 3–7.
- Westrenen W. Van, Blundy J. D. and Wood B. J. (2000) Effect of Fe<sup>2+</sup> on garnet-melt trace element partitioning: experiments in FCMAS and quantification of crystal-chemical controls in natural systems. *Lith* **53**, 189–201.
- Weyer S., Münker C., Rehkämper M. and Mezger K. (2002) Determination of ultra-low Nb, Ta, Zr and Hf concentrations and the chondritic Zr/Hf and Nb/Ta ratios by isotope dilution analyses with multiple collector ICP-MS. *Chem. Geol.* **187**, 295–313.
- Wiemer D., Schrank C. E., Murphy D. T., Wenham L. and Allen C. M. (2018) Earth's oldest stable crust in the Pilbara Craton formed by cyclic gravitational overturns. *Nat. Geosci.* **11**, 357–361.
- Wilde S. a, Valley J. W., Peck W. H. and Graham C. M. (2001) Evidence from detrital zircons for the existence of continental crust and oceans on the Earth 4.4 Gyr ago. *Nature* **409**, 175–178.
- Willbold M., Elliott T. and Moorbath S. (2011) The tungsten isotopic composition of the Earth's mantle before the terminal bombardment. *Nature* **477**, 195–198.
- Willbold M., Mojzsis S. J., Chen H. W. and Elliott T. (2015) Tungsten isotope composition of the Acasta Gneiss Complex. *Earth Planet. Sci. Lett.* **419**, 168–177.
- Williams J. P. and Cieza L. A. (2011) Protoplanetary Disks and Their Evolution. *Annu. Rev. Astron. Astrophys.* **49**, 67–117.
- Wilson A. C. (1982) 1:250,000 Geological Map of Swaziland. *Geol. Surv. Mines Dep. Mbabane, Swazil.*
- Wingate M. T. D. (1999) Ion microprobe baddeleyite and zircon ages for Late Archaean mafic dykes of the Pilbara Craton, Western Australia. *Aust. J. Earth Sci.* **46**, 493–500.
- Workman R. K. (1998) Geochemical Characterization of Endmember Mantle Components. *PhD Thesis Massachuse*, 1–248.
- Workman R. K., Hart S. R., Jackson M., Regelous M., Farley K. A., Blusztajn J., Kurz M. and Staudigel H. (2004) Recycled metasomatized lithosphere as the origin of the Enriched Mantle II (EM2) end-member: Evidence from the Samoan Volcanic Chain. *Geochemistry, Geophys. Geosystems* **5**, 1–44.
- Wyman D. A. (2013) A critical assessment of neoproterozoic “plume only” geodynamics: Evidence from the superior province. *Precambrian Res.* **229**, 3–19.
- Yin Q. Z., Jacobsen S. B., Yamashita K., Blichert-Toft J., Télouk P. and Albarède F. (2002) A short timescale for terrestrial planet formation from Hf-W chronometry of meteorites. *Nature* **418**, 949–952.
- Yokoyama T., Makishima A. and Nakamura E. (1999) Evaluation of the coprecipitation of incompatible trace elements with fluoride during silicate rock dissolution by acid digestion. *Chem. Geol.* **157**, 175–187.
- Zegers van K. P. E. (2001) Middle Archean continent formation by crustal delamination. *Geology* **29**, 1083–1086.

- Zeh A., Gerdes A. and Millonig L. (2011) Hafnium isotope record of the Ancient Gneiss Complex , Swaziland , southern Africa : evidence for Archaean crust – mantle formation and crust reworking. *J. Geol. Soc. London.* **168**, 953–963.
- Zhang C., Holtz F., Koepke J., Wolff P. E., Ma C. and Bédard J. H. (2013) Constraints from experimental melting of amphibolite on the depth of formation of garnet-rich restites, and implications for models of Early Archean crustal growth. *Precambrian Res.* **231**, 206–217.

# Appendix

## Appendix A

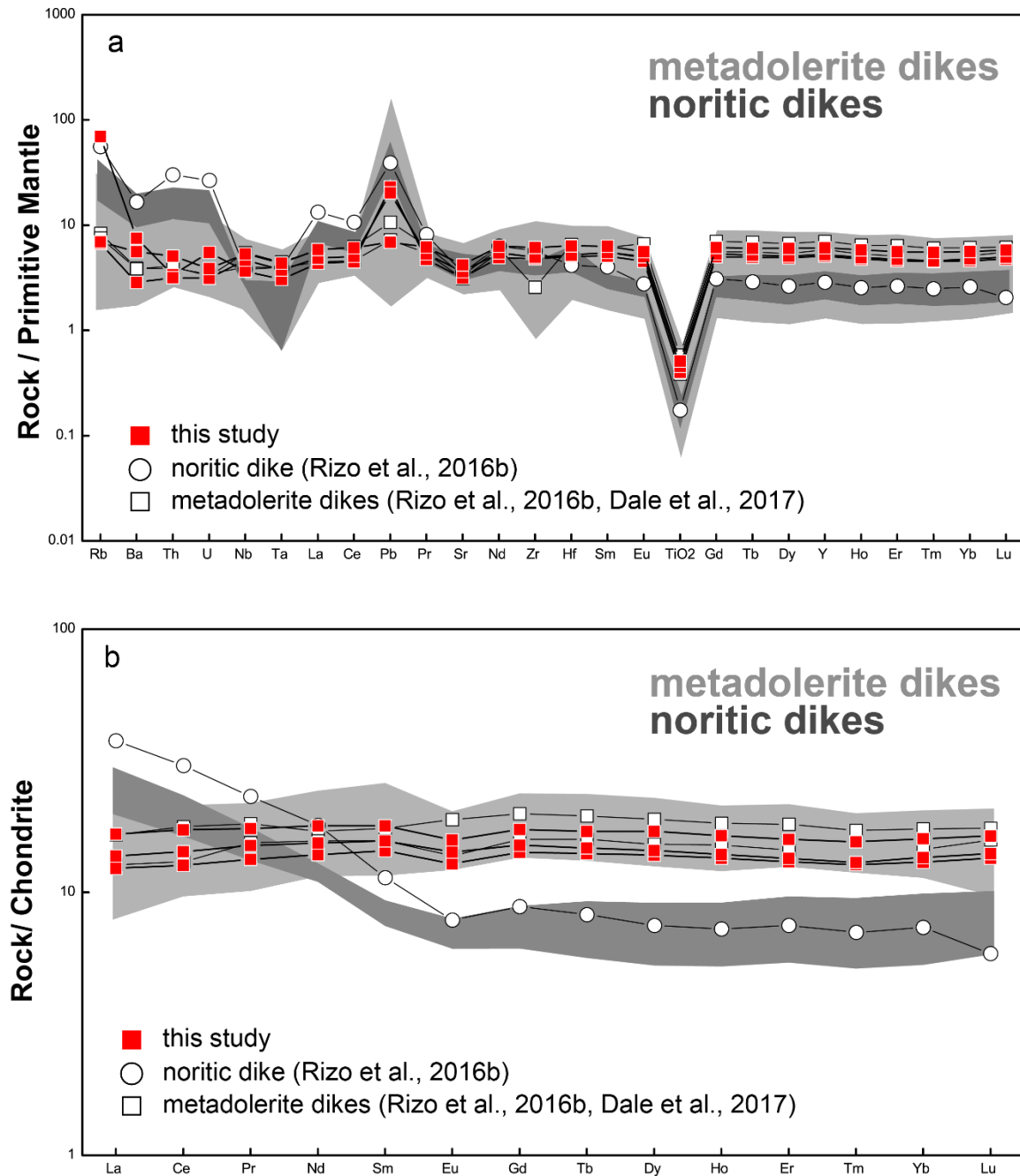


**Fig. A1:** Trace element patterns for noritic and doleritic Ameralik dikes that were analysed for their  $^{182}\text{W}$  isotope composition (red symbols for this study and open symbols for Rizo et al. (2016b) and Dale et al. (2017)). Bright and dark grey fields give the range of trace element patterns defined by doleritic and noritic Ameralik dikes, respectively (Rizo et al., 2012; Dale et al., 2017; Saji et al., 2018). (a): Incompatible trace element spidergram normalized to primitive mantle. (b): chondrite-normalized REE patterns. Values for primitive mantle and chondrite are taken from Palme and O'Neill (2014).

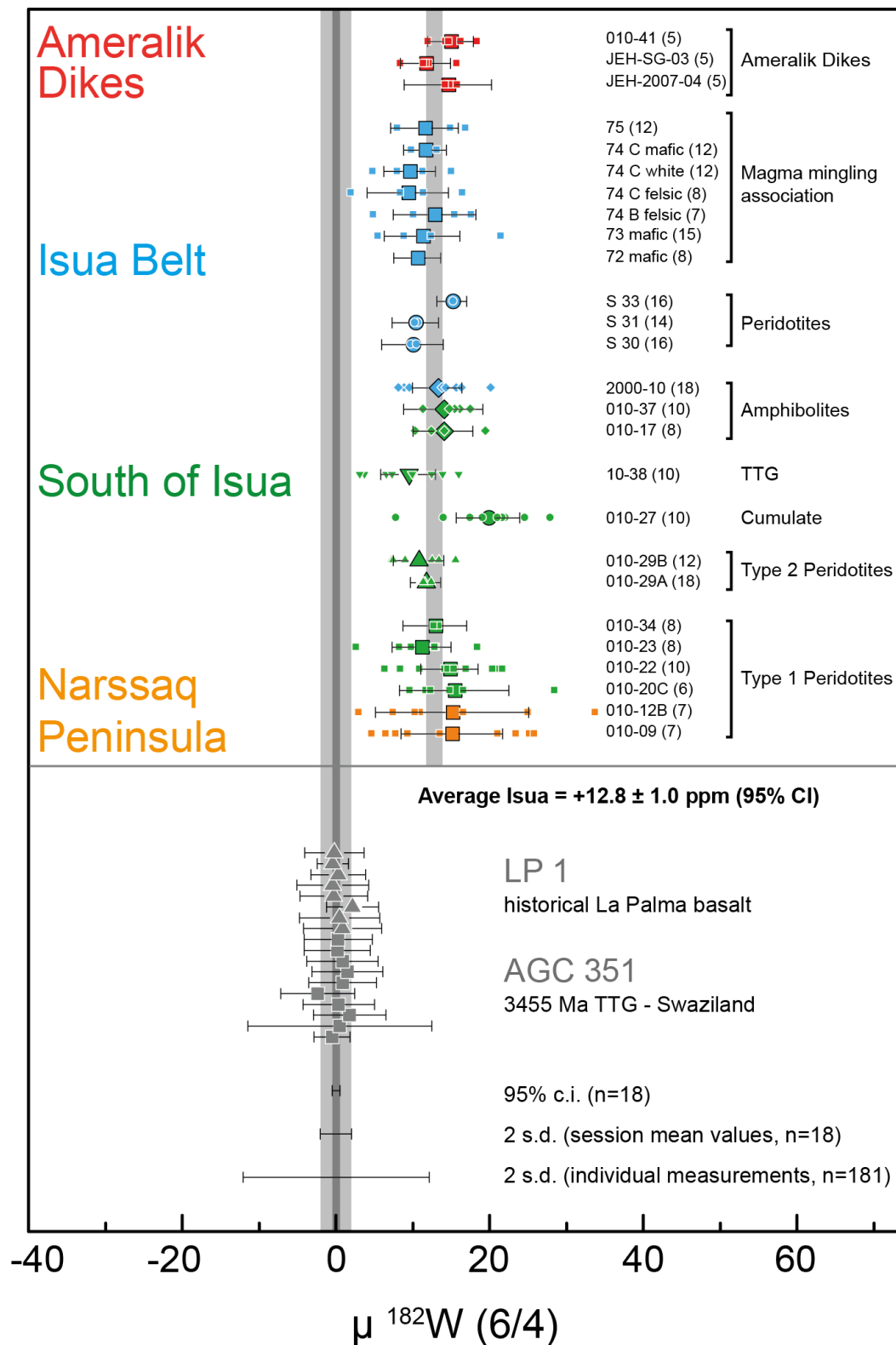


**Fig. A2:** High precision  $\mu^{182}\text{W}$  isotope measurements for rocks from southern West Greenland (upper panel) and our in-house rock standards (lower panel). Larger symbols correspond to the average for repeated measurements ( $n$ ) of multiple digestions, which are shown by smaller symbols. Uncertainties for the sample averages are given by the corresponding 95% CI. Uncertainties for individual digestions are omitted for visual clarity. The grey shaded areas defined by the rock standards correspond to the 2 SD and 95% CI of the repeated analysis of our in-house rock standards LP1 and AGC 351. The grey bar defined by the Greenland samples defines the average  $\mu^{182}\text{W}$  for Eoarchean rocks and Paleoarchean Ameralik dikes and gives the corresponding 95% CI for all 26 samples ( $+12.8 \pm 1.0$  ppm).



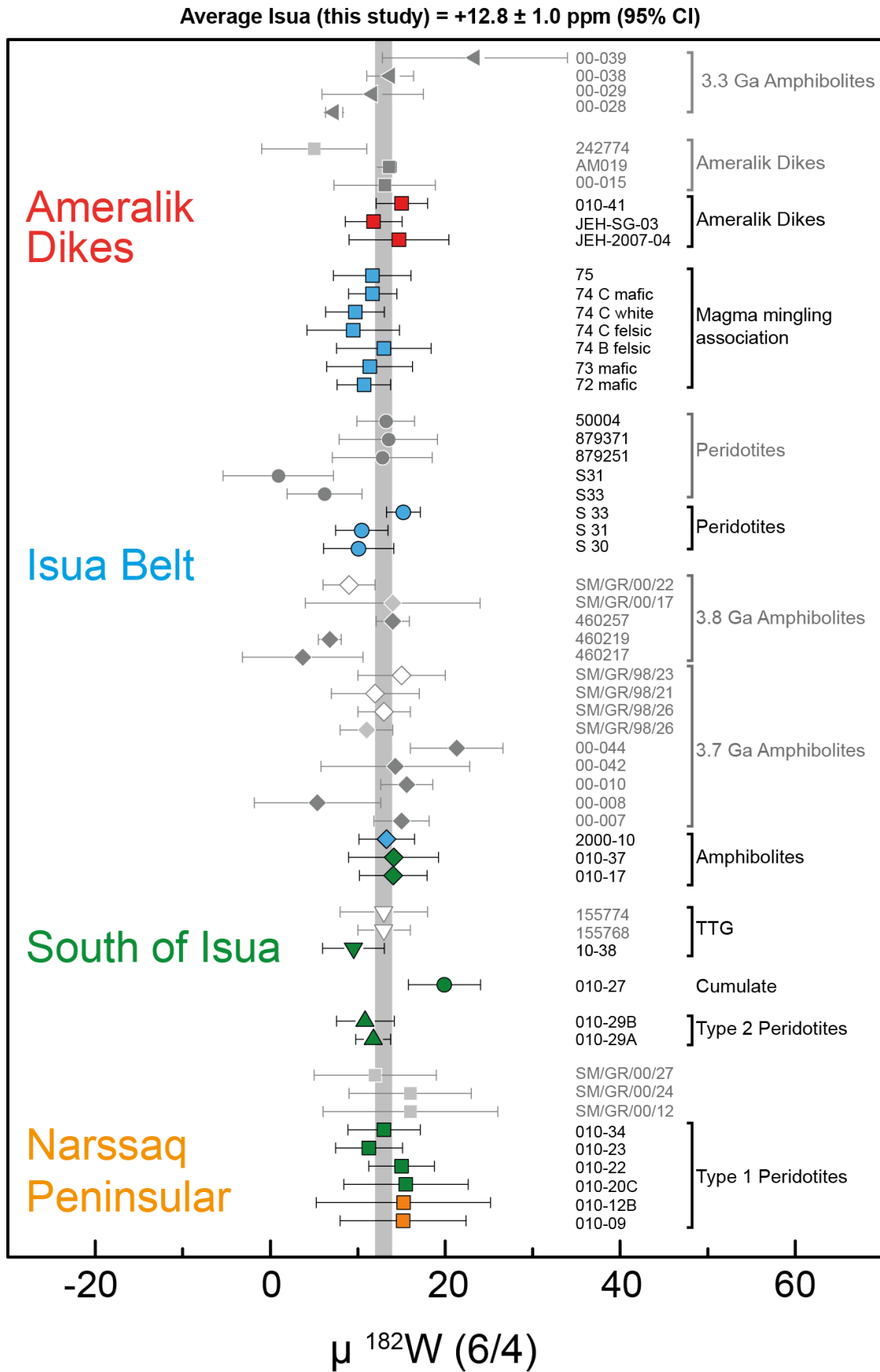


**Fig. A3:** Compilation of  $^{182}\text{W}$  isotope data for rocks from SW Greenland from our and previous studies. Literature data taken from Rizo et al. (2016b) (dark grey symbols), Dale et al. (2017) (light grey symbols), and Willbold et al. (2011) (open symbols).

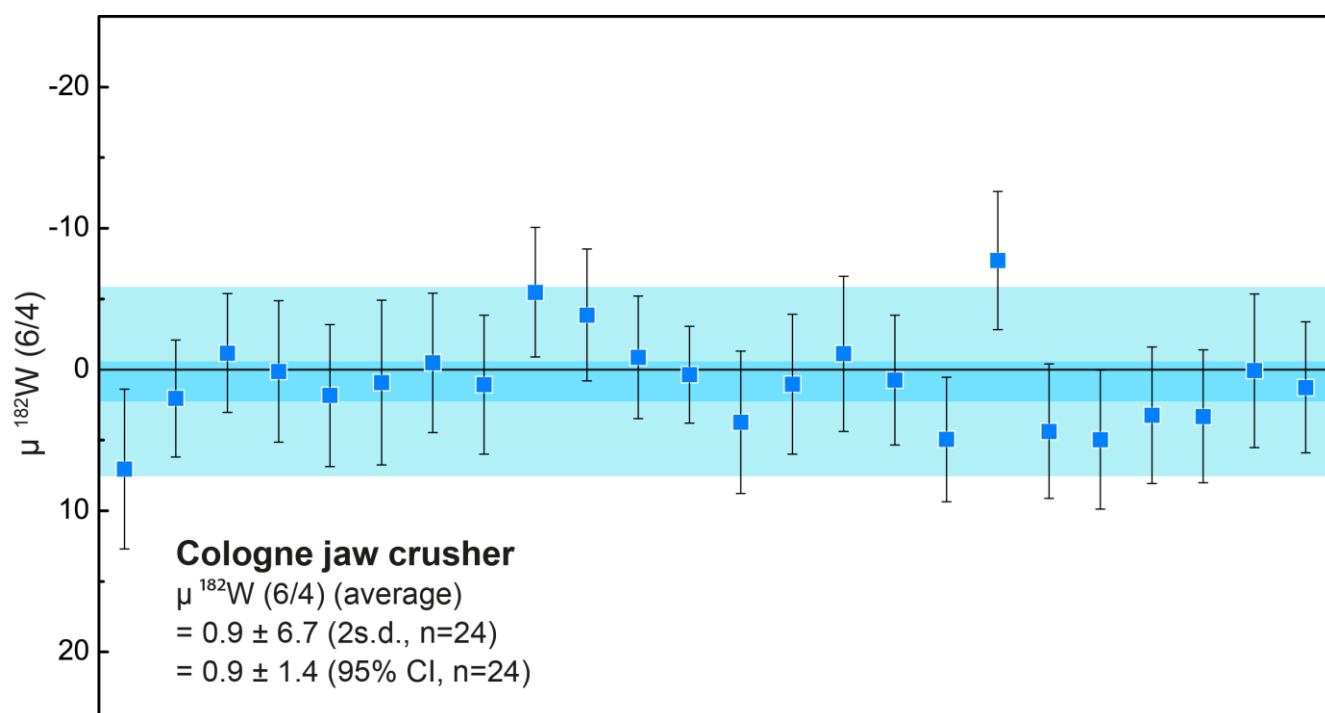


**Fig. A4:**  $^{182}\text{W}$  isotope composition of the jaw crusher material that is used in the rock-preparation facility at the University of Cologne. The bars in pale and bright blue colors represent the 2 SD and 95% CI of the repeated analysis (n=24), respectively.

Sample	JEH-2007-04	JEH-SG-03	010-41	010-41 duplicate	10-09	10-12B	10-20C
Rock	Amphibolite Ameralik dike	Amphibolite Ameralik dike	Amphibolite Ameralik dike	Amphibolite Ameralik dike	Ultramafic Peridotite NUB	Ultramafic Peridotite NUB	Ultramafic Peridotite SOISB
Longitude [N]	65° 5'50.82"	65° 4'27.72"	65° 6'36.72"		63° 58'06.0"	63° 58'21.1"	65° 0'44.4"
Latitude [W]	50° 7'32.64"	50° 9'8.40"	50° 9'57.78"		51° 28'17.3"	51° 28'39.4"	50° 14'58.6"
SiO <sub>2</sub>	49.2	49.5	49.4	n.d.	39.5	43.5	41.3
TiO <sub>2</sub>	0.856	0.971	1.09	n.d.	0.088	0.0636	0.081
Al <sub>2</sub> O <sub>3</sub>	14.2	14.3	13.9	n.d.	1.92	1.70	1.25
Fe <sub>2</sub> O <sub>3</sub>	13.4	13.7	14.6	n.d.	9.81	8.43	11.3
MnO	0.210	0.216	0.232	n.d.	0.137	0.127	0.153
MgO	7.80	7.44	6.62	n.d.	42.5	41.8	40.9
CaO	10.5	11.2	10.9	n.d.	1.66	1.99	2.33
K <sub>2</sub> O	0.663	0.161	0.199	n.d.	0.032	0.0072	0.016
Na <sub>2</sub> O	1.69	1.94	2.10	n.d.	n.d.	n.d.	n.d.
P <sub>2</sub> O <sub>5</sub>	0.0652	0.0724	0.0800	n.d.	0.015	0.0078	0.008
L.O.I.	1.91	1.26	0.690	n.d.	3.73	1.39	3.23
Total	100.7	100.8	100.0	n.d.	100.2	99.9	100.9
Mg#	56.1	54.4	50.0	n.d.	90.5	91.6	88.9
Li	n.d.	n.d.	n.d.	n.d.	10.6	7.74	5.71
V	260	275	306	304	43.5	30.1	29.6
Cr	220	164	86.8	87.0	5996	5397	1834
Co	52.2	48.6	50.5	50.7	115	99.2	122
Ni	114	108	80.4	79.3	2116	2539	2410
Cu	54.2	29.9	58.1	n.d.	0.396	1.27	21.5
Zn	105	106	117	n.d.	54.5	66.4	55.1
Ga	16.4	16.9	17.4	17.4	2.31	1.85	1.67
Rb	42.2	4.05	4.21	4.24	2.76	0.281	0.280
Sr	69.4	79.2	91.9	92.4	1.73	3.59	7.63
Y	21.0	21.7	25.2	25.5	1.72	2.33	1.83
Zr	49.4	51.2	63.4	n.d.	3.30	2.79	4.58
Nb	2.17	2.77	3.18	n.d.	<i>0.102</i>	<i>0.170</i>	<i>0.191</i>
<b>Mo</b>	<b>0.202</b>	<b>0.177</b>	<b>0.259</b>	<b>0.266</b>	<b>0.256</b>	<b>0.293</b>	<b>0.411</b>
Sn	n.d.	n.d.	n.d.	n.d.	0.131	0.138	0.274
Cs	n.d.	n.d.	n.d.	n.d.	0.307	0.0411	0.0575
Ba	51.7	19.5	38.3	38.4	1.38	0.456	0.234
La	2.98	3.31	4.02	3.99	0.222	0.509	0.413
Ce	7.85	8.83	10.7	10.5	0.610	1.21	1.15
Pr	1.25	1.41	1.64	1.64	0.100	0.179	0.189
Nd	6.57	7.27	8.47	8.40	<i>0.440</i>	<i>0.730</i>	<i>0.920</i>
Sm	2.21	2.40	2.75	2.75	<i>0.166</i>	<i>0.237</i>	<i>0.304</i>
Eu	0.755	0.837	0.928	0.920	0.0773	0.0813	0.124
Gd	2.93	3.12	3.59	3.54	0.273	0.360	0.402
Tb	0.532	0.559	0.646	0.643	0.0494	0.0654	0.0670
Dy	3.54	3.69	4.35	4.34	0.340	0.441	0.413
Ho	0.761	0.786	0.927	0.920	0.0723	0.096	0.0810
Er	2.16	2.22	2.63	2.63	0.206	0.278	0.219
Tm	0.332	0.338	0.406	0.403	0.0321	0.0435	0.0321
Yb	2.19	2.28	2.70	2.68	0.218	0.291	0.210
Lu	0.337	0.351	0.410	n.d.	<i>0.0307</i>	<i>0.0386</i>	<i>0.0293</i>
Hf	1.53	1.56	1.92	n.d.	<i>0.122</i>	<i>0.0897</i>	<i>0.144</i>
Ta	0.131	0.162	0.187	n.d.	0.0069	0.00753	0.0089
W	0.419	0.135	0.156	n.d.	0.0604	0.115	0.281
Pb	4.27	3.76	1.27	1.28	0.446	0.311	0.809
Th	0.287	0.269	0.432	n.d.	0.0226	0.0675	0.0444
U	0.126	0.0718	0.0881	n.d.	0.0163	0.0624	0.0368

**Table A1:** Major and trace element data for rock samples from the Isua Supracrustal Belt (ISB), the area south of it (SOISB), the Narssaq Ultramafic Body (NUB), and international rock standard BHVO-2. Data for sample 2000-10 are taken from Polat et al. (2003) and Hoffmann et al. (2011), for sample 10 - 38 from Hoffmann et al. (2014). Data for the ultramafic rocks from NUB and SOISB are taken from van de Löcht et al. (2018a), and data for samples from the magma mingling association are taken from Boyd (2018). Data in italics were determined by isotope dilution.

Sample	10-22	10-23	10-34	10-29A	10-29B	10-27	10-17
Rock	Ultramafic	Ultramafic	Ultramafic	Ultramafic	Ultramafic	Ultramafic	Amphibolite
	Peridotite SOISB	Peridotite SOISB	Peridotite SOISB	Peridotite SOISB	Peridotite SOISB	Cumulate SOISB	SOISB
Longitude [N]	65° 0'53.7"	65° 0'55.3"	65° 0'44.7"	65° 0'59.8"	65° 0'59.8"	65° 2'57.9"	65° 2'28.1"
Latitude [W]	50° 15'0.4"	50° 14'59.5"	50° 11'57.9"	50° 12'34.8"	50° 12'34.8"	50° 14'15.0"	50° 13'18.7"
SiO <sub>2</sub>	40.9	39.9	42.6	44.2	41.6	45.6	50.4
TiO <sub>2</sub>	0.030	0.040	0.077	0.122	0.13	0.177	0.794
Al <sub>2</sub> O <sub>3</sub>	0.382	0.474	2.38	3.67	6.42	5.30	14.0
Fe <sub>2</sub> O <sub>3</sub>	10.0	11.2	8.69	9.34	8.34	9.83	13.3
MnO	0.149	0.156	0.152	0.134	0.13	0.161	0.190
MgO	47.5	46.2	36.5	40.9	34.2	31.6	7.29
CaO	0.460	0.398	6.19	0.751	5.61	5.66	9.81
K <sub>2</sub> O	n.d.	0.004	0.032	0.070	0.13	0.059	0.306
Na <sub>2</sub> O	n.d.	n.d.	0.005	n.d.	0.84	0.030	2.21
P <sub>2</sub> O <sub>5</sub>	0.010	0.010	0.013	0.012	n.d.	0.015	0.0649
L.O.I.	0.79	0.88	3.48	1.61	2.34	1.46	0.58
Total	100.4	99.9	100.5	101.3	100.2	100.3	98.5
Mg#	91.3	90.1	90.2	90.6	90.0	87.6	54.7
Li	8.23	6.61	5.83	6.41	6.52	7.25	34.8
V	16.71	27.1	55.6	80.1	91.0	90.7	261
Cr	1549	4432	1642	2627	2344	2728	287
Co	130	141	91.3	93.3	87.7	79.2	52.5
Ni	2858	3140	1673	2549	1647	1510	95.6
Cu	1.07	5.11	34.1	6.96	12.7	1.45	99.8
Zn	47.6	67.0	55.1	52.9	64.8	35.3	94.8
Ga	0.621	1.04	3.05	4.17	5.24	3.13	19.5
Rb	n.d.	0.271	0.432	0.419	0.765	0.410	2.48
Sr	0.411	1.22	37.9	24.0	28.2	25.7	124
Y	0.766	0.348	6.79	2.89	4.34	4.88	20.8
Zr	0.586	1.13	3.12	3.57	5.12	7.51	53.4
Nb	0.0603	0.0757	0.0967	0.119	0.185	0.224	2.14
<b>Mo</b>	<b>0.310</b>	<b>0.322</b>	<b>0.215</b>	<b>0.379</b>	<b>0.290</b>	<b>0.187</b>	<b>0.246</b>
Sn	n.d.	0.215	0.508	0.215	0.364	0.115	0.623
Cs	n.d.	0.0586	0.0465	n.d.	n.d.	n.d.	0.0346
Ba	n.d.	0.939	0.156	2.27	3.35	1.98	24.4
La	0.0961	0.129	0.628	0.244	0.485	0.419	3.82
Ce	0.256	0.274	1.83	0.426	0.879	1.30	9.63
Pr	0.0463	0.0396	0.324	0.0565	0.106	0.230	1.46
Nd	0.211	0.146	1.58	0.220	0.360	1.08	7.44
Sm	0.0832	0.0425	0.649	0.0927	0.133	0.449	2.37
Eu	0.0352	n.d.	0.256	0.0820	0.0755	0.161	0.782
Gd	0.142	0.0726	1.16	0.238	0.361	0.690	3.13
Tb	0.0261	0.0120	0.211	0.0564	0.0846	0.129	0.567
Dy	0.169	0.0753	1.40	0.467	0.705	0.909	3.81
Ho	0.0348	0.0160	0.285	0.117	0.175	0.199	0.797
Er	0.098	0.0472	0.754	0.368	0.551	0.583	2.24
Tm	0.0158	n.d.	0.101	0.0604	0.0893	0.0908	0.332
Yb	0.102	n.d.	0.581	0.426	0.618	0.617	2.16
Lu	0.0139	0.0088	0.0688	0.0625	0.0855	0.0886	0.327
Hf	0.0224	0.0344	0.111	0.134	0.200	0.254	1.48
Ta	0.00265	0.00395	0.00545	0.00391	0.0064	0.0129	0.142
W	0.401	0.387	5.05	1.40	0.207	0.0473	0.201
Pb	0.895	0.299	0.748	2.69	2.04	1.84	4.95
Th	0.0110	0.0165	0.0316	0.0139	0.0688	0.0273	0.486
U	0.0314	0.0221	0.0319	0.0796	0.179	0.00753	0.144

Table A1: continued

Sample	10-37	2000-10	S 30	S 31	S 33	10-38	72 mafic
Rock	Amphibolite SOISB	Amphibolite ISB	Ultramafic Cumulate lens A	Ultramafic Cumulate lens A	Ultramafic Cumulate lens A	TTG SOISB	Amphibolite mingling association
Longitude [N]	65° 0'21.8"	65° 5'60"	65° 8'21.90''	65° 8'21.90''	65° 8'21.90''	65° 0'49.62"	65° 5'3.06"
Latitude [W]	50° 12'26.3"	50°	50° 9'7.80''	50° 9'7.80''	50° 9'7.80''	50° 13'44.64"	50° 10'15.00"
SiO2	51.6	51.2	40.4	41.2	31.5	68.6	50.0
TiO2	0.688	0.62	0.0412	0.0588	0.0619	0.250	0.5
Al2O3	9.24	8.38	0.625	2.01	1.23	16.7	6.1
Fe2O3	12.2	12.8	8.92	7.15	8.09	2.15	10.3
MnO	0.211	0.19	0.113	0.0519	0.0954	0.040	0.23
MgO	11.1	14.4	46.5	39.1	33.1	0.87	14.3
CaO	12.1	10.0	0.139	0.0369	7.05	3.85	14.5
K2O	0.442	2.19	n.d.	n.d.	n.d.	0.98	0.14
Na2O	1.47	0.07	n.d.	n.d.	n.d.	5.26	1.02
P2O5	0.0482	0.06	0.0088	0.0104	0.0089	0.06	0.02
L.O.I.	1.34	0.98	3.29	10.7	19.5	0.42	3.29
Total	100.6	101.0	100.0	100.4	100.7	99.2	100.3
Mg#	66.8	71.2	92.0	92.3	90.0	47.1	75.4
Li	14.2	n.d.	1.83	0.671	0.209	44.5	n.d.
V	219	149	19.2	62.7	32.4	18.1	210
Cr	871	1621	720	727	470	25.8	n.d.
Co	54.1	80	108	77.8	62.0	3.69	53.8
Ni	235	516	2900	2386	2001	12.6	5.5
Cu	49.2	n.d.	1.20	1.19	7.25	11.5	0.3
Zn	80.0	n.d.	46.1	40.6	33.1	51.6	2
Ga	12.5	n.d.	0.942	2.42	1.65	23.9	8.7
Rb	3.67	1.9	0.0440	0.0853	0.137	36.4	0.6
Sr	106	131	0.896	0.347	31.2	453	143
Y	17.1	12.1	0.929	3.15	4.48	4.95	11.5
Zr	48.6	55.6	1.77	3.41	3.54	121	27.8
Nb	2.33	1.4	0.119	0.382	0.132	1.43	1.8
<b>Mo</b>	<b>0.170</b>	<b>n.d.</b>	<b>0.303</b>	<b>0.276</b>	<b>0.237</b>	<b>0.152</b>	<b>0.1</b>
Sn	0.599	n.d.	0.0853	0.164	0.255	0.144	n.d.
Cs	0.0204	n.d.	0.0365	0.0756	0.163	2.03	n.d.
Ba	15.1	8.2	0.261	0.328	0.488	141	10
La	4.94	3.84	0.130	0.194	1.46	6.63	2.5
Ce	11.3	9.24	0.340	0.621	3.91	12.7	6.4
Pr	1.65	1.35	0.0521	0.117	0.545	1.65	0.89
Nd	8.14	5.80	0.257	0.694	2.50	6.82	4.6
Sm	2.48	1.73	0.0900	0.314	0.680	1.58	1.2
Eu	0.762	0.55	0.0140	0.0362	0.218	0.538	0.38
Gd	3.02	2.09	0.115	0.441	0.804	1.42	1.67
Tb	0.524	0.31	0.0218	0.0879	0.133	0.197	0.31
Dy	3.37	2.23	0.150	0.595	0.834	1.01	1.92
Ho	0.683	0.47	0.0350	0.1244	0.167	0.179	0.44
Er	1.86	1.2	0.110	0.335	0.435	0.488	1.26
Tm	0.270	0.17	0.0192	0.0481	0.0588	0.0702	0.18
Yb	1.74	1.24	0.139	0.304	0.345	0.447	1.09
Lu	0.263	0.167	0.0242	0.0470	0.0483	0.0552	0.17
Hf	1.30	1.59	0.0515	0.0877	0.113	3.28	0.9
Ta	0.166	0.12	0.00768	0.0208	0.0118	0.0780	0.1
W	0.150	0.145	0.383	0.662	0.657	0.102	4.26
Pb	4.25	1.3	0.33	0.302	0.970	10.7	0.4
Th	0.598	0.666	0.0347	0.134	0.122	0.887	0.476
U	0.158	0.131	0.0108	0.106	0.144	0.380	0.284

Table A1: continued

Sample	73 mafic	74B felsic	74C felsic	74C white	74C mafic	75	BHVO-2
Rock	Amphibolite mingling association	Tonalite mingling association	Tonalite mingling association	Leucosome mingling association	Amphibolite mingling association	Tonalite mingling association	Basalt Hawaii
Longitude [N]	65° 5'2.76"	65° 5'2.46"	65° 5'2.46"	65° 5'2.46"	65° 5'2.46"	65° 5'1.98"	
Latitude [W]	50° 10'14.94"	50° 10'15.30"	50° 10'15.30"	50° 10'15.30"	50° 10'15.30"	50° 10'14.88"	
SiO2	53.8	67.3	67.0	79.4	52.7	66.05	n.d.
TiO2	1.02	0.46	0.45	0.06	0.5	0.55	n.d.
Al2O3	13.2	16.0	16.2	12.4	7.06	16.57	n.d.
Fe2O3	16.3	3.21	3.53	0.48	12.6	4.38	n.d.
MnO	0.18	0.07	0.08	0.01	0.28	0.08	n.d.
MgO	4.01	2.91	2.99	0.46	16.8	1.89	n.d.
CaO	7.87	3.97	4.29	2.68	7.62	4.23	n.d.
K2O	0.43	0.04	0.05	0.03	0.1	1.54	n.d.
Na2O	2.37	5.76	5.67	4.63	1.19	4.11	n.d.
P2O5	0.05	0.13	0.13	0.01	0.01	0.15	n.d.
L.O.I.	0.11	0.25	0.22	0.02	1.27	0.35	n.d.
Total	99.3	100.0	100.6	100.2	100.1	99.9	n.d.
Mg#	35.1	66.6	65.1	67.8	74.6	48.7	n.d.
Li	n.d.	n.d.	n.d.	n.d.	n.d.	n.d.	4.57
V	259	54	61	n.d.	150	66	315
Cr	n.d.	n.d.	n.d.	n.d.	n.d.	n.d.	283
Co	52.6	16.3	15.9	2.7	71.6	12	44.5
Ni	16	16.3	28.8	5.8	86.6	23.1	119
Cu	253	1.7	2.3	2.5	1.5	5.3	131
Zn	12	4	3	n.d.	12	49	101
Ga	19.3	13.6	14.2	10.4	10.8	19.9	21.7
Rb	2.9	0.1	0.3	n.d.	1.4	67.1	9.07
Sr	300	489	476	365	61.5	494	369
Y	18.9	7	8.1	4.2	14.8	10.7	25.1
Zr	67.1	114	125	66.1	31.9	139	167
Nb	2.5	3.7	3.5	3.5	3.1	4.6	17.8
<b>Mo</b>	<b>0.2</b>	<b>0.5</b>	<b>0.1</b>	<b>1.9</b>	<b>n.d.</b>	<b>0.2</b>	<b>3.57</b>
Sn	1	n.d.	n.d.	n.d.	n.d.	n.d.	1.74
Cs	n.d.	n.d.	n.d.	n.d.	0.1	2.8	0.111
Ba	39	30	36	26	10	321	129
La	4.2	18.4	24.5	27	5.8	34.1	15.3
Ce	9.8	40	47.5	53.4	10.3	68.3	37.1
Pr	1.31	4.15	4.89	5.03	1.83	7.67	5.29
Nd	6.5	15	17.2	15.3	8.1	28.9	24.4
Sm	2.44	2.39	2.54	2.07	2.12	4.57	6.13
Eu	0.91	0.54	0.6	0.33	0.5	1	2.09
Gd	3.3	1.79	1.94	1.44	2.51	3.26	6.20
Tb	0.56	0.24	0.27	0.16	0.41	0.4	0.933
Dy	3.45	1.3	1.48	0.81	2.5	1.96	5.28
Ho	0.74	0.24	0.29	0.15	0.53	0.36	0.971
Er	2.05	0.69	0.83	0.39	1.53	0.94	2.44
Tm	0.28	0.1	0.13	0.06	0.24	0.14	0.331
Yb	1.86	0.63	0.73	0.46	1.49	0.86	2.01
Lu	0.27	0.09	0.12	0.08	0.21	0.13	0.276
Hf	1.9	3	3.2	3.9	1	3.8	4.12
Ta	0.2	0.3	0.2	0.8	0.2	0.3	1.10
W	0.310	0.668	0.446	0.471	6.36	0.732	0.299
Pb	0.7	1.6	1.5	3.3	0.4	1.8	1.75
Th	1.40	2.64	4.76	7.35	0.816	2.81	1.23
U	0.264	0.683	0.687	2.88	0.253	0.828	0.490

Table A1: continued

## Appendix B

Group / Supersuite	Subgroup	Warrawoona					
		Coonterunah					
Formation	Mount Webber	Tabletop					Coucal
Age in Ma	3578	3525					3515
Rock Type	Gabbro	Basalt	Pillow basalt	Pillow basalt	Komatiite	Komatiite	Pillow basalt
Longitude [S]	21°28.426'	21°06.440'	21°06.440'	21°06.37'			21°07.276'
Latitude [E]	119°20.691'	119°03.373'	119°03.373'	119°03.418'			119°02.505'
Sample name	<b>Pil 17-007</b>	<b>Pil 16-054a</b>	<b>Pil 16-54B</b>	Pil 16-55	179756 <sup>a</sup>	179757 <sup>a</sup>	<b>Pil 16-56</b>
SiO <sub>2</sub>	49.4	47.4	48.4	51.9	43.7	41.5	46.1
TiO <sub>2</sub>	0.866	1.07	0.963	0.944	0.251	0.224	1.99
Al <sub>2</sub> O <sub>3</sub>	14.1	14.9	13.7	14.5	5.74	5.03	12.4
Fe <sub>2</sub> O <sub>3</sub>	12.3	14.0	14.7	13.2	10.0	10.2	17.1
MnO	0.269	0.234	0.281	0.199	0.141	0.152	0.188
MgO	5.38	5.90	6.48	7.04	26.9	29.9	4.69
CaO	12.1	11.3	12.1	11.4	5.24	2.95	6.99
K <sub>2</sub> O	0.876	2.34	0.193	0.257	0.0090	0.0050	0.135
Na <sub>2</sub> O	3.35	0.657	1.99	2.18	0.0750	0.0240	2.63
P <sub>2</sub> O <sub>5</sub>	0.0697	0.0832	0.0763	0.0779	0.0230	0.0190	0.270
L.O.I.	0.44	2.25	1.77	1.20	7.64	9.71	7.92
Total	99.1	100.1	100.7	102.9	100.1	99.7	100.5
Mg#	49.0	48.1	49.2	54.0	85.5	86.6	37.7
Li	40.4	15.3	13.5	9.56	2.60	1.09	23.1
Sc	39.4	46.0	40.3	37.2	21.4	19.4	37.7
V	297	332	294	269	111	99.3	313
Cr	94.4	227	218	184	3449	3976	105
Co	54.0	47.6	52.6	52.4	83.8	91.2	51.0
Ni	77.6	115	103	161	1092	1334	54.9
Cu	35.0	40.6	5.85	68.2	7.69	13.2	71.8
Zn	113	115	135	99.6	61.2	68.5	179
Ga	16.4	19.1	17.4	18.7	5.27	4.58	20.6
Rb	15.7	29.1	5.59	7.86	0.106	0.0759	4.69
Sr	139.4	94.6	92.2	191	49.2	13.0	132
Y	19.9	26.0	23.1	23.1	5.21	4.08	41.2
<b>Zr</b>	<b>54.6</b>	<b>61.9</b>	<b>57.3</b>	<b>56.5</b>	<b>13.8</b>	<b>10.8</b>	<b>174</b>
<b>Nb</b>	<b>2.80</b>	<b>2.87</b>	<b>2.49</b>	<b>2.42</b>	<b>0.556</b>	<b>0.418</b>	<b>8.07</b>
Mo	0.629	0.323	0.260	0.406	0.146	0.167	0.591
Cd	0.196	0.145	0.134	0.171	0.0976	0.0645	0.263
Sn	0.315	0.745	0.779	0.755	0.680	0.635	2.73
Sb	0.0705	0.113	0.232	0.229	0.182	0.0819	0.0550
Cs	0.317	0.587	0.147	0.208	0.0745	0.0505	0.653
Ba	49.5	57.9	30.9	41.8	7.51	5.07	33.8
La	4.33	3.41	3.09	3.58	0.856	0.620	12.7
Ce	10.9	9.07	8.19	8.97	2.27	1.46	30.3
Pr	1.57	1.44	1.28	1.38	0.342	0.241	4.28
Nd	8.04	7.48	6.63	7.03	1.75	1.27	20.1
Sm	2.43	2.48	2.14	2.26	0.573	0.413	5.44
Eu	0.811	0.923	0.805	0.838	0.131	0.0963	1.55
Gd	2.98	3.31	2.85	2.93	0.721	0.557	6.27
Tb	0.517	0.613	0.534	0.539	0.132	0.101	1.06
Dy	3.42	4.21	3.67	3.66	0.899	0.684	6.81
Ho	0.723	0.914	0.807	0.795	0.199	0.152	1.43
Er	2.06	2.65	2.33	2.30	0.572	0.447	4.05
Tm	0.312	0.406	0.359	0.352	0.0914	0.0703	0.612
Yb	2.06	2.76	2.40	2.40	0.632	0.481	4.07
Lu	0.322	0.433	0.380	0.373	0.100	0.0790	0.632
<b>Hf</b>	<b>1.62</b>	<b>1.85</b>	<b>1.70</b>	<b>1.66</b>	<b>0.410</b>	<b>0.326</b>	<b>4.49</b>
<b>Ta</b>	<b>0.181</b>	<b>0.161</b>	<b>0.156</b>	<b>0.148</b>	<b>0.0347</b>	<b>0.0243</b>	<b>0.532</b>
<b>W</b>	<b>0.540</b>	<b>1.29</b>	<b>0.432</b>	<b>0.146</b>	<b>0.0787</b>	<b>0.0412</b>	<b>0.385</b>
Tl	0.199	0.315	0.0786	0.107	0.00654	0.00571	0.0591
Pb	9.01	0.929	0.555	1.25	0.290	0.176	3.72
<b>Th</b>	<b>0.426</b>	<b>0.329</b>	<b>0.294</b>	<b>0.297</b>	<b>0.0693</b>	<b>0.0396</b>	<b>1.89</b>
<b>U</b>	<b>0.453</b>	<b>0.0803</b>	<b>0.0715</b>	<b>0.0756</b>	<b>0.0144</b>	<b>0.0189</b>	<b>0.517</b>

**Table B1: Major, minor and trace element data as well as GPS coordinates of sample localities for rock samples from the Pilbara Craton.** Data in bold and italic (Zr, Nb, Hf, Ta, W, Th, and U) were determined by isotope dilution. <sup>a</sup> major elements from Maier et al, (2009). n.d. = not determined

Group / Supersuite	Warrawoona				
Subgroup	Talga Talga				
Formation	North Star Basalt				Dresser Fm
Age in Ma	3490				3480
Rock Type	Basalt	Basalt	Basalt	Komatiite	Komatiitic basalt
Longitude [S]	21°00.465'	21°22.873'	21°10.080'	21°09.047'	21°5.566920
Latitude [E]	119°49.908'	119°33.614'	119°23.982'	119°24.508'	119°26.761140
Sample name	<b>Pil 16-44A</b>	<b>Pil 16-37A</b>	Pil 16-17	Pil 16-020b	Pil 16-21
SiO <sub>2</sub>	46.1	50.8	46.6	47.6	51.4
TiO <sub>2</sub>	1.41	1.11	1.24	1.07	0.530
Al <sub>2</sub> O <sub>3</sub>	13.0	9.00	13.2	6.3	12.3
Fe <sub>2</sub> O <sub>3</sub>	14.9	14.8	15.2	17.2	8.8
MnO	0.196	0.225	0.265	0.320	0.130
MgO	6.26	9.59	5.11	12.6	11.6
CaO	7.56	12.5	10.9	12.2	7.66
K <sub>2</sub> O	0.195	0.233	0.416	0.791	0.0541
Na <sub>2</sub> O	2.28	2.24	3.19	0.145	0.435
P <sub>2</sub> O <sub>5</sub>	0.108	0.0942	0.0972	0.0789	0.0478
L.O.I.	8.88	4.63	7.21	2.95	10.7
Total	100.9	105.4	103.6	101.3	103.8
Mg#	48.1	58.7	42.5	61.6	74.5
Li	58.7	17.2	17.2	9.41	33.2
Sc	35.0	29.2	19.4	32.1	40.7
V	312	219	203	224	224
Cr	170	686	26.1	305	1129
Co	51.3	59.1	58.4	77.6	41.9
Ni	97.5	196	90.0	245	152
Cu	7.11	169	182	41.8	29.5
Zn	111	90.3	108	140	65.7
Ga	17.6	12.5	14.9	10.2	11.3
Rb	9.71	4.00	6.29	2.30	2.74
Sr	133	115	220	46.8	64.4
Y	26.7	22.3	17.8	16.1	11.9
<b>Zr</b>	<b>78.6</b>	<b>78.3</b>	<b>67.2</b>	<b>63.7</b>	<b>31.5</b>
<b>Nb</b>	<b>3.93</b>	<b>4.20</b>	<b>5.20</b>	<b>5.59</b>	<b>1.33</b>
Mo	0.0965	0.332	0.246	0.251	0.151
Cd	0.177	0.212	0.170	0.157	0.112
Sn	0.790	0.853	0.660	0.731	0.343
Sb	1.48	0.0979	0.231	0.663	0.671
Cs	1.15	0.191	0.143	0.829	1.00
Ba	82.4	65.0	633	147	43.6
La	3.37	5.89	6.77	6.76	2.05
Ce	11.3	15.0	17.5	18.0	5.01
Pr	1.62	2.28	2.66	2.78	0.728
Nd	8.25	11.6	13.2	13.7	3.54
Sm	2.74	3.42	3.43	3.50	1.10
Eu	0.727	1.05	1.17	1.05	0.415
Gd	3.42	3.85	3.50	3.45	1.44
Tb	0.643	0.640	0.550	0.538	0.270
Dy	4.38	3.99	3.33	3.10	1.88
Ho	0.946	0.806	0.658	0.605	0.421
Er	2.71	2.20	1.78	1.61	1.22
Tm	0.415	0.323	0.255	0.228	0.193
Yb	2.76	2.09	1.65	1.46	1.29
Lu	0.428	0.314	0.252	0.219	0.201
<b>Hf</b>	<b>2.28</b>	<b>2.22</b>	<b>1.88</b>	<b>1.80</b>	<b>0.923</b>
<b>Ta</b>	<b>0.228</b>	<b>0.247</b>	<b>0.271</b>	<b>0.321</b>	<b>0.0796</b>
<b>W</b>	<b>0.950</b>	<b>0.127</b>	<b>0.0509</b>	<b>0.238</b>	<b>0.0394</b>
Tl	0.109	0.0642	0.0649	0.0310	0.0336
Pb	3.61	1.16	1.12	2.33	1.58
<b>Th</b>	<b>0.388</b>	<b>0.834</b>	0.490	0.649	<b>0.269</b>
<b>U</b>	<b>0.0873</b>	<b>0.205</b>	<b>0.118</b>	<b>0.156</b>	<b>0.0654</b>

Table B1: continued



Group / Supersuite	Warrawoona					
	Coongan					
	Mt Ada					Duffer
	3475					3471 - 3461
Formation						
Age in Ma						
Rock Type	Komatiitic basalt	Komatiite	Pillow basalt	Komatiite	Pillow basalt	BIF
Longitude [S]	21°21.893'	21°22.150'	21°12.113'	21°22.150'	21°12'18.0065	20°57.470'
Latitude [E]	119°34.345'	119°34.416'	119°19.069'	119°34.416'	119°18'34.9749	119°52.485'
Sample name	<b>Pil 16-28</b>	Pil 16-030a	<b>Pil 17-010</b>	Pil 16-030c	Pil 16-007	<b>Pil 16-062-B)</b>
SiO <sub>2</sub>	48.4	48.1	52.0	47.9	48.0	73.4
TiO <sub>2</sub>	1.55	0.603	0.798	0.541	0.453	0.00362
Al <sub>2</sub> O <sub>3</sub>	11.2	11.3	14.4	11.1	13.7	0.368
Fe <sub>2</sub> O <sub>3</sub>	14.9	11.2	9.49	10.2	9.67	25.7
MnO	0.197	0.183	0.158	0.206	0.141	0.00693
MgO	8.91	8.57	7.84	9.50	8.50	0.0504
CaO	7.86	8.37	8.11	9.11	8.25	0.105
K <sub>2</sub> O	0.00570	1.37	0.774	1.69	0.262	0.00322
Na <sub>2</sub> O	2.07	0.0109	3.41	0.262	0.455	n.d.
P <sub>2</sub> O <sub>5</sub>	0.141	0.0524	0.0806	0.0459	0.0417	0.0458
L.O.I.	6.86	10.8	2.85	9.55	11.6	0.410
Total	101.6	100.5	100.0	100.1	101.2	100.0
Mg#	56.7	62.7	64.5	67.2	65.9	
Li	18.3	53.3	17.8	46.4	58.2	0.439
Sc	40.0	34.5	35.6	36.5	36.7	0.407
V	303	206	255	210	205	1.79
Cr	423	383	430	713	433	36.7
Co	51.5	48.6	38.1	46.5	43.5	3.13
Ni	117	86.3	91.8	107	123	16.2
Cu	32.5	24.0	76.5	20.8	12.1	2.17
Zn	127.6	141	93.6	90.4	61.9	10.0
Ga	16.4	10.9	16.3	10.3	11.6	1.21
Rb	0.319	0.553	20.1	6.99	6.98	0.241
Sr	171	62.8	113.9	73.4	29.4	9.16
Y	31.5	14.0	22.9	11.4	14.4	5.28
<b>Zr</b>	<b>102</b>	<b>35.7</b>	<b>94.3</b>	<b>30.2</b>	<b>43.1</b>	<b>0.518</b>
<b>Nb</b>	<b>5.16</b>	<b>1.56</b>	<b>4.86</b>	<b>1.31</b>	<b>1.59</b>	<b>0.0584</b>
Mo	0.256	0.0667	0.362	0.0643	0.0577	0.482
Cd	0.165	0.0767	0.234	0.0835	0.116	0.0630
Sn	0.772	0.200	0.771	0.145	0.334	0.173
Sb	0.147	0.0826	0.607	0.0762	2.29	1.45
Cs	0.882	0.285	1.46	0.782	0.353	0.147
Ba	24.4	13.0	328	120	53.7	9.60
La	6.47	2.23	8.70	1.82	2.85	1.51
Ce	17.4	5.80	20.1	4.60	6.58	3.78
Pr	2.66	0.905	2.71	0.718	0.910	0.511
Nd	13.3	4.75	12.6	3.72	4.25	2.26
Sm	3.92	1.55	3.28	1.20	1.28	0.559
Eu	1.16	0.694	1.01	0.431	0.418	0.203
Gd	4.64	1.94	3.67	1.56	1.69	0.682
Tb	0.819	0.352	0.621	0.277	0.323	0.118
Dy	5.34	2.35	4.00	1.88	2.30	0.803
Ho	1.13	0.501	0.827	0.408	0.509	0.180
Er	3.19	1.42	2.33	1.18	1.51	0.543
Tm	0.486	0.217	0.351	0.183	0.237	0.0876
Yb	3.21	1.45	2.30	1.21	1.61	0.595
Lu	0.495	0.226	0.353	0.191	0.253	0.0957
<b>Hf</b>	<b>2.91</b>	<b>1.05</b>	<b>2.55</b>	<b>0.881</b>	<b>1.21</b>	<b>0.00990</b>
<b>Ta</b>	<b>0.312</b>	<b>0.0951</b>	<b>0.329</b>	<b>0.0769</b>	<b>0.112</b>	<b>0.000316</b>
<b>W</b>	<b>0.0733</b>	<b>0.0311</b>	<b>0.117</b>	<b>0.111</b>	<b>0.0355</b>	<b>0.222</b>
Tl	0.0102	0.0137	0.0498	0.0601	0.0141	0.00978
Pb	1.72	0.603	2.17	0.810	0.951	1.95
<b>Th</b>	<b>0.709</b>	<b>0.300</b>	<b>1.60</b>	<b>0.252</b>	<b>0.464</b>	<b>0.0259</b>
<b>U</b>	<b>0.176</b>	<b>0.0985</b>	<b>0.384</b>	<b>0.0803</b>	<b>0.130</b>	<b>0.0659</b>

Table B1: continued

Group / Supersuite	Warrawoona					
Subgroup	Salgash					
Formation	Apex Basalt					
Age in Ma	3465					
Rock Type	Basalt	Basalt	Pillow basalt	Pillow basalt	Dolerite dyke	Komatiite
Longitude [S]	21°10.552'	21°10.641'	21°10.624'	21°10.530'	21°06.760'	
Latitude [E]	119°42.011'	119°42.124'	119°41.762'	119°41.933'	119°22.667'	
Sample name	<b>Pil 16-24</b>	<b>Pil 16-025</b>	Pil 16-22A	Pil 16-23A	Pil 16-009	<b>179738<sup>a</sup></b>
SiO <sub>2</sub>	47.1	50.2	54.1	48.0	47.3	48.8
TiO <sub>2</sub>	0.920	1.11	0.558	0.997	0.390	0.378
Al <sub>2</sub> O <sub>3</sub>	14.5	14.0	11.1	13.8	6.66	7.95
Fe <sub>2</sub> O <sub>3</sub>	12.6	14.1	9.43	12.7	13.0	10.3
MnO	0.158	0.210	0.146	0.197	0.204	0.217
MgO	10.1	5.92	11.5	7.24	20.3	17.4
CaO	5.03	7.82	5.93	8.18	9.03	13.5
K <sub>2</sub> O	1.57	3.14	0.0683	0.0350	0.0413	0.0190
Na <sub>2</sub> O	n.d.	0.138	3.06	1.28	0.326	0.104
P <sub>2</sub> O <sub>5</sub>	0.0673	0.0791	0.0406	0.0767	0.0355	0.0240
L.O.I.	9.28	2.98	3.06	8.36	3.99	1.83
Total	101.5	99.7	99.1	101.0	101.6	100.0
Mg#	63.8	48.0	72.8	55.6	77.4	78.7
Li	45.7	12.6	22.9	43.9	34.2	13.0
Sc	41.7	41.5	40.2	38.5	29.0	33.9
V	298	338	225	301	156	162
Cr	224	24.3	461	252	1925	1374
Co	48.2	46.5	41.4	46.8	90.5	61.3
Ni	119	47.1	107	129	624	232
Cu	153.9	125	87.7	143	42.4	53.9
Zn	76.5	102	125	127	79.6	65.5
Ga	16.0	17.8	10.2	15.7	8.60	7.35
Rb	51.1	3.04	2.11	1.95	0.928	0.731
Sr	17.2	169	97.4	130	18.1	16.9
Y	9.12	21.6	11.1	21.7	9.04	11.9
<b>Zr</b>	<b>47.2</b>	<b>57.8</b>	<b>26.7</b>	<b>52.7</b>	<b>22.8</b>	<b>34.5</b>
<b>Nb</b>	<b>1.92</b>	<b>2.57</b>	<b>0.912</b>	<b>2.27</b>	<b>0.756</b>	<b>1.98</b>
Mo	0.146	0.142	0.158	0.136	0.112	0.174
Cd	0.190	0.174	0.138	0.158	0.0940	0.0985
Sn	0.433	0.445	0.252	0.520	0.251	0.899
Sb	3.80	1.26	0.525	5.54	0.133	0.0193
Cs	1.35	0.189	0.313	0.394	0.346	0.481
Ba	164	41.0	102	22.9	32.0	7.29
La	1.88	3.11	1.21	2.98	1.47	2.53
Ce	5.05	8.38	3.37	7.85	3.54	6.59
Pr	0.788	1.31	0.558	1.24	0.551	0.965
Nd	4.01	6.84	3.02	6.50	2.78	4.60
Sm	1.26	2.24	1.09	2.16	0.925	1.36
Eu	0.376	0.907	0.360	0.791	0.357	0.614
Gd	1.43	2.90	1.45	2.81	1.22	1.65
Tb	0.248	0.536	0.277	0.524	0.229	0.296
Dy	1.62	3.67	1.90	3.56	1.52	1.99
Ho	0.346	0.793	0.414	0.773	0.324	0.428
Er	1.03	2.30	1.20	2.23	0.902	1.23
Tm	0.168	0.356	0.187	0.340	0.136	0.192
Yb	1.24	2.38	1.26	2.29	0.884	1.29
Lu	0.221	0.372	0.197	0.355	0.135	0.199
<b>Hf</b>	<b>1.39</b>	<b>1.72</b>	<b>0.803</b>	<b>1.57</b>	<b>0.666</b>	<b>1.01</b>
<b>Ta</b>	<b>0.118</b>	<b>0.155</b>	<b>0.0642</b>	<b>0.140</b>	<b>0.0546</b>	<b>0.115</b>
<b>W</b>	<b>3.95</b>	<b>0.0593</b>	<b>0.0218</b>	<b>0.0322</b>	<b>0.0617</b>	<b>0.0223</b>
Tl	0.140	0.0206	0.0173	0.0213	0.0153	0.0163
Pb	0.824	0.825	0.305	2.50	0.425	0.360
<b>Th</b>	<b>0.256</b>	<b>0.322</b>	<b>0.134</b>	<b>0.274</b>	<b>0.220</b>	<b>0.306</b>
<b>U</b>	<b>0.0665</b>	<b>0.0793</b>	<b>0.0365</b>	<b>0.0687</b>	<b>0.0546</b>	<b>0.0805</b>

Table B1: continued

Group / Supersuite	Kelly							
Subgroup								
Formation	Euro Basalt							
Age in Ma	3340							
Rock Type	Basalt	Pillow basalt	Pillow basalt	Gabbroic cumulat	Peridotite lense	Pillow basalt	Komatiite	Komatiite
Longitude [S]	21°07.871'	21°21.709'	21°12'50.03856	21°08.300'	21°21.551'	21°12.853'		
Latitude [E]	119°03.724'	119°48.040'	119°18'26.9000	119°00.484'	119°47.963'	119°18.398'		
Sample name	<b>Pil 16-53A</b>	<b>Pil 16-39A</b>	Pil 16 001	Pil 16-58b	Pil 16-040	Pil 17-009	179815 <sup>a</sup>	179816 <sup>a</sup>
SiO <sub>2</sub>	47.6	50.1	49.0	46.7	43.7	51.7	43.6	44.3
TiO <sub>2</sub>	1.56	0.967	0.549	1.83	0.218	0.609	0.187	0.257
Al <sub>2</sub> O <sub>3</sub>	13.8	11.6	11.8	12.8	4.9	12.5	4.41	5.4
Fe <sub>2</sub> O <sub>3</sub>	15.7	12.9	10.9	15.9	10.5	10.4	10.2	10.9
MnO	0.235	0.217	0.119	0.175	0.159	0.181	0.168	0.172
MgO	7.38	8.01	9.52	4.11	29.2	8.35	32.0	28.1
CaO	7.53	13.6	7.63	7.43	5.98	9.57	4.58	5.62
K <sub>2</sub> O	0.369	0.0773	0.735	3.00	0.276	0.0179	0.0610	0.0190
Na <sub>2</sub> O	2.11	1.57	n.d.	0.135	0.0130	2.70	0.254	0.225
P <sub>2</sub> O <sub>5</sub>	0.139	0.0784	0.0478	0.124	0.0211	0.0551	0.0150	0.020
L.O.I.	4.05	1.19	10.9	7.80	5.31	3.68	4.37	5.03
Total	100.7	100.4	101.4	100.0	100.3	99.8	99.9	100.0
Mg#	50.8	57.6	65.7	36.3	85.9	63.8	87.3	85.0
Li	23.2	3.06	27.4	24.9	5.75	13.1	5.87	5.00
Sc	42.0	34.9	35.1	17.8	20.8	43.1	20.1	23.2
V	411	268	200	321	110	265	98.9	127
Cr	654	594	648	4.78	2378	529	2091	2106
Co	55.8	54.4	52.3	47.6	99.2	48.6	91.4	89.0
Ni	105	138	155	33.8	1345	157	1415	1184
Cu	133	20.0	65.2	384	28.0	80.7	16.5	26.6
Zn	127	99.8	68.3	122	61.4	83.0	59.3	61.6
Ga	20.0	15.1	10.5	17.0	4.96	13.1	4.29	5.85
Rb	6.18	0.660	23.0	3.05	0.239	0.354	2.81	1.08
Sr	184	129	30.6	118	18.5	66.3	16.3	18.8
Y	34.9	20.8	11.1	25.3	5.05	14.1	4.46	5.89
<b>Zr</b>	<b>84.9</b>	<b>62.6</b>	<b>33.9</b>	<b>88.4</b>	<b>8.86</b>	<b>38.8</b>	<b>6.89</b>	<b>12.2</b>
<b>Nb</b>	<b>4.21</b>	<b>3.09</b>	<b>1.57</b>	<b>5.01</b>	<b>0.266</b>	<b>1.64</b>	<b>0.295</b>	<b>0.484</b>
Mo	0.292	0.342	0.162	0.207	0.157	0.0945	0.192	0.168
Cd	0.254	0.137	0.121	0.185	0.0830	0.139	0.0504	0.0723
Sn	0.917	0.735	0.316	0.632	0.108	0.238	0.652	0.655
Sb	1.66	0.423	2.61	0.568	0.0895	0.0976	0.0389	0.103
Cs	0.0530	0.0359	0.575	2.03	0.201	0.567	0.757	1.34
Ba	87.8	33.2	599	55.2	2.50	16.4	4.69	2.39
La	6.47	4.58	2.71	6.92	0.393	2.67	0.381	0.657
Ce	17.0	11.9	6.36	17.3	1.15	6.82	1.07	1.80
Pr	2.53	1.81	0.898	2.62	0.199	1.01	0.182	0.286
Nd	12.3	9.13	4.26	13.2	1.12	5.14	1.02	1.53
Sm	3.63	2.72	1.25	3.91	0.428	1.57	0.373	0.544
Eu	1.27	1.00	0.466	1.44	0.153	0.600	0.157	0.222
Gd	4.46	3.26	1.54	4.40	0.604	1.97	0.539	0.758
Tb	0.815	0.554	0.278	0.729	0.114	0.353	0.103	0.143
Dy	5.57	3.58	1.88	4.54	0.809	2.38	0.731	0.990
Ho	1.23	0.737	0.413	0.906	0.182	0.514	0.161	0.214
Er	3.59	2.05	1.21	2.44	0.522	1.48	0.475	0.621
Tm	0.553	0.305	0.189	0.350	0.0841	0.228	0.0745	0.0929
Yb	3.73	2.00	1.28	2.27	0.550	1.52	0.499	0.621
Lu	0.587	0.305	0.203	0.339	0.0881	0.240	0.0797	0.0974
<b>Hf</b>	<b>2.45</b>	<b>1.78</b>	<b>0.982</b>	<b>2.46</b>	<b>0.275</b>	<b>1.10</b>	<b>0.233</b>	<b>0.376</b>
<b>Ta</b>	<b>0.244</b>	<b>0.197</b>	<b>0.104</b>	<b>0.291</b>	<b>0.0188</b>	<b>0.109</b>	<b>0.0167</b>	<b>0.0290</b>
<b>W</b>	<b>0.0888</b>	<b>0.158</b>	<b>0.0566</b>	<b>0.0348</b>	<b>0.394</b>	<b>0.0369</b>	<b>0.0204</b>	<b>0.0353</b>
Tl	0.0509	0.0158	0.171	0.0384	0.00875	0.0169	0.0179	0.0124
Pb	1.22	1.54	0.861	2.38	0.239	0.521	0.671	1.08
<b>Th</b>	<b>0.723</b>	<b>0.475</b>	0.473	0.655	<b>0.0295</b>	<b>0.306</b>	<b>0.0295</b>	0.0631
<b>U</b>	<b>0.174</b>	<b>0.118</b>	<b>0.120</b>	<b>0.171</b>	<b>0.0115</b>	<b>0.0740</b>	<b>0.00671</b>	<b>0.0140</b>

Table B1: continued

Group / Supersuite	Roebourne			Soanesville			
Subgroup							
Formation	Ruth Well			Honeyeater Basalt			Paddy Market
Age in Ma	3270			3180			3190
Rock Type	Komatiite	Komatiite	Komatiite	Pillow basalt	Gabbro	Peridotite lense	Shale
Longitude [S]	20°47.265'			21°07.696'	21°08.058'	21°08.058'	21°08.522'
Latitude [E]	117°11.940			119°12.319'	119°13.112'	119°13.112'	119°12.125'
Sample name	<b>Pil 16-66b</b>	160242 <sup>a</sup>	<b>160245<sup>b</sup></b>	<b>Pil 16-51</b>	<b>Pil 16-52B</b>	Pil 16-052a	<b>Pil 16-050 b)</b>
SiO <sub>2</sub>	44.4	38.3	37.0	44.0	48.7	48.7	55.4
TiO <sub>2</sub>	0.409	0.210	0.170	0.599	0.656	0.250	0.744
Al <sub>2</sub> O <sub>3</sub>	3.96	2.50	2.44	9.76	10.2	4.82	25.7
Fe <sub>2</sub> O <sub>3</sub>	13.0	7.61	9.80	10.7	13.4	12.3	6.67
MnO	0.141	0.220	0.120	0.230	0.203	0.162	0.0209
MgO	25.7	35.7	35.3	6.84	14.0	19.5	0.968
CaO	6.61	1.20	0.810	14.6	9.37	10.6	0.0463
K <sub>2</sub> O	0.384	0.040	0.040	0.520	0.00460	0.0255	5.72
Na <sub>2</sub> O	0.0623	0.230	0.230	n.d.	0.865	n.d.	0.267
P <sub>2</sub> O <sub>5</sub>	0.0337	0.030	0.030	0.0503	0.0494	0.0355	0.0439
L.O.I.	6.01	13.9	13.4	14.8	3.72	3.99	4.47
Total	100.7	99.9	99.3	102.3	101.4	100.5	100.2
Mg#	81.3	91.2	88.8	58.4	69.6	77.7	24.2
Li	3.6	1.67	2.91	16.8	13.6	4.2	32.8
Sc	19.9	9.93	8.06	37.8	37.6	22.5	19.1
V	128	59.4	52.2	250	271	137	192
Cr	2258	1362	3781	483	943	3098	291
Co	112	98.0	94.3	38.7	66.6	118	14.3
Ni	1453	1949	2191	108	302	923	95.1
Cu	5.54	2.24	2.39	21.9	106	126	98.2
Zn	62.6	73.0	123	65.5	71.2	101	41.0
Ga	6.17	3.03	3.45	13.7	13.6	7.98	35.0
Rb	1.42	3.33	1.85	18.6	0.428	0.189	195
Sr	53.6	11.9	5.81	27.1	18.9	4.65	16.6
Y	7.73	2.94	2.19	14.0	13.2	6.61	25.4
<b>Zr</b>	<b>21.2</b>	<b>9.54</b>	<b>10.4</b>	<b>29.6</b>	<b>33.3</b>	<b>12.2</b>	<b>106</b>
<b>Nb</b>	<b>0.479</b>	<b>0.399</b>	<b>0.467</b>	<b>1.09</b>	<b>1.04</b>	<b>0.366</b>	<b>11.3</b>
Mo	0.192	0.253	0.388	0.107	0.151	0.209	0.113
Cd	0.101	0.0362	0.0338	0.0737	0.106	0.0845	0.118
Sn	0.305	0.687	0.726	0.336	0.280	0.323	1.62
Sb	0.678	1.73	0.545	0.0255	0.146	0.274	0.346
Cs	1.44	0.651	1.95	0.343	0.316	0.0624	2.04
Ba	429	35.0	58.9	62.0	10.6	10.1	1306
La	1.44	0.264	1.72	1.46	1.57	0.780	35.6
Ce	3.39	0.848	3.37	3.70	4.01	1.98	60.4
Pr	0.503	0.150	0.397	0.598	0.643	0.302	6.27
Nd	2.66	0.821	1.63	3.30	3.50	1.54	23.0
Sm	0.968	0.304	0.381	1.24	1.23	0.538	3.98
Eu	0.415	0.0765	0.157	0.443	0.557	0.236	1.47
Gd	1.25	0.414	0.390	1.77	1.76	0.797	3.93
Tb	0.216	0.0741	0.0642	0.337	0.333	0.152	0.602
Dy	1.38	0.505	0.395	2.31	2.26	1.07	3.76
Ho	0.279	0.107	0.0825	0.499	0.476	0.234	0.796
Er	0.751	0.312	0.234	1.39	1.32	0.658	2.27
Tm	0.109	0.0511	0.0371	0.206	0.194	0.098	0.336
Yb	0.698	0.341	0.247	1.33	1.25	0.641	2.20
Lu	0.105	0.0538	0.0414	0.202	0.192	0.099	0.340
Hf	0.624	0.288	0.300	0.911	1.03	0.383	2.98
<b>Ta</b>	<b>0.0359</b>	<b>0.0240</b>	<b>0.0341</b>	<b>0.0626</b>	<b>0.0685</b>	<b>0.0228</b>	<b>1.00</b>
<b>W</b>	<b>1.16</b>	<b>0.316</b>	<b>19.1</b>	<b>0.0311</b>	<b>0.0241</b>	<b>0.0252</b>	<b>1.79</b>
Tl	0.0297	0.0236	0.0176	0.271	0.0153	0.0242	0.877
Pb	0.527	0.202	0.799	0.183	0.269	0.372	2.81
<b>Th</b>	<b>0.160</b>	<b>0.114</b>	<b>0.370</b>	<b>0.122</b>	<b>0.108</b>	<b>0.0535</b>	<b>5.32</b>
<b>U</b>	<b>0.0558</b>	<b>0.0217</b>	<b>0.103</b>	<b>0.0446</b>	<b>0.0343</b>	<b>0.0273</b>	<b>2.31</b>

Table B1: continued

Group / Supersuite	Whundo group					
Subgroup						
Formation	Regal			Bradley Basalt		
Age in Ma	3120					
Rock Type	Komatiite	Komatiite	Komatiite	Basalt	Basalt	Pillow Basalt
Longitude [S]				20°55.196'	20°56.862'	20°57.717'
Latitude [E]				117°04.128'	117°02.890'	117°02.232'
Sample name	176721 <sup>a</sup>	176724 <sup>a</sup>	176725 <sup>a</sup>	<b>Pil 16-67</b>	<b>Pil 16-74</b>	Pil 16-73
SiO <sub>2</sub>	40.0	42.2	40.0	48.8	54.6	50.7
TiO <sub>2</sub>	0.220	0.260	0.280	1.89	1.02	1.60
Al <sub>2</sub> O <sub>3</sub>	1.77	3.02	3.09	15.4	15.3	14.0
Fe <sub>2</sub> O <sub>3</sub>	8.15	9.62	10.8	12.9	9.24	15.9
MnO	0.120	0.150	0.140	0.166	0.175	0.262
MgO	36.8	32.8	31.3	5.79	5.96	5.3
CaO	0.160	1.99	3.26	8.47	5.26	10.6
K <sub>2</sub> O	0.010	0.010	0.010	0.855	2.45	0.261
Na <sub>2</sub> O	0.240	0.260	0.330	1.59	2.32	2.06
P <sub>2</sub> O <sub>5</sub>	0.030	0.040	0.040	0.397	0.139	0.142
L.O.I.	12.4	9.84	10.8	3.49	3.30	2.58
Total	99.9	100.1	100.1	100.0	100.0	103.7
Mg#	90.8	88.2	86.5	49.7	58.7	42.2
Li	1.52	2.62	2.56	16.9	22.4	8.07
Sc	9.76	16.0	16.5	31.1	28.3	41.4
V	59.0	91.2	95.1	247	206	381
Cr	1260	1973	1897	148	151	113
Co	95.2	85.8	104.3	40.1	35.0	50.6
Ni	2190	1560	1580	70.1	85.7	85.1
Cu	5.84	3.53	3.22	58.6	54.5	108
Zn	66.8	96.0	52.7	119	93.0	129
Ga	2.78	4.13	4.54	18.2	17.1	23.3
Rb	0.458	0.610	0.527	24.3	71.0	5.94
Sr	7.03	11.5	26.8	447	172	229
Y	2.93	4.50	4.79	32.8	23.9	39.1
<b>Zr</b>	<b>6.69</b>	<b>9.07</b>	<b>13.0</b>	<b>140</b>	<b>111</b>	<b>107</b>
<b>Nb</b>	<b>0.215</b>	<b>0.355</b>	<b>0.370</b>	<b>9.25</b>	<b>5.32</b>	<b>4.72</b>
Mo	0.352	0.199	0.396	0.894	0.452	0.416
Cd	0.0354	0.0898	0.0484	0.254	0.186	0.270
Sn	0.926	0.664	0.684	0.897	0.840	1.01
Sb	0.0798	0.0768	0.0516	0.174	0.298	0.451
Cs	0.682	1.40	0.936	0.909	1.83	0.181
Ba	4.60	0.616	1.30	357	643	169
La	0.474	0.757	0.603	14.7	13.2	6.42
Ce	1.21	1.76	1.55	38.4	28.9	16.8
Pr	0.193	0.260	0.244	5.63	3.71	2.60
Nd	1.05	1.34	1.33	26.1	15.8	13.3
Sm	0.387	0.477	0.489	6.14	3.55	4.18
Eu	0.149	0.169	0.150	1.97	1.10	1.43
Gd	0.493	0.670	0.695	6.12	3.66	5.25
Tb	0.0871	0.121	0.127	0.954	0.593	0.945
Dy	0.544	0.807	0.834	5.73	3.79	6.30
Ho	0.113	0.166	0.177	1.16	0.802	1.35
Er	0.298	0.454	0.487	3.20	2.33	3.89
Tm	0.0442	0.0672	0.0724	0.475	0.364	0.590
Yb	0.283	0.442	0.470	3.11	2.48	3.95
Lu	0.0433	0.0660	0.0735	0.480	0.394	0.612
<b>Hf</b>	<b>0.201</b>	<b>0.309</b>	<b>0.405</b>	<b>3.53</b>	<b>2.94</b>	<b>3.13</b>
<b>Ta</b>	<b>0.0139</b>	<b>0.0207</b>	<b>0.0230</b>	<b>0.485</b>	<b>0.353</b>	<b>0.282</b>
<b>W</b>	<b>0.312</b>	<b>0.360</b>	<b>0.272</b>	<b>0.108</b>	<b>0.144</b>	<b>0.0863</b>
Tl	0.0107	0.0148	0.00984	0.166	0.347	0.0531
Pb	0.230	0.273	0.477	1.94	2.46	1.65
<b>Th</b>	<b>0.0541</b>	<b>0.104</b>	<b>0.0908</b>	<b>0.958</b>	<b>1.82</b>	<b>0.633</b>
<b>U</b>	<b>0.0159</b>	<b>0.0790</b>	<b>0.0298</b>	<b>0.245</b>	<b>0.460</b>	<b>0.162</b>

Table B1: continued

Group / Supersuite	Bookingarra			Fortescue		
Subgroup						
Formation	Opaline Well intru	Louden Volcanics		Mt. Negri Volcani	Black Range	Hardey
Age in Ma	2990			2775	2756 - 2766	
Rock Type	Gabbroic cumula	Pyroxene spinifex	Ultramafic cumula	Basalt	Dolerite dyke	Shale
Longitude [S]	20°50.816'	20°43.054'	20°43.372'	20°59.936'	21°26.823'	21°19.882'
Latitude [E]	117°47.701'	117°52.056'	117°51.616'	117°33.440'	119°32.209'	119°36.015'
Sample name	<b>Pil 16-63</b>	<b>Pil 16-65</b>	Pil 16-064	<b>Pil 16-75</b>	<b>Pil 16-31</b>	<b>Pil 16-038b</b>
SiO <sub>2</sub>	41.5	53.3	41.0	56.7	54.2	58.0
TiO <sub>2</sub>	0.122	0.308	0.165	0.567	0.616	0.729
Al <sub>2</sub> O <sub>3</sub>	2.61	9.30	3.98	10.6	13.9	23.1
Fe <sub>2</sub> O <sub>3</sub>	11.0	10.6	10.1	9.12	10.0	6.06
MnO	0.170	0.203	0.152	0.136	0.152	0.0232
MgO	34.1	15.6	31.9	11.7	7.26	2.62
CaO	1.93	6.87	2.88	6.01	8.93	0.173
K <sub>2</sub> O	0.0712	0.515	n.d.	1.06	1.30	3.51
Na <sub>2</sub> O	n.d.	0.478	0.0949	1.40	1.89	0.914
P <sub>2</sub> O <sub>5</sub>	0.0181	0.0331	0.0242	0.0715	0.0899	0.0458
L.O.I.	7.77	4.15	7.95	2.83	2.24	5.20
Total	100.2	101.5	98.2	100.4	100.7	100.6
Mg#	87.2	76.4	87.5	73.8	61.6	48.7
Li	1.84	19.5	7.65	15.7	96.9	22.3
Sc	11.5	29.0	13.5	25.8	30.4	27.8
V	66.2	142	85.3	159	190	241
Cr	6358	1653	6524	1367	333	588
Co	118	67.0	112	56.2	45.9	26.2
Ni	1447	258	1322	370	169	227
Cu	9.39	68.8	21.8	47.0	93.3	72.3
Zn	76.2	115	69.5	64.6	161	101
Ga	3.42	9.45	4.54	11.7	14.7	31.7
Rb	4.06	21.6	6.11	30.7	74.1	123
Sr	16.5	65.5	12.4	170	232	134
Y	2.77	8.51	4.15	14.5	17.8	25.0
<b>Zr</b>	<b>11.8</b>	<b>33.4</b>	<b>14.6</b>	<b>62.3</b>	<b>76.7</b>	<b>120</b>
<b>Nb</b>	<b>0.418</b>	<b>1.30</b>	<b>0.539</b>	<b>2.46</b>	<b>3.84</b>	<b>8.47</b>
Mo	0.211	0.293	0.172	0.454	0.439	0.700
Cd	0.0842	0.176	0.0827	0.112	0.169	0.215
Sn	0.145	0.482	0.158	0.241	0.806	2.33
Sb	0.463	4.62	0.0611	0.133	0.117	1.67
Cs	2.05	1.94	1.48	2.48	2.15	13.1
Ba	18.1	184	40.2	249	366	697
La	1.76	5.69	2.12	8.55	13.0	36.5
Ce	3.39	10.4	4.04	17.7	26.0	69.5
Pr	0.400	1.19	0.474	2.17	3.10	7.85
Nd	1.63	4.70	1.93	9.03	12.4	29.9
Sm	0.395	1.09	0.491	2.07	2.73	5.81
Eu	0.126	0.383	0.160	0.664	0.829	1.38
Gd	0.422	1.22	0.570	2.23	2.83	5.20
Tb	0.0713	0.213	0.101	0.369	0.465	0.776
Dy	0.453	1.40	0.668	2.35	2.97	4.54
Ho	0.0984	0.303	0.145	0.497	0.621	0.888
Er	0.285	0.881	0.429	1.42	1.76	2.48
Tm	0.0466	0.138	0.0670	0.217	0.268	0.372
Yb	0.313	0.933	0.458	1.44	1.79	2.46
Lu	0.0508	0.148	0.0729	0.227	0.278	0.377
Hf	0.340	0.952	0.419	1.71	2.15	3.44
<b>Ta</b>	<b>0.0360</b>	<b>0.116</b>	<b>0.0469</b>	<b>0.219</b>	<b>0.302</b>	<b>0.847</b>
<b>W</b>	<b>0.233</b>	<b>0.582</b>	<b>0.0567</b>	<b>0.196</b>	<b>0.205</b>	<b>3.02</b>
Tl	0.0309	0.204	0.0534	0.211	0.633	1.08
Pb	1.78	3.62	0.990	2.53	5.03	10.0
<b>Th</b>	<b>0.520</b>	<b>1.61</b>	<b>0.690</b>	<b>2.67</b>	<b>3.64</b>	<b>5.48</b>
<b>U</b>	<b>0.136</b>	<b>0.453</b>	<b>0.184</b>	<b>1.06</b>	<b>0.972</b>	<b>2.76</b>

Table B1: continued

Group / Supersuite	Callina			Split Rock	
Subgroup					
Formation	North Pole Monzogranite	North Shaw Tonalite		Homeward Bound Granite	Spearhill Monzogranite
Age in Ma	3450	3468		3466	2850
Rock Type	Granodiorite	Qtz-Monzodiorite	Qtz-Monzodiorite	Granodiorite	Granite
Longitude [S]	21°06.971'	21°21.290'	21°21.415'	21°10.443'	21°31.112'
Latitude [E]	119°22.409'	119°27.321'	119°27.249'	119°45.636'	119°24.228'
Sample name	<b>Pil 16-12</b>	<b>Pil 16-34</b>	<b>Pil 16-35</b>	<b>Pil 16-41</b>	<b>Pil 16-36a</b>
SiO <sub>2</sub>	72.8	63.5	63.3	75.6	75.7
TiO <sub>2</sub>	0.240	0.407	0.531	0.158	0.127
Al <sub>2</sub> O <sub>3</sub>	14.2	16.0	16.0	12.0	13.1
Fe <sub>2</sub> O <sub>3</sub>	2.20	4.70	5.16	2.54	1.32
MnO	0.0239	0.111	0.0925	0.0242	0.0382
MgO	0.492	1.80	2.29	0.0936	0.0953
CaO	1.88	4.19	4.50	1.16	0.773
K <sub>2</sub> O	3.20	3.00	2.23	2.58	4.81
Na <sub>2</sub> O	4.52	5.82	5.13	4.82	3.86
P <sub>2</sub> O <sub>5</sub>	0.0767	0.247	0.227	0.0135	0.0266
L.O.I.	1.10	0.620	1.01	1.35	0.590
Total	100.8	100.4	100.4	100.3	100.4
Mg#	33.0	45.8	49.4	7.5	13.7
Li	10.1	5.66	23.4	2.33	101
Sc	1.70	6.89	8.20	3.18	1.76
V	20.4	70.3	80.7	0.329	5.37
Cr	32.5	44.3	58.5	46.0	14.2
Co	3.61	13.7	15.4	0.312	0.903
Ni	5.08	26.5	36.4	0.666	0.744
Cu	16.8	26.5	27.1	28.9	13.3
Zn	72.5	72.2	67.8	23.8	38.7
Ga	20.0	20.9	21.0	20.3	21.1
Rb	59.3	74.0	51.2	49.8	371
Sr	228	1086	847	42.7	47.1
Y	9.04	17.8	14.5	51.5	31.7
<b>Zr</b>	134	131	189	399.4	134
<b>Nb</b>	1.28	11.9	7.04	17.4	36.8
Mo	0.0634	0.450	0.530	0.677	0.120
Cd	0.220	0.164	0.220	0.282	0.155
Sn	0.832	0.633	0.724	3.38	7.43
Sb	0.0760	0.0904	0.0636	0.427	0.103
Cs	1.42	1.41	2.13	1.97	10.4
Ba	509	1189	873	768	284.9
La	27.7	96.9	66.3	64.8	31.4
Ce	42.5	187	133	90.2	54.8
Pr	5.20	20.3	15.2	16.8	7.02
Nd	18.7	72.8	56.6	64.1	24.3
Sm	3.12	10.4	8.53	11.9	5.11
Eu	0.742	2.70	1.96	1.64	0.291
Gd	2.41	7.07	5.84	10.2	4.67
Tb	0.317	0.798	0.670	1.54	0.809
Dy	1.62	3.54	3.02	9.04	5.00
Ho	0.293	0.614	0.513	1.85	1.02
Er	0.799	1.59	1.32	5.35	3.02
Tm	0.116	0.213	0.174	0.817	0.485
Yb	0.765	1.36	1.10	5.54	3.37
Lu	0.117	0.204	0.169	0.851	0.524
<b>Hf</b>	<b>3.86</b>	<b>3.34</b>	<b>3.98</b>	<b>10.5</b>	<b>5.77</b>
<b>Ta</b>	0.113	0.517	0.310	1.13	4.72
<b>W</b>	<b>1.15</b>	<b>0.228</b>	<b>0.217</b>	<b>0.525</b>	<b>0.622</b>
Tl	0.678	0.68	0.47	0.464	3.45
Pb	22.7	14.7	14.9	6.29	37.8
<b>Th</b>	10.1	20.6	18.4	14.7	34.4
<b>U</b>	1.76	2.47	2.18	2.93	13.0

Table B1: continued

locality	sample #	rock type	$\mu^{182}\text{W}$	$\pm$	$\mu^{142}\text{Nd}$	$\pm$	W [ng/g]	Th [ng/g]	W/Th	references			
										$\mu^{182}\text{W}$	$\mu^{142}\text{Nd}$	W	Th
Acasta Geniss Complex	<b>JR13-102</b>	<b>Metagabbro</b>	<b>11.6</b>	<b><math>\pm</math> 2.5</b>	-9.7	$\pm$ 2.8	272	1760	<b>0.15</b>	c	c	c	d
	<b>JR12-172</b>	<b>Amphibolite</b>	<b>9.1</b>	<b><math>\pm</math> 1.6</b>	-5.0	$\pm$ 2.8	429	2520	<b>0.17</b>	c	c	c	d
	<b>JR13-136</b>	<b>Metagabbro</b>	<b>10.9</b>	<b><math>\pm</math> 2.9</b>			249	2250	<b>0.11</b>	c		c	d
	AG09-17N	Mafic gneiss	9.0	$\pm$ 2.0	-9.2	$\pm$ 3.8	974	498	2.0	a	az	a	b
	AG09-020	Mafic gneiss	10.0	$\pm$ 2.0	-10.1	$\pm$ 3.5	2300	888	2.6	a	az	a	b
Labrador	SB-19	Amphibolite	10.4	$\pm$ 3.5			547	338	1.6	e		e	e
	KC87-111E	Pyroxene hornblende	8.3	$\pm$ 2.8			69	137	0.50	e		e	e
	KC87-111G	Olivine-pyroxene hornblende	9.5	$\pm$ 4.4			48	123	0.39	e		e	e
	KC87-111K	Olivine hornblende	9.4	$\pm$ 2.0			34	39	0.87	e		e	e
	KC87-104D	Dunite	18.0	$\pm$ 4.7			205	25	8.2	e		e	e
	KC91-52B	Dunite	15.4	$\pm$ 5.0			131	27	4.9	e		e	e
	KC91-52C	Hornblende	9.7	$\pm$ 4.7			297	170	1.7	e		e	e
	KC91-52D	Dunite	10.5	$\pm$ 6.5			201	21	9.6	e		e	e
	KC87-114G	Meta-harzburgite	-2.6	$\pm$ 4.6			53	44	1.2	e		e	e
	KC87-114I	Meta-lherzolite	10.5	$\pm$ 5.5			88	68	1.3	e		e	e
	KC87-114K	Meta-olivine websterite	8.3	$\pm$ 3.1			1754	126	14	e		e	e
	KC87-106A	Meta-pyroxenite	10.4	$\pm$ 3.2			102	131	0.78	e		e	e
	KC91-32A	Amphibole harzburgite	9.9	$\pm$ 3.4			287	67	4.3	e		e	e
	KC91-32E	Amphibole harzburgite	8.9	$\pm$ 5.6			235	41	5.7	e		e	e

a	Willbold et al., 2015	q	Puchtel et al., 2016	ae	Debaille et al., 2009	at	Huang et al., 2003
b	Mojzsis et al., 2014	r	Archer et al. 2019	af	Ellam et al., 1998	au	Helz, 2012
c	Reimink et al., 2018	s	Rizo et al., 2019	ag	Starkey et al., 2009	av	Jochum et al., 2005
d	Reimink et al., 2016	t	This study	ah	Larsen and Pedersen, 2009	aw	Ireland et al., 2009
e	Liu et al., 2016	u	Touboul et al., 2012	ai	Herzberg et al., 2014	ax	Vlastelic et al., 2018
f	Rizo et al., 2016	v	Puchtel et al., 2013	ak	Füri et al., 2011	ay	Mundt et al., 2020
g	Rizo et al., 2013	w	Puchtel et al., 1998	al	Jackson et al., 2014	az	Roth et al., 2014
h	Rizo et al., 2012	x	Puchtel et al., 2018	am	Konter and Jackson, 2012	ba	Rizo et al., 2013
i	Rizo et al., 2011	y	Puchtel et al., 2016	an	Workman et al., 2004	bb	Rizo et al., 2011
k	Tusch et al., 2019	z	Rizo et al., 2016	ao	Workman, 1998	bc	Caro et al., 2006
l	Dale et al., 2017	aa	Kruijer et al., 2018	ap	Dax et al., 2010	bd	Rizo et al., 2012
m	Willbold et al., 2011	ab	Arevalo and McDonough 2008	aq	Garapic et al., 2015	be	O'Neil et al., 2012
n	Touboul et al., 2014	ac	Mundt et al., 2017	ar	Thompson et al., 1984	bf	O'Neil et al., 2008
o	O'Neil et al., 2011	ad	Mundt-Petermeier et al., 2019	as	Norman and Garcia, 1999	bg	Boyett and Carlson (2006)
p	Mei et al., 2019						

**Table B2: Compilation of all available  $^{182}\text{W}$  isotope literature data available for mantle-derived rocks.** Also given are elemental concentrations for W and Th. References for  $^{182}\text{W}$  isotope compositions, as well as for elemental W and Th concentrations are indicated by small letters and also reported. For every location, samples with pristine W concentrations are given first (by bold characters), followed by samples with overprinted elemental W budgets and samples where Th concentrations were not reported.



locality	sample #	rock type	$\mu^{182}\text{W}$ $\pm$		$\mu^{142}\text{Nd}$ $\pm$		W [ng/g]	Th [ng/g]	W/Th	references			
			$\mu^{182}\text{W}$	$\mu^{142}\text{Nd}$	W	Th				$\mu^{182}\text{W}$	$\mu^{142}\text{Nd}$	W	Th
Isua	<b>73 mafic</b>	<b>Amphibolite</b>	<b>11.4</b>	$\pm$ <b>4.9</b>			310	1404	<b>0.22</b>	k		k	k
	<b>10-37</b>	<b>Amphibolite</b>	<b>14.1</b>	$\pm$ <b>5.1</b>			150	598	<b>0.25</b>	k		k	k
	<b>2000-10</b>	<b>Amphibolite</b>	<b>13.3</b>	$\pm$ <b>3.2</b>			145	666	<b>0.22</b>	k		k	k
	<b>SM/GR/98/21</b>	<b>Meta-pillow basalt</b>	<b>12.0</b>	$\pm$ <b>5.0</b>	10.5	$\pm$ 2.7	44	266	<b>0.17</b>	m	bc	l	l
	<b>460257</b>	<b>Amphibolite</b>	<b>14.0</b>	$\pm$ <b>1.9</b>	10.9	$\pm$ 3.3	123	692	<b>0.18</b>	f	ba	f	g
	<b>00-008</b>	<b>Amphibolite</b>	<b>5.4</b>	$\pm$ <b>7.2</b>	9.4	$\pm$ 1.4	250	1130	<b>0.22</b>	f	bb	f	i
	<b>00-010</b>	<b>Amphibolite</b>	<b>15.6</b>	$\pm$ <b>3.0</b>	4.5	$\pm$ 1.5	356	3430	<b>0.10</b>	f	bb	f	i
	<b>00-044</b>	<b>Amphibolite</b>	<b>21.3</b>	$\pm$ <b>5.3</b>	8.2	$\pm$ 4.8	317	1540	<b>0.21</b>	f	bb	f	i
	<b>Am019</b>	<b>Norite</b>	<b>13.6</b>	$\pm$ <b>0.8</b>	8.4	$\pm$ 3.7	352	2564	<b>0.14</b>	f	bd	f	h
	<b>00-015</b>	<b>Metadolerite dyke</b>	<b>13.1</b>	$\pm$ <b>5.8</b>			174	1814	<b>0.10</b>	f		f	h
	00-028	Amphibolite	7.3	$\pm$ 1.0	1.7	$\pm$ 8.0	469	168	2.8	f	ba	f	g
	00-029	Amphibolite	11.7	$\pm$ 5.8	0.8	$\pm$ 0.3	500	99	5.1	f	ba	f	g
	00-038	Amphibolite	13.7	$\pm$ 2.7	-3.4	$\pm$ 1.0	539	242	2.2	f	ba	f	g
	00-007	Amphibolite	15.0	$\pm$ 3.2	8.3	$\pm$ 2.0	394	1330	0.30	f	bb	f	i
	00-042	Amphibolite	14.3	$\pm$ 8.5	2.6	$\pm$ 7.7	442	250	1.8	f	bb	f	i
	460217	Amphibolite	3.7	$\pm$ 6.9	7.3	$\pm$ 3.1	2552	671	3.8	f	ba	f	g
	460219	Amphibolite	6.8	$\pm$ 1.3	10.2	$\pm$ 6.4	3084	811	3.8	f	ba	f	g
	S33	Peridotite	6.2	$\pm$ 4.3			873	122	7.2	f		f	k
	S31	Peridotite	0.9	$\pm$ 6.3			566	134	4.2	f		f	k
	SM/GR/00/12	Ultramafic rock	16.0	$\pm$ 10.0			129	346	0.37	l		l	l
	SM/GR/00/24	Ultramafic rock	16.0	$\pm$ 7.0			286	22	13	l		l	l
	SM/GR/00/27	Ultramafic rock	12.0	$\pm$ 7.0			318	60	5.3	l		l	l
	SM/GR/00/17	Amphibolite	14.0	$\pm$ 10.0			326	63	5.2	l		l	l
	SM/GR/00/22	Amphibolite	9.0	$\pm$ 3.0	13.7	$\pm$ 2.4	189	133	1.4	m	bc	l	l
	SM/GR/98/23	Meta-pillow basalt	15.0	$\pm$ 5.0	10.8	$\pm$ 2.1	167	491	0.34	m	bc	l	l
	SM/GR/98/26	Meta-pillow basalt	11.0	$\pm$ 3.0	10.7	$\pm$ 4.4	213	412	0.52	l	bc	l	l
	242774	Ameralik dyke	5.0	$\pm$ 6.0			148	332	0.45	l		l	l
	10-17	Amphibolite	14.1	$\pm$ 3.9			201	486	0.41	k		k	k
	10-20C	Harzburgite	15.5	$\pm$ 7.1			281	44	6.3	k		k	k
	10-22	Dunite	14.9	$\pm$ 3.7			401	11	36	k		k	k
	10-23	Dunite	11.3	$\pm$ 3.8			387	16	23	k		k	k
	10-34	Harzburgite	13.0	$\pm$ 4.1			5048	32	160	k		k	k
	10-29A	Harzburgite	11.8	$\pm$ 2.0			1399	14	101	k		k	k
	10-29B	Harzburgite	10.9	$\pm$ 3.3			207	69	3.0	k		k	k
	10-27	Cumulate	19.9	$\pm$ 4.1			47	27	1.7	k		k	k
	10-09	Harzburgite	15.2	$\pm$ 7.2			60	23	2.7	k		k	k
	10-12B	Harzburgite	15.2	$\pm$ 10.0			115	68	1.7	k		k	k
	72 mafic	Amphibolite	10.7	$\pm$ 3.0			4256	476	8.9	k		k	k
	74C mafic	Amphibolite	11.7	$\pm$ 2.8			6360	816	7.8	k		k	k
	S 30	Peridotite	10.1	$\pm$ 4.0			383	35	11	k		k	k
	S 31	Peridotite	10.5	$\pm$ 3.0			662	134	4.9	k		k	k
	S 33	Peridotite	15.2	$\pm$ 1.9			657	122	5.4	k		k	k
	JEH-2007-04	Ameralik dyke	14.7	$\pm$ 5.7			419	287	1.5	k		k	k
	JEH-SG-03	Ameralik dyke	11.8	$\pm$ 3.3			135	269	0.50	k		k	k
	010-41	Ameralik dyke	15.0	$\pm$ 2.9			156	432	0.36	k		k	k
	00-039	Amphibolite	23.4	$\pm$ 10.6	-6.3	$\pm$ 3.9	791	n.d.		f	ba	f	g
	879251	Serpentinite	12.8	$\pm$ 5.7			241			f		f	
879371	Serpentinite	13.5	$\pm$ 5.6			218			f		f		
50004	Serpentinite	13.2	$\pm$ 3.3			943			f		f		
Nuvuagittuq	<b>PC-227</b>	<b>Mafic rock</b>	<b>15.0</b>	$\pm$ <b>14.4</b>	1.5	$\pm$ 3.5	16	330	<b>0.05</b>	n	be	n	o
	<b>PC-162</b>	<b>Mafic rock</b>	<b>11.9</b>	$\pm$ <b>5.5</b>	-3.6	$\pm$ 3.3	92	1790	<b>0.05</b>	n	be	n	o
	<b>PC-282</b>	<b>Mafic rock</b>	<b>12.4</b>	$\pm$ <b>2.4</b>	-12.1	$\pm$ 4.3	439	2560	<b>0.17</b>	n	bf	n	o
	PC-129	Mafic rock	16.0	$\pm$ 1.4	-10.1	$\pm$ 3.9	231	730	0.32	n	bf	n	o
	PC-132	Mafic rock	8.2	$\pm$ 2.4	-8.0	$\pm$ 5.8	325	810	0.40	n	be	n	o
	PC-410	Mafic rock	9.8	$\pm$ 6.9	-5.1	$\pm$ 5.5	160	520	0.31	n	be	n	o
	PC-092	Ultramafic rock	10.6	$\pm$ 3.9			637			n		n	
	PC-095	Ultramafic rock	11.1	$\pm$ 3.2			111			n		n	
	PC-425	Mafic rock	14.8	$\pm$ 5.7	-5.7	4.9	2225			n	be	n	
	PC-437	Mafic rock	13.0	$\pm$ 2.0			167			n		n	
	PC-213	Ultramafic rock	7.8	$\pm$ 3.2	4.6	$\pm$ 3.9	98			n	be	n	
	PC-218	Ultramafic rock	11.3	$\pm$ 4.5	-1.7	$\pm$ 1.1	122			n	bf	n	
	PC-504	Ultramafic rock	16.1	$\pm$ 3.0			1343			n		n	
	PC-018	Ultramafic rock	14.5	$\pm$ 2.9	8.0	$\pm$ 5.4	1439			n	be	n	
	PC-128	Ultramafic rock	15.4	$\pm$ 2.9			441			n		n	
	PC-220	Ultramafic rock	13.8	$\pm$ 2.4	5.9	$\pm$ 5.5	228			n	be	n	

Table B2: continued

locality	sample #	rock type	$\mu^{182}\text{W}$	$\pm$	$\mu^{142}\text{Nd}$	$\pm$	W [ng/g]	Th [ng/g]	W/Th	references			
										$\mu^{182}\text{W}$	$\mu^{142}\text{Nd}$	W	Th
Barberton Greenstone Belt	SA20	Amphibolite	3.9	$\pm$ 3.9			880	2700	0.33	p		p	p
Schapenburg	Sch 1.5	Komatiite	-6.4	$\pm$ 3.2	-5.5	$\pm$ 1.8	1015	107	9.5	q	q	q	q
	Sch 1.9	Komatiite	-11.4	$\pm$ 2.8			1074	77	14	q		q	q
	Sch 1.10	Komatiite	-8.2	$\pm$ 2.4			1019	75	14	q		q	q
	Sch 1.21	Komatiite	-6.9	$\pm$ 2.5			798	87	9.2	q		q	q
	Sch 2.1	Komatiite	-6.3	$\pm$ 3.1	-5.8	$\pm$ 2.6	849	121	7.0	q	q	q	q
	Sch 2.2	Komatiite	-10.2	$\pm$ 2.0	-5.5	$\pm$ 4.6	908	105	8.6	q	q	q	q
	Sch 2.6	Komatiite	-6.5	$\pm$ 1.7	-7.9	$\pm$ 1.8	866	98	8.8	q	q	q	q
	Sch 3.6	Komatiite	-7.8	$\pm$ 2.1	-1.6	$\pm$ 1.5	535	102	5.2	q	q	q	q
	Sch 1.19	Komatiite	-8.7	$\pm$ 1.9			1055			q		q	q
Pilbara	AH-25	Pillow metabasalt	15.3	$\pm$ 4.6			59	220	0.27	s		s	s
	AH-26	Pillow metabasalt	13.1	$\pm$ 4.1			96	820	0.12	s		s	s
	Pil 16-67	Basalt	5.3	$\pm$ 4.8			108	958	0.11	t		t	t
	Pil 16-74	Basalt	5.9	$\pm$ 3.2			144	1824	0.08	t		t	t
	Pil 16-56	Pillow basalt	12.0	$\pm$ 3.0			385	1892	0.20	t		t	t
	Pil 16-37a	Basalt	10.0	$\pm$ 2.8			127	834	0.15	t		t	t
	Pil 16-28	Komatiitic basalt	13.2	$\pm$ 4.7			73	709	0.10	t		t	t
	Pil 17-10	Pillow basalt	11.1	$\pm$ 2.6			117	1604	0.07	t		t	t
	Pil 16-25	Basalt	14.3	$\pm$ 4.6			59	322	0.18	t		t	t
	179738	Komatiite	11.9	$\pm$ 2.9			22	306	0.07	t		t	t
	Pil 16-53a	Basalt	5.2	$\pm$ 2.6			89	723	0.12	t		t	t
	Pil 16-51	Pillow Basalt	1.1	$\pm$ 3.9			31	122	0.25	t		t	t
	Pil 17-07	Leucogabbro	6.7	$\pm$ 2.6			540	426	1.3	t		t	t
	Pil 16-54a	Basalt	7.0	$\pm$ 1.6			1290	329	3.9	t		t	t
	Pil 16-54b	Pillow basalt	7.8	$\pm$ 2.0			432	294	1.5	t		t	t
	Pil 16-44a	Basalt	9.1	$\pm$ 2.0			950	388	2.4	t		t	t
	Pil 16-24	Basalt	7.4	$\pm$ 2.2			3946	256	15	t		t	t
	Pil 16-39a	Pillow basalt	8.5	$\pm$ 2.1			158	475	0.33	t		t	t
	Pil 16-66b	Olivine komatiite	11.6	$\pm$ 2.0			1162	160	7.3	t		t	t
	160245	Komatiite	6.8	$\pm$ 2.3			19082	370	51.6	t		t	t
70RWD1	Komatiite	9.9	$\pm$ 8.2			101			r		r		
71RWD16	Andesite	11.9	$\pm$ 6.0	-1.8	$\pm$ 4.7	697			r	r	r		
EM62	Komatiitic basalt	8.0	$\pm$ 5.7			73			r		r		
EM65	Komatiitic basalt	10.1	$\pm$ 5.4	-0.3	$\pm$ 4.7	101			r	r	r		
EM70	Komatiitic basalt	5.7	$\pm$ 3.4			47			r		r		
EM71	Komatiitic basalt	7.2	$\pm$ 4.1	-1.6	$\pm$ 4.7	50			r	r	r		
EM78	Komatiitic basalt	9.3	$\pm$ 3.3			70			r		r		
Komati	BV 02	Olivine spinifex	2.6	$\pm$ 5.8			30	223	0.13	u		u	v
	BV 09	Olivine spinifex	2.9	$\pm$ 7.3			27			u		u	
	BV 14A	Olivine cumulate	5.2	$\pm$ 3.9			99			u		u	
	BV 14B	Olivine cumulate	0.2	$\pm$ 7.1			32			u		u	
Kostomuksha	KGB 9496	Olivine spinifex	13.7	$\pm$ 3.4	1.0	$\pm$ 5.0	103	60	1.7	u	bg	u	w
	KGB 94100	Olivine cumulate	15.1	$\pm$ 3.5			78	42	1.9	u		u	w
	KGB 94114	Olivine spinifex	13.6	$\pm$ 4.6			47	56	0.84	u		u	w
	KGB 94123	Olivine spinifex	15.2	$\pm$ 5.0			43	64	0.67	u		u	w
	KGB 9495	Olivine spinifex	18.3	$\pm$ 4.7			44			u		u	
	KGB 94126	Olivine cumulate	15.0	$\pm$ 8.2			71			u		u	
KGB 9497	Olivine spinifex	15.8	$\pm$ 1.7			53			u		u		
Boston Creek	BC 03	Komatiitic basalt	14.6	$\pm$ 3.4	-1.5	$\pm$ 3.5	247	940	0.26	x	x	x	x
	BC 01	Komatiitic basalt	7.5	$\pm$ 3.5	-4.4	$\pm$ 1.9	389	936	0.42	x	x	x	x
	BC 02	Komatiitic basalt	16.9	$\pm$ 2.8	-2.9	$\pm$ 2.0	345	936	0.37	x	x	x	x
	BC 06	Komatiitic basalt	11.2	$\pm$ 3.1	-4.7	$\pm$ 2.1	477	851	0.56	x	x	x	x
	BC 07	Komatiitic basalt	12.4	$\pm$ 4.8			622	384	1.6	x		x	x
	BC 08	Komatiitic basalt	10.6	$\pm$ 2.7	-3.8	$\pm$ 2.5	460	271	1.7	x	x	x	x
	BC 09	Komatiitic basalt	8.3	$\pm$ 2.6	-5.4	$\pm$ 2.1	813	372	2.2	x	x	x	x
	BC 10	Komatiitic basalt	13.9	$\pm$ 3.3	-5.0	$\pm$ 2.8	316	289	1.1	x	x	x	x
Vetreny Belt	average	Komatiitic basalts	-0.5	$\pm$ 4.5						y			
Otong Java	192-1187A-009R-04R	Flood Basalt	23.9	$\pm$ 5.3			23			z		z	
	192-1187A-009R-04W	Flood Basalt	-0.4	$\pm$ 5.1			16			aa		aa	
Discovery	EW9309 5D 5g		-7.9	$\pm$ 3.6			176			ay		ay	
	EW9309 3D 3g		-5.2	$\pm$ 2.7			78			ay		ay	
	EW9309 4D 2g		-5.2	$\pm$ 2.8			138			ay		ay	
	EW9309 3D 1g		-6.3	$\pm$ 2.8			139			ay		ay	
	EW9309 4D 3g		-9.0	$\pm$ 2.7			155			ay		ay	
East Pacific Rise	VE-32	Mid-ocean ridge basalt	-0.8	$\pm$ 4.5			54	353	0.15	z		z	ab

Table B2: continued

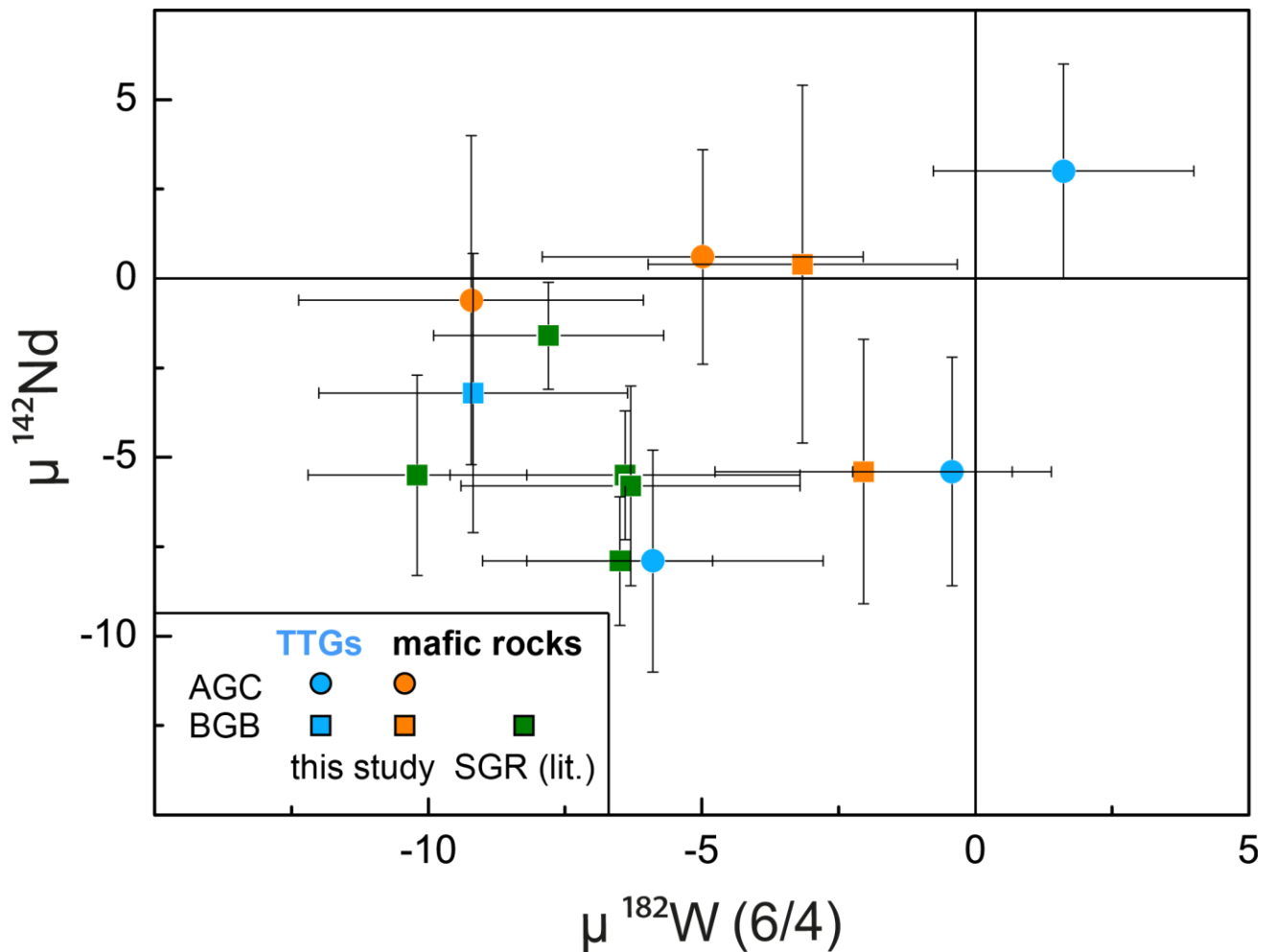
locality	sample #	rock type	$\mu^{182}\text{W}$ $\pm$	$\mu^{142}\text{Nd}$ $\pm$	W [ng/g]	Th [ng/g]	W/Th	references			
								$\mu^{182}\text{W}$	$\mu^{142}\text{Nd}$	W	Th
Caroline	<b>PON-13-13</b>		<b>-3.1</b> $\pm$ <b>5.0</b>		150	3200	<b>0.05</b>	ay	ay	ay	
	<b>KOS-13-19</b>		<b>-4.6</b> $\pm$ <b>4.0</b>		91	1900	<b>0.05</b>	ay	ay	ay	
	KOS-13-4		-3.6 $\pm$ 4.0		84	6900	0.01	ay	ay	ay	
Iceland plume	<b>SNS214</b>	<b>Basalt</b>	<b>-0.7</b> $\pm$ <b>3.5</b>		398	2260	<b>0.18</b>	ad	ad	ae	
	<b>400230</b>	<b>Picrite</b>	<b>-1.8</b> $\pm$ <b>4.5</b>		22	227	<b>0.10</b>	ad	ad	ag	
	<b>332901</b>	<b>Picrite</b>	<b>-6.2</b> $\pm$ <b>4.5</b>		38	352	<b>0.11</b>	ad	ad	ag	
	<b>332788</b>	<b>Picrite</b>	<b>-4.8</b> $\pm$ <b>4.5</b>		36	389	<b>0.09</b>	ad	ad	ah	
	<b>228055</b>	<b>Basalt</b>	<b>-4.7</b> $\pm$ <b>4.5</b>		103	700	<b>0.15</b>	ad	ad	af	
	<b>SNS206</b>	<b>Basalt</b>	<b>-0.6</b> $\pm$ <b>4.5</b>		380	1580	<b>0.24</b>	ad	ad	ae	
	<b>ICE-14-16</b>	<b>Basalt</b>	<b>-11.7</b> $\pm$ <b>4.5</b>		74	900	<b>0.08</b>	ad	ad	ay	
	Pi-23a	Flood Basalt	11.9 $\pm$ 5.9		62			z		z	
	Pi 23b	Flood Basalt	8.3 $\pm$ 5.6		62			z		z	
	Pd-2	Flood Basalt	48.4 $\pm$ 4.6		26			z		z	
	408614	Basalt	-7.1 $\pm$ 4.0		59			ac		ac	
	408616	Basalt	-9.3 $\pm$ 2.9		34			ad		ad	
	408617	Basalt	-7.2 $\pm$ 4.5		48			ad		ad	
	ICE-14-18	Basalt	-4.5 $\pm$ 4.5		62			ad		ad	
	ICE-14-27	Basalt	-6.5 $\pm$ 3.3		49			ad		ad	
	ICE-14-29	Basalt	-8.7 $\pm$ 2.8		46			ad		ad	
	ICE-16-03	Basalt	-7.8 $\pm$ 4.5		33			ad		ad	
	A27	Basalt	-4.8 $\pm$ 4.2		117			ad		ad	
	ICE-14-32A	Basalt	1.7 $\pm$ 4.4		9			ac		ac	
	STAP-1	Basalt	-3.5 $\pm$ 3.4		285			ad		ad	
	THOR-1	Basalt	-12.9 $\pm$ 3.6		339			ad		ad	
	TRI-1	Basalt	-11.2 $\pm$ 4.5		290			ad		ad	
TRI-2	Basalt	-9.5 $\pm$ 4.5		199			ad		ad		
227987	Basalt	-2.6 $\pm$ 4.5		126			ad		ad		
Kerguelen	CT02-358	Alkaline basalt	-8.4 $\pm$ 4.0		387			s		s	
	CT02-548	Alkaline basalt	-15.2 $\pm$ 4.6		299			s		s	
	TC06-03	Alkaline basalt	-11.9 $\pm$ 4.7		589			s		s	
Mangaia	<b>MG 1001-1</b>		<b>-2.8</b> $\pm$ <b>5.4</b>		346	1700	<b>0.20</b>	ad	ad	ai	
	<b>MG 1001-8</b>		<b>2.6</b> $\pm$ <b>2.1</b>		305	1700	<b>0.18</b>	ad	ad	ai	
Central Indian Ridge	<b>D9</b>	<b>Mid-ocean ridge basalt</b>	<b>3.5</b> $\pm$ <b>2.5</b>		178	1380	<b>0.13</b>	ad	ad	ak	
Juan Fernandez	<b>PIN-8</b>		<b>-14.7</b> $\pm$ <b>3.8</b>		115	1300	<b>0.09</b>	ay		ay	
	<b>PIN-12</b>		<b>-15.6</b> $\pm$ <b>2.8</b>		175	1400	<b>0.13</b>	ay		ay	
	<b>MF-3</b>		<b>-5.9</b> $\pm$ <b>3.0</b>		220	1500	<b>0.15</b>	ay		ay	
Samoa	<b>AVON3-63-2</b>	<b>Basalt</b>	<b>-4.9</b> $\pm$ <b>2.1</b>		306	2530	<b>0.12</b>	ac	ac	am	
	<b>AVON3-70-9</b>	<b>Basalt</b>	<b>-5.8</b> $\pm$ <b>5.2</b>		523	4290	<b>0.12</b>	ac	ac	an	
	<b>AVON3-71-22</b>	<b>Basalt</b>	<b>-2.8</b> $\pm$ <b>4.0</b>		342	2620	<b>0.13</b>	ac	ac	an	
	<b>AVON3-73-1</b>	<b>Basalt</b>	<b>-7.7</b> $\pm$ <b>3.8</b>		693	6080	<b>0.11</b>	ac	ac	an	
	<b>AVON3-77-1</b>	<b>Basalt</b>	<b>-7.5</b> $\pm$ <b>4.9</b>		720	5140	<b>0.14</b>	ac	ac	ao	
	<b>OFU-04-14</b>	<b>Basalt</b>	<b>-17.3</b> $\pm$ <b>4.7</b>		213	1950	<b>0.11</b>	ac	ac	al	
	<b>OFU-05-18</b>	<b>Basalt</b>	<b>-13.8</b> $\pm$ <b>3.3</b>		414	3960	<b>0.10</b>	ac	ac	al	
	<b>T33</b>	<b>Basalt</b>	<b>-4.6</b> $\pm$ <b>3.5</b>		304	1750	<b>0.17</b>	ac	ac	an	
	ALIA 115-18	Basalt	3.0 $\pm$ 4.5		844			ac		ac	
OFU-04-15	Basalt	-13.7 $\pm$ 4.8			3900		ay		ay		
La Palma	<b>LP 15</b>	<b>Basalt</b>	<b>0.2</b> $\pm$ <b>2.9</b>		855	7562	<b>0.11</b>	u	u	ap	
	<b>LP 15</b>	<b>Basalt</b>	<b>0.1</b> $\pm$ <b>1.8</b>		855	7562	<b>0.11</b>	ac	ac	ap	
	<b>LP 1</b>	<b>Basalt</b>	<b>-0.8</b> $\pm$ <b>0.8</b>		1010	7380	<b>0.14</b>	k+t	t	t	
Galapagos	<b>NSK97-206</b>		<b>-22.7</b> $\pm$ <b>3.3</b>		150	900	<b>0.17</b>	ay	ay	ay	
	<b>NSK97-214</b>		<b>-22.0</b> $\pm$ <b>4.7</b>		227	1300	<b>0.17</b>	ay	ay	ay	
	<b>NSK97-229</b>		<b>-21.1</b> $\pm$ <b>3.2</b>		141	1200	<b>0.12</b>	ay	ay	ay	
	DRFT04-D3-A		-5.2 $\pm$ 2.7		98			ay		ay	
	DRFT04-D4-A		-3.7 $\pm$ 2.9		149			ay		ay	
	W95-59		-4.2 $\pm$ 3.0		126			ay		ay	
Moorea	<b>MO-01-01</b>		<b>-8.2</b> $\pm$ <b>3.6</b>		122	2100	<b>0.06</b>	ay	ay	ay	
Pitcairn	<b>PIT-1</b>	<b>Basalt</b>	<b>-2.7</b> $\pm$ <b>2.4</b>		385	6590	<b>0.06</b>	ac	ac	aq	
	<b>PIT-8</b>	<b>Basalt</b>	<b>-1.9</b> $\pm$ <b>2.0</b>		178	4350	<b>0.04</b>	ac	ac	aq	
	PIT-16		-8.0 $\pm$ 4.5			7600		ay		ay	
Tristan da Cunha	<b>20171</b>	<b>Basalt</b>	<b>-3.3</b> $\pm$ <b>4.5</b>		1143	10100	<b>0.11</b>	e	e	ar	
	110014		-4.4 $\pm$ 3.4		1811			ay		ay	
	110020		-4.8 $\pm$ 3.0		629			ay		ay	

Table B2: continued

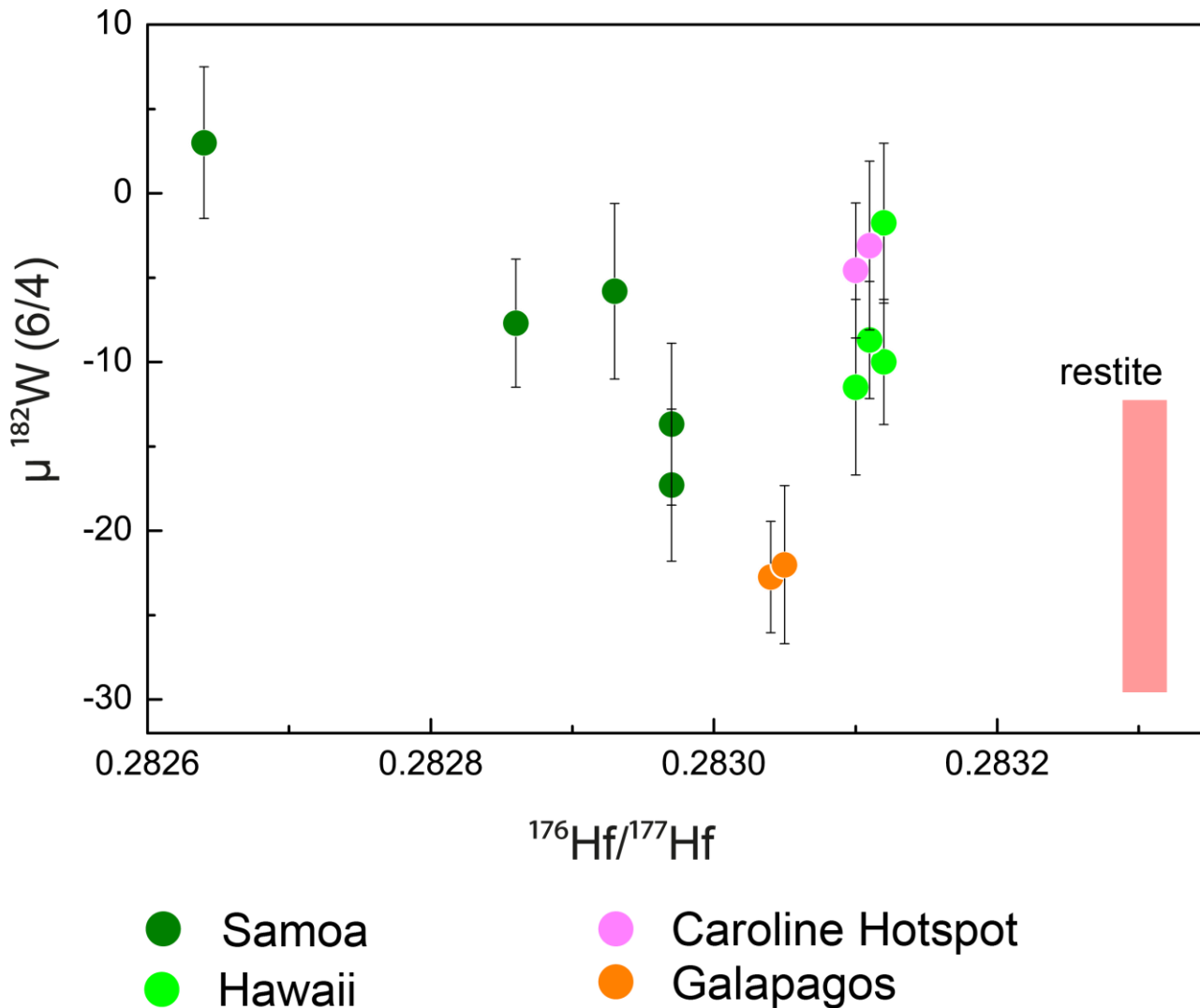
locality	sample #	rock type	$\mu^{182}\text{W}$ $\pm$	$\mu^{142}\text{Nd}$ $\pm$	W [ng/g]	Th [ng/g]	W/Th	references			
								$\mu^{182}\text{W}$	$\mu^{142}\text{Nd}$	W	Th
	<b>MK 1-6</b>	<b>Basalt</b>	<b>-2.3</b> $\pm$ <b>3.1</b>		209	810	<b>0.26</b>	ac	ac	as	
	<b>SR0891-15.10</b>	<b>Basalt</b>	<b>-10.0</b> $\pm$ <b>3.7</b>		90	479	<b>0.19</b>	ac	ac	at	
	<b>SR0750-12.45</b>	<b>Basalt</b>	<b>-11.5</b> $\pm$ <b>5.2</b>		114	623	<b>0.18</b>	ac	ac	at	
	<b>KI81-2-88.6</b>	<b>Basalt</b>	<b>-11.4</b> $\pm$ <b>3.5</b>		935	5310	<b>0.18</b>	ac	ac	au	
	<b>KI67-2-85.7</b>	<b>Basalt</b>	<b>-10.0</b> $\pm$ <b>3.2</b>		967	5190	<b>0.19</b>	ac	ac	au	
	<b>LO-02-02</b>	<b>Basalt</b>	<b>-11.8</b> $\pm$ <b>3.6</b>		173	640	<b>0.27</b>	ac	ac	as	
	<b>BHVO-1</b>	<b>Basalt</b>	<b>-2.3</b> $\pm$ <b>7.7</b>		274	1225	<b>0.22</b>	z	z	av	
	<b>BHVO-2</b>	<b>Basalt</b>	<b>-2.2</b> $\pm$ <b>11.2</b>		251	1224	<b>0.21</b>	aa	av	av	
	<b>BHVO-2</b>	<b>Basalt</b>	<b>-6.5</b> $\pm$ <b>3.1</b>		251	1224	<b>0.21</b>	ac	av	av	
	<b>BHVO-2</b>	<b>Basalt</b>	<b>-6.6</b> $\pm$ <b>3.2</b>		224	1224	<b>0.18</b>	s	s	av	
Hawaii	ML 1868-9	Basalt	-0.3 $\pm$ 3.1		162			ac		aw	
	H-2	Basalt	-13.4 $\pm$ 2.9		97			ac		ac	
	KIL 3-1	Basalt	-8.8 $\pm$ 3.8		230			ac		aw	
	KIL 1840-2	Basalt	-11.9 $\pm$ 4.4		230			ac		aw	
	J2-374-R5	Basalt	-15.2 $\pm$ 5.0		205			ac		ac	
	H27	Basalt	1.0 $\pm$ 1.6		108			q		aw	
	SR0683-5.75	Basalt	-1.8 $\pm$ 4.7			600		ay		ay	
	SR0762-4.6	Basalt	-8.7 $\pm$ 3.5					ay			
	KOH 1-28	Basalt	-5.3 $\pm$ 3.6		157			ay		ay	
	ML 2-50	Basalt	-12.3 $\pm$ 4.3		121			ay		ay	
	LO-02-04	Basalt	-20.2 $\pm$ 9.7		113			ay		ay	
	<b>Reu 1001-053</b>	<b>Basalt</b>	<b>-15.7</b> $\pm$ <b>3.2</b>		317	2280	<b>0.14</b>	s	s	ax	
Reunion	<b>Reu 863-204</b>	<b>Basalt</b>	<b>-8.9</b> $\pm$ <b>2.8</b>		364	2640	<b>0.14</b>	s	s	ax	
	<b>Reu 0609-131</b>	<b>Basalt</b>	<b>-8.2</b> $\pm$ <b>3.3</b>		309	2240	<b>0.14</b>	s	s	ax	
	Reu 1406-24.9	Basalt	-20.2 $\pm$ 5.1		320			s		s	
Azores	ACO 2000-52		-9.9 $\pm$ 4.5		271			ay		ay	
	116420		1.3 $\pm$ 3.2		347			ay		ay	
Mac Donald Seamount	<b>SO47 64DS2</b>		<b>-8.7</b> $\pm$ <b>4.5</b>		799	3800	<b>0.21</b>	ay		ay	ay
	<b>HB 24A</b>		<b>-18.3</b> $\pm$ <b>3.7</b>		950	9100	<b>0.10</b>	ay		ay	ay
Heard	65054		-14.2 $\pm$ 4.5		1035			ay		ay	
	65085		-6.3 $\pm$ 4.5		459			ay		ay	
	HD11		-7.1 $\pm$ 4.5		838			ay		ay	

Table B2: continued

## Appendix C



**Fig. C1: Compilation of  $\mu^{182}\text{W}$  and  $\mu^{142}\text{Nd}$  for crustal and mantle derived rocks from the Kaapvaal Craton.** The  $^{142}\text{Nd}$  isotope compositions for samples from our study were previously reported in Schneider et al. (2018) and combined  $^{182}\text{W} - ^{142}\text{Nd}$  systematics for komatiites from the Schapenburg Greenstone Remnant (SGR) were taken from Puchtel et al. (2016a). The combined data show a tendency towards negative anomalies but reveal no clear correlation due to the comparatively large uncertainties.



**Fig. C2: Compilation of  $^{182}\text{W}$  and  $^{176}\text{Hf}$  isotope compositions for modern OIBs.** Data were compiled from Mundl-Petermeier et al. (2020) and references therein. As for  $\mu^{182}\text{W}$  vs.  $^{143}\text{Nd}/^{144}\text{Nd}$  (see Fig. 3.4) the global compilation for modern OIBs displays a similar trend for  $\mu^{182}\text{W}$  vs.  $^{176}\text{Hf}/^{177}\text{Hf}$ , although only poorly constrained by less available  $^{176}\text{Hf}$  isotope data. Also shown is the present  $^{182}\text{W}$  and  $^{143}\text{Nd}$  isotope composition calculated for restites that remained after prolonged TTG formation (4.35 – 4.25 Ga) via partial anatexis of a mafic protocrust that formed between 40 and 50 Ma after solar system formation (red pale array).

Ancient Gneiss Complex									
Sample	AGC 351	AGC 352	AGC 445	AGC 473	AGC 83	AGC 86	AGC 38	AGC 350	AGC 222
Formation	Ngwane Gnei:	Ngwane Gnei:	Piggs Peak	Dwalile	Dwalile	Dwalile	Dwalile komatiitic	Mtimate River	Kubuta
Rock type	grey gneiss	grey gneiss	grey gneiss	thronhjemitic	komatiite	komatiite	basalt	foliated metag	amphibolite
Age (Ma)	3455	3442	3216	3241	3460	3460	3460	3455	>3400
<b>Major elements (wt. %)</b>									
SiO <sub>2</sub>	80.9	70.1	58.0	68.7	38.0	38.3	53.7	55.4	46.8
TiO <sub>2</sub>	0.210	0.493	1.15	0.487	0.390	0.240	0.580	1.08	1.66
Al <sub>2</sub> O <sub>3</sub>	9.70	14.7	18.4	16.4	2.50	1.85	5.26	15.0	14.6
Fe <sub>2</sub> O <sub>3</sub>	1.34	4.19	7.46	3.18	5.48	8.52	1.77	9.89	15.4
FeO	n.d.	n.d.	n.d.	n.d.	6.10	4.15	8.45	n.d.	n.d.
MnO	0.0300	0.0604	0.0813	0.0405	0.170	0.20	0.270	0.131	0.201
MgO	0.640	1.48	1.93	0.862	33.4	34.3	13.0	6.38	7.16
CaO	0.380	2.49	5.76	2.96	1.34	0.20	13.8	7.00	10.9
K <sub>2</sub> O	2.38	1.44	1.59	1.76	0.040	0.010	0.110	1.46	2.11
Na <sub>2</sub> O	3.73	4.92	5.31	5.50	0.020	0.010	1.46	3.49	0.803
P <sub>2</sub> O <sub>5</sub>	n.d.	4.92	0.345	0.152	0.040	0.040	0.050	0.158	0.301
LOI	0.530	0.131	0.345	0.152	12.5	11.8	1.56	0.158	1.140
<b>Total</b>	<b>99.8</b>	<b>100.0</b>	<b>100.0</b>	<b>100.0</b>	<b>99.9</b>	<b>99.6</b>	<b>99.9</b>	<b>100.0</b>	<b>100.7</b>
<b>Mg#</b>	<b>51.2</b>	<b>43.73</b>	<b>36.27</b>	<b>37.32</b>	<b>93.0</b>	<b>89.8</b>	<b>94.2</b>	<b>58.65</b>	<b>50.51</b>
<b>Trace elements (ppm)</b>									
Li	13.1	14.0	178	63.4	n.d.	n.d.	n.d.	17.2	12.2
Sc	1.44	5.91	3.27	2.10	13.1	10.6	35.6	25.2	41.0
V	6.21	54.8	104	27.2	n.d.	n.d.	n.d.	152	404
Cr	264	28.8	4.10	7.97	1870	5829	851	205	127
Co	1.09	10.6	15.7	5.23	n.d.	n.d.	n.d.	41.6	62.1
Ni	3.26	17.9	5.23	3.80	2176	2010	321	139	127
Cu	3.57	3.09	37.9	10.5	4.04	1.18	91.5	25.3	100
Zn	33.2	77.7	128	68.4	n.d.	n.d.	n.d.	125	121
Ga	18.6	20.7	22.9	21.0	n.d.	n.d.	n.d.	22.8	18.8
Rb	17.6	38.5	50.6	28.8	0.517	0.713	11.7	56.3	69.4
Sr	29.2	595	499	367	7.75	0.684	69.1	418	143
Y	64.6	16.2	11.7	11.2	4.28	3.31	13.9	39.5	27.4
Zr	589	176	218	183	17.6	9.73	48.0	139	
Nb	35.3	6.95	9.25	8.85	1.26	0.574	2.37	9.34	3.90
Mo	12.3	0.254	0.565	0.243	n.d.	n.d.	n.d.	0.170	0.304
Cd	0.337	0.132	0.325	0.157	n.d.	n.d.	n.d.	0.200	0.167
Sn	2.86	1.55	3.52	1.77	n.d.	n.d.	n.d.	1.69	0.370
Sb	0.0495	0.0689	0.0442	0.0367	n.d.	n.d.	n.d.	0.0400	0.0691
Cs	0.607	0.760	13.8	2.46	0.827	0.226	0.516	0.850	2.67
Ba	362	376	446	384	1.01	1.32	26.9	234	45.0
La	29.7	20.1	37.3	28.8	1.31	0.712	4.77	12.2	5.30
Ce	58.9	36.5	47.6	37.8	3.46	1.80	11.4	32.7	13.8
Pr	9.76	4.65	9.21	6.20	0.533	0.265	1.64	4.97	2.06
Nd	43.9	18.1	37.5	23.2	2.69	1.29	7.65	24.1	10.2
Sm	10.7	3.73	6.80	4.02	0.798	0.405	2.27	6.54	3.06
Eu	2.32	1.04	1.90	1.07	0.218	0.133	0.730	1.66	1.25
Gd	11.6	3.37	5.26	3.14	0.986	0.557	2.74	7.02	4.01
Tb	1.79	0.510	0.626	0.391	0.151	0.0939	0.446	1.15	0.690
Dy	10.9	2.96	2.70	1.92	0.871	0.584	2.67	7.10	4.58
Ho	2.29	0.580	0.390	0.337	0.170	0.121	0.519	1.41	0.970
Er	6.60	1.60	0.857	0.865	0.478	0.352	1.50	3.81	2.72
Tm	0.968	0.229	0.103	0.119	0.0644	0.0505	0.207	0.540	0.406
Yb	6.64	1.49	0.611	0.725	0.417	0.328	1.35	3.39	2.68
Lu	1.06	0.222	0.0844	0.101	0.0591	0.0459	0.197	0.488	0.418
Hf	16.2	4.47	5.23	4.48	0.486	0.270	1.26	3.15	2.02
Ta	1.00	0.544	0.486	0.786	0.0951	0.0318	0.163	0.483	0.230
W	13.2	0.144	0.293	0.120	n.d.	n.d.	n.d.	0.250	2.31
Tl	0.130	0.285	0.631	0.402	n.d.	n.d.	n.d.	0.280	0.331
Pb	2.53	4.78	9.69	9.87	0.614	0.994	0.831	3.94	5.17
Th	4.33	3.86	4.75	4.71	0.135	0.0728	0.578	0.680	0.440
U	0.568	0.625	2.55	0.838	0.0381	0.0488	0.145	0.260	0.153

**Table C1: Compilation of major, minor and trace element data together with high-precision element concentration data obtained by isotope dilution and isotope compositions for rock samples from the Kaapvaal Craton. n.d. = not determined**

Barberton Greenstone Belt								
Sample	BA 132	KS-BA 189 Sandspruit	KS-BA 171 Sandspruit	KS-BA 181	KS-BA 182	ZA-32a	ZA-31a	ZA-38
Formation	Steynsdorp P Fm	Fm tholeiitic	Fm tholeiitic	Theespruit Fn	Theespruit Fn	Komati Fm.	Komati Fm.	Komati Fm.
Rock type	thronthjemite	basalt	basalt	amphibolite	amphibolite	tholeiite	tholeiite	komatiite
Age (Ma)	3509	3553	3553	3530	3530	3482	3482	3482
<b>Major elements (wt. %)</b>								
SiO <sub>2</sub>	71.9	52.1	54.7	50.8	49.6	52.8	52.6	46.0
TiO <sub>2</sub>	0.295	0.500	0.920	1.31	1.39	0.766	0.664	0.380
Al <sub>2</sub> O <sub>3</sub>	15.3	13.8	13.2	10.9	10.2	12.1	8.56	4.03
Fe <sub>2</sub> O <sub>3</sub>	2.59	10.6	11.9	13.7	14.0	11.5	12.8	11.1
FeO	n.d.	n.d.	n.d.	n.d.	n.d.	n.d.	n.d.	n.d.
MnO	0.0509	0.163	0.304	0.212	0.210	0.192	0.177	0.164
MgO	0.570	10.0	4.53	7.85	10.8	8.88	11.8	25.1
CaO	2.24	10.3	9.64	10.9	9.85	9.59	9.79	7.46
K <sub>2</sub> O	2.10	0.537	1.81	0.368	0.0475	0.16	0.0860	0.0250
Na <sub>2</sub> O	4.94	1.81	0.941	2.21	2.06	3.25	2.43	0.375
P <sub>2</sub> O <sub>5</sub>	0.0611	0.0799	0.0972	0.149	0.199	0.090	0.0740	0.0350
LOI	0.0611	0.0799	1.04	1.24	1.04	0.920	1.15	5.51
Total	100.0	100.0	99.1	99.7	99.4	100.2	100.1	100.2
Mg#	32.65	67.49	45.6	55.7	63.1	62.9	66.9	83.3
<b>Trace elements (ppm)</b>								
Li	111	n.d.	n.d.	n.d.	n.d.	5.76	6.92	12.3
Sc	1.86	30.3	29.7	44.1	25.8	27.1	28.2	13.4
V	14.9	165	282	255	158	218	198	71.6
Cr	5.16	n.d.	123	592	1197	691	2167	1563
Co	3.00	58.6	46.8	63.9	69.0	52.1	60.8	108
Ni	4.09	n.d.	78.9	178	453	173	251	1717
Cu	8.16	67.4	89.3	135	125	123	132.6	23.7
Zn	48.5	74.5	127	164	145	74.4	85.4	55.8
Ga	20.2	12.7	15.5	17.5	14.5	11.4	10.7	3.05
Rb	33.0	n.d.	59.0	6.07	n.d.	2.71	2.73	2.23
Sr	312	182	86.4	142	396	198	140	8.11
Y	13.4	16.7	20.4	40.5	34.0	18.5	15.6	4.77
Zr	170	65.5	61.5	158	155	66.5	61.0	14.7
Nb	9.20	3.10	2.69	10.0	13.3	3.66	3.58	0.827
Mo	0.117	0.513	0.970	0.788	1.12	0.336	0.536	0.172
Cd	0.155	0.0949	n.d.	n.d.	n.d.	n.d.	n.d.	n.d.
Sn	0.184	0.568	0.905	1.70	3.44	0.623	0.522	0.145
Sb	0.295	n.d.	0.0455	0.0964	0.164	0.0631	0.181	0.761
Cs	6.38	n.d.	n.d.	n.d.	0.163	0.272	0.306	1.11
Ba	479	89.1	73.4	32.4	10.9	53.9	65.3	15.3
La	19.6	8.71	4.42	12.9	17.8	4.40	4.66	1.07
Ce	25.4	18.0	11.2	30.1	40.9	11.3	11.9	2.78
Pr	4.11	2.22	1.62	4.16	5.57	1.66	1.74	0.408
Nd	15.2	9.08	7.50	18.4	24.1	7.94	8.19	1.98
Sm	2.91	2.18	2.22	5.12	5.78	2.29	2.23	0.605
Eu	0.735	0.600	0.893	1.41	1.75	0.756	0.769	0.226
Gd	2.58	2.52	2.36	5.14	6.01	2.84	2.61	0.763
Tb	0.390	0.405	0.532	0.993	0.958	0.496	0.443	0.133
Dy	2.29	2.71	3.59	6.38	5.84	3.28	2.83	0.860
Ho	0.454	0.586	0.769	1.36	1.21	0.688	0.588	0.177
Er	1.29	1.69	2.16	3.73	3.24	1.94	1.63	0.482
Tm	0.193	0.255	0.327	0.553	0.477	0.290	0.240	0.0709
Yb	1.30	1.68	2.09	3.52	3.02	1.92	1.56	0.454
Lu	0.221	0.251	0.312	0.508	0.435	0.298	0.239	0.0686
Hf	4.34	1.78	1.92	4.06	3.89	1.63	1.47	0.379
Ta	0.921	0.202	0.210	0.592	0.819	0.216	0.217	0.0494
W	0.392	0.294	0.406	0.743	0.297	0.105	0.179	0.197
Tl	0.336	n.d.	n.d.	n.d.	n.d.	0.0280	0.0250	0.0465
Pb	6.79	2.43	2.33	4.02	n.d.	0.707	0.486	0.302
Th	3.73	1.43	0.477	1.76	2.12	0.403	0.495	0.0842
U	0.705	0.203	0.109	0.400	0.505	0.101	0.106	0.0233

Table C1: continued



<b>Ancient Gneiss Complex</b>									
<b>Sample</b>	AGC 351	AGC 352	AGC 445	AGC 473	AGC 83	AGC 86	AGC 38	AGC 350	AGC 222
<b>Formation</b>	Ngwane Gneiss	Ngwane Gneiss	Pigg's Peak	Dwalile	Dwalile	Dwalile	Dwalile	Mtimane River	Kubuta
<b>Rock type</b>	grey gneiss	grey gneiss	grey gneiss	grey gneiss	komatiite	komatiite	komatiitic basalt	metagabbro	amphibolite
<b>Age (Ma)</b>	3455	3442	3216	3241	3460	3460	3460	3455	>3400
<b>High-precision element concentration data obtained by isotope dilution technique</b>									
Zr - ID	<i>n.d.</i>	176	<i>n.d.</i>	<i>n.d.</i>	18.3	8.26	34.3	<i>n.d.</i>	<i>n.d.</i>
Nb - ID	<i>n.d.</i>	6.95	<i>n.d.</i>	<i>n.d.</i>	1.44	0.484	1.92	<i>n.d.</i>	<i>n.d.</i>
Nd - ID	65.2	18.4	37.5	30.5	2.52	1.24	6.98	22.4	9.41
Sm - ID	14.6	3.71	6.80	4.93	0.743	0.377	1.99	6.09	2.85
Lu - ID	1.38	0.222	0.0840	0.111	<i>n.d.</i>	0.0456	0.193	0.488	0.414
Hf - ID	16.9	4.47	5.23	4.62	<i>n.d.</i>	0.260	1.23	3.12	2.22
Ta - ID	<i>n.d.</i>	0.544	<i>n.d.</i>	<i>n.d.</i>	0.0882	0.0287	0.117	<i>n.d.</i>	<i>n.d.</i>
W - ID	11.0	<i>n.d.</i>	<i>n.d.</i>	<i>n.d.</i>	0.574	0.557	0.262	<i>n.d.</i>	<i>n.d.</i>
Th - ID	<i>n.d.</i>	<i>n.d.</i>	<i>n.d.</i>	<i>n.d.</i>	0.196	0.0923	0.459	<i>n.d.</i>	<i>n.d.</i>
U - ID	<i>n.d.</i>	<i>n.d.</i>	<i>n.d.</i>	<i>n.d.</i>	0.0417	0.0500	0.120	<i>n.d.</i>	<i>n.d.</i>
<b>High-precision isotope compositions</b>									
$\mu^{142}\text{Nd}$		-7.9	-5.4	3.0				-0.6	0.6
$\pm$		3.1	3.2	3.0				4.6	3.0
$\mu^{182}\text{W}$	-0.2	-5.9	-0.5	1.6	-8.2	-5.4	-2.0	-9.2	-4.8
$\pm$	0.3	3.1	1.8	2.4	3.4	1.8	2.9	3.2	2.9
$^{147}\text{Sm}/^{144}\text{Nd}$	0.135	0.122	0.1095	0.0978	0.1783	0.1843	0.1726	0.1642	0.1830
$^{143}\text{Nd}/^{144}\text{Nd}_0$	0.511314	0.511004	0.510736	0.510545	0.51233	0.512378	0.512113	0.511922	0.512410
$\pm$	15	16	7	6	26	8	8	10	8
$\epsilon^{143}\text{Nd}(t)$	1.5	1.1	-1.1	-1.0	2.1	0.5	0.4	0.5	1.6
$^{176}\text{Lu}/^{177}\text{Hf}_0$	0.01163	0.007050	0.002289	0.003429	0.01673	0.02487	0.02229	0.02220	0.02647
$^{176}\text{Hf}/^{177}\text{Hf}_0$	0.281427	0.281174	0.280854	0.280894	0.281802	0.282343	0.282100	0.282105	0.282472
$\pm$	7	6	11	7	13	5	8	5	7
$\epsilon\text{Hf}(t)$	3.8	5.4	0.2	-0.3	5.1	5.0	2.5	2.8	6.0
<b>references</b>									
age	a	b	e	e	d	d	d	e	b
major	a	c	c	c	d	d	d	c	c
traces	#	b	c	c	d	d	d	c	b
Zr - ID					#	#	#		
Nb - ID					#	#	#		
Nd - ID	a	c	c	c	d	d	d	c	c
Sm - ID	a	c	c	c	d	d	d	c	c
Lu - ID	a	c	c	c	d	d	d	c	c
Hf - ID	a	c	c	c	d	d	d	c	c
Ta - ID					#	#	#		
W - ID	#				#	#	#		
Th - ID					#	#	#		
U - ID					#	#	#		
$\mu^{142}\text{Nd}$		c	c	c				c	c
$\mu^{182}\text{W}$	#								
$\epsilon^{143}\text{Nd}(t)$	a	c	c	c	d	d	d	c	c
$\epsilon\text{Hf}(t)$	a	c	c	c	d	d	d	c	c
		# chapter 3				c - Schneider et al., 2018			
		a - Kröner et al., 2014				d - Hofmann et al., 2020 in Review			
		b - Hoffmann et al., 2016				e - Schneider et al., 2019			

Table C1: continued

Barberton Greenstone Belt								
<b>Sample</b>	BA 132	KS-BA 189	KS-BA 171	KS-BA 181	KS-BA 182	ZA-32a	ZA-31a	ZA-38
<b>Formation</b>	Steynsdorp Pluton	Sandspruit	Sandspruit	Theespruit	Theespruit	Komati	Komati	Komati
<b>Rock type</b>	thronhjemitite	tholeiitic basalt	tholeiitic basalt	amphibolite	amphibolite	tholeiite	tholeiite	komatiite
<b>Age (Ma)</b>	3509	3553	3553	3530	3530	3482	3482	3482
<b>High-precision element concentration data obtained by isotope dilution technique</b>								
Zr - ID	<i>n.d.</i>	<i>n.d.</i>	<i>n.d.</i>	<i>n.d.</i>	<i>n.d.</i>	57.5	50.1	22.2
Nb - ID	<i>n.d.</i>	<i>n.d.</i>	<i>n.d.</i>	<i>n.d.</i>	<i>n.d.</i>	3.22	2.90	1.30
Nd - ID	18.1	8.42	6.99	16.9	22.2	7.31	7.51	3.57
Sm - ID	3.38	1.99	2.07	4.58	5.27	2.10	2.02	1.05
Lu - ID	0.217	0.257	0.311	0.515	0.444	0.295	0.235	0.120
Hf - ID	4.20	1.77	1.85	4.01	3.85	1.70	1.52	0.700
Ta - ID	<i>n.d.</i>	<i>n.d.</i>	<i>n.d.</i>	<i>n.d.</i>	<i>n.d.</i>	0.216	0.213	0.0895
W - ID	<i>n.d.</i>	<i>n.d.</i>	<i>n.d.</i>	<i>n.d.</i>	<i>n.d.</i>	0.0891	0.152	0.330
Th - ID	<i>n.d.</i>	<i>n.d.</i>	<i>n.d.</i>	<i>n.d.</i>	<i>n.d.</i>	<i>n.d.</i>	<i>n.d.</i>	<i>n.d.</i>
U - ID	<i>n.d.</i>	<i>n.d.</i>	<i>n.d.</i>	<i>n.d.</i>	<i>n.d.</i>	<i>n.d.</i>	<i>n.d.</i>	<i>n.d.</i>
<b>High-precision isotope compositions</b>								
$\mu^{142}\text{Nd}$	-3.2	0.4				-5.4		
$\pm$	3.9	5.0				3.7		
$\mu^{182}\text{W}$	-9.2	-3.2	-2.4	0.8	-0.2	-2.0	-5.6	-2.6
$\pm$	2.8	2.8	1.7	3.3	2.0	2.7	1.4	2.3
$^{147}\text{Sm}/^{144}\text{Nd}$	0.1125	0.1426	0.1789	0.1634	0.1431	0.1738	0.1626	0.1782
$^{143}\text{Nd}/^{144}\text{Nd}_0$	0.510663	0.511431	0.512247	0.511827	0.511384	0.512134	0.511874	0.512261
$\pm$	6	7	11	8	6	8	7	5
$\epsilon^{143}\text{Nd}(t)$	-0.4	1.1	0.3	-0.8	-0.2	0.3	0.4	0.8
$^{176}\text{Lu}/^{177}\text{Hf}_0$	0.007347	0.02059	0.02386	0.01824	0.01637	0.02463	0.02184	0.02432
$^{176}\text{Hf}/^{177}\text{Hf}_0$	0.281013	0.281991	0.282196	0.281752	0.281651	0.282255	0.282065	0.282254
$\pm$	6	11	11	7	9	5	6	4
$\epsilon\text{Hf}(t)$	0.1	3.5	2.8	0.5	1.4	2.6	2.5	3.3
<b>references</b>								
age	e	e	e	e	e	e	e	e
major	c	c	e	e	e	c	e	e
traces	c	c	e	e	e	c	e	e
Zr - ID						#	#	#
Nb - ID						#	#	#
Nd - ID	#	c	e	e	e	c	e	e
Sm - ID	#	c	e	e	e	c	e	e
Lu - ID	#	c	e	e	e	c	e	e
Hf - ID	#	c	e	e	e	c	e	e
Ta - ID						#	#	#
W - ID						#	#	#
Th - ID								
U - ID								
$\mu^{142}\text{Nd}$	c	c				c		
$\mu^{182}\text{W}$								
$\epsilon^{143}\text{Nd}(t)$	c	c	e	e	e	c	e	e
$\epsilon\text{Hf}(t)$	c	c	e	e	e	c	e	e
		# chapter 3				c - Schneider et al., 2018		
		a - Kröner et al., 2014				d - Hofmann et al., 2020 in Review		
		b - Hoffmann et al., 2016				e - Schneider et al., 2019		

Table C1: continued

## Acknowledgements

I would like to express my special thanks to Carsten Munker, Peter Sprung, and Elis Hoffmann.

I thank Carsten, who supported and mentored me not only throughout the course of this project but also since the first year of my studies. He has been a constant source of knowledge, support and great discussions and I always benefited greatly from his guidance. His door was always open to me and other colleagues. His stoic peace of mind often calmed me down in times I lost my temper. Having you as a colleague makes me feel confident about looking into the future. I am very much looking forward into follow-up projects and our future work! Thank you so much for this great PhD with all the field campaigns and conferences.

Without Peters great help during the development of our analytical protocol for high precision  $^{182}\text{W}$  isotope measurements the project would not have started so well. He provided invaluable assistance in the lab, taught me how to have patience during all the innumerable yield tests and greatly contributed to the development of our separation procedure. I always enjoyed the instructive time we spent together in front of the mass spectrometers – this was a great experience. Peter is one of the most careful and precise scientists I have met. I benefited so much from discussions with him and I am glad our paths crossed in Cologne!

I was an undergraduate student when Elis taught me how to work in the clean lab; and he taught me how to work independently straight away. This was the best thing that could have happened to me because I gained a lot of practical experience very early. I am very thankful that he gave me this opportunity. I am grateful for encouraging me to work on Archean rocks. I have rarely met a person that is so energetic and creative than Elis – working with him is confusing and fascinating at the same time. It is often difficult to follow his thoughts but discussing with him always provides new impulses and positive impetus. Chapter 3 benefited greatly from discussions with Elis and his ideas paved the way for the geodynamic model that we propose for the Kaapvaal Craton.

I would like to thank Martin Van Kranendonk for showing us the amazing geology of the Pilbara Craton and the beautiful nature of NW Australia during two field campaigns in 2016 and 2017. I always enjoyed spending time with you in the field.

Special thanks to Frank Wombacher for managing the clean lab and for keeping ICap-Q, both Neptune MC-ICP-MS and many other equipment in excellent conditions.

I thank Chris Marien for all the great time we shared over the past 10 years. Discussions with you were always stimulating and you were a great help. We have taken our first steps together and I hope that our paths will cross in the future.

I would like to acknowledge Mike Jansen who provided important assistance in the lab, especially during our second project. You have been a great help and I am pleased that you started your own  $^{182}\text{W}$  isotope projects.

There is a very long list of other colleagues who have contributed to my growth in this project. Thanks to Kristoffer Szilas for introducing me into how to conduct field work in SE Greenland and for a very fruitful collaboration. Many thanks to Florian Kurzweil. I always appreciate your perspective and I am happy that you were my office mate. Your comments on my manuscripts (especially the Pilbara manuscript) greatly improved this PhD thesis. I am grateful to Mario Fischer-Gödde for helpful discussions. I have often benefitted from your experience and enjoyed sharing the lab with you. I thank Eric Hasenstab for very inspiring discussions on all kind of topics. Your perspective was always helpful.

I would further like to thank Markus Pfeifer, Bo-Magnus Elfers, Raul Fonseca, Sebastian Kommescher, Ninja Braukmüller, Alessandro Bragagni, Maxwell Thiemens, Julia van de Löcht, Jens Barosch, Sebastian Viehmann, Ramon Reifenröther, Christiane Schnabel, Daniela Hülle, Almut Katzemich. Thank you for your support and encouragement. I very much enjoyed our interactions.

Financial support for this thesis has been provided by the German Research Foundation (DFG, grant no. MU 1406/18-1) to C. Münker as part of the priority program 1833 "*Building a Habitable Earth*", and through the European Commission by ERC grant 669666 '*Infant Earth*'.

## Erklärung

Ich versichere, dass ich die von mir vorgelegte Dissertation selbstständig angefertigt, die benutzten Quellen und Hilfsmittel vollständig angegeben und die Stellen der Arbeit – einschließlich Tabellen, Karten und Abbildungen –, die anderen Werken im Wortlaut oder dem Sinn nach entnommen sind, in jedem Einzelfall als Entlehnung kenntlich gemacht habe; dass diese Dissertation noch keiner anderen Fakultät oder Universität zur Prüfung vorgelegen hat; dass sie – abgesehen von unten angegebenen Teilpublikationen – noch nicht veröffentlicht worden ist, sowie, dass ich eine solche Veröffentlichung vor Abschluss des Promotionsverfahrens nicht vornehmen werde. Die Bestimmungen der Promotionsordnung sind mir bekannt. Die von mir vorgelegte Dissertation ist von Prof. Dr. Carsten Münker betreut worden.

Nachfolgend genannte Teilpublikationen liegen vor:

- **J. Tusch**, P. Sprung, J. van de Locht, J.E. Hoffmann, A.J. Boyd, M.T. Rosing, C. Münker (2019), *Geochemica et Cosmochemica Acta* (257), 284-310 - *Uniform  $^{182}\text{W}$  isotope compositions in Eoarchean rocks from the Isua region, SW Greenland: The role of early silicate differentiation and missing late veneer*  
Chapter 1, Appendix A
- **J. Tusch**, C. Münker, E. Hasenstab, M. Jansen, C.S. Marien, F. Kurzweil, M.J. van Kranendonk, H. Smithies, W. Maier, D. Garbe-Schönberg (2021), *Proceedings of the National Academy of Sciences* (118), 1-6 - *Convective isolation of Hadean mantle reservoirs through Archean time*  
Chapter 2, Appendix B
- **J. Tusch**, J.E. Hoffmann, E. Hasenstab, C. Münker (submitted) - *Long-term preservation of Hadean protocrust in Earth's mantle*  
Chapter 3, Appendix C

Datum:

Unterschrift: